IMPROVING PHYSICAL PARAMETERIZATION FOR WARM BIAS OF REGCM4.0 ON ARCTIC AND SUB-ARCTIC (MID, MID-EAST AND NORTHEAST) ASIA REGIONS

by
Tuğba ÖZTÜRK
B.S., Physics, Işık University, 2004
M.S., Physics, Boğaziçi University, 2008

Submitted to the Institute for Graduate Studies in
Science and Engineering in partial fulfillment of
the requirements for the degree of
Doctor of Philosophy

Graduate Program in Physics
Boğaziçi University
2014

ACKNOWLEDGEMENTS

I would like to express my thanks to Prof. Levent Kurnaz for his comments, help and supervision on the topic, and for his trust.

I would like to thank Prof. Murat Türkeş for guidance, his advises, encouraging comments on my faults, his great help and time.

I would like to thank Prof. Metin Arık, Prof. Teoman Turgut and Assoc. Prof. İbrahim Semiz for evaluating my thesis.

I would like to thank Prof. Nafiye Güneç Kıyak for her support and the work opportunity.

I would like to thank my friends Nazan An, Mustafa Tufan Turp and Berna Avcı for their great help and time.

Lastly, I would like to thank my family for their psychological support.

ABSTRACT

IMPROVING PHYSICAL PARAMETERIZATION FOR WARM BIAS OF REGCM4.0 ON ARCTIC AND SUB-ARCTIC (MID, MID-EAST AND NORTHEAST) ASIA REGIONS

In this thesis, the semi-empirical cloudiness parameterization adapted to the regional climate model of the Abdus Salam International Center for Theoretical Physics (ICTP), RegCM to improve the model's ability to simulate the temperature climatology of Central Asia region. The new semi-empirical cloudiness parameterization was tested by using ERA-interim and ERA40 reanalysis data and the global climate model ECHAM5 as the boundary condition for different periods of time. The performance of the regional climate model RegCM in simulating the climate of the region were improved. Investigation of the future temperature and precipitation climatology of Central Asia was done for periods of 2010-2040, 2040-2070 and 2070-2100 with respect to the period of 1970-2000 by using RegCM4.3.5 which was driven by two global climate models. RCP4.5 and RCP8.5 emission scenario (IPCC) output of HadGEM2 and MPI-ESM-MR global climate model were dynamically downscaled to 50 km for the domain. Results showed that strong warming in the winter and a decrease in precipitation in almost all parts of the domain will be seen for the future periods. The future mean air temperature and precipitation climatology and variability were also projected over the Mediterranean region by using A2, A1B and B1 scenario outputs of 16 global climate models. Results showed that strong warming up to 6.5 °C in the summer and lowest warming in the winter season will be observed. Decrease in precipitation will be seen in all seasons excluding the Switzerland and Caucasian region during the winter season for future period of 2070-2100 with respect to reference period of 1970-2000.

ÖZET

REGCM4.0 MODELİNİN ARKTİK VE ALT-ARKTİK (ORTA, ORTADOĞU VE KUZEY DOĞU) ASYA BÖLGELERİNDEKİ SICAKLIĞIN SICAK TARAFA SAPMASINI İYİLEŞTİRMEK İÇİN FİZİKSEL PARAMETRİZASYON GELİŞTİRİLMESİ

Bu çalışmada, Abdus Salam Uluslararası Teorik Fizik Merkezi (ICTP) tarafından geliştirilen bölgesel iklim modelininin Orta Asya bölgesi sıcaklık klimotolojisini benzetme becerisini geliştirmek amacı ile, *yarı ampirik bulutluluk parametrizasyonu* adapte edilmiştir. Yeni yarı ampirik bulutluluk parametrizasyonu farklı zaman periyodları için yeniden analiz edilmiş veri setleri ERA-40 ve ERA-interim ve küresel iklim modeli ECHAM5 sınır koşulları olarak kullanılarak test edildi. Bu kapsamda, bölgesel iklim modeli RegCM'in bölgenin iklimini benzetmedeki performansı arttırıldı. Aynı zamanda Orta Asya bölgesinin gelecek sıcaklık ve yağış klimatolojisi 2010-2040, 2040-2070 ve 2070-2100 periyodları için 1970-2000 normaline göre bölgesel iklim modeline iki farklı küresel model çıktıları girdi olarak verilerek incelenmiştir. MPI-ESM-MR ve HadGEM2 küresel iklim modellerinin RCP4.5 ve RCP8.5 senaryo setleri alt ölçeklendirme yöntemi ile 50 km çözünürlükte koşuldu. Sonuçlar gelecek periyodlar için kış mevsiminde kuvvetli ısınma ve bölgenin büyük bir bölümünde yağışlarda azalma görüleceğini gösterdi. Gelecek ortalama sıcaklık ve yağış klimatolojisi ve değişkenliği projeksiyonları, aynı zamanda Akdeniz Havzası için de 16 küresel iklim modelinin A2, A1B ve B1 senaryo çıktıları kullanarak gerçekleştirildi. Sonuçlar, kuvvetli ısınmanın yazın 1970-2000 normaline göre 2070-2100 gelecek dönemi için 6.5 °C'ye kadar çıkacağını, kışın ise en düşük seviyede olacağını gösterdi. Yağışlardaki azalma kışın İsviçre ve Kafkas bölgesi dışında tüm mevsimlerde görülecek.

TABLE OF CONTENTS

LIST OF FIGURES

LIST OF TABLES

LIST OF SYMBOLS

a	Absorptance
ABE	Buoyant energy available for convection
ABE''	Buoyant energy available for convection
c	Speed of light
C	Heat capacity
C_{acc}	Coefficient of accretion rate
C_{acs}	Autoconversion scale factor
C_D	Drag coefficient
C_{evap}	Rate coefficient
c_{pm}	Specific heat for moist air at constant pressure
C_s	Stratiform cloud amount
D	Diffusion coefficient
ΔA	Horizontal cross sectional area
dq	Differential amount of heat added
dQ	Amount of heat of a closed system
Δt	Time interval
dU	Amount of internal energy of a closed system
dW	Amount of work
Δz	Height
e	Vapor pressure
E	Radiant Emittance
e_s	Saturation vapor pressure
f	Relative humidity-derived low cloud fraction
F	Total diffusive flux
FC	Cloud fraction
F_HT	Effect of horizontal diffusion
F_VT	Effect of vertical mixing and dry convective adjustment
g	Gravitational acceleration
h	Planck constant

I_1	Normalized condensation
I_2	Normalized downdraft evaporation
k	Boltzmann's constant
K_e	Turbulent kinetic energy diffusivity
K_m	Eddy diffusivity
L_f	Latent Heat of fusion
L_λ	Radiance
L_s	Latent heat of sublimation
L_v	Latent Heat of Vaporization
M	Amount of mass
m_0	Downdraft mass flux
m_b	Updraft mass flux
m_i	Molecular weight of a species
m_s	Molecular weight of solute
N	Number of identical molecules
N_a	Avogadro's number
n_s	Number of solute molecules
n_w	Number of water molecules
p	Pressure
P	Precipitation
P_{acc}	Accreted cloud water
P_{evap}	Evaporated precipitation
p_i	Partial pressure
p_s	Surface pressure
P_{sum}	Accumulated precipitation
p_t	Top pressure
q	Grid-box mean specific humidity
q_c	Cloud water or ice mixing ratio
$\bar{q}_l$	Cloud water and ice mixing ratio
q_r	Rain water or snow mixing ratio
q_v	Water vapor mixing ratio

r	Radius
R	Universal gas constant
R_{icr}	Critical bulk Richardson number
R_m	Gas constant for moist air
r_v	Mixing ratio
Re	Reynolds number
RH	Relative Humidity
$\overline{RH}$	Average relative humidity
S_f	Shear frequency
$S_{h,m}$	Stability function
Σp_i	Sum of the pressures
T	Temperature
T_c	Condensation Temperature
T_d	Dew Point Temperature
T_v	Virtual temperature
T_w	Wet Bulb Temperature
U	Grid scale relative humidity
$u(h)$	Horizontal wind component
$v(h)$	Horizontal wind component
V	Volume
w_t	Turbulent convective velocity

β	A portion of the moisture convergence
γ	Environmental lapse rate
γ_C	Countergradient transport term
Γ_d	Dry adiabatic lapse rate
ϵ	Emittance
θ	Potential temperature
θ_v	Virtual potential temperature at the h
λ	Wavelength
μ	Dynamic viscosity of fluid

ν	Number of moles of gas
ρ	Density
σ	Surface tension
τ	Transmittance
ϕ	Specific entropy
ω	Single scattering albedo

LIST OF ACRONYMS/ABBREVIATIONS

AMIP	Atmospheric Model Inter-comparison Project
AOGCMs	Atmosphere-Ocean General Circulation Models
AR4	Fourth Assessment Report
AR5	Fifth Assessment Report
BATS	Biosphere-Atmosphere Transfer Scheme
CCM1	Community Climate Model Version 1
CCM2	Community Climate Model Version 2
CCM3	Community Climate Model Version 3
CLM	Community Land Models
CMIP	Coupled Model Inter-comparison Project
CORDEX	The Coordinated Regional Climate Downscaling Experiment
CRU	Climate Research Unit
DJF	December, January, February
ECHAM5	The fifth generation of the European Centre Hamburg Model
ECMWF	European Center for Medium Range Weather Forecasting
ENIAC	Electronic Numerical Integrator and Computer
ENSIP	El-Nino Simulation Inter-comparison Project
ESMs	Earth System Models
FAR	First Assessment Report
GCMs	General Circulation Models
GHGs	Greenhouse Gases
ICBC	Initial Conditions, Boundary Conditions
ICTP	International Centre for Theoretical Physics
IPCC	Intergovernmental Panel on Climate Change
JJA	June, July, August
LAMs	Limited area models
MAM	March, April, May
MIT	Massachusetts Institute of Technology
MM4	Mesoscale model Version 4

MM5	Mesoscale Model Version 5
NCAR	National Center of Atmospheric Research,USA
NCAR/PSU	National Center for Atmospheric Research / Pennsylvania State University
PMIP	Paleoclimate Modelling Inter-comparison Project
RCM	Regional Climate Model
RegCM	Regional Climate Model
RegCM1	Regional Climate Model version 1
RegCM2	Regional Climate Model version 2
RegCM2.5	Regional Climate Model version 2.5
RegCM3	Regional Climate Model version 3
RegCM4	Regional Climate Model version 4
RCPs	Representative Concentration Pathways
SAR	Second Assessment Report
SMIP	Seasonal Model Inter-comparison Project
SON	September, October, November
SRES	Special Report on Emissions Scenarios
SST	Sea Surface Temperature
SUBEX	Sub-grid Explicit Moisture Scheme
TAR	Third Assessment Report
UCLA	University of California,USA
UNEP	United Nations Environment Program
UNFCCC	United Nations Framework Convention on Climate Change
WCRP	World Climate Research Programme
WMO	World Meteorological Organisation

1. INTRODUCTION

Climate change is one of the most significant and far-reaching challenges that human societies living on the Earth's surface have faced in this century. Climate tends to change on all temporal and spatial scales beyond that of individual weather events due to various factors and mechanisms including natural changes and variability in atmospheric and surface feedbacks and forcing factors associated with internal and/or external interactions. The evidence of human-induced climate change has been getting stronger on different spatial and temporal scales. Climate change has been damaging the ecological, social and economic systems. However, today, climate change is a much more complex issue than it was before the industrial revolution, due mainly to human activities, such as the burning of fossil fuels, industrial processes, mining activities, land-use changes and deforestation.

According to the Fifth Scientific Assessment Report of the Intergovernmental Panel on Climate Change [1], each of the last three decades has been successively warmer at the Earth's surface than any preceding decade since 1850. In the Northern Hemisphere, 1983–2012 was likely the warmest 30–year period of the last 1400 years. According to the report the globally averaged combined land and ocean surface temperature data as calculated by a linear trend, show a warming of 0.85 [0.65 to 1.06] °C, over the period 1880 to 2012, when multiple independently produced datasets exist. The total increase between the average of the 1850–1900 period and the 2003–2012 period is 0.78 [0.72 to 0.85] °C, based on the single longest dataset available.

Thus, it is of great importance to understand and project the nature and magnitude of the changes in the climate. The impacts of climate change on weather events and climate conditions are generally obtained by running general circulation models (GCMs) based on various scenarios, and by statistical and physical/dynamical downscaling of model simulations and projections from these GCMs.

On the other hand, according to the Intergovernmental Panel on Climate Change's

(IPCC) 4th Assessment Report, Central Asia's environment, ecological and socio-economic systems are seriously threatened by climate change, particularly because of the semi-arid nature of the region [2]. Agricultural production in the region has already decreased quantitatively, and water resources are at risk due to climatic change. The region consists mostly of arid and semi-arid lands, grasslands, rangelands, deserts and some woodlands [3–5]. With respect to the climate change in Central Asia, grasslands, livestock and water resources are the most vulnerable entities in the region because they are primarily located in marginal physiographic areas.

Even though the region is vulnerable to climate change, relatively few studies have investigated Central Asia's climatology, including precipitation and temperature [6–8]. Some studies have only focused on parts of the domain, namely the Caspian Sea basin [9, 10], and there have only been a few climate impact studies for the Central Asian region [11]. The Coordinated Regional Climate Downscaling Experiment (CORDEX) is a framework designed to coordinate international efforts on regional climate simulations. CORDEX domains encompass the majority of land areas of the world. Region 8 of the CORDEX covers Central Asia, with the corners of the domain at 54.76° N, 11.05° E; 56.48° N, 139.13° E; 18.34° N, 42.41° E; and 19.39° N, 108.44° E and with a horizontal resolution of 50 km. The main aim of this thesis is to use the regional climate model of the Abdus Salam International Center for Theoretical Physics (ICTP), RegCM, to investigate the ability of the model to simulate the climatology of Region 8 domain (Central Asia) in the CORDEX framework. To date, RegCM 4.0 has been used to study the climatology of 4 domains within the CORDEX framework (Africa, South America, East Asia and Europe) [12]. This is the first time that RegCM was used to simulate the Central Asian region.

Even though this Regional Climate Modeling system has been effectively used for climatic change studies and applications during the last decade [13], it fails to simulate cold climates such as arctic and subarctic regions. Currently, the existing simulations indicate the presence of a warm bias in the arctic and subarctic regions of Central Asia Domain [14]. Results of simulation of temperature climatology for the Central Asia showed that there is a strong warm bias of about 12 °C degrees on the northeastern part

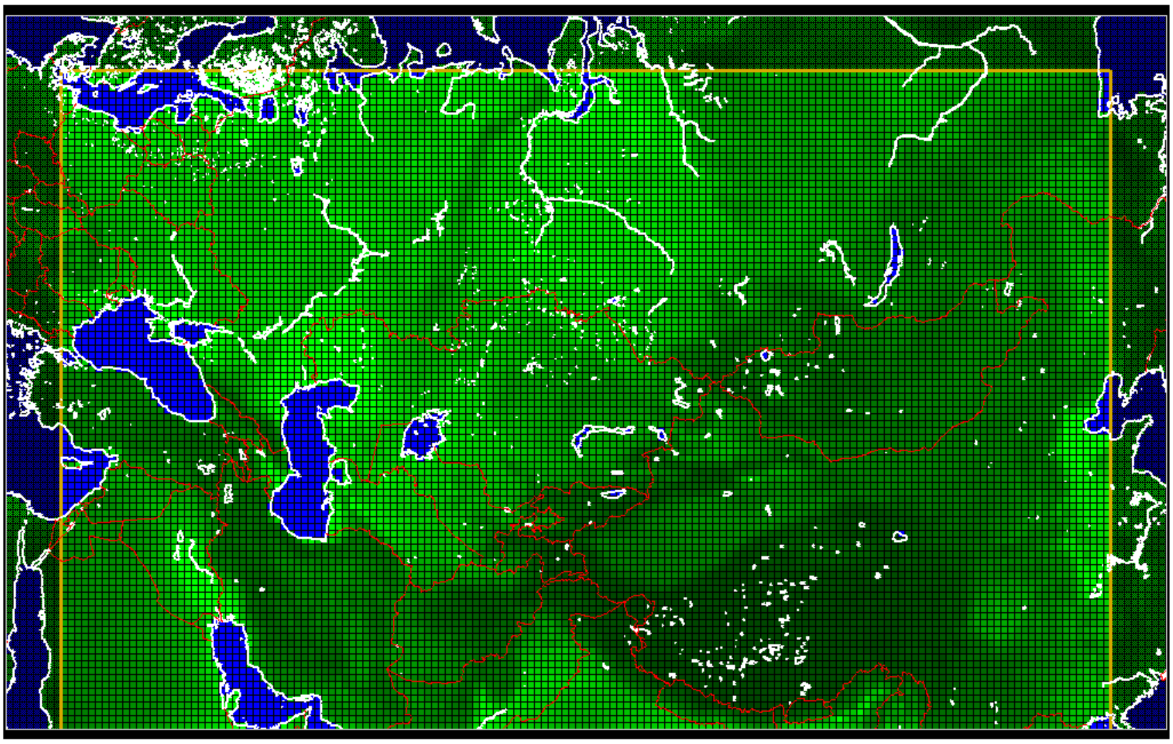

Figure 1.1. CORDEX-Region 8 Central Asia.

of the domain during winter seasons. However, this strong warm bias was inherited from the ERA-Interim reanalysis data since ERA-Interim itself has also warm bias in the northern part of the domain. RegCM4.0 can also not decrease warm bias inherited from forcing data.

Based on the previous studies, cloud fraction schemes which use the relative humidity (RH) are not suitable for regions located on high latitudes due to the extremely cold and dry conditions [15]. In regional climate model, RegCM 4.0, Subgrid Explicit Moisture Scheme (SUBEX) is used to simulate nonconvective clouds. SUBEX computes the subgrid variability in clouds by coupling the relative humidity in the grid cell with the cloud fraction and cloud water [16]. To overcome these deficiencies, Xu and Randall (1996) [17] proposed a new semiempirical cloudiness parameterization. In this thesis, we applied this new cloud fraction parameterization to the regional climate model RegCM in order to improve the ability of the model to simulate cold climates.

With this aim, we have used different forcing datasets for past periods of 1970-2000 and 1989−2010. ERA-40 global reanalysis dataset was used as a forcing data to regional climate model for the period of the years 1970−2000. To compare the results, the ERA-Interim [18] which is the latest reanalysis dataset, was also used as input to RegCM for the period of 1989–2010. To validate the outputs of regional climate model, the observational data (i.e. the Climate Research Unit [CRU] dataset) is used [19]. We also investigated the change in the future temperature and precipitation climatology for the Central Asia domain.

The thesis is comprised of the following sections: the climate system, climate models and predictions, regional climate model RegCM, semiempirical cloudiness parameterization, projections of future temperature and precipitation climatology for the Central Asia, projections of future temperature and precipitation climatology for the Mediterranean Basin and conclusion. In the climate system chapter, components of the climate system, complex interaction among them and physics of climate are described. Climate modeling, climate models, evolution of climate models, model intercomparison projects, reanalysis datasets, and emission scenarios are described in the Chapter 3.

The regional climate model RegCM and the new cloud fraction parameterization are discussed in the Chapters 4 and 5, respectively. The results of simulation of future climate change for the domains Central Asia and Mediterranean are reported in the Chapters 6 and 7 respectively. And finally, results and discussions are given in the conclusion Chapter.

2. THE CLIMATE SYSTEM

The climate system is an interactive system which involves atmosphere, land, ocean; ice on the surface and radiation from the Sun (Figure 2.1). Climate is described as the mean and variability of weather conditions observed over a certain area during a certain time period (usually 30 years). Climate observed on the Earth is the result of the complex interaction among components of climate system and external forcing. External forcing consists of solar variability, volcanic eruptions and human activities changing atmospheric composition. Solar radiation drives the climate system and it is the source of all atmospheric motion. Atmosphere which characterizes the climate is the most important component of the climate system. Solar radiation reaches the surface by passing through the atmosphere. Atmosphere absorbs some portion of this energy and gets warm. Most part of the solar energy is absorbed by the surface. First, the surface is heated and then it heats the air above. This makes the surface the heat source of atmosphere. Unequal distribution of solar energy causes the formation of wind and clouds, horizontal and vertical motion of air.

The atmosphere plays a crucial role in the physical climate system. It is partly responsible for distribution of heat coming from the sun. Dry atmosphere is composed of mainly nitrogen (78.1% volume mixing ratio), oxygen (20.9% volume mixing ratio), argon (0.93% volume mixing ratio) and other gases. Main constituents (O_2,N_2) of the atmosphere does not interact either with the incoming solar radiation (limited interaction) or with the outgoing infrared radiation emitted by the Earth. However, trace gases like carbon dioxide (CO_2), methane (CH_4), nitrous oxide (N_2O) and ozone (O_3), called greenhouse gases, interact with outgoing infrared radiation. Even though their proportion in the atmosphere is less than 0.1% by volume, their concentration is very important since they absorb and emit infrared radiation. On the other hand, water which is the most variable constituent of atmosphere plays an essential role in the energy budget of the Earth. Water is found in atmosphere in various phases such as vapor, cloud droplets and ice. Water vapor is the most dangerous greenhouse gas. The role of clouds in these energy calculations is very difficult and complex to understand.

Water absorbs and releases energy to the system due to transition between its phases. Water is very important for the climate system because of these reasons. Atmosphere is also comprised of solid particles called aerosols which interact with radiation.

The amount of energy which is received from the Sun and is returned to the atmosphere is controlled by vegetation and soil at the land surface. Some of this energy is returned to the atmosphere as long-wave radiation to heat the atmosphere as the surface warms. Some of the energy evaporates the water in the soil and leaves of plants causing water vapor to go back into the atmosphere. Amount of soil moisture is very important for the surface temperature since soil moisture needs energy to evaporate. The texture of the land surface affects the atmosphere as well since wind blows dust from the surface into the atmosphere, dust interacts with the atmospheric radiation as well.

The marine and terrestrial biospheres have a strong influence on the atmospheric composition. The biota can contribute to the uptake and release of greenhouse gases. Significant amount of carbon is stored by both marine and terrestrial plants because of the photosynthetic process. The biosphere is also very important for carbon cycle and budgets of methane and nitrous oxide. Feedbacks between climate change and trace gases in the atmosphere occur because climate affects the storage of carbon and the exchange of trace gases. The affects of climate are conserved as fossils, tree rings, pollen and other records on the biosphere. Such biotic indicators and records tell us about past climatic conditions.

The hydrosphere includes all liquid water such as saline water of oceans and seas, fresh water of rivers, lakes and aquifers. Excess fresh water runoff from land returns to the oceans. It affects circulation of the oceans due to being salt free. Oceans store large quantities of heat and transport it from the warmer parts to cooler parts of the world. They cover 70% of the Earth's surface. They also dissolve and store large amount of carbon dioxide. Wind and density contrasts due to salinity and thermal gradients are responsible for ocean's circulation. It is much slower with respect to the atmospheric circulation. Due to large heat capacity of the oceans, it absorbs heat and work as a compensator of climate and source of natural climate variability.

The cryosphere contains the ice sheets of Greenland, Antarctica and Arctic, continental glaciers and snow fields, sea ice and permafrost. It is also very important for the climate system because of the high reflectivity (albedo) of ice to solar radiation. The cryosphere has low thermal conductivity and large thermal inertia. It is also responsible for deep ocean water circulation. Due to the large amount of water stored in the ice sheets, they control sea level variations as well.

In the climate system which is in an equilibrium state the net radiation at the top of the atmosphere is expected to be zero. This is altered by a change in either the incoming solar radiation or the outgoing infrared radiation. Imbalance in net radiation is called “radiative forcing”. Change in external forcings including the solar radiation or the large amounts of aerosols emitted by volcanic eruption into the atmosphere on different time-scales can also alter the radiative forcing. This change may be negative or positive. A positive radiative forcing tries to warm the surface on average, whereas a negative radiative forcing tends to cool it. Internal processes and feedbacks change radiative balance as well by their effect on reflected incoming solar radiation or outgoing infrared radiation, but these are not considered as a radiative forcing [20].

The climate has changed over the ages, and present day climate is still changing. The primary factors inducing past, present and future climate change are astronomical changes in the Earth’s orbit, changes in the energy output of the Sun, changes in the albedo of the Earth, changes in the composition of the atmosphere, and changes in the ocean circulation. Astronomical changes in the Earth’s orbit called the Milankovitch cycles can be evidence regarding the explanation of long term climate change. Main astronomical changes which can affect the global climate include change in the eccentricity of the ellipse that the Earth describes in its orbit around the Sun (with period of $\sim$ 100000 years), change in the Earth’s obliquity (with period of $\sim$ 41000 years) and change in the precession of the spin axis around the normal to the orbital plane (with period of $\sim 19 - 23000$ years) (Figure 2.2) [22].

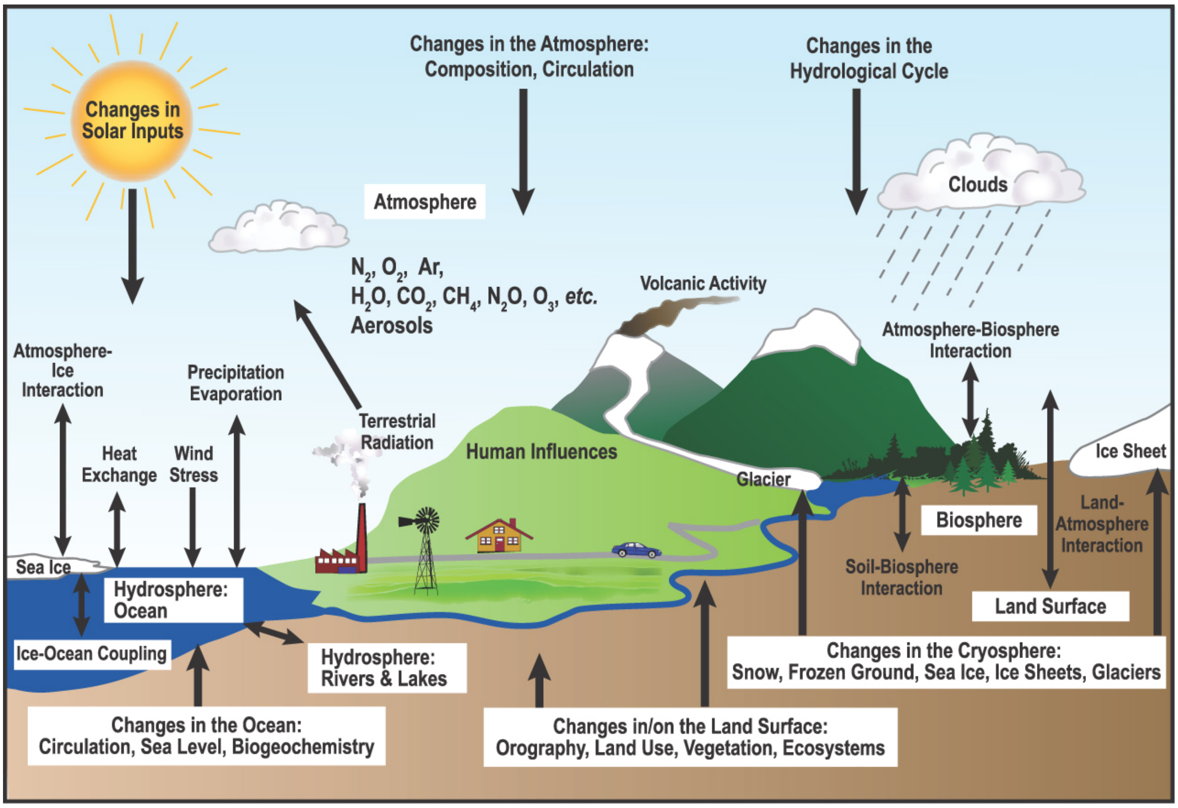

Figure 2.1. A schematic view of interactions among components of the global climate system [21].

Solar radiation runs the global climate system. There are three main factors that change the radiation balance of the Earth such as changes in incoming shortwave radiation from the Sun, changes in albedo of the Earth and changes in outgoing longwave radiation from the Earth. The climate system reacts to these changes through various feedback mechanisms directly or indirectly. Climate feedbacks mechanisms include CO_2 and other greenhouse gases feedback, water vapor feedback, ice-albedo feedback and cloud-albedo or cloud radiative feedback. Increase in concentration of the greenhouse gases in the atmosphere warms the Earth and cause melting of snow and ice sheet. Water vapor feedback has an essential effect on the climate sensitivity. Increase in air temperatures cause increase in vaporization and the amount of water vapor. This is a very good example of positive feedback. Since water vapor is an important greenhouse gas, increase in the amount of water vapor in the atmosphere intensify the greenhouse effect and cause more warming. Melting of snow cover and ice sheet decreases the albedo of the Earth since color of surface of oceans is darker than ice. It also causes more warming as well. Clouds can also form positive or negative feedback mechanism according to their types. High clouds cause positive feedback whereas low clouds cause negative feedback without taking into consideration of day/night effects [22].

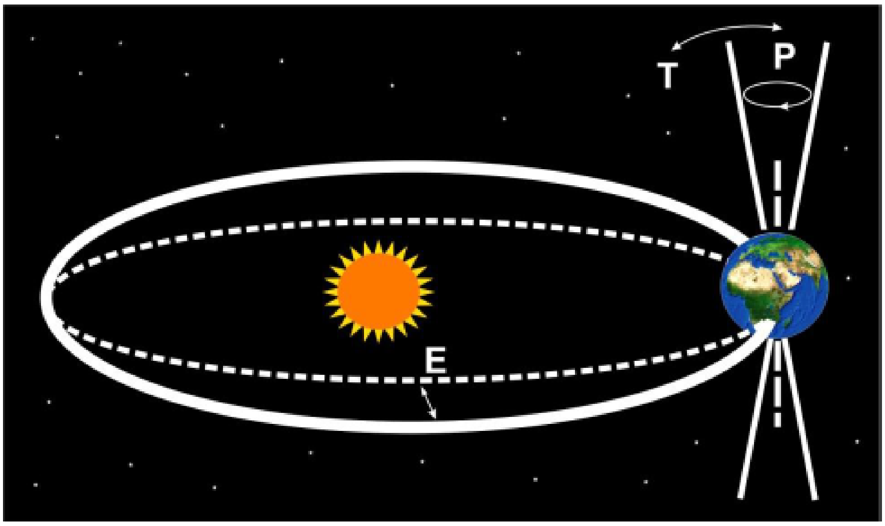

Figure 2.2. The three Milankovitch cycles, in orbital eccentricity, obliquity, and precession of the spin axis [22].

The increase in the concentration of the human induced greenhouse gases in the atmosphere has been observed since the industrial revolution. Mauna Loa Observatory (MLO) has been monitoring and collecting data of atmospheric carbon dioxide (CO_2) since 1958. According to these measurements, atmospheric concentration of carbon dioxide (CO_2) is increasing very fast (Figure 2.3).

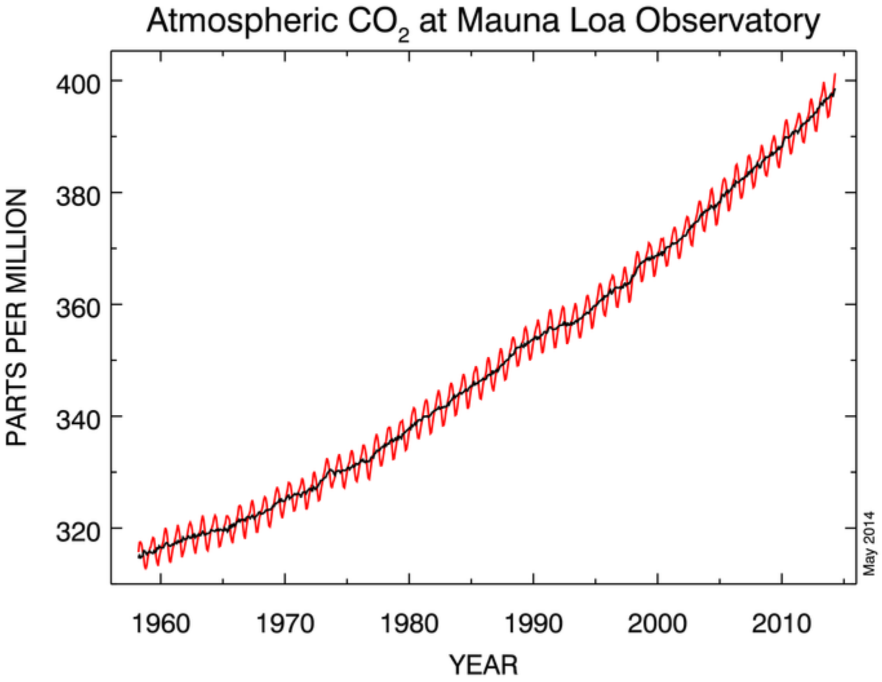

Figure 2.3. Monthly mean atmospheric carbon dioxide at Mauna Loa Observatory, Hawaii [23].

2.1. Solar Radiation and The Energy Budget ofThe Earth

The Sun is a star of the spectral class G2 on the main sequence of the Hertzsprung-Russell diagram. The Sun consists mostly of hydrogen (91.2%) and helium (8.7%) and age of it is believed to be 4.5 billion years. The temperature of the visible surface or photosphere is about 6000K (or, more precisely, 5780K) on average. This temperature fluctuates mostly due to sunspots. The temperature of relatively cool regions with sunspots is closer to 4000K. The number of sunspots fluctuates randomly, but in general it has a period of 11 years. The solar constant varies 0.08% (or about 1.1 Wm^{-2}) between the minimum and the maximum of the 11-yr sunspot cycle according to measurements by satellite instruments. Source of the Sun's energy comes from thermonuclear fusion. The overall reaction is

$$6(\mathrm{H}) \rightarrow 4\mathrm{He} + 2\ \mathrm{neutrinos} + \mathrm{energy} + 2\mathrm{H} \qquad (2.1)$$

2.1.1. The solar spectrum

Total energy emitted by the Sun is almost equal to emission of a blackbody at a temperature of 5780K. The distribution of the solar intensity with wavelength is also about the same as that of a blackbody at this temperature (Figure 2.4). The differences between observed solar intensity on the surface of the Earth and calculated intensity of blackbody radiation are most significant in the UV region, where the ozone layer absorbs part of the radiation. More deviation is due to the fact that Planck's formula assumes that a body emits the radiation at a single uniform temperature. However, the temperature of the Sun increases with depth and emission comes from different depths to space. The radiation from the Sun is the ultimate source of energy driving the climate system. About 9% of the solar energy coming to the Earth is in the form of ultraviolet radiation ($\lambda \leq 0.40\ \mu m$), approximately 38% is visible ($0.40 \leq \lambda \leq 0.70\ \mu m$) and about 53% lies in the near infrared ($0.7 \leq \lambda \leq 4.0\ \mu m$) according to measurements above the atmosphere. There are also emissions from the Sun of shorter wavelength X-rays and gamma rays, and longer wavelength thermal infrared ($4.0 \leq \lambda \leq 100\ \mu m$), microwave ($0.1 \leq \lambda \leq 10\ mm$) and radio ($1\ cm \leq \lambda$) photons, but contribution of these radiation to the solar energy input to the Earth is negligible [24]. An average of 342 Watts of solar radiation throughout the year comes from the Sun to each square meter of the Earth's spherical surface outside the atmosphere. The atmosphere is transparent to shortwave radiation from the Sun. 31% (107 Wm^{-2}) of this radiation is immediately reflected back into space by clouds, aerosols, atmosphere, the Earth's surface, by snow, ice and water. About half (168 Wm^{-2}) of incoming radiation reaches the surface and warms the land and the ocean. Gases in the atmosphere and clouds absorb the remaining 20% (67 Wm^{-2}) of solar radiation. The Earth's surface returns this energy as heat to the atmosphere in the form of infrared radiation, sensible heat and latent

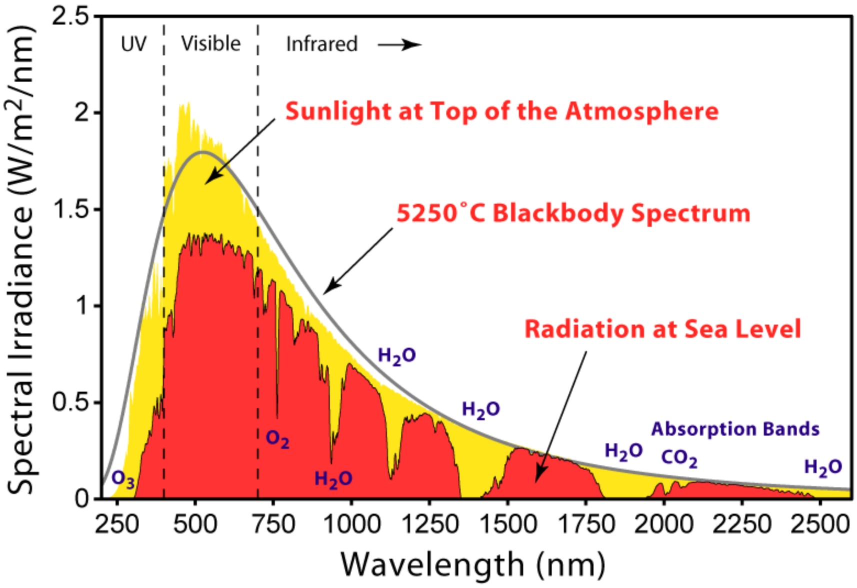

Figure 2.4. Solar radiation spectrum [25].

heat of water vapor. The incoming solar radiation and the outgoing radiation emitted by the climate system must be in equilibrium for a stable climate. An average 235 Wm^{-2} of radiation must be emitted from the climate system back into space. Figure 2.5 shows exchange of energy between surface and atmosphere, incoming solar radiation and outgoing long wave radiation [20].

2.1.2. Absorption of solar radiation in the atmosphere

The atmosphere consists of several trace gases which are going through an interaction such as absorption and emission with an infrared radiation. These gases are called greenhouse gases which absorb infrared radiation, emitted by the Earth's surface, the atmosphere and clouds. Then they also emit this infrared radiation downward to the Earth's surface and in all directions. These greenhouse gases prevent heat from escaping in the atmosphere. This is called the natural greenhouse effect which is part of energy balance of the Earth (Figure 2.5) [20]. The important greenhouse gases are water vapor, carbon dioxide, methane, ozone and nitrous oxide. Atmospheric absorption of these four molecules of greenhouse gases (H_2O, CO_2, O_3 and N_2O) and the

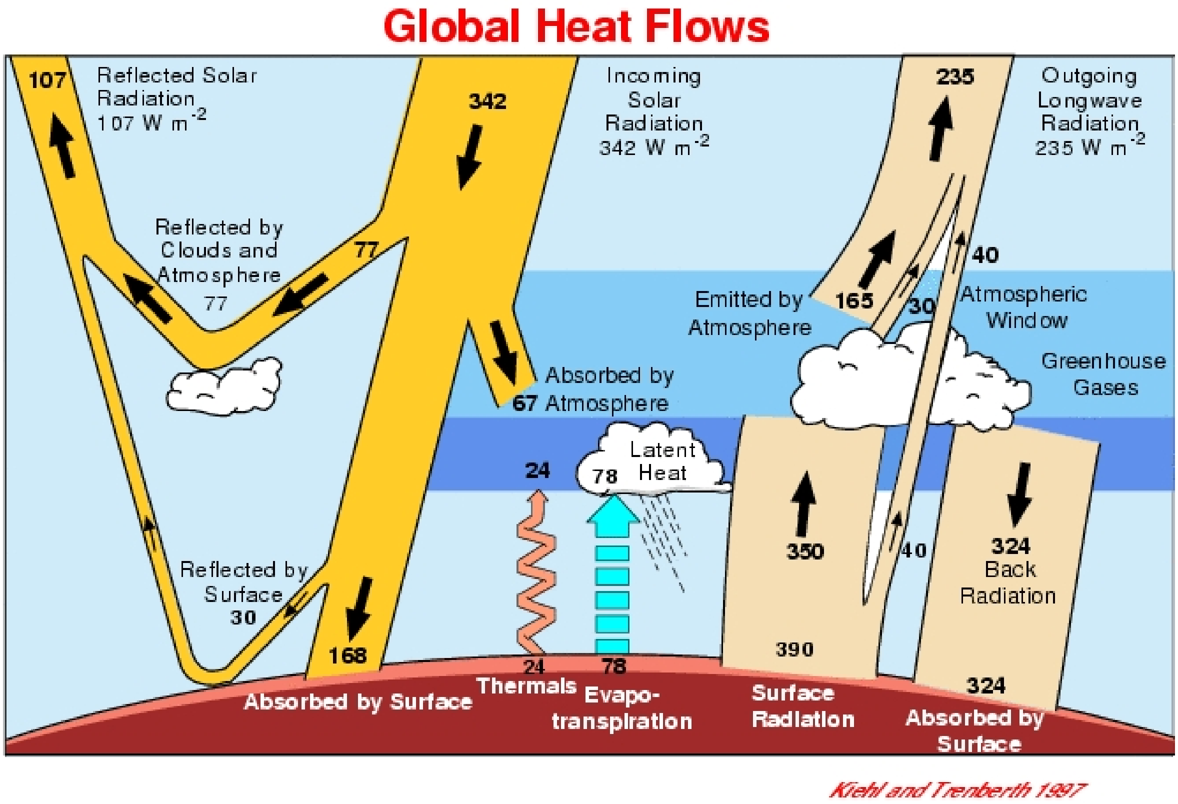

Figure 2.5. The Earth's annual global mean energy budget. Units are Wm^{-2} [26].

solar radiation passing through the Earth's atmosphere are shown in the Figure 2.6. Ozone molecule absorbs mainly UV radiation. It causes warming at around 50 km of the atmosphere. Ozone also absorbs the visible at 0.6 μm wavelength, and in the infrared at 9.6 μm. Oxygen molecules absorbs UV in the atmosphere as well. Water vapor contributes to atmospheric absorption at 6.3 μm, and in the far infrared beyond 20 μm. Carbon dioxide absorbs in the near infrared, mid infrared at 4.3 and 15 μm strongly. The peak of the Planck function for temperature of atmosphere corresponds to the 15 μm band. Other gases such as CH_4, CO, N_2O, NO, etc. contribute to atmospheric absorption at different wavelengths and consistent absorption by clouds and aerosols [24].

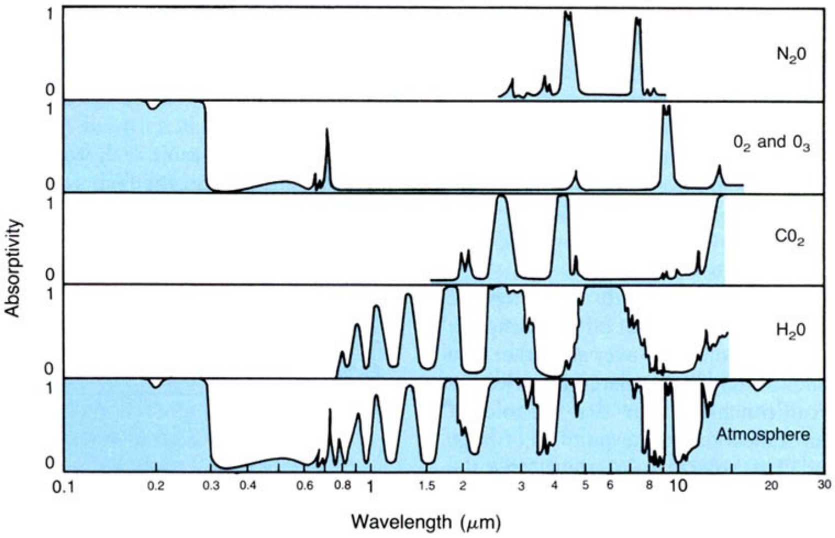

Figure 2.6. Absorption spectra of atmospheric gases [27].

2.2. Atmosphere and Climate

The Earth's atmosphere is the most significant component of the climate system, since several of physical processes takes place in the atmosphere. Molecular nitrogen and molecular oxygen are the major constitutents of the atmosphere. Although concentrations of carbon dioxide, water vapor and ozone are less than the major constitutents, they play important roles in the energy budget of the Earth.

The atmosphere is considered to be in hydrostatic balance in the vertical direction meaning that there is a balance between vertical pressure gradients and the gravitational force per unit volume acting on each portion of the atmosphere. By combining the hydrostatic balance equation with the ideal gas law, we find that the pressure and density decrease exponentially with altitude. We explain many atmospheric processes by thermodynamic principles. First Law of Thermodynamics explains the effects of atmospheric heating or cooling and the concept of entropy helps to understand atmospheric behaviour. Macroscopic definitions of the variables (temperature and pressure) are used in atmospheric physics [28].

In theoretical meteorology, air is considered as a mixture of two ideal gases: dry air and water vapor. The thermodynamic properties of this moist air are defined by combining the separate thermodynamic behaviors of dry air and water vapor [29].

2.2.1. Dry Thermodynamics

2.2.1.1. The ideal gas law. We assume that the atmosphere is an ideal gas with each mole of gas obeying the ideal gas law. In the ideal gas model, the molecules are considered as non-interacting point particles which are moving in a random motion by conserving the energy. The equation of state for an ideal gas expresses the relationship among pressure p, volume V and temperature T of a gas by

$$pV = NkT = \nu R^{*}T \tag{2.2}$$

where N is the number of identical molecules, ν is the number of moles of gas, $k = 1.3806 \times 10^{-23}$ J K^{-1} is Boltzmann's constant, $R^{*} \equiv N_a k = 8.341$ J mol^{-1} K^{-1} is the universal gas constant, with $N_a = 6.022 \times 10^{23}$ mol^{-1} Avogadro's number.

We use intensive forms of variables in thermodynamic equations. Like the temperature and pressure, value of an intensive variable does not depend on the amount of matter in the system. We convert extensive variables to their intensive form by normalizing them by the amount of matter. Given a system whose volume V contains an amount of mass M,

$$v = \frac{V}{M} \tag{2.3}$$

denotes the specific volume of the system. Lower case letters are generally used to show specific intensive quantities, e.g. the specific volume v and the volume V. We define the partial pressure p_i of the i^{th} gas for a mixture of ideal gases as the pressure p_i that it would have if the same mass (M_i) existed alone at the same temperature T and occupying the same volume V. Then, we can write the gas law in terms of kilograms rather than moles and use the molecular weight of a species i, m_i (g/mol), and the total mass of the gas is M_i. Then we can express the gas law as

$$p_i V = \frac{M_i}{m_i} R^* T \tag{2.4}$$

We can define the specific gas constant R_i for a species i as

$$R_i \equiv R^*/m_i \tag{2.5}$$

By combining Equation 2.4 and Equation 2.5 the partial pressure for an ideal gas can be expressed as

$$p_i = \frac{T}{V} M_i R_i \tag{2.6}$$

Dalton's law of partial pressures said that the total pressure p of a mixture of (ideal) gases is the sum of the pressures Σp_i of each species i as if it alone has a volume V,

$$p = \frac{T}{V} \Sigma_i \left(M_i R_i \right) = \rho R_m T \tag{2.7}$$

If $M_{tot} = \Sigma_i M_i$ is the total mass, then $R_m = 1/M_{tot} \Sigma_i M_i R_i$ the specific gas constant for the mixture, and $\rho = M_{tot}/V$ is the density. Then Equation 2.7 is the ideal gas law or alternatively if we use the specific volume instead of density ($v = 1/\rho$), thus

$$pv = R_m T \tag{2.8}$$

2.2.1.2. The First Law of Thermodynamics. The First Law of Thermodynamics states that heat is a form of energy and energy is conserved. The internal energy of a closed system increases by amount dU, only if heat (dQ) is added or if work (dW) is done on the system by its surroundings:

$$dU = dQ + dW \tag{2.9}$$

and for a unit mass of gas:

$$du = dq + dw \tag{2.10}$$

The rate of work is given by

$$dw = -pdv \tag{2.11}$$

such that Equation 2.9 can be expressed as

$$du = dq - pdv \tag{2.12}$$

2.2.1.3. Enthalpy and specific heat. The heat capacity C is the amount of heat needed to increase the temperature of a substance by 1 °C, and is defined as:

$$C = dQ/dT \tag{2.13}$$

We define the specific heat capacity at constant pressure, c_p and the specific heat capacity at constant volume, c_v as,

$$c_v = \left(\frac{\partial q}{\partial T}\right)_v \tag{2.14}$$

$$c_p = \left(\frac{\partial q}{\partial T}\right)_p \tag{2.15}$$

For dry air, $c_p = 1005$ J kg^{-1}K^{-1} and $c_v = 718$ J kg^{-1}K^{-1}. We can express the specific internal energy in terms of the specific volume v and the temperature T as,

$$du = \left(\frac{\partial u}{\partial v}\right)_T dv + \left(\frac{\partial u}{\partial T}\right)_v dT = \left(\frac{\partial u}{\partial T}\right)_v dT \tag{2.16}$$

where the last equality is due to the fact that the internal energy of an ideal gas does not depend on its volume,

$$\left(\frac{\partial u}{\partial v}\right)_T = 0 \tag{2.17}$$

If we equate Equation 2.12 and Equation 2.16, it gives

$$dq = \left(\frac{\partial u}{\partial T}\right)_v dT + pdv \tag{2.18}$$

where dq indicates the differential amount of heat added. For an isometric process $dv = 0$, we get $(\frac{\partial u}{\partial T})_v dT = (\frac{\partial q}{\partial T})_v dT$ by using Equation 2.12. From the definition of c_v, Equation 2.18 becomes

$$dq = c_v dT + pdv \tag{2.19}$$

However, it is not easy to measure the change of the volume of an air mass. So, we use the chain-rule to write the Equation 2.19 in terms of pressure change instead of volume change.

$$dq = c_v dT + RdT - vdp \tag{2.20}$$

$$dq = (c_v + R)dT - vdp \tag{2.21}$$

For an isobaric process $dp = 0$, therefore it is clear that

$$c_p = c_v + R \tag{2.22}$$

which we use to write the first law in terms of changes of easier measurable quantities:

$$dq = c_p dT - vdp \tag{2.23}$$

The specific enthalpy h which gives a measure of total energy of a unit mass of the atmosphere is also defined as

$$h = u + pv \tag{2.24}$$

Given this definition, the first law can be expressed as

$$dq = du + pdv = dh - d\,(pv) + pdv = dh - vdp \tag{2.25}$$

2.2.1.4. Adiabatic Processes. An air parcel is an imaginary finite volume of air with all of the basic dynamic and thermodynamic properties of atmospheric air that is a continuous entity. An air parcel is large enough to include a very high number of molecules, but small enough so that the properties assigned to it are approximately uniform within it. An air parcel conserves its shape and general characteristics as it moves up (or down) relative to the surrounding atmospheric environment. We sometimes assume that parcel volume and pressure adapt quickly to stay in equilibrium state with the parcel surroundings, but in general this is not the case for temperature.

Heat can be fed to a parcel of air and its pressure can change. First we will examine the case of no input of heat to a parcel of air. This is called an adiabatic process, since $dq = 0$,

$$c_p dT = v dp \tag{2.26}$$

When the pressure changes, temperature will change as well. Many motions in the atmosphere can be considered as adiabatic processes [30].

Hydrostatic balance. In static equilibrium, the net forces acting on an air parcel must be equal to zero. The force due to gravity is balanced by the vertical pressure gradient force. Hydrostatic balance is widely valid on horizontal scale exceeding 10 km. We consider a small cylinder of air, of height Δz and horizontal cross sectional area ΔA, as shown in Figure 2.7. There is a gravitational force $g\Delta m$ acting on this air parcel downwards, where its mass $\Delta m = \rho\Delta A\Delta z$ and g is the gravitational acceleration. Gravitational force must be balanced by the vertical pressure gradient force. We therefore have

$$g\rho\Delta A\Delta z = p\left(z\right)\Delta A - p\left(z+\Delta z\right)\Delta A \tag{2.27}$$

Canceling ΔA, and using the first term in the Taylor expansion,

$$p\left(z+\Delta z\right) \approx p\left(z\right) + \frac{dp}{dz}\Delta z \tag{2.28}$$

we get the equation for hydrostatic balance,

$$\frac{dp}{dz} = -\rho g \tag{2.29}$$

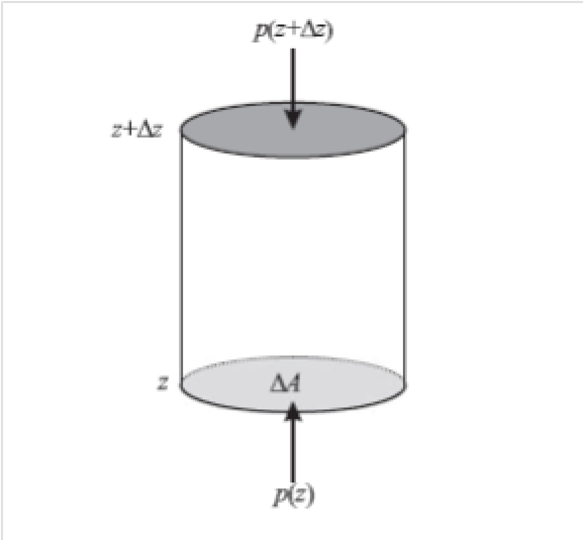

Figure 2.7. The vertical pressure forces acting on a small cylinder of air [28].

Assuming adibaticity, that the atmosphere is in a hydrostatic balance, $dp/dz = -\rho g$, then Equation 2.26 can be written

$$c_p dT = -v\rho g dz = -g dz \tag{2.30}$$

This gives the adiabatic lapse rate as

$$\Gamma = \frac{dT}{dz} = -\frac{g}{c_p} \tag{2.31}$$

Thus if a dry air parcel is lifted without heat input, its temperature will fall by 9.8 K km^{-1} as it expands to keep its pressure in equilibrium with its surroundings.

Potential Temperature. When we try to explain atmospheric processes, it is desirable to use conserved quantities under certain types of motion. Thus we will try to derive a quantity that is conserved in adiabatic motion. By using the equation of state in Equation 2.26 we get

$$c_p dT = v dp = \frac{RT}{p} dp \tag{2.32}$$

$$\frac{dT}{T} = \frac{R}{c_p p} dp \tag{2.33}$$

When we integrate Equation 2.33 we get Poisson's Equation:

$$\frac{T}{T_0} = \left(\frac{p}{p_o}\right)^{\frac{R_d}{c_p}} \tag{2.34}$$

where T_0 and p_0 are constants of integration. Note that the subscript d on the gas constant indicates that dry air is considered. If the reference pressure p_0 equals to 1000 hPa then T_0 is defined as the potential temperature (for dry air), also denoted by θ:

$$\theta = T \left(\frac{p_o}{p}\right)^{\frac{R_d}{c_p}} \tag{2.35}$$

In other words, the potential temperature θ is the temperature a parcel would have if it were subjected to an adiabatic compression or expansion to a final pressure is $p_0 = 1000 hPa$. We can find the lapse rate of the potential temperature by differentiating Equation 2.35 with respect to height

$$\frac{d\theta}{dz} = \frac{\theta}{T} \left(\frac{dT}{dz} - \frac{R_d T}{p c_p} \frac{dp}{dz}\right) \tag{2.36}$$

By assuming that the atmosphere is in a hydrostatic balance,

$$\frac{dp}{dz} = -\rho g \tag{2.37}$$

then by using the gas law Equation 2.7, Equation 2.36 can be written as

$$\frac{d\theta}{dz} = \frac{\theta}{T}\left(\frac{dT}{dz} + \frac{g}{c_p}\right) \tag{2.38}$$

If the temperature profile follows the dry adiabatic lapse rate, the potential temperature is constant with height, since $\frac{-g}{c_p} = \Gamma_d$ is the dry adiabatic lapse rate. Therefore, potential temperature θ is a constant in any adiabatic process.

Entropy. The specific entropy ϕ is defined as

$$d\phi = \frac{dq}{T} \tag{2.39}$$

where $d\phi$ is the increase in entropy, dq is the addition of heat to unit mass of gas at temperature T. The entropy is a state variable. The second law of thermodynamics states that entropy of an isolated system never decreases, thus $Td\phi = du+pdv \geq 0$. We can define the potential temperature in terms of the entropy. It follows from Equation 2.23 that

$$d\phi = \frac{1}{T}\left[c_p dT - vdp\right] = c_p\frac{dT}{T} - R_d\frac{dp}{p} = c_p\left[\frac{dT}{T} - \frac{R_d}{c_p}\frac{dp}{p}\right] \tag{2.40}$$

$$d\phi = c_p\frac{d\theta}{\theta} \tag{2.41}$$

Integration gives

$$\phi = c_p \ln\theta + \text{const.} \tag{2.42}$$

Buoyancy force on a parcel. We will again assume that the atmosphere is in hydrostatic balance and pressure field is not changed by the presence of the air parcel. We consider a parcel of dry air with volume V, temperature T and density ρ. It displaces an equal volume of ambient environmental (noted by subscript env) air having temperature T_{env} and density ρ_{env}. The downward force on the parcel is $\rho g V$. The downward force on the air it displaces is equal to $\rho_{env} g V$. The upward force $-V\frac{\delta p}{\delta z}$ is same for parcel and displaced air. So the net upward force is $Vg(\rho_{env} - \rho)$ and the buoyancy force per unit mass

$$F_B = g\left(\frac{\rho_{env} - \rho}{\rho}\right) \tag{2.43}$$

by using Poisson's Equation, Equation 2.43 can be written as

$$F_B = g\left(\frac{\theta - \theta_{env}}{\theta_{env}}\right) \tag{2.44}$$

This force is positive when a parcel of air is warmer than its environment and it will be subject to a net upwards buoyancy force and will accelerate upwards. It is negative when a parcel of air is colder than its environment and it will be subject to a net downwards buoyancy force and will accelerate downwards. Equal temperatures are referred to as neutral buoyancy. A parcel of air that is neutrally buoyant may become positively or negatively buoyant if it is subjected to a small vertical displacement. It depends on whether the parcel's temperature changes more or less rapidly than the environmental lapse rate [30].

Stability criteria for dry air. We use the dry adiabatic lapse rate to determine the stability of atmosphere with respect to the vertical displacement of a parcel. If a restoring force which aims to move air parcel toward its original position is acting after vertical displacement of air parcel, then the atmosphere is said to be stable. If a force is acting in the direction of displacement of air parcel, then the atmosphere is said to be unstable. This condition is related to the environmental lapse rate γ, which is the decrease of temperature with height at the level of air parcel. When the environmental lapse rate is greater than the dry adiabatic lapse rate, the parcel will be warmer than its surroundings and it will continue to rise. Then air is said to be unstable. Conversely, when the environmental lapse rate is less than the dry adiabatic lapse rate, the parcel will be colder than its surroundings and it will sink. Then air is said to be stable. For the case of equality of the environmental lapse rate and the dry adiabatic lapse rate, parcel will not be subjected to any buoyancy force. Then air is said to be neutral.

- $\gamma < \Gamma$ Stable
- $\gamma = \Gamma$ Neutral
- $\gamma > \Gamma$ Unstable

All these criteria can be defined by potential temperature as well. We assume the lifted parcel cool adiabatically and potential temperature θ of the parcel is invariant. When we rewrite Equation 2.38, we get

$$\frac{\partial \theta}{\partial z} = \frac{\theta}{T}\left(\Gamma - \gamma\right) \tag{2.45}$$

We can thus define three situations:

- $\frac{\partial \theta}{\partial z} < 0$: Unstable
- $\frac{\partial \theta}{\partial z} = 0$: Neutral
- $\frac{\partial \theta}{\partial z} > 0$: Stable

Thus, a region of atmosphere is statically stable if potential temperature increases with height and is statically unstable if potential temperature decreases with height [29].

2.2.2. Moist Thermodynamics

We will include water in our calculations of dry air. Water is a constituent which can be found in atmosphere in all its three states: solid, liquid and vapor.

2.2.2.1. Equation of state for water vapor. Water vapor is assumed to be an ideal gas to a good approximation and thus from the gas law it follows that

$$e = \rho_v R_v T \tag{2.46}$$

where e is the vapor pressure, ρ_v is the density of water vapor, and R_v is the specific gas constant for water vapor which is equal to 461.5 J kg^{-1} K^{-1}. In the literature we use the ratio between the gas constants for dry air and water vapor:

$$\epsilon = \frac{R_d}{R_v} = \frac{m_v}{m_d} \tag{2.47}$$

where $\epsilon = 0.622$ from the values of the gas constants. From Dalton's law, the total pressure of moist air is the sum of the partial pressures of the dry air and the vapor since atmospheric air is a mixture of the ideal gases of dry air and water vapor.

$$p = p_d + e \tag{2.48}$$

2.2.2.2. Saturation. First consider a closed and thermally insulated system containing water and a vacuum above. Molecules from the surface layer of water are in a state of thermal agitation and some break away as vapor molecules. This process is evaporation and increases vapor pressure. On the other hand some of the vapor molecules collide with the water surface and stick to the surface. The process is called condensation, and decreases the vapor pressure. Condensation and evaporation thus occur simultaneously. For a given temperature, a state of equilibrium will eventually be attained when condensation and evaporation have the same rate. Then the vapor is said to be saturated in this case, and the vapor pressure e is equal to the so-called saturation vapor pressure e_s with respect to water. It is found that the saturation vapor pressure depends only on temperature.

2.2.2.3. Clausius Clapeyron Equation. Heat must be given to convert water from liquid to vapor phase at a constant temperature. This is the Latent Heat of Vaporization; L_v. Saturation vapor pressure is constant as well throughout the process of evaporation since it is a function of T only. For the transition from liquid phase q_1 to vapor phase q_2,

$$L_v = \int_{q_1}^{q_2} dq = \int_{u_1}^{u_2} du + \int_{v_1}^{v_2} pdv = u_2 - u_1 + e_s \left(v_2 - v_1\right) \tag{2.49}$$

Due to the fact that temperature is also constant we can write

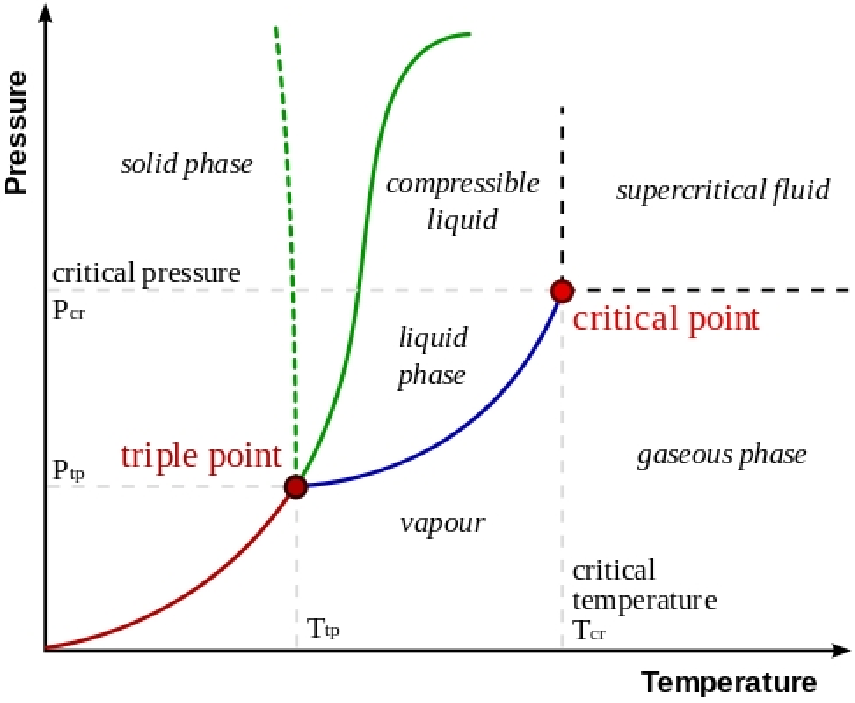

Figure 2.8. A typical phase diagram for water.

$$L_v = T \int_{q_1}^{q_2} \frac{dq}{T} = T \left(\phi_2 - \phi_1\right) \tag{2.50}$$

Equating Equation 2.49 and Equation 2.50 gives

$$u_1 + e_s v_1 - T\phi_1 = u_2 + e_s v_2 - T\phi_2 \tag{2.51}$$

This shows that this combination of these variables is constant during isothermal and isobaric change of phase. This is called Gibbs free energy of the system.

$$g = u + e_s v - T\phi \tag{2.52}$$

Even though Gibbs free energy is constant during phase transition, it changes with temperature and pressure. When we differentiate the Gibbs free energy Equation Equation 2.52, we get:

$$dg = du + v de_s + e_s dv - T d\phi - \phi dT \tag{2.53}$$

Substituting $T d\phi = dq = du + e_s d\nu$ into Equation 2.53 will reduce the equation as

$$dg = v de_s - \phi dT \tag{2.54}$$

Since The Gibbs Free Energy is the same for two phases, $dg_1 = dg_2$ gives:

$$v_1 de_s - \phi_1 dT = v_2 de_s - \phi_2 dT \tag{2.55}$$

By reorganizing Equation 2.55 we obtain:

$$\frac{de_s}{dT} = \frac{\phi_2 - \phi_1}{v_2 - v_1} = \frac{L_v}{T\left(v_2 - v_1\right)} \tag{2.56}$$

where the last relationship uses Equation 2.50. This equation expresses the change of saturation vapor pressure with temperature and is called the Clausius Clapeyron Equation. The Clausius Clapeyron Equation defines the water-holding capacity of the atmosphere. According to this equation, water-holding capacity of the atmosphere increases by about 7% for every 1°C rise in temperature [21]. To increase the average temperature of the Earth is very dangerous since it will increase the amount of water vapor in the atmosphere causing enhanced greenhouse effect. Under normal atmospheric conditions the specific volume for water vapor is much greater than that of liquid, $\nu_2 \gg \nu_1$. Then Equation 2.56 reduces to

$$\frac{de_s}{dT} \approx \frac{L_v}{Tv_2} = \frac{L_v e_s}{R_v T^2} \tag{2.57}$$

We integrate the Clausius Clapeyron Equation by assuming the latent heat constant as a first approximation. We get

$$e_s = e_{s0} \exp\left[\frac{L_v}{R_v}\left(\frac{1}{T_0} - \frac{1}{T}\right)\right] \tag{2.58}$$

e_{s0} is the vapor pressure at temperature T_0, it is found that at $T = 0°\mathrm{C}$ we have $e_{s0} = 6.11$ hPa, and the latent heat of vaporization, L_v around 0°C is assumed approximately a value of 2.50×10^6 J kg^{-1}. By putting these constants in Equation 2.58, we get an approximate for e_s as

$$e_s(T) = Ae^{\frac{-B}{T}} \tag{2.59}$$

where the constants are $A = 2.53 \times 10^8$ kPa and $B = 5.42 \times 10^3$ K. Bolton (1980) constructed an empirical formula for the saturation vapor pressure as a function of T in °C:

$$e_s(T) = 611.2 \exp\left(\frac{17.67T}{T + 243.5}\right) \tag{2.60}$$

e_s doubles for every 10°C increase in temperature. The saturation vapor pressure of ice e_i can also be defined by Equation 2.57 at temperatures below freezing ice crystals may be present, by replacing L_v with L_s, the Latent heat of Sublimation, for which a value of 2.83×10^6 J kg^{-1} can be used. The ratio between the two at subfreezing temperatures is

$$\frac{e_s(T)}{e_i(T)} = \exp\left[\frac{L_f}{R_v T_0}\left(\frac{T_0}{T} - 1\right)\right] \tag{2.61}$$

where L_f is the Latent Heat of Fusion and is equal to $L_s - L_v$.

2.2.2.4. Other measures of water vapor. Atmospheric water vapor is one of the most significant factors in determining weather and climate of the Earth due to its greenhouse effect. There are several different measures of water vapor content of air in meteorology. Some of these measures are defined to describe the actual amount of water vapor in the air. Others are defined to relate the actual amount to the potential amount that the air could have if it were saturated.

Mixing Ratio r_v. This is defined as the mass of water vapor per unit mass of dry air

$$r_v = \frac{m_v}{m_d} = \frac{\rho_v}{\rho_d} \tag{2.62}$$

From the equation of state, $\rho_d = \frac{p-e}{R_d T}$, so that

$$r_v = \frac{\rho_v R_d T}{p-e} = \frac{\rho_v R_v T \frac{R_d}{R_v}}{p-e} = \frac{\epsilon e}{p-e} \tag{2.63}$$

To calculate the saturation mixing ratio r_s, with respect to liquid water, e is replaced with e_s. It is a function of pressure and temperature.

Specific Humidity q_v. Specific humidity is the mass of water vapor per unit mass of moist air

$$q_v = \frac{\rho_v}{\rho} = \frac{\rho_v}{\rho_d + \rho_v} \tag{2.64}$$

and using the same substitution as above we get

$$q_v = \frac{\epsilon e}{p - (1-\epsilon)\, e} \tag{2.65}$$

To define the saturation specific humidity, e is replaced with e_s. Since at all ordinary atmospheric conditions $e \ll p$, in practice we get

$$q_v \approx r_v \approx \frac{\epsilon e}{p} \tag{2.66}$$

Relative Humidity RH. Relative Humidity is the ratio of the vapor pressure to its saturation value:

$$RH = \frac{e}{e_s} \tag{2.67}$$

Note that the relative humidity can be approximated as

$$RH \approx \frac{r}{r_s} \tag{2.68}$$

Relative humidity is usually given in percentage.

Virtual Temperature T_v. A hypothetical temperature, the virtual temperature is the temperature dry air would have to have same density as a sample of moist air at the same pressure. To derive T_v we reclaim:

$$p = p_d + e = p_d R_d T + \rho_v R_v T = \rho_d R_d T + \rho_d \frac{\rho_v}{\rho_d} R_d \frac{R_v}{R_d} T \tag{2.69}$$

By using the definitions of $\epsilon = R_d/R_v$ and $r_v = \rho_v/\rho_d$, Equation 2.69 can be simplified to

$$p = \rho R_d T \left(1 + \frac{r_v}{\epsilon}\right) \tag{2.70}$$

And then using the relation $\rho_d = \frac{\rho}{1+r_v}$

$$p = \rho R_d T \left(\frac{1 + \frac{r_v}{\epsilon}}{1 + r_v} \right) \tag{2.71}$$

Thus the equation of state for dry air can be adjusted to moist air by including the adjustment factor in brackets. We thus define the virtual temperature as

$$T_v \equiv T \left(\frac{1 + \frac{r_v}{\epsilon}}{1 + r_v} \right) \tag{2.72}$$

This lets us write the equation of state for moist air as

$$p = \rho R_d T_v \tag{2.73}$$

Since $e \ll p$ and thus $r_v \ll 1$, by ignoring second order terms the definition of T_v can be reduced to

$$T_v \equiv T \left(1 + \frac{1-\epsilon}{\epsilon} r_v \right) \tag{2.74}$$

We see that for moist air $T_v > T$ always since a unit volume of moist air is less dense than a unit volume of dry air. We also define the virtual potential temperature in terms of T_v

$$\theta_v \equiv T_v \left(\frac{p_0}{p} \right)^{\frac{R_d}{c_p}} \tag{2.75}$$

and virtual potential temperature is conserved in adiabatic motion of moist air as well. We can write the equation of state of moist air by replacing T with T_v, or use the gas constant for moist air R_m:

$$pv = R_d T_v = R_m T \tag{2.76}$$

$$R_m = R_d \left(\frac{1 + \frac{r_v}{\epsilon}}{1 + r_v} \right) \tag{2.77}$$

<u>2.2.2.5. Specific heat of moist air.</u> The specific heat capacity of air is changed due to the existence of moisture. We take into account the addition of heat to a sample of air which contains one kilogram of dry air and r kilograms of water vapor

$$(1 + r)\, dq = c_v dT + r c_{vv} dT \tag{2.78}$$

This gives

$$c_{vm} = \frac{dq}{dT} = c_v \left(\frac{1 + \frac{c_{vv}}{c_v} r}{1 + r} \right) \tag{2.79}$$

Since $c_{vv}/c_v = 1.96 \approx 2$ by neglecting second order terms, we get

$$c_{vm} \approx c_v\,(1 + r) \tag{2.80}$$

We can get the specific heat at constant pressure by doing same calculations as

$$c_{pm} \approx c_p\,(1 + 0.9r) \tag{2.81}$$

Since $r < 10^{-2}$ these correction factors can often be ignored.

<u>2.2.2.6. Ways of reaching saturation.</u> There are certain ways to make a parcel of air saturated. These processes bring out new temperatures telling about the moisture content of air.

Diabatic Cooling: Dew Point Temperature T_d. Dew point temperature is defined as the temperature which moist air must be cooled with conservation of pressure to be saturated with respect to water. Since air is cooled isobarically, the amount of water vapor, r is also conserved, and saturation of air occurs when T is such that

$$r_s(T) = r \tag{2.82}$$

It is known as the Dew Point Temperature T_d. Thus we can write $e(T) = e_s(T_d)$. If the air temperature cools to the dew point, then dew, fog or clouds begin to form.

Adiabatic Cooling: Condensation Temperature T_c. Condensation temperature is defined as the temperature which moist air must be cooled adibatically to be saturated with r held constant. Since air is cooled adiabatically, θ_v is conserved and the air will be saturated at the isentropic condensation temperature and pressure. This pressure level is sometimes called as the lifting condensation level or LCL.

If lifting and expansion continues, air will condense and released latent heat will tend to increase temperature of air. The rate of decrease in temperature with decreasing pressure will therefore be slower after condensation than before. We need to make assumptions about the condensed water whether it remains in the parcel in form of cloud droplet or precipitate to calculate the dependence of T on p in this process. If condensed water is assumed to remain in the parcel, we should take into account its water loading effect and how to change heat capacity. Then if the temperature reaches the freezing point, we should account for if and how the liquid droplets freeze. After comparisons of the different assumptions, results show that dependence of T on p is not totally dependent on the selection of assumptions. We choose the simplest case called pseudoadiabatic process in which it is assumed that condensed water will precipitate. In this assumption, we do not need to consider heat content of the condensed water in calculating temperature changes of air parcel and temperature that sublimation is important.

For moist saturated lifting and by ignoring the correction factor for the specific heat,

$$c_p dT - vdp + L_v dr_s \simeq 0 \tag{2.83}$$

Then the saturated moist adiabatic lapse rate Γ_s is

$$\Gamma_s = \frac{dT}{dz} = \frac{v}{cp}\frac{dp}{dz} - \frac{L_v}{c_p}\frac{dr_s}{dz} = \Gamma_d - \frac{L_v}{c_p}\frac{dr_s}{dz} \tag{2.84}$$

$\frac{dr_s}{dz}$ is negative because of falling of temperature with height indicates that $\Gamma_s > \Gamma_d$. Note that $\Gamma_d = -9.8$ K km^{-1}, Γ_s is usually between -3 to -4 K km^{-1} in the lower troposphere. There is a difference between the dry and moist adiabatic lapse rate values because latent heat is released when water condenses. It decreases the rate of temperature drop with height.

Evaporation: Wet Bulb Temperature T_w. The wet-bulb temperature is the temperature a parcel of air would have if water is evaporated into it by cooling to saturation, with the latent heat supplied by the parcel. We take into account an air parcel with r_v mass of water vapor and unit mass of dry air. Heat needed to evaporate dr_v is $-L_v dr_v$. Then

$$(1 + r_v)\, C_{pm} dT = -L_v dr_v \tag{2.85}$$

By substituting the equation of specific heat capacity of moist air at constant pressure, C_{pm} we get,

$$C_p dT \simeq \frac{-L_v dr_v}{(1 + r_v)\,(1 + 0.9r)} \tag{2.86}$$

We can ignore the correction factors since r and $r_v < 10^{-2}$ and assume

$$C_p dT \simeq -L_v dr_v \tag{2.87}$$

By considering L_v as constant we can integrate Equation 2.87, then we get

$$T_w = T - \frac{L_v}{C_p}\left(r_s\left(p, T_w\right) - r_v\right) \tag{2.88}$$

By using Equation 2.59 we get T_w as,

$$T_w = T - \frac{L_v}{C_p}\left(\frac{\epsilon}{p} A e^{\frac{-B}{T}} - r_v\right) \tag{2.89}$$

Wet-bulb potential temperature θ_w is the temperature a parcel of air would have, if air parcel is lifted adiabatically to reach saturation and then descended along moist-adiabat to a reference pressure $P_0 = 1000hPa$ [29,30].

2.2.2.7. Static stability in a moist environment. There are five categories of static stability in a moist environment.

- $\gamma < \Gamma_s$ Absolutely Stable
- $\gamma = \Gamma_s$ Saturated Neutral
- $\Gamma_s < \gamma < \Gamma_d$ Conditionally Unstable
- $\gamma = \Gamma_d$ Dry Neutral
- $\gamma > \Gamma_d$ Absolutely Unstable

If the environmental lapse rate is less than the moist adiabatic lapse rate, the atmosphere is absolutely stable. Temperature of a saturated or unsaturated parcel will be less than the surrounding environment and will sink. If the environmental lapse rate greater than the dry adiabatic lapse rate, then the atmosphere is said to be an absolutely unstable. The temperature of an unsaturated or saturated parcel will always be greater than the surrounding environment and will continue to rise. In conditionally unstable atmosphere, the environmental lapse rate is between the moist adiabatic and the dry adiabatic lapse rates. The temperature of an unsaturated parcel will be less than the surrounding environment and sink where as the temperature of saturated parcel will greater than the surrounding environment and rise [29].

Convective Instability. Stability of atmosphere is affected by ascending a column of moist air until it is saturated. We can make initially stable moist air absolutely unstable or conditionally unstable by ascending. To make a column of air unstable by ascending to saturation is said to be convectively unstable. We use the lapse rate of wet bulb potential temperature for criteria of convective stability.

- $\frac{\theta_w}{dz} < 0$: Convectively Unstable
- $\frac{\theta_w}{dz} = 0$: Convectively Neutral
- $\frac{\theta_w}{dz} > 0$: Convectively Stable

In an unstable atmosphere, vertical movements of air incline to become larger, and it results in turbulent airflow and convective activity. Instability of the atmosphere can cause significant turbulence, vertical clouds, and severe weather such as thunderstorms.

2.3. Clouds and Aerosols

Clouds play a crucial role in the energy balance of the climate system. Clouds absorb and then reemit infrared radiation coming from the Earth's surface. Therefore they bring additional warming to the Earth's surface. On the other hand, most clouds behave as a reflector of incoming shortwave solar radiation and cool the system. As the effect of clouds on the energy balance of atmosphere and the Earth's surface is highly variable and changes according to height, type and optical properties of clouds, it is very difficult to predict their net effect on climate system [20, 24].

2.3.1. Formation of Clouds

Clouds form by condensation of water vapor in the air into water droplets or ice crystals. Condensation occurs in two ways. First condition is the air to be saturated so that it can not contain any more water vapor. For saturation, sufficient amount of water vapor needs to be added to air parcel or the air should be cooled to its dew point temperature. As the air rises, it will cool; the height at which the dew point temperature reached and formation of clouds occur is called the condensation level.

Second condition is that water vapor needs a surface to condensate on. In the air, there are tiny particles called condensation nuclei that can work as a surface for water vapor to condensate on. Aerosols are also condensation nuclei. In the absence of aerosols, relative humidity should be more than 100% for formation of clouds. So the existence of these condensation nuclei is crucial for clouds. Condensation nuclei could be microscopic dust, smoke and salt particles. Water vapor collides with aerosols and sticks to them and condensation occurs. It is not always the case that water vapor in excess of the saturation mixing ratio immediately condenses into cloud droplets.

We assume that when an air parcel is saturated, water vapor condenses and clouds are formed. Type of clouds formed depends on the water vapor content and the ways of formation of clouds. There are three main ways that formation of cloud occur [3].

2.3.1.1. Mixing of air masses without cooling. Two air parcels having different temperature and humidity content meet and mix. The mixture of air parcels can be saturated because of the new temperature it has, although they were not saturated at the beginning since saturation vapor pressure is a nonlinear function of temperature. This mixing usually results in a formation of stratus, altostratus and stratocumulus clouds.

Mixing in Cumulus clouds. When we consider two air parcels having different temperature and humidity content at pressure p and are mixing isobarically, the specific humidity of the mixture is

$$q_v = \frac{M_1}{M_1 + M_2} q_{v1} + \frac{M_2}{M_1 + M_2} q_{v2} \tag{2.90}$$

In terms of mixing ratios and vapor pressure, it can be written as

$$r_v \approx \frac{M_1}{M_1 + M_2} r_{v1} + \frac{M_2}{M_1 + M_2} r_{v2} \tag{2.91}$$

$$e \approx \frac{M_1}{M_1 + M_2} e_1 + \frac{M_2}{M_1 + M_2} e_2 \tag{2.92}$$

With the assumption of net change of heat being zero, then we write

$$M_1 \left(c_p + c_{pv} r_{v1}\right) \left(T - T_1\right) + M_2 \left(c_p + c_{pv} r_{v2}\right) \left(T - T_2\right) = 0 \tag{2.93}$$

By ignoring effect of water vapor to heat capacities, temperature of mixture can be written as

$$T \approx \frac{M_1}{M_1 + M_2} T_1 + \frac{M_2}{M_1 + M_2} T_2 \tag{2.94}$$

2.3.1.2. Cooling of air parcel without lifting. There are two mechanisms that air parcel is saturated by cooling to dew point occurring near surface level [3]. In these processes, there is no need any lifting of air parcel.

- Radiative cooling

  Condensation by radiative cooling occurs because of the variation of infrared radiation at surface. This type of cooling generally takes place when the sky is clear. When the net radiation is negative means that surface loses heat by infrared radiation, nearby air condensate due to cool surface. It produces a radiation fog.
- Advective cooling

  Advective cooling occurs when air parcel passes over a cool surface because of its horizontal motion. When warm air passes over a colder surface, it is cooled and water vapor will condense.

2.3.1.3. Cooling of air parcel by lifting. Formation of clouds generally occurs when water vapor rises by lifting mechanisms and cools adiabatically to its dew point temperature. There are four general lifting mechanisms that are orographic lifting, convergent lifting, frontal lifting and convective lifting [3].

- Orographic lift

  The topography, high plateaus and mountainous regions can cause clouds to be produced. When air parcel meet elevation, it is forced to rise and cools to its dew point. Saturation is reached and condensation occurs.
- Convergence

  Air streams coming from different directions, come close to each other and are forced to rise where they flow together. This can cause cumulus clouds to be formed.
- Frontal lift

  When a warm and moist air is forced to climb over a colder and drier air, clouds are formed. Border between warm and cold air is called front.
- Convective lifting

  Warm and less dense air rises where dense and cold air sinks. This process is called convection. The air at the lower levels is heated by solar heating at surface level and rises. When air rises, it begins to cool to dew point temperature at which condensation occurs. Lifting by convection occurs faster than other mechanisms. Cumulus (Cu), cumulus congestus and cumulonimbus (Cb) clouds are formed by convective lifting. Precipitation related to these types of clouds is called convective precipitation. These precipitations are generally local and short term. On the contrary, stable or conditionally unstable air parcels cannot be lifted by their own energy. These kinds of air parcels need some mechanisms such as orographic lifting, convergence and frontal lifting for vertical motion. Especially if there is a low center or a trough at the upper atmosphere of standard pressure level 500 hPa, convective cells (Cb clouds) are formed due to strong warming of surface in summer when low temperatures or low pressure system ease progress of convective instability. In this type of cells, severe heavy rain with hail and thunderstorms occur. Rain and snow can occur in cold, moist and unstable air parcel when it passes over warm land surface. Tropical cyclones consist of cloud bands where vertically developed clouds (Cb) are dominant. These clouds generate precipitations in the form of rainstorm especially over land areas. They can affect thousands of kilometers square [3, 30].

2.3.2. Cloud drop formation

In this part, we consider processes that an air parcel takes part in such as formation of liquid droplets or ice crystals, conversion of small cloud droplets into larger rain drops, freezing and refreezing of cloud droplets, precipitation and evaporation of precipitation and cloud.

The saturation vapor pressure depends strongly on temperature. When we consider formation of cloud droplets, we should take into account saturation vapor pressure of a liquid at the surface of a spherical droplet. Then saturation vapor pressure should also be a function of the curvature of the droplet. Since molecules can evaporate more easily from curved surface, saturation vapor pressure at a curved surface is higher than that above a flat surface of the same liquid. The saturation vapor pressure of a liquid droplet of radius r given by:

$$\frac{e_r\left(r\right)}{e_s\left(\infty\right)}=\exp\left(\frac{2\sigma}{rR_{v\rho L}T}\right) \tag{2.95}$$

where σ is the surface tension, $\sigma \approx 7.5 \times 10^{-2}\ \mathrm{Nm}^{-1}$ for normal conditions, $e_s(\infty)$ is the saturation vapor pressure value over a plane surface. This is called as Kelvin's formula. We can rewrite above equation as

$$\frac{e_r\left(r\right)}{e_s\left(\infty\right)}=\exp\left(\frac{a}{rT}\right) \tag{2.96}$$

where $a=\sigma/R_{v\rho L}$ which is approximately constant at 3.3×10^{-7}mK. The formula can be expanded as

$$\frac{e_r\left(r\right)}{e_s\left(\infty\right)}\approx 1+\frac{a}{rT} \tag{2.97}$$

The rate of growth depends on the difference $e-e_s(r)$. If $e<e_s(r)$ then the cloud droplet will evaporate. If $e>e_s(r)$ then it will grow. Droplet formation by collision of molecules is called homogeneous nucleation. In the homogeneous nucleation process, at least 183 molecules of water vapor should be involved in forming a cloud droplet of radius of approximately 10^{-3} m at a temperature of 273 K. It would need a saturation ratio of $S = 3$ to carry on and grow. The relative humidity should be equal to 300% to reach this value of saturation ratio, $S = \frac{e}{e_s(\infty)}$. Such values are not observed in the atmosphere therefore homogeneous nucleation is not a convenient mechanism for cloud formation. As homogeneous nucleation is not often observed we need another mechanism for droplet formation.

The kind of droplet formation where water molecules are collected on a foreign substance is called heterogeneous nucleation. Many hydrophilic aerosols in the atmosphere (cloud condensation nuclei or CCN) play a role of surface where water molecules can collect on. CCNs can usually be found in the lower and middle troposphere to begin cloud growth process. CCN aerosols are wettable meaning that the surface tension between their surface and water is low enough and water can form a spherical cap surrounding the aerosol completely. Radius of these aerosols can range from 10^{-4} to 10μm with concentrations ranging from 10^3 cm^{-3} to $> 10^5$ cm^{-3}. The sources of aerosols could be natural and anthropogenic like mineral soil dust, sea salt, gas to particle conversion SO_2 (sulphate aerosols) and combustion of fossil fuels / biomass burning.

2.3.2.1. The solution term. The saturation vapor pressure is decreased for a solute when some water molecules are displaced from surface of droplet in the case of presence of dissolved substances. The decrease in vapor pressure is expressed as

$$\frac{e_s\left(sol\right)}{e_s^{\infty}} = \frac{n_w}{n_w + n_s} = \left(1 + \frac{n_s}{n_w}\right)^{-1} \simeq 1 - \frac{n_s}{n_w} \tag{2.98}$$

where $e_s(sol)$ is the saturation vapor pressure over a solute and n_w and n_s are the number of water and solute molecules, respectively. The final approximation follows the assumption of $n_s \ll n_w$. The number of molecules in a solute of mass M is given by

$$n_s = N_0 M / m_s \tag{2.99}$$

where N_0 is Avogadro's number (the number of molecules per mole) and m_s is the molecular weight of the solute. And the number of water molecules in mass m can be written as

$$n_w = N_0 m/m_w \tag{2.100}$$

with mass of water $m = \frac{4}{3}\pi r^3 \rho_L$ we note that Equation 2.98 can now be expressed as

$$\frac{e_s\,(sol)}{e_s^{\infty}} = \left(1 - \frac{b}{r^3}\right) \tag{2.101}$$

where b is a constant, $b = 3m_w M/4\pi\rho_L m_s$. Effects of the curvature (Equation 2.97) and solute (Equation 2.101) can be merged to obtain equilibrium curve referred to as the Köhler curve (Figure 2.9) given by:

$$\frac{e_s^r(sol)}{e_s^{\infty}} = (1 - \frac{b}{r^3})exp(\frac{a}{r}) \approx (1 + \frac{a}{r} - \frac{b}{r^3}) \tag{2.102}$$

In this form, we can call a/r term as a "curvature term" which indicates that saturation ratio over a droplet is higher than that of a plane surface. The term b/r^3 may also be called as "solution term" which expresses the decrease in vapor pressure because of

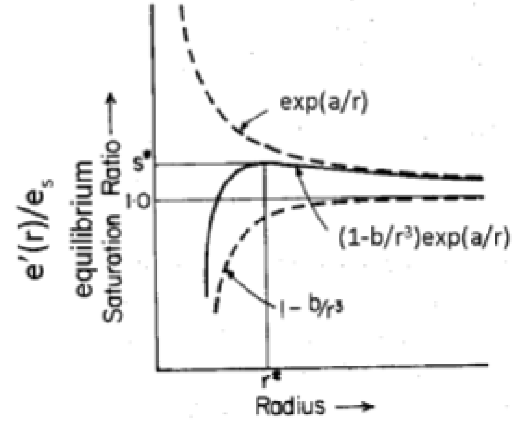

Figure 2.9. Köhler curve for the equilibrium saturation vapor pressure [30].

existence of dissolved substance.

2.3.2.2. Diffusional growth. When condensation occurs, a cloud droplet grows by diffusion of water vapor. As condensation occurs, released latent heat warms the droplet, reducing the condensation rate. The growth of a drop is given by the diffusion law assuming that diffusive flux is proportional to vapor gradient. When we integrate diffusive flux over a sphere of radius n, the total diffusive flux F (kg s^{-1}) is given as:

$$F = 4\pi n^2 D \frac{d\rho_v}{dn} \tag{2.103}$$

where D is the diffusion coefficient ($2.2 \times 10^{-5}\text{m}^2\text{s}^{-1}$ at 273K) and ρ_v is the vapor density. We equate the diffusion rate to rate of increase of mass of droplet M in a steady state as,

$$\frac{dM}{dt} = 4\pi n^2 D \frac{d\rho_v}{dn} \tag{2.104}$$

By assuming the growth as a constant we get

$$\frac{dM}{dt} \int_r^{\infty} \frac{dn}{n^2} = 4\pi D \int_{\rho_v(r)}^{\rho_v(\infty)} d\rho_v \tag{2.105}$$

giving that

$$\frac{dM}{dt} = 4\pi D r \left(\rho_v(\infty) - \rho_v(r)\right) \tag{2.106}$$

To get the rate of change of radius, we use mass equation

$$M = \frac{4}{3}\pi r^3 \rho_L \tag{2.107}$$

and differentiate it to get

$$\frac{dM}{dt} = 4\pi r^2 \rho_L \frac{dr}{dt} \tag{2.108}$$

Putting Equation 2.108 into Equation 2.106 gives

$$\frac{dr}{dt} = \frac{D}{\rho_L r}\left(\rho_v\left(\infty\right) - \rho_v\left(r\right)\right) \tag{2.109}$$

by using the ideal gas law ($e = \rho_v(\infty)R_vT$) to obtain the rate of change of radius related to vapor pressure. And we consider that air is exactly saturated over droplet surface.

$$\frac{dr}{dt} = \frac{D}{\rho_L r R_v T}\left(Se_s^{\infty} - e_s^{r}\left(sol\right)\right) \tag{2.110}$$

Dividing Equation 2.110 by e_s^{∞}, and using the approximation for the Köhler curve given in Equation 2.102:

$$\frac{dr}{dt} = \frac{De_s^{\infty}}{\rho_L r R_v T}\left(S + \frac{a}{r}\frac{b}{r^3} - 1\right) \tag{2.111}$$

For $r > 1\mu m$ this equation becomes

$$\frac{dr}{dt} \simeq \frac{De_s^{\infty}}{\rho_L r R_v T}\left(S - 1\right) \tag{2.112}$$

2.3.2.3. Terminal velocity. To calculate terminal fall speed of droplet, gravity and drag force should be in balance. The drag force exerted on a sphere of radius r by a fluid is given as,

$$F_R = \frac{\pi}{2} r^2 V^2 \rho C_D \tag{2.113}$$

where V is velocity of the sphere, ρ is fluid density and C_D is drag coefficient. We can write drag force in terms of the Reynolds number $Re = 2\rho V r/\mu$, where μ is the dynamic viscosity of fluid.

$$F_R = 6\pi\mu V\left(C_D Re/24\right) \tag{2.114}$$

The force of gravity on the sphere is given by

$$F_G = \frac{4}{3}\pi r^3 g\left(\rho_L - \rho\right) \approx F_G = \frac{4}{3}\pi r^3 g\rho_L \tag{2.115}$$

where ρ_L is the density of sphere. Since for raindrop falling through air $\rho_L \gg \rho$, we can simplify the equation for the force of gravity. When we equate force of gravity and drag force, we get terminal velocity by using the assumption of Stokes solution for very small Reynolds number $((C_D Re/24) = 1)$,

$$V = \frac{2}{9}\frac{r^2 g\rho_L}{\mu} \tag{2.116}$$

2.3.2.4. Collision and coalescence. Here we consider a large rain drop of radius R which is falling over a small droplet with radius r. Larger droplets fall faster, since $V \propto r^2$. We assume that all small cloud droplets which are on the way of falling larger drop will be in contact with large drop and be collected. The volume of droplets congregated per unit time is $\pi(R+r)^2(V-v)$ (as shown in the Figure 2.10). By using the liquid water content of the small droplets ($L = q_l\rho$ in kgm^{-3}), we obtain a mass accumulation rate of

$$\frac{dM}{dt} = L\pi\left(R+r\right)^2\left(V-v\right) \tag{2.117}$$

By using $\frac{dM}{dt} = 4\pi R^2\rho_L\frac{dr}{dt}$ and assuming that $R \gg r$ and $V \gg v$, we get the following:

$$\frac{dR}{dt} = \frac{LV}{4\rho_L} \tag{2.118}$$

In the case of the initial growth of small droplets ($r < 30\mu m$) the terminal velocity is $V = X_1R^2$ where $X_1 \sim 1.2 \times 10^8$s^{-1}m^{-1} giving

$$\frac{dR}{dt} = \frac{LX_1R^2}{4\rho_L} \tag{2.119}$$

Growth rate of radius due to collision and coalescence is proportional to the square of the droplet radius where as it is proportional to the inverse of radius in diffusion process. Thus, as the radius increases collision and coalescence process dominate over diffusion process.

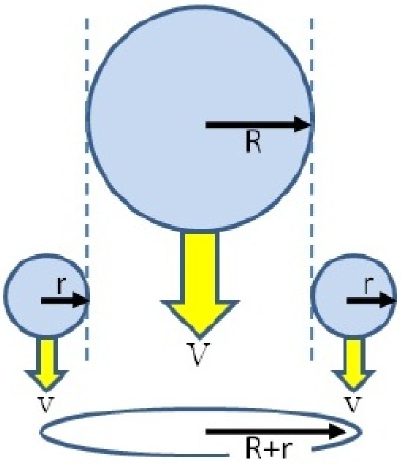

Figure 2.10. Schematic of collision and coalescence.

2.3.3. Ice crystal nucleation

Similarly, saturation over a planar ice surface occurs if the deposition ($vapor \rightarrow ice$) rate equals the sublimation ($ice \rightarrow vapor$) rate. Since the evaporation rate is larger than the sublimation rate, at a given temperature, the intermolecular bonding energy of molecules in ice is greater than that in liquid water. Then, $e_{si}(T) < e_{sw}(T)$ where e_{si} is the saturation vapor pressure over ice and e_{sw} is the saturation vapor pressure over liquid water.

It is not certain that liquid cloud droplets will freeze below 0°C. Nucleation of ice particles occurs either from the liquid or from the vapor phase. The homogeneous nucleation of ice from the liquid phase is similar to that of liquid drops from vapor. Statistical variations of the liquid molecular arrangement cause the formation of the initial crystal. Then if the crystal reaches a critical size depending on temperature, other water molecules will tie to ice crystal and water will freeze quickly. It is also not impossible that ice crystal can nucleate directly from the vapor phase theoretically. For this to be possible high super saturations ($> 1000\%$) with respect to ice should be reached. There are also aerosols which can behave as ice nuclei (IN) in the atmosphere if formation of their molecular is similar enough to the lattice structure of ice. However, it is not much common for aerosols to have this formation. Thus, the number of ice nuclei is much less than cloud condensation nuclei. It depends on the increase of ice super saturation and decrease of the temperature that aerosols can behave as a cloud nuclei. Silver iodide and clay are common ice nuclei. There are many ways that heterogeneous nucleation can occurs such as deposition of the vapor directly onto the ice nuclei, acting of ice nuclei first as a CCN to form a liquid droplet, and then behaving as a ice nuclei to initiate freezing. Freezing of a super-cooled liquid droplet can also occur just after contacting with the ice nuclei. Finally, the ice nuclei which are absorbed into a liquid droplet may trigger the freezing mechanism.

2.3.3.1. Ice crystal growth. Bergeron-Findeisen effect is a crucial growth process in cold clouds where mixed phase occurs. This effect explains ice crystal growth with regard to two important properties of water. First one is nonfreezing of cloud droplets at 0°C. Second feature of water is that saturation vapor pressure over ice crystal is less than that of over liquid droplets. Therefore, air becomes supersaturated for ice crystal when saturation is reached with respect to liquid droplets. First assume that one liquid droplet freezes in a super-cooled liquid water cloud. Initially, saturation is reached for liquid water. Then, ice crystal is supersaturated. Growth of ice crystal occurs by diffusion of water vapor towards the ice crystal. The vapor pressure decreases below the saturation vapor pressure value for the liquid water due to this process. Then, the liquid droplets evaporate rapidly. This again increases the vapor pressure to the liquid water saturation pressure value. Therefore, a chain reaction develops and several snowflakes occur [29, 30].

2.4. Radiative Transfer

The major energy source for the Earth is the solar radiation. Redistribution of this heat is done by the large-scale weather patterns. Change in these processes leads to climate variability. Solar radiation covers the entire electromagnetic spectrum from gamma rays to radiowaves. However, the most significant bands for atmospheric radiative processes are the ultraviolet, visible (400 to 700nm), and the near/thermal infra-red bands. The radiant energy propagates in the electromagnetic wave form with speed of light $c = 3 \times 10^8$ m/s. The speed, frequency and wavelength λ of electromagnetic waves are related by

$$c = v\lambda \tag{2.120}$$

2.4.1. Black Body

A black body is a perfect absorber by definition. It absorbs all electromagnetic radiation that coming on it. Electromagnetic radiation neither passes through it nor is reflected. It is a perfect emitter as well. It emits the maximum possible amount of energy at temperature T. The spectrum of the energy emitted by a perfect black body depends only on temperature. There is also a relation between the temperature of the object and the wavelengths of electromagnetic radiation emitted by this object. We assume that emission from the sun is a result of a black body.

2.4.1.1. Planck Function. The radiance of radiation (energy per unit time per unit area of emitting surface, per unit solid angle, per unit wavelength) emitted by a black body for wavelength λ as a function of T is given by the Planck Function:

$$L_\lambda = \frac{2hc^2}{\lambda^5 \left(e^{\frac{ch}{k\lambda T}-1} \right)} \tag{2.121}$$

where $h = 6.63 \times 10^{-34}$ J s is the Planck constant and $k = 1.38 \times 10^{-23}$ J K^{-1} is the Boltzmann constant. Mostly infrared light ($\lambda > 4\mu m$) is emitted by black bodies at room temperature, they start to emit in visible band only as temperatures reach a few hundred degrees Celsius.

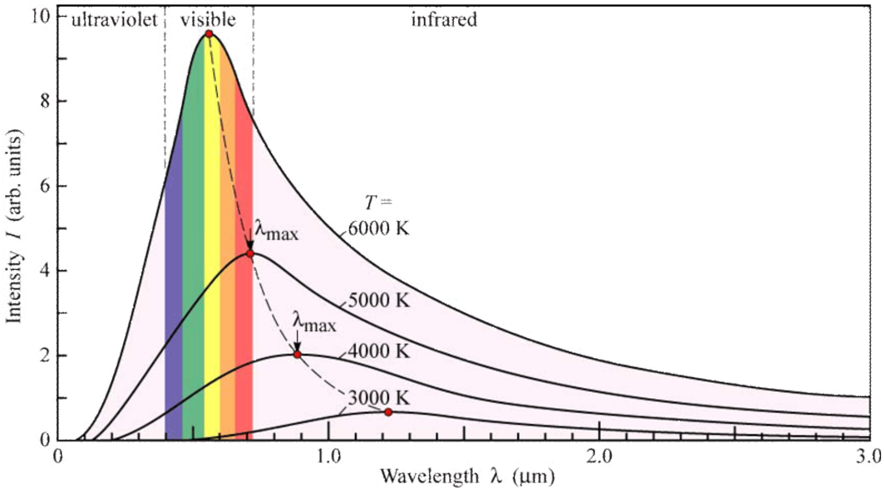

Figure 2.11. Planck Function describes black body radiation [31].

2.4.2. Wien's Displacement Law

Wien's displacement law gives the wavelength of maximum emission by setting the derivative of $dL_\lambda/d\lambda$ equal to zero as

$$\lambda_{max} = \frac{2897\mu K}{T} \tag{2.122}$$

where T is temperature and $\mu = 10^{-6}$. According to Wien displacement law, the wavelength of maximum emission for black body radiation is inversely proportional to the absolute temperature. Maximum wavelength of the radiation emitted from the surface ($T \approx 293$K) is 9.9 μ m in the infrared band of spectrum. The radiance L which is the total emitted energy per unit area per unit solid angle can be obtained by integrating Equation 2.121 across all wavelengths,

$$L \equiv \int_0^\infty L_\lambda d\lambda = \frac{\sigma T^4}{\pi} \tag{2.123}$$

where σ is the Stefan Boltzmann constant ($= 5.67 \times 10^{-8}\mathrm{Wm}^{-2}\mathrm{K}^{-4}$).

2.4.3. Stephan-Boltzmann Law

Since the integral of L over the hemisphere is the Radiant Emittance E, which is equal to πL, we get

$$E = \sigma T^4 \tag{2.124}$$

This is known as the Stephan-Boltzmann Law. Thus, the energy per unit area per unit time emitted by a blackbody is proportional to the fourth power of the temperature.

2.4.4. Energy balance models of the atmosphere

To understand the energy balance model of the Earth-atmosphere system, we consider Sun as a black body with emittance of σT_{sun}^4 where T_{sun} is the surface temperature of the sun. Total emitted energy over a surface area of $4\pi r_s^2$ is equal to $4\pi r_s^2 \sigma T_{sun}^4$. By using the inverse square law, the irradiance E (Wm^{-2}) of the sun at a distance of r_d over the surface of a sphere of area $4\pi r_d^2$ becomes

$$E = \sigma T_{sun}^4 \left(\frac{r_s}{r_d}\right)^2 \tag{2.125}$$

Since r_d is equal to the distance between the Earth and the sun, then we define $S_0 \equiv E$, called the solar constant. S_0, is the average irradiance reaching to the top of the Earth's atmosphere. We have $S_0 \simeq 1370\mathrm{Wm}^{-2}$ by using measurements from satellites. We can calculate the surface temperature of the sun by using the solar constant as,

$$T_{sun} = \sqrt[4]{\left(\frac{r_s}{r_d}\right)^2 \frac{S_o}{\sigma}} \tag{2.126}$$

getting T_{sun} as 5800 K. Incoming solar radiation intercepted by the Earth is $S_0 \pi r_e^2$. E_e, the average incident solar radiation on the Earth's surface area of $4\pi r_e^2$ is

$$E_e = \frac{S_0 \pi r_e^2}{4\pi r_e^2} \frac{S_0}{4} \tag{2.127}$$

which has a value of 340 Wm^{-2}. Some amount of this incoming solar radiation is reflected back to space by surface, clouds and atmospheric gases. The ratio of reflected irradiance and incident solar irradiance is called as α_p the planetary albedo.

$$\alpha_p = \frac{\text{Reflected solar irradiance (at top of atmosphere)}}{\text{Incident solar irradiance}} \tag{2.128}$$

Measurements made by satellites show that the Earth's albedo is $\alpha_p \simeq 0.3$. Thus, the average irradiance that the Earth is absorbed is $\frac{S_0}{4}(1 - \alpha_p)$ which is 240 Wm^{-2}. The Earth is also assumed to emit the outgoing radiation as a black body at some effective temperature T_e. The amount of emission of the Earth/atmosphere system is $4\pi r_e^2 \sigma T_e^4$. We assume that absorbed incoming solar and emitted outgoing infrared radiation on the Earth are in an equilibrium.

$$S_0 \pi r_e^2 (1 - \alpha_p) = 4\pi r_e^2 \sigma T_e^4 \tag{2.129}$$

Thus

$$T_e = \sqrt[4]{\frac{S_0}{4\sigma}(1 - \alpha_p)} = 255K \tag{2.130}$$

We obtain the effective temperature of the Earth as $T_e = 255K$. However, the average global temperature of the Earth is approximately 288K which is found by surface and satellite measurements. They are different because surface temperature and effective emitting temperature is not same thing. Greenhouse gases in the atmosphere are blocking the outgoing infrared radiation and this warms the surface, which in the simplest term is called the Natural Greenhouse Effect.

2.4.4.1. A simple model for the Greenhouse Effect. To see the results of the Greenhouse Effect, we will study a simple radiative balance model consist of the Earth surface with an overlying atmosphere. Atmosphere is considered to be a single homogeneous slab which is radiatively active. We assume that the Earth surface is a black body, solar radiation is not absorbed by the atmosphere and the atmosphere is a grey body (imperfect black body).

Grey Bodies and Kirchoff's Law. According to the Kirchoff's Law, radiative emission and absorption of black body is in thermodynamic equilibrium. It says that absorptance a is equal to emittance ϵ and transmittance τ is equal to $1-\epsilon$. Emittance of a grey body is given as

$$E_{grey} = \epsilon\sigma T^4 \tag{2.131}$$

where ϵ is the fractional emittance ($\epsilon \leq 1$).

Now, we can write the energy balance equation for the top of atmosphere, layer of the atmosphere and surface of the Earth by assuming a state of equilibrium as:

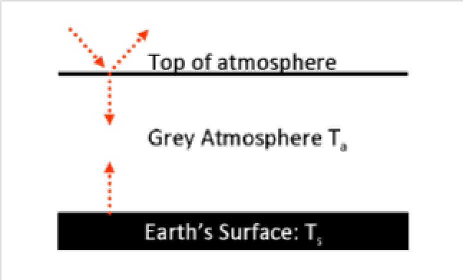

Figure 2.12. Sketch of simple greenhouse slab model.

Top of atmosphere.

$$\frac{S_0}{4}\left(1-\alpha_p\right)=\sigma T_s^4\left(1-\epsilon\right)+\epsilon\sigma T_\alpha^4 \tag{2.132}$$

Incoming solar radiation is not absorbed by atmosphere and transmitted to the Earth's surface, so outgoing radiation from top of atmosphere is equal to $\frac{S_0}{4}(1-\alpha_p)$. Incoming irradiance to top of atmosphere is coming from both atmosphere at the temperature T_a and the Earth's surface at the temperature T_s. Since we assume that atmosphere is grey body, irradiance of atmosphere is $\epsilon\sigma T_\alpha^4$. The term $\sigma T_s^4(1-\epsilon)$ is the irradiance transmitted from atmosphere and reaching to top of atmosphere.

Atmosphere.

$$\epsilon\sigma T_s^4=2\epsilon\sigma T_a^4 \tag{2.133}$$

In the grey atmosphere, incoming irradiance which is equal to $\epsilon\sigma T_s^4$ is the radiation emitted from the Earth's surface. The outgoing irradiance of the atmosphere is amount of $2\epsilon\sigma T_a^4$ which is radiated both to top of atmosphere ($\epsilon\sigma T_a^4$) and to the Earth's surface ($\epsilon\sigma T_a^4$).

Surface.

$$\epsilon\sigma T_a^4+\frac{S_0}{4}\left(1-\alpha_p\right)=\sigma T_s^4 \tag{2.134}$$

The incoming irradiance of the Earth's surface is coming from both the Sun $\frac{S_0}{4}(1-\alpha_p)$ and the atmosphere $\epsilon\sigma T_a^4$. Outgoing irradiance from surface is σT_s^4 since it is assumed to be a black body. By using three equations, we can calculate the temperature of surface and atmosphere as,

$$T_\alpha=\frac{T_s}{\sqrt[4]{2}} \tag{2.135}$$

and substituting T_a into Equation 2.132 we get

$$T_s = \sqrt[4]{\frac{s_0\left(1-\alpha_p\right)}{2\sigma\left(2-\epsilon\right)}} = 278\text{K} \tag{2.136}$$

2.4.5. Radiation interaction with a slab

When we study the incoming and the outgoing irradiance between layers of the atmosphere in more detail, we take into consideration a homogenous and horizontally infinite atmosphere layer with a finite vertical depth of Δz (Figure 2.13). The radiance L_λ has three components which are the direct solar component, the scattered component and emission. The direct solar component passes through the slab direction (θ, ϕ) without being blocked by any obstacle. The scattered component is radiative flux coming from different direction and scatters within the slab to go through direction (θ, ϕ). Emission is radiative flux emitted from the slab in direction (θ, ϕ).

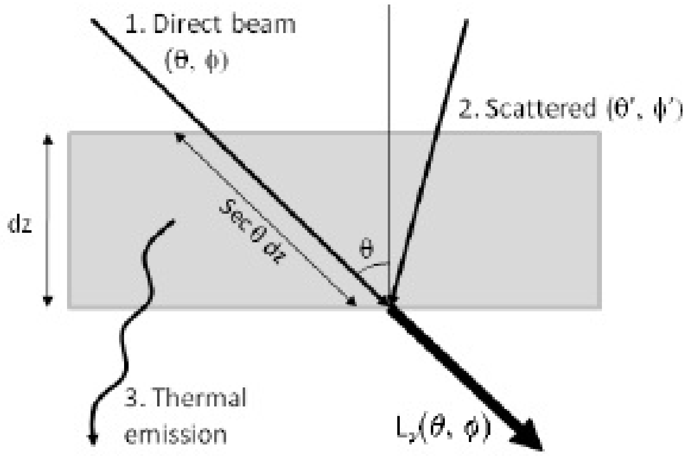

Figure 2.13. Schematic of radiation interaction with a medium of thickness dz.

2.4.5.1. Direct Radiation - Beer's Law. This law expresses the change in radiation intensity due to absorption of the radiation. We consider radiative beam passing through an absorbing medium. The finite change dL_λ in the direct component of the radiance is directly proportional to L_λ: the original intensity, $sec\theta dz$: the path length through the slab, k^e_λ: the mass extinction coefficient at wavelength λ. The infinitesimal decrease is given as

$$dL_\lambda = -L_\lambda k^e_\lambda \rho sec\theta dz \tag{2.137}$$

where ρ is the density of the material.

The mass extinction coefficient is equal to the sum of the absorption k^a_λ and scattering k^s_λ coefficients with units of $m^2 kg^{-1}$.

$$k^e_\lambda = k^a_\lambda + k^s_\lambda \tag{2.138}$$

We define the single scattering albedo as the ratio of scattering coefficients and the mass extinction coefficient. When the single scattering albedo ω is equal to 1, radiative beam is purely scattered. It is purely absorbed when ω is equal to 0.

$$\omega = \frac{k^s_\lambda}{k^e_\lambda} \tag{2.139}$$

We obtain the direct component of radiation by integrating Equation 2.137 over dz as

$$L^{z_1}_\lambda = L^{z_2}_\lambda \exp\left(-\int_{z_1}^{z_2} k^e_\lambda \rho sec\theta dz\right) \tag{2.140}$$

When we set δ_λ as

$$\delta_\lambda = \int_{z_1}^{z_2} k^e_\lambda \rho sec\theta dz \tag{2.141}$$

from Equation 2.140 then we call δ_λ as the optical thickness or optical depth of the layer between z_1 and z_2. Then we can write Beer's Law as

$$L_\lambda^{z_1} = L_\lambda^{z_2} e^{-\delta_\lambda} \tag{2.142}$$

We can say that the transmittance depends on optical depth by

$$\tau_\lambda = e^{-\delta_\lambda} \tag{2.143}$$

All variables such as the transmittance, absorption, extinction and optical depth are functions of wavelength. The emission from a slab in direction (θ, ϕ) and absorption are equal to each other and given as

$$L_\lambda^{emitted} = L_\lambda k_\lambda^\alpha \rho sec\theta dz \tag{2.144}$$

We can define the scattering from other directions (θ', ϕ') as

$$L_\lambda^{scatter} = \frac{\omega_\lambda}{4\pi} \int_0^{2\pi} \int_{\frac{-\pi}{2}}^{\frac{\pi}{2}} L_\lambda \left(\theta', \phi'\right) P \left(\theta', \phi', \theta, \phi\right) sin\theta d\theta d\phi \tag{2.145}$$

where 4ϕ is a normalization factor, integration of the solid angle over a sphere, ω_λ is the single scattering albedo, $P(\theta', \phi', \theta, \phi)$ is the Phase function. Phase function is the probability that a radiative beam will be scattered from direction (θ', ϕ') into direction (θ, ϕ) [29, 30].

3. CLIMATE MODELS AND PREDICTIONS

3.1. Modeling and Projection of Anthropogenic Climate Change

Climate models are used as tools to predict and simulate the behavior of the components of the climate system and interactions among them. Models are constructed to simulate climate and its natural variability and to project the response of the climate to anthropogenic forcing. The question that arises in modeling climate change is whether the change of the state of the climate system is predictable or not. According to the work done by Lorenz in the 1960s, despite the mathematical equations defining the change of the system being perfectly deterministic, the predictability of complex non-linear systems are limited. The climate system is a non-linear complex system as well. Climate system predictability is based on kind of climate event investigated, time and space scales considered and variability of the system involved.

Climate variations due to the change in external forcing are partly predictable on a global scale. The anthropogenic climate change on global and continental scale is reproducible by models considering the increasing greenhouse gas concentration. Climate change due to external force may be reproducible since external forcing is known or be predictable. The climate processes on large scales are less affected by internal variations of climate system than regional and local climate. Since regional climate is much more affected by internal dynamics of the system, climate change on a global scale may be more easily predicted.

Reasonable and consistent projection of future climate is essential to study the impact of climate change. The impact of future climate change is investigated by developing climate change scenarios depending on the results of model projections. Response of the climate to present and future activities of human is simulated by using climate models. First, the simulation of present climate for periods of many decades is done by considering present conditions without any change in external climate forcing. These simulation results are evaluated by using observations of the present climate.

The quality of the results is assessed to establish confident model results for projecting anthropogenic climate change. After validating model results, two methods have been used to simulate future change of climate. Equilibrium method is used by doubling the carbon dioxide concentration and running the climate model for a new equilibrium state. Estimation of climate change regarding double carbon dioxide concentration and climate sensitivity to altered radiative forcing is done by assessing the difference between two simulations. Systematic errors are handled with this method however the time dependence of climate change is not well understood by this method.

Transient method is used by forcing the model with time-dependent profile of greenhouse gas and aerosol scenario. This method is commonly used these days due to the improved computer resources. Time dependence of climate change is obtained by using transient method. Time-dependent greenhouse gas and aerosol concentrations can be provided by so-called emission scenarios. These emission scenarios have been developed by IPCC based on the assumptions of future socio-economic and demographic developments [32]. Different assumptions are corresponding to different emission scenarios. These scenarios have been developed based on artificial construction such as supposing step-by-step increase in greenhouse gas concentrations by stabilizing at some levels.

There is an agreement among results of different models but at the same time results of various models show a significant ambiguity and difference. Increase in the averaged global surface temperature and mean precipitation is projected by all models. However, different results are obtained by models about the regional patterns of climate change. Regional based climate change signal depends on modeling of climate processes, time dependence of external forcing and spatial range of aerosol concentrations.

Climate models are constructed by using mathematical equations which are represented by physical laws describing the dynamics of climate as discussed in the previous chapter. These non-linear equations are solved numerically on a three-dimensional grid over the global scale. To simulate climate, sub models must be used to represent the components of the climate system and processes taking place within and interactions among them.

The core of climate models which the atmosphere and ocean are included together are known as Atmosphere-Ocean General Circulation Models (AOGCMs). In the atmospheric component of models, equations are solved to define the change of momentum, heat and moisture in large scales. In the ocean, similar equations are solved as well. The horizontal resolution of atmospheric component of global circulation model is roughly 100 km. Since spatial scale that many physical processes related to clouds and convection from ocean occurs is much smaller than the model resolution, these processes cannot be modelled explicitly. However, the average effects of these processes are included by using the physical relationships with the larger-scale variables. This technique is called as parameterization [20].

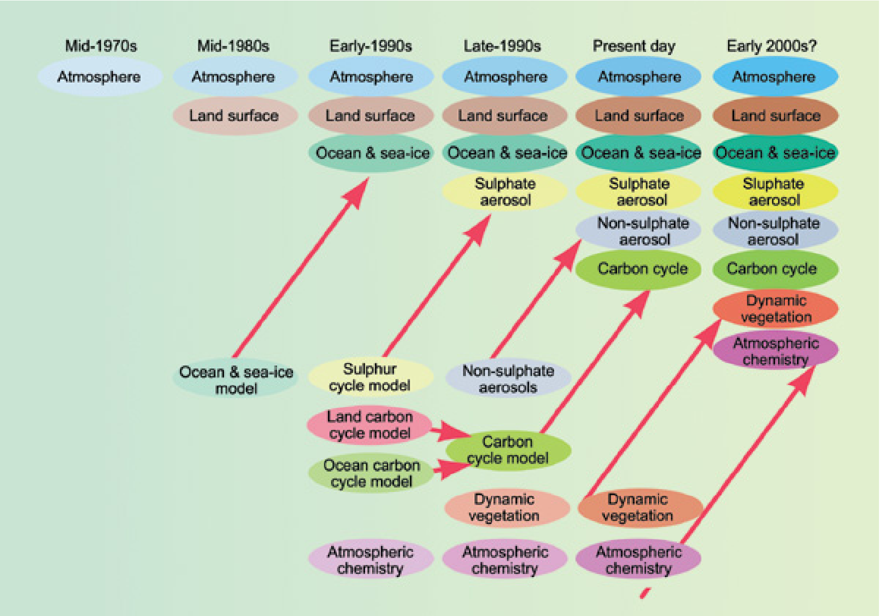

Figure 3.1. The past, present and possible future evolution of climate models with different components over the last 25 years is presented [20].

3.2. Model Evolution

Climate scenarios are constructed by using of climate models. Increase in computer power allowed the evolution of these models. This progress also increases the complexity of models, time and spatial resolution (Figure 3.2). Models have started to include more climate components and processes by improved computational capacity. As computer power increases, models began to simulate future climatic change. Most of the early work on modeling CO_2 induced future climate change was using atmospheric general circulation models combined with simple slab ocean models [33, 34]. Physical content of the models has been progressing over time as well. Current climate models are much more complex and include ocean-atmosphere component together. They sometimes contain interactive chemical or biochemical components as well (Figure 3.3). Models provide time-dependent results on future climate change. On the other hand, it is obvious that climate models cannot simulate climate perfectly since representation all of spatial and temporal scale processes is not possible with current capabilities, and the complex climate system may behave chaotically due to nonlinearity. Simple models which include ocean-atmosphere, biosphere components and interactions among them or interactions of climate with economy may even show similar characteristics. They may behave partially unpredictably and become chaotic. Additionally, almost all important processes in climate system such as clouds, vegetation, and convection from ocean, take place in very small scales. Global climate models cannot represent them in detail due to their coarse resolution. Because of that reason, these processes cannot be understood well in scientific manner. Therefore, help in usage and comprehension of these complex models is still needed by models which are either simple or do not include all climate processes, or are studying only a specific region. It enables us to understand climate processes better and compare results with observations in a more relevant manner. Hierarchy of models links theoretical consideration to complexity of models [35].

Simple models are the models which may study few numbers of equations and may be one or two dimensional or may work on few processes. The concept of model hierarchy is related to the scale of climate models as well. Regional climate models that

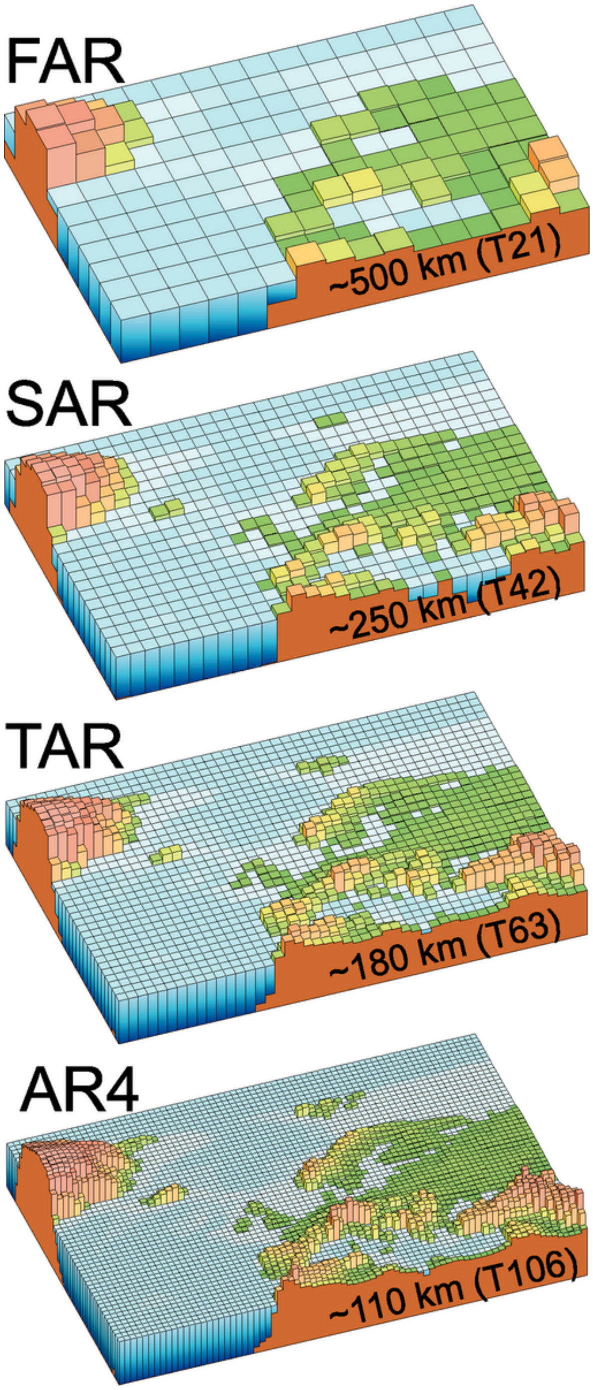

Figure 3.2. Resolution characteristic of the generations of climate models used in the IPCC Assessment Reports: FAR (IPCC, 1990), SAR (IPCC, 1996), TAR (IPCC, 2001), and AR4 (2007) [36].

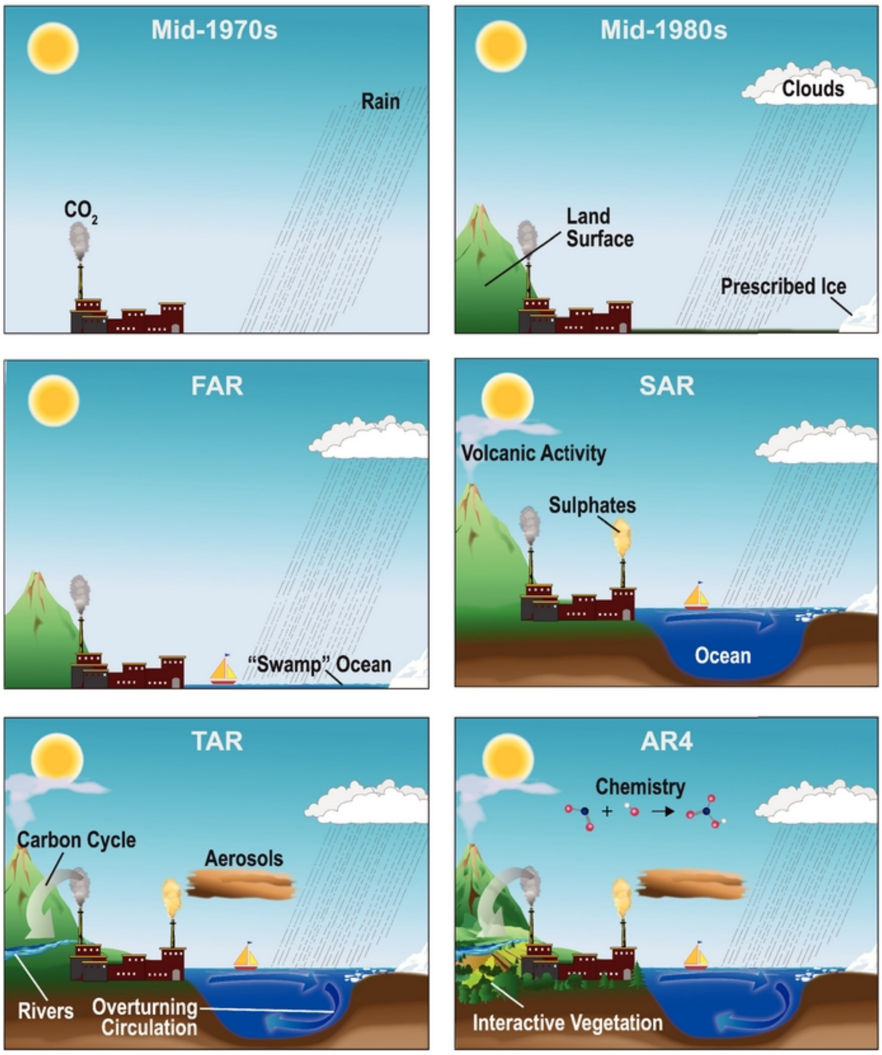

Figure 3.3. Development of the complexity of climate models are shown over the last few decades [36].

simulate a specific area with finer resolution, or study only one process like cloud models complement global circulation models. Earth Models of Intermediate Complexity also study on long time scales such as glacial and interglacial periods [37]. This variety of climate models in scale develops as computational capacity increases. Simple models have been used to interpret the results of IPCC scenarios [36].

3.3. Coupled Models: Evolution, Use, Assessment

Two models that investigated the effect of double CO_2 concentration in atmosphere was used by National Academy of Sciences of the USA in their first report on global warming. Model results showed an increase between 1.5°C and 4.5°C in the global mean surface temperatures [38]. These simple models and most of the models given in the First Assessment Report of IPCC were the atmospheric models which are coupled with slab ocean model [39].

Coupling atmospheric and oceanic models were first performed on late 1960s and early 1970s [40–42]. Slab ocean model were replaced by full ocean models. This progress was very essential improvement in climate modeling during the last 20 years [43]. In the meantime, atmosphere and ocean components have been already improved individually. Progression in constructing coupled atmosphere and ocean models allowed significant improvements in simulation of climate change. It also led to investigate time-dependent simulation of climate change scenarios and triggered the development of comprehensive ‘Earth-system models’ which represent chemical and biogeochemical cycles explicitly.

There were many problems in climate modeling while transition from simple models to coupled models. One of them is not to know the initial state of the ocean definitely. The magnitude of imbalance of surface flux in energy and momentum is much smaller than the magnitude of observational error, so that it cannot be detected in observational accuracy. It made coupled global circulation models to give unrealistic results. Additionally, there is no controlling mechanism about simulated salinity. Most important of these problems is to give an underlying reason to introduce ‘flux adjustments’ or ‘flux corrections’ into early simulations [44, 45]. These adjustments can be added into models arbitrarily by empirical equations since they could not be explained by physical principles.

After all these advances in coupled models, there was still uncertainty in the results of the models [46]. According to definition by Lorenz [47] there are two kinds of problems in climate prediction. The first kind of problem is an initial-value problems and it is to predict how the climate system behaves with a given initial state. Such systems are difficult to predict due to the nonlinearity and instability of the equations. Second kind of problem is to know how climate system responds to changes in the external forcings. Therefore, models predict long-term average statistics of climate variable instead of predicting time dependent profile of climate processes. They are simulating how statistics of climate variable such as global average mean temperature or average total precipitation change with varied external forcings. Prediction of future climate change with respect to altered concentration of greenhouse gas in atmosphere can be an example of the second kind.

Model errors and uncertainties are the cause of problems of second kind in climate predictions. Projects including comparison of distinct climate models has been arranged by scientific community in order to evaluate uncertainty in climate models. Its aim was to increase number and temporal and spatial range of simulations in order to assess agents which affect accurate results. Comparison simulation was first achieved by Cess *et al.* [48]. Cess *et al.* investigated response of different models in representing cloud feedback mechanism to doubled concentration of CO_2 and effects on atmospheric radiation [36].

3.4. Model Intercomparison Projects (MIP)

World Climate Research Programme established 'model intercomparison projects' (MIPs) in the 1990s. The Atmospheric Model Intercomparison Project (AMIP) was the first of this kind of attempts working with atmospheric general circulation models. Coupled Model Intercomparison Project (CMIP), which is working on coupled ocean-atmosphere general circulation models also established by the Working Group on Coupled Modelling (WGCM) under the World Climate Research Programme (WCRP). This project allows many scientists to assess general circulation models systematically and enables model improvement. The whole climate modeling community joined this project since it has started in 1995. Archiving and storage of almost all CMIP data is provided by the Program for Climate Model Diagnosis and Intercomparison (PCMDI).

CMIP has started via gathering data from models' control runs in which external forcing is constant. Output data belonging to future scenario of global warming have been collected in later versions of CMIP. Climate model results from past, present and future climate simulations was gathered between the years 2005 and 2006 by PCMDI and data in question forms phase 3 of the Coupled Model Intercomparison Project (CMIP3). This attempt officially known as the "WCRP CMIP3 multi-model dataset" has been organized to serve for providing data to IPCC's Working Group 1, which works on physical basis of the climate system. The WCRP's Working Group on Coupled Modelling (WGCM) and 20 modeling group from all around the world decided to develop a new set of climate model experiment with the input of the IGBP AIMES project on September 2008. These experiments cover the fifth phase of the Coupled Model Intercomparison Project (CMIP5). CMIP5 provides set of simulations of climate models to assess model performance in simulating the past, give future climate simulations for near term period up to about 2035 and long term period up to 2100 and beyond, and explain the reason behind the difference in model simulations regarding clouds and the carbon cycle [49].

These kinds of projects are very essential in developing climate models developing since they allowed standardization of forcing parameters, output file formats; variable names etc. for easy use of model outputs by scientific studies. In these projects, every modeling center save their model results by themselves, and the outputs of these models of different centers were analyzed by individual research groups different from modelers in order to make model outputs more accurate.

The AMIP and CMIP projects are crucial for climate modeling because of standardization of quality control, providing sustainability and reproducible results. The results of the MIPs show that cloud radiation processes, the deep ocean, the cryosphere and ocean-atmosphere interactions are very difficult to simulate. However, to compare results of distinct models is not enough to resolve these processes. Therefore, ensemble approach which means multiple simulations from single model is needed to predict climate processes. The first study of ensemble approach is the investigation of results of global circulation model which is ran with different initial and boundary conditions [50, 51]. Intercomparison and ensemble model studies are still under development [36].

3.5. Overview of Model Types

There is range of climate models from simple models to complex Earth System Models used in climate research. The choice of model types are decided according to the scientific problem to be solved [35, 52]. The climate models are used to simulate palaeo or historical climate, climate sensitivity and variability, predict future climate change of near-term and long term periods and downscale projections to obtain finer resolution results in regional and local base. As models are getting more complex, computational cost increases.

3.5.1. Three-dimensional Climate Models

Coupled atmosphere ocean general circulation models are the most complex three dimensional climate models whose main goals are to realize the dynamics of climate system and interactions among its components such as atmosphere, ocean, land and sea-ice. Coupled models are used to project seasonal to decadal future climate change based on greenhouse gas concentration forcing. Additionally, high-resolution atmosphere-ocean general circulation models are often run for process based studies and particular region. Some sub-grid scaled processes in climate system are parameterized according to the computational cost [53].

3.5.2. Simple Climate Models

Simple climate models with reduced complexity are one or two dimensional climate models. These models are run to simulate climate sensitivity to one particular process. Wigley [54] simulated increases in global mean temperature and sea level rise as Kyoto Protocol implications by using modified version of the upwelling diffusion-energy climate model [55–58]. Simple models are also run within larger integrated assessment models to investigate impacts of climate change [59, 60] and the costs of decrease in emission [20, 36, 61, 62].

3.5.3. Earth System Models (ESMs)

Earth System Models (ESMs) expand upon AOGCMs and contain different biogeochemical cycle modules involving the carbon, the sulphur or ozone cycle [63]. They are essential modeling tools to simulate response of the climate system to external forcing in which biogeochemical cycles take place for past and future periods [1].

3.5.4. Earth System Models of Intermediate Complexity

Earth System Models of Intermediate Complexity (EMICs) are models which are between three dimensional models and simple models in terms of complexity. The main feature of EMICs is that many processes implicit in comprehensive models are defined in EMICs even though in a more parameterized form. Interactions among components of the climate system such as biogeochemical cycles are also described in EMICs. On the other hand, their computational complexity allows for longer term simulations like tens of thousands of years or sensitivity simulations over several millennia. There are many EMICs which investigated many applications such as two dimensional ocean models coupled to simple atmospheric component [64, 65] or two dimensional geostrophic [66] or statistical-dynamical (e.g., [67]) atmospheric components, and models that have statistical-dynamical atmosphere and ocean components in three dimension [68,69] and comprehensive models in reduced-form [70]. Some of EMICS are used for simulating the last glacial maximum period [71,72]. On the other hand, EMICs are not convenient to use for simulating regional climate [20].

3.5.5. Regional Climate Models (RCMs)

Regional climate models are limited-area models that include atmospheric and land-surface components and they are run without interactive ocean and sea ice. RCMs downscale the global model outputs dynamically for some particular domain. The driving data from global circulation models can also contain greenhouse gas and aerosol forcing. Regional modeling technique is a one-way nesting technique with no effect of regional climate output to the driving global circulation model output. The strategy behind the regional climate modeling is that response of global circulation to external forcing influencing large scale domains are investigated by global models. Regional climate models are used to investigate the effects of sub GCM grid scale forcings such as complex topography and inhomogeneous land cover and simulate climate variables and atmospheric circulation at finer scales.

Regional climate models started to be used in climate modeling application with studies done by Dickinson *et al.* [73] and Giorgi [74]. Today, they are used in climate modeling studies from palaeoclimate [75, 76] to human-induced climate change. They are run for multi-decadal simulations in higher resolution up to 10 to 20 km and investigate feedback mechanisms influencing the regional scale. Regional modeling technique has two main limitations which are the inherited systematic errors in forcing global model data and one was nesting not allowing two way interactions between regional and global climate models. Consideration of choice of physical parameterization, size of model domain and resolution, technique to simulate large scale meteorological conditions, and internal variability because of non-linear dynamics not related with the boundary forcing [77–79] is very essential for regional climate predictions. Regional climate models are demanded since they have computationally low cost because of domain size.

The choice of domain where simulation takes place is important. Increase in model domain size reduces the influence of the boundary data [80, 81] and internal model physics for specific variables and seasons may weaken this influence [82]. Choosing of domain can allow regional climate model to differ from driving global data [83]. The size of domain is an essential as well in order not to damp local forcings. It should be large enough not to be affected negatively by the application of the boundary conditions [84]. The location of the lateral boundaries can influence the sensitivity to internal parameters [85] or may have no significant effect [86].

The selection of resolution of regional climate model can lighten the influences of physical forcings and parametrizations [87, 88]. Increase in resolution advances the description of the hydrologic cycle due to the better representation of topography [89, 90]. Better representation of cyclonic systems and vertical velocities can be done due to simulating atmospheric motions in high resolution. In order to capture concerned forcings in different sub-regions, different resolutions may be needed [89, 91–93].

Coupled regional climate models were built as well. They are composed of atmospheric regional climate models coupled to models including other climate system components such as lake, ocean/sea ice, chemistry/aerosol, and land biosphere/hydrology models [20, 93–103].

3.6. Reanalysis and Observational Datasets

3.6.1. Atmospheric Reanalysis

Reanalyzing past observations to produce data sets for climate studies has become a very essential approach for climate modeling and research. Reanalysis data sets are more convenient than operational analyses to use in climate variability studies since they are generated by using consistent modern data assimilation systems. The only changing component of this approach is the sources of the raw input data because of the varying observing tools including radiosonde, satellite, buoy, aircrafts, ships and etc. Spatially complete and consistent record for the global circulation can be obtained by reanalysis data. Different from the weather analyses using operational forecasting systems, a reanalysis is generated by a unique version of a data assimilation system and changes in method does not affect the reanalysis [104].

Atmospheric reanalysis consists of series of analysis steps which integrate background information for a typically 6 hour period with observations for the period to predict the state of the atmosphere at a given time. Even though observations are obtained from several kinds of measurement that have their own accuracy and distribution, the analysis is complete with respect to variable, domain and resolution. The background information which is very important to obtain the complete dataset is generated by short-range forecast triggered from recent preceding analysis in the series. The forecast of background information carries the information forward temporally and spread spatially from the observations used in previous assimilation sequences [105].

Multivariate reanalysis must be coherent with the observations and the laws of physics as well. This property of reanalysis is a requirement that distinguishes it from other methods for predicting geophysical variables from observations. In order to accomplish this property, a forecast model must be used as a synthesizer tool in assimilation and comparison of observations of various types and from different sources. For a model to be an adequately realistic, it should be able to extrapolate unobserved parameters at closer locations from locally observed parameters, and it should also carry this information forward in time. Then it is possible to acquire for example precipitation value from a reanalysis of other variables such as temperature, humidity and wind observations.

Nevertheless, changes in the observing systems and biases in models and observations unavoidably affect the climate data that is produced by reanalysis. This is not particular to reanalysis; it is valid for all existing analyses of observations. Since direct measurements of most of global variables of atmosphere including average temperature do not exist, statistical modeling and analysis which require extrapolation of data from incomplete and indefinite measurements must be included to estimate climate parameters.

Atmospheric reanalysis at many institutes have developed as better models, input data and assimilation methods are generated. These institutions are from NCEP (National Centers for Environmental Prediction) [106, 107], from JMA (The Japan Meteorological Agency) [108], and NASA (National Aeronautics and Space Administration) [109, 110], from ECMWF (European Centre for Medium-Range Weather Forecasts) [104, 105, 111].

3.6.1.1. Reanalyses at ECMWF. European Centre for Medium-Range Weather Forecasts has carried out reanalysis since 1980s. The first project, ERA-15 was generated in 1995 whereas the second reanalysis project, ERA-40 in 2002. The outputs of these projects have been widely used by the climate modeling community. ECMWF is generating a global reanalysis data ERA-Interim spanning the period from 1 January 1989 onwards. There is a progression in generating ERA-Interim data from 1979 to 1989 as well. The ERA-Interim project with a grid resolution of 0.75° × 0.75° was generated to replace ERA-40 with a grid resolution of 1.125 ° x 1.125 ° as a new atmospheric reanalysis. There are specific differences between the ERA-40 and ERA-Interim datasets in the assimilation of data and use of observations. According to Simmons *et al.* [112], the main improvements in ERA-Interim over ERA-40 data assimilation include 12 h, 4-dimensional variation analysis, finer horizontal resolution, better formulation of background error constraints, new humidity analysis, improved physics of the model, data quality control, variability bias correction of satellite radiance data, along with some other improvements in bias handling and an improved fast radiative transfer model. ERA-Interim uses most of the same sets of observations that ERA-40 used, with a few exceptions, for example, ERA-Interim provides more uniform quality altimeter wave height data and uses the reprocessed Meteosat data for winds and clear-sky radiances by EUMETSAT and ozone profile information from 1995 onwards provided by the Rutherford Appleton Laboratory [104, 113].

3.6.2. The Climate Research Unit Dataset

The Climate Research Unit dataset comprises a 0.5° grid resolution monthly mean climatology of multiple variables for global land surface excluding Antarctica.

Monthly time series for the period 1901-2002 at the same resolution have been constructed together with a mean climatology constrained to period of 1961-1990. Precipitation (PRE), wet-day frequency (WET), mean temperature (TMP), daily maximum and minimum temperature (TMX, TMN); vapor pressure (VAP), relative humidity (REH); sunshine percentage (SUN) and cloud cover (CLD); frost frequency (FRS); and wind speed (WND) are included in the mean 1961-1990 climatology. However, climate grids of the time series component consists of nine climate variables (temperature, diurnal temperature range, daily minimum and maximum temperatures, precipitation, wet-day frequency, frost-day frequency, vapour pressure, and cloud cover) for the period 1901–2002 and it is known as CRU TS 2.1 and available at (http://www.cru.uea.ac.uk/).

The mean of climate surfaces data have been generated by using a new dataset from the stations for 1961–90 climatological normals. Data constructed from station were interpolated by using thin-plate splines as a function of latitude, longitude, and altitude. Evaluation of the accuracy of the interpolations is done by using cross validation and by comparing with other climatologies [114].

The anomaly time series were generated by using historic anomalies having its source from the monthly database of the Climatic Research Unit (CRU) and the Global Historic Climatology Network (GHCN). The variables were categorized according to their availabilities as primary and secondary for the goals of generating monthly gridded time series. Data for the primary variables of precipitation, mean, maximum and minimum temperatures were sufficiently available to make interpolation directly from the station time series possible. The station time series that contain data for the secondary variables of cloud cover, vapor pressure, relative humidity and wet-day frequency were sparsely distributed in space and time. The secondary variables must be derived indirectly from gridded time series of primary variables. Those stations that have measurements for secondary variables were used for verification of the derived gridded time series [19].

3.7. Emission Scenarios

3.7.1. The Emissions Scenarios of the Special Report on Emissions Scenarios

The Intergovernmental Panel on Climate Change (IPCC) generated set of emissions scenarios. It is very difficult to predict how the world will change by 2100. Storyline of each emissions scenario correspond to different assumption of a distinct irreversible direction for future progress and they include uncertainties inherited from the main driving forces. Scenarios are categorized according to future characteristics such as demographic change, economic development, and technological change.

3.7.1.1. A1 Storyline. Very fast economic growth, increase in global population until mid-century and decrease thereafter, and the rapid introduction of new technologies are defined for a future world in the A1 storyline and scenario family. It describes a homogeneous world in which all mentioned themes are equally distributed among regions. Cultural and social interactions increase whereas regional differences in per capita income decrease. This storyline divided into three categories according to their directions of technological change in the energy system. Their technological emphasis are fossil intensive (A1FI), non-fossil energy sources (A1T), or a balance across all sources (A1B).

3.7.1.2. A2 Storyline. On the contrary to A1, a very heterogeneous world is defined in the A2 storyline and scenario family. Important features of this scenario family are self-reliance and conservation of local identities. Fertility patterns across regions diverge resulting in constant increase in global population. Development in economy and technology is in regional base and slower than other scenario families.

3.7.1.3. B1 Storyline. A convergent world with the same population scenario as in the A1 storyline is defined in the B1 storyline and scenario family. However, it describes rapid change in economy by reducing material intensity and introducing green and resource efficient technologies. Global solutions to sustainability in economy, social life and environment are important in this scenario family in the absence of additional climate initiatives.

3.7.1.4. B2 Storyline. A world in which local solutions to sustainability in economy, social life and environment is very important is defined in the B2 storyline and scenario family. Global population will constantly increase, at a rate lower than A2, development in economy will occur in intermediate level, and technological change will occur less quickly and more diversely than in the B1 and A1 storylines. Protecting environment and social equity is essential in the B2 storyline, while its focus is on local and regional levels [32].

3.7.2. The New RCP Scenarios

Future human induced emissions of greenhouse gases, aerosols and forcing agents like change in land use depends on socio-economic factors, and agreements signed by governments to control emissions to accomplish mitigation may also affect future anthropogenic emissions of greenhouse gases. However, SRES scenarios do not contain additional climate initiatives meaning that no emission scenarios were included according to implementation of the United Nations Framework Convention on Climate Change (UNFCCC) or the emissions targets of the Kyoto Protocol. In the Fifth Assessment Report of IPCC (AR5), outputs of climate models that use new emission scenarios called “Representative Concentration Pathways” (RCPs) are evaluated. The four RCPs, RCP2.6, RCP4.5, RCP6, and RCP8.5, include a larger set of scenarios to accomplish mitigation and were chosen to have different goals in terms of radiative forcing at 2100 (about 2.6, 4.5, 6.0 and 8.5 Wm^{-2} respectively). They considered reasonable and illustrative and are not directly dependent on socio-economic storylines like the SRES scenarios. RCP2.6 which is the lowest of the four, peaks at 3.0 Wm^{-2} and then decreases to 2.6 Wm^{-2} in 2100, RCP4.5 which is medium-low and RCP6.0 is medium-high stabilize after 2100 at 4.5 and 6.0 Wm^{-2} respectively, while RCP8.5 is the highest of the four reaches 8.5 Wm^{-2} in 2100 on a rising trajectory. They were generated by using Integrated Assessment Models (IAMs) in which economic, demographic, energy and basic climate components are typically included. Then, outputs of these assessment models are run by a simple model to generate time series of greenhouse gas concentrations to be input for AOGCMs [1].

3.8. Cordex

The Coordinated Regional Climate Downscaling Experiment (CORDEX) is a World Climate Research Programme (WCRP)-sponsored program designed to develop a framework to evaluate regional climate downscaling techniques for use in downscaled global climate projections for input into impact and adaptation studies within the AR5 timeline (Figure 3.4). Within the CORDEX framework an ensemble of dynamical and statistical downscaling models using multiple forcing GCMs as input will be produced. CORDEX data will provide 50 km ensembles of downscaled regional climate projections for most land regions of the world. Multiple common domains are selected to cover almost all of the land areas in the world. These regions are chosen to take advantage of existing regional projects such as ENSEMBLES, NARCCAP, ARCMIP, CLARIS and RCMIP. For the future, 6 h 3-dimensional model level fields will be saved by CMIP5 GCMs making climate projections as boundary forcing for regional climate models (RCMs). Prior to GCM-forced runs for a given region, RCMs had to be run with ERA-Interim (1989−2008) for the same region [115].

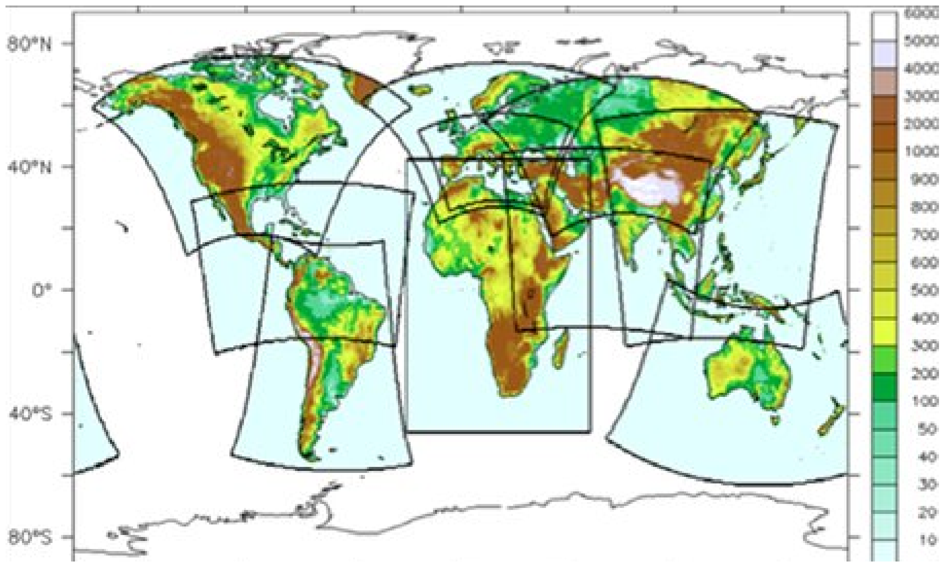

Figure 3.4. Map of the CORDEX domains (excluding Arctic and Antarctic).

4. REGIONAL CLIMATE MODEL RegCM

4.1. The RegCM

The RegCM is a regional climate model which was first developed in the late eighties (RegCM1, [73, 74]) by F. Giorgi, and it has evolved to later versions in the early nineties (RegCM2, [116,117]), late nineties (RegCM2.5, [78]) and 2000s (RegCM3, [118]) by the Earth System Physics section of the Abdus Salam International Centre for Theoretical Physics (ICTP). The RegCM has been the first limited area model designed to be a public, open source, user friendly and portable code that can be applied to any region of the World.

This regional climate modeling system has been effectively used for regional climate processing (e.g. [119–123]), regional climatic change studies (e.g. [13,78,124–128]) and interannual climate variability applications (e.g. [129,130]) during the last decade. Some studies were also done for Europe (e.g. [131]), Africa (e.g. [132–135]) and some parts of Asia (e.g. [136,137]).

Dickinson *et al.* (1989) [73] and Giorgi (1990) [74] originally suggested the idea that limited area models (LAMs) could be applied for regional studies. This idea includes one-way testing meaning that high resolution Regional Climate Model (RCM) simulations are forced by General Circulation Model (GCM) outputs. Outputs of General Circulation Models provide initial and time-dependent meteorological lateral boundary conditions (LBCs) for regional climate models with no feedback from the RCM to the driving GCM (hence one way).

The dynamical structure of the first generation NCAR RegCM originated from the hydrostatic version of the National Center for Atmospheric Research (NCAR)-Pennsylvania State University (PSU) Mesoscale Model version 4 (MM4) in the late 1980s [73,138]. MM4 is a compressible, finite difference model with vertical s-coordinates. Later, addition of the usage of a split-explicit time integration scheme with an algorithm to reduce horizontal diffusion in the presence of steep topographical gradients [116,139] has occurred.

Consequently, the dynamical structure of the RegCM is similar to that of the hydrostatic version of Mesoscale Model version 5 (MM5) [140]. The RegCM4 is thus a hydrostatic, compressible, sigma-p vertical coordinate model. In hydrostatic models, vertical acceleration is negligible with respect to vertical pressure gradients and vertical buoyancy forces, a good approximation for synoptic and subsynoptic scales of motion. Because of that reason, hydrostatic models have been successfully applied with horizontal resolutions as small as about 10 km. RegCM4 runs on an Arakawa B-grid that wind and thermodynamical variables are horizontally staggered by using a time-splitting explicit integration scheme. In this scheme, the two fastest gravity modes are first apart from the model solution and then they are integrated with smaller time steps.

For surface process representation, RegCM includes the biosphere−atmosphere transfer scheme (BATS; [141]) as well as the community land model (CLM), Version 3.5, as an option in its dynamical core for land surface processes. For radiative transfer, RegCM uses the radiation package of NCAR's community climate model, Version CCM3 [142]. The solar radiative transfer of the model follows the δ-Eddington approximation described by Kiehl *et al.* (1996) [142]. The cloud radiation part contains 3 parameters, including cloud fractional cover, cloud liquid water content and cloud effective droplet radius. RegCM uses the planetary boundary layer scheme developed by Holtslag *et al.* (1990) [143] based on a nonlocal diffusion concept. Convective precipitation is computed using 1 of 3 modified schemes: the Kuo scheme [144], the Grell scheme [145], or the MIT-Emanuel scheme [146,147]. Within the Grell scheme 2 different closures can be adopted: an Arakawa-Schubert type closure or a Fritsch-Chappell type closure.

4.1.1. Model components

The RegCM regional climate modelling system includes four components called Terrain, ICBC, RegCM, and Postprocessor. Terrestrial variables such as elevation, landuse and sea surface temperature and three-dimensional isobaric meteorological variables are interpolated from a lattice of a latitude-longitude to a finer resolution domain on different projections including a Rotated (and Normal) Mercator, Lambert Conformal, and Polar Stereographic projection horizontally. On the other hand, variables are vertically interpolated from pressure levels to the sigma coordinate system of RegCM as well. In the sigma coordinate system, sigma surfaces are following the terrain when it comes closer to the ground, and tend to approximate isobaric surfaces when the higher level surfaces obtained.

4.1.2. The RegCM Model Horizontal and Vertical Grid

The modeling system is usually doing data analysis on pressure surfaces but data has to be interpolated to the vertical coordinate of the model before it is given as an input to the model. The vertical coordinate of the modeling system is terrain following sigma coordinate system (Figure 4.1). The lower surfaces follow the terrain while the upper levels are flatter in this coordinate system. Intermediate surfaces increasingly flatten as the pressure decreases up to the top of the model. The model levels in a dimensionless sigma coordinate system is defined as

$$\sigma = \left(\frac{p - p_t}{p_s - p_t}\right) \tag{4.1}$$

where p is the pressure, p_t is a specified constant top pressure, p_s is the surface pressure. Sigma is zero at the top of the model, and one at the surface. Each vertical level of the model is defined as values of sigma. The values between zero and one determine the vertical resolution of the model and they do not have to be equally spaced. The vertical resolution in the levels near the surface is much finer than above levels. Users can change the number of vertical levels in the model. The horizontal grid of the model has an Arakawa-Lamb B-staggering of the velocity variables with respect to the scalar

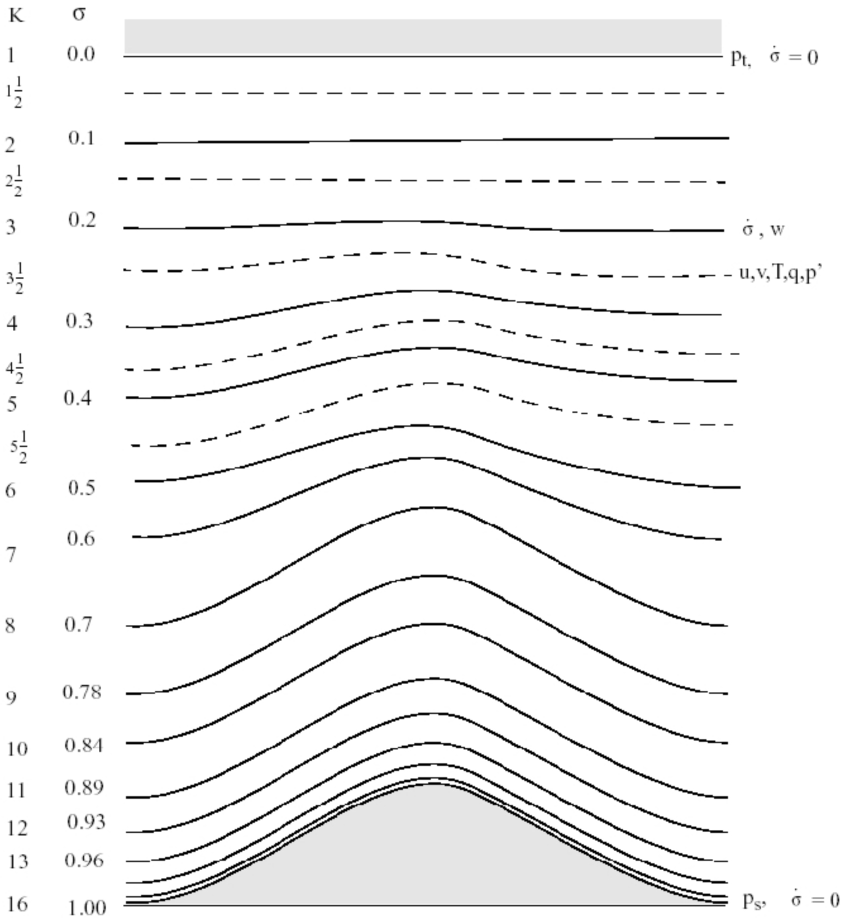

Figure 4.1. Schematic representation of the vertical structure of the model. This example is for 16 vertical layers. Dashed lines denote half-sigma levels, solid lines denote full-sigma levels [148].

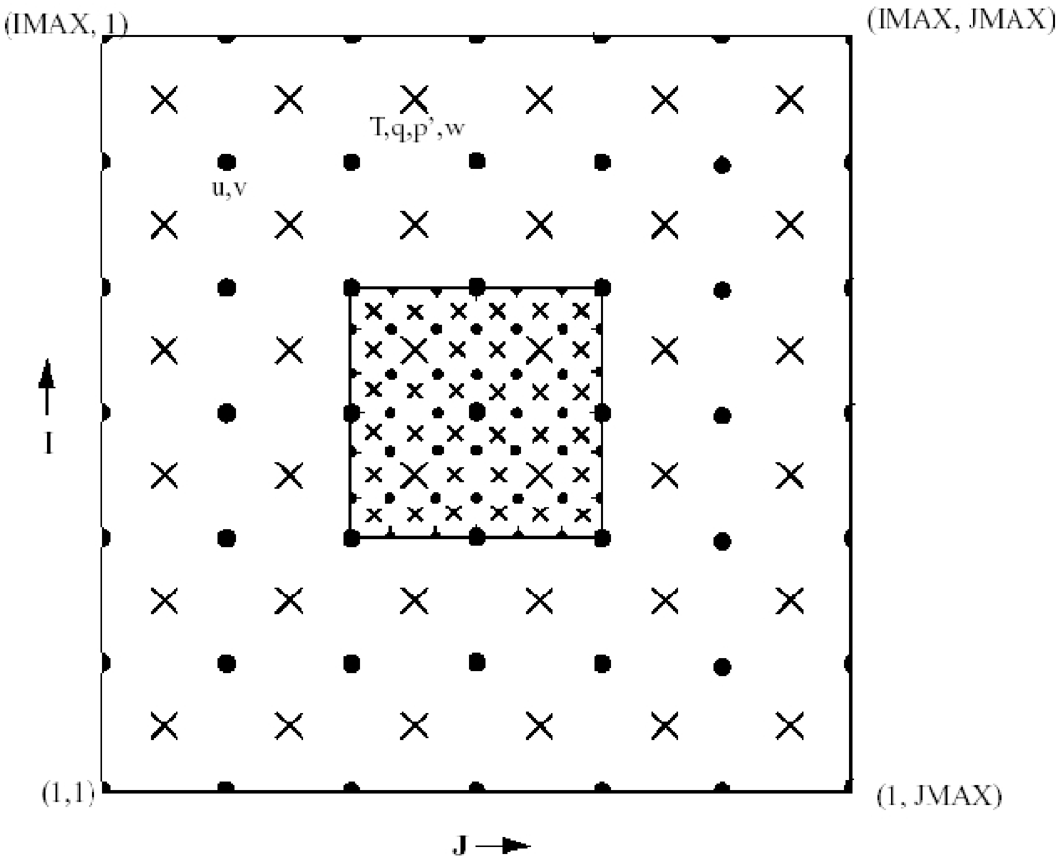

Figure 4.2. Schematic representation showing the horizontal Arakawa B-grid staggering of the dot and cross grid points.

variables. The scalar variables (T, q, p, etc) are assigned to the center of the grid box, while the velocity components such as eastward (u) and northward (v) are defined at the corners (Figure 4.2). The cross points refer to the center points of grid square and dot points refer to the corner points of grid square. Interpolation of input data is done by the preprocessors (Terrain and ICBC) in order to obtain consistency with the grid.

All variables except vertical velocity are assigned in the middle of each vertical layer of the model called half-levels and shown by the dashed lines in Figure 4.1. Vertical velocity is defined at the full levels (solid lines) of the model. We define the sigma levels as full levels including levels at $\sigma = 0$ and 1. Hence, the number of full sigma levels is always one more than the number of model layers.

4.1.3. Map Projections and Map-Scale Factors

The modeling system uses four different map projections. Lambert Conformal is convenient for mid-latitudes, Polar Stereographic for high latitudes, Normal Mercator for low latitudes, and Rotated Mercator for extra choice. Except for the Normal Mercator projection, the x and y directions in the model do not coincide with west-east and north-south directions. Hence, the model output of u and v components has to be rotated to a lat/lon grid before comparison with observation. These transformations are done by the model pre-processors that provide data on the model grid.

The map scale factor, m, is defined as m = (distance on grid) / (actual distance on earth), and its value is generally close to one, varying with latitude.

The shape of small areas are conserved in the model by the projections, so that $dx = dy$ everywhere. On the other hand, representation of a spherical surface on a plane surface is enabled by varying the grid length across the domain. Map-scale factors need to be considered in the model equations wherever horizontal gradients are used.

4.2. Model Physics

4.2.1. Dynamics

The dynamic equations of the RegCM are described by Grell *et al.* (1994) [140].

4.2.1.1. Horizontal Momentum Equations. Horizontal momentum equations are defined as

$$\frac{\partial p^* u}{\partial t} = -m^2 \left(\frac{\partial p^* uu/m}{\partial x} + \frac{\partial p^* vu/m}{\partial y} \right) - \frac{\partial p^* u\dot{\sigma}}{\partial \sigma} - mp^* \left[\frac{RT_v}{(p^* + p_t/\sigma)} \frac{\partial p^*}{\partial x} + \frac{\partial \phi}{\partial x} \right] + fp^* v + F_H u + F_V u \tag{4.2}$$

$$\frac{\partial p^* v}{\partial t} = -m^2 \left(\frac{\partial p^* uv/m}{\partial x} + \frac{\partial p^* vv/m}{\partial y} \right) - \frac{\partial p^* v\dot{\sigma}}{\partial \sigma} - mp^* \left[\frac{RT_v}{(p^* + p_t/\sigma)} \frac{\partial p^*}{\partial y} + \frac{\partial \phi}{\partial y} \right] + fp^* u + F_H v + F_V v \tag{4.3}$$

where u and v are the eastward and northward components of velocity respectively, T_v is virtual temperature, ϕ is geopotential height, f is the coriolis parameter, R is the gas constant for dry air, m is the map scale factor for map projection (either the Polar Stereographic, Lambert Conformal, or Mercator), $\dot{\sigma} = \frac{d\sigma}{dt}$ and F_H and F_V represent the effects of horizontal and vertical diffusion respectively, and $p^* = p_s - p_t$.

4.2.1.2. Continuity and Sigmadot ($\dot{\sigma}$) Equations. Continuity equation is given by

$$\frac{\partial p^*}{\partial t} = -m^2 \left(\frac{\partial p^* u/m}{\partial x} + \frac{\partial p^* v/m}{\partial y} \right) - \frac{\partial p^* \dot{\sigma}}{\partial \sigma} \tag{4.4}$$

By taking the vertical integral of Equation 4.4, the temporal variation of the surface pressure in the model can be computed,

$$\frac{\partial p^*}{\partial t} = -m^2 \int_0^1 \left(\frac{\partial p^* u/m}{\partial x} + \frac{\partial p^* v/m}{\partial y} \right) d\sigma \tag{4.5}$$

After calculation of the surface-pressure tendency $\frac{\partial p^*}{\partial t}$, the vertical velocity in sigma coordinates ($\dot{\sigma}$) is calculated at each level in the model from the vertical integral of

Equation 4.4.

$$\dot{\sigma} = -\frac{1}{p^*}\int_0^{\sigma}\left[\frac{\partial p^*}{\partial t} + m^2\left(\frac{\partial p^* u/m}{\partial x} + \frac{\partial p^* v/m}{\partial y}\right)\right] d\sigma' \tag{4.6}$$

where σ' is a dummy variable of integration and $\dot{\sigma}(\sigma = 0) = 0$.

4.2.1.3. Thermodynamic Equation and Equation of Omega (ω). The thermodynamic equation is

$$\frac{\partial p^* T}{\partial t} = -m^2\left(\frac{\partial p^* uT/m}{\partial x} + \frac{\partial p^* vT/m}{\partial y}\right) - \frac{\partial p^* T\dot{\sigma}}{\partial \sigma} + \frac{RT_v\omega}{c_{pm}\left(\sigma + P_t/p_{ast}\right)} + \frac{p^* Q}{c_{pm}} + F_H T + F_V T \tag{4.7}$$

where c_{pm} is the specific heat for moist air at constant pressure, Q is the diabatic heating, $F_H T$ represents the effect of horizontal diffusion, $F_V T$ represents the effect of vertical mixing and dry convective adjustment, and ω is

$$\omega = p^*\dot{\sigma} + \sigma\frac{dp^*}{dt} \tag{4.8}$$

where,

$$\frac{dp^*}{dt} = \frac{\partial p^*}{at} + m\left(u\frac{\partial p^*}{\partial x} + v\frac{\partial p^*}{\partial y}\right) \tag{4.9}$$

The expression for $c_{pm} = c_p(1+0.8)q_v$, where c_p is the specific heat at constant pressure for dry air and q_v is the mixing ratio of water vapor.

4.2.1.4. Hydrostatic Equation. The hydrostatic equation is used to calculate the geopotential heights from the virtual temperature T_v,

$$\frac{\partial \phi}{\partial \ln\left(\sigma + p_t/p^*\right)} = -RT_v\left[1 + \frac{q_c + q_r}{1 + q_v}\right]^{-1} \tag{4.10}$$

where $T_v = T(1 + 0.608q_v)$, q_v, q_c, and q_r are the water vapor, cloud water or ice, and rain water or snow, mixing ratios, respectively.

4.3. Physics parameterizations

4.3.1. Radiation Scheme

The radiation package of the NCAR CCM3, which is described in Kiehl *et al.* (1996) [142] is used in RegCM for radiative transfer. The solar component accounting for the absorption and scattering effect of O_3, H_2O, CO_2, and O_2 is following δ-Eddington approximation [149]. The solar spectrum is composed of 18 spectral intervals (7 for O_3, 1 for the visible, 7 for H_2O, and 3 for CO_2) from 0.2 to 5 μm. For parameterization of the cloud scattering and absorption, the radiative parameterization of Slingo (1989) [150] is used. In this parameterization, optical properties of the cloud droplets consisting of extinction optical depth, single scattering albedo, and asymmetry parameter are defined in terms of the cloud liquid water content and an effective droplet radius. When formation of cumulus clouds occurs, the grid point fractional cloud cover is such that the total cover for the vertical column starting from base level to top level of cloud is a function of horizontal grid point spacing. It is assumed that thicknesses of the cloud and model layer equals to each other, and distinct cloud water contents is specified for middle and low clouds.

4.3.2. Land Surface Models

The biosphere-atmosphere transfer scheme BATS, as coupled with the NCAR Community Climate Model CCM, is a default surface package in the RegCM. It is generated to define the effect of vegetation and soil moisture in altering the exchanges of momentum, energy and water vapor between surface and atmosphere [141]. The main goals of BATS, are to (a) define the fraction of absorption of incident solar radiation by different surfaces and their net exchange of thermal infrared radiation, (b) compute the surface-atmosphere exchanges of momentum, sensible heat, and moisture, (c) calculate the variables such as wind, moisture, and temperature in the atmosphere, within vegetation canopies, and at the surface observation level, and (d) to determine temperature and moisture variables over land and sea ice. The model includes a vegetation layer, a snow layer, and a soil layer, which is divided into three layers such as surface soil layer, 10 cm thick, root zone layer, 1-2 m thick, and a third deep soil layer 3 m thick. Soil layer temperatures are obtained by solving prognostic equations using a generalization of the force-restore method of Deardoff (1978) [151]. The temperature of the canopy and canopy foliage is determined diagnostically by using an energy balance equations comprising sensible, radiative, and latent heat fluxes. Calculations about the soil hydrology are done by using predictive equations for the water content of the soil layers. These predictive equations account for precipitation, snowmelt, canopy foliage drip, evapotranspiration, surface runoff, infiltration below the root zone, and diffusive exchange of water between soil layers. Formulation of the soil water motion is acquired from a fit to results obtained from a high-resolution soil model [152] and the rates of surface runoff are defined as functions of the rates of precipitation and the degree of saturation of soil water. Snow depth is prognostically obtained from snowfall, snowmelt, and sublimation. If the temperature of the lowest level in the model is less than 271 K, it is assumed that precipitation is in the form of snow.

The fluxes of sensible heat, water vapor, and momentum at the surface are determined by using a surface-layer similarity theory based standard surface drag coefficient formulation. In this formulation, the drag coefficient is dependent on the surface roughness length and on the atmospheric stability in the surface layer. Rates of the surface evapotranspiration depend on the soil water availability. There are 20 vegetation types (Table 4.1) such as soil textures ranging from coarse (sand), to intermediate (loam), to fine (clay); and different soil colors (light to dark) for the calculations of soil albedo in BATS [153].

Modifications to BATS have been made in the latest version of the RegCM in order to take into account the subgrid variability of topography and landcover by using a mosaic-type approach [154]. This parameterization adopts a regular finescale surface subgrid for each coarse model grid cell. Disaggregation of meteorological variables from the coarse grid to the fine grid based on the elevation differences is performed. Then, land surface calculations are carried out separately for each subgrid cell, and aggregation of surface fluxes onto the coarse grid cell are performed in order to be given as an input to the atmospheric model. This modification improves the representation of the surface hydrological cycle remarkably especially in mountainous regions [154]. Two new land use types were added to BATS for representation of urban and sub-urban environments in RegCM4. This addition modifies albedo of the surface and changes the surface energy balance, as well as it also produces impervious surfaces with large effects on runoff and evapotranspiration. These effects can be defined by altering relevant properties of the land surface types in the BATS package, like maximum vegetation cover, roughness length, albedo, and soil characteristics.

The Community Land Model (CLM) [155] is the optional land surface model generated by the National Center of Atmospheric Research (NCAR) as part of the Community Climate System Model (CCSM) [52] in the RegCM. CLM version 3.5 was combined to RegCM to have a more detailed description of land surface option. CLM includes five snow layers as well as an additional representation of trace snow and ten soil layers with solutions of temperature, liquid water and ice water explicitly in each layer. It uses a tile or mosaic approach to taking account land surface complexity within a grid cell of climate model and to capture surface heterogeneity. Four different types of land cover such as glacier, wetland, lake, and vegetated are included in each CLM grid cell. The vegetated land cover type can further contain 17 different plant functional types. Solution of hydrological and energy balance equations for each land cover type is performed and they then aggregated back to the grid cell level.

4.3.3. Planetary Boundary Layer Scheme

The lowest layer of the atmosphere is called Planetary Boundary Layer (PBL) where wind is influenced by friction. In other words, PBL is the layer below the free atmosphere. The PBL's depth is not constant and in this part of the atmosphere turbulent wind is occurred because of the interaction with surface. Advection and thermal energy budgets are also dominant factors that influence the temperature within the PBL.

4.3.3.1. Holtslag PBL. The Holtslag planetary boundary layer scheme is based on a nonlocal diffusion concept that consider countergradient fluxes arising from large-scale eddies in an unstable, well-mixed atmosphere [143]. The vertical eddy flux within the planetary boundary layer is given by

$$F_c = -K_c \left(\frac{\partial C}{\partial z} - \gamma_c \right) \tag{4.11}$$

where γ_c is a "countergradient" transport term defining nonlocal transport because of dry deep convection. The eddy diffusivity is given as

$$K_c = k w_t z \left(1 - \frac{z}{h} \right)^2 \tag{4.12}$$

where k is the von Karman constant; w_t is a turbulent convective velocity depending on the friction velocity, height, and the Monin–Obhukov length; and h is the PBL height. The countergradient term for temperature and water vapor is given as

$$\gamma_c = C \frac{\phi_c^0}{w_t h} \tag{4.13}$$

where C equals to 8.5, and ϕ_c^0 is the flux of surface temperature or water vapor. Equation 4.13 is used between the top of the PBL and the top of the surface layer, which is assumed to be equal to 0.1h. It is assumed that outside this region and for momentum γ_c is 0. To compute the eddy diffusivity and countergradient terms, h is diagnostically computed from

$$h = \frac{R_{icr[u(h)^2+v(h)^2]}}{(g/\theta_s)[\theta_v(h) - \theta_s]} \tag{4.14}$$

where $u(h)$, $v(h)$, and θ_v are the horizontal wind components and the virtual potential temperature at the h (PBL height), g is gravitational acceleration, R_{icr} is the critical bulk Richardson number, and θ_v is an appropriate temperature of air near the surface [143, 156].

4.3.3.2. The UW Turbulence Closure Model. The University of Washington turbulence closure model was added to RegCM as a different PBL scheme [157, 158]. The UW model which is a parameterization of down-gradient diffusion, is a 1.5-order, local model. Although UW model will be denoted as a PBL model, computations of vertical fluxes outside of the PBL can also be achieved. Bretherton *et al.* (2004) [158] denotes it as a moist turbulence parameterization. In the UW model, parameterization of turbulent fluxes is also done as the product of diffusivity and a gradient like the Holtslag model. On the other hand, in contrast to other 1^{st} order models, UW model defines the turbulent kinetic energy (TKE, also denoted as e) prognostically, and it uses TKE to determine the diffusivities.

Similar with the Holtslag mode, diffusivity is determined as the product of a length scale and a velocity scale, which is defined as the square root of local TKE rather than the convective velocity scale. The length is either $l = kz$ or $l = kz/(1 + \frac{kz}{\lambda})$. This choice can be made in the RegCM configuration file. The length scale is multiplied by the correction factor which is called the stability function $S_{h,m}$ depending on local stability [159]. The velocity scale is the square root of 2e. Then, the diffusivity of scalar quantities and momentum at a given height, z, are given by

$$K_{h,m}(z) = l(z)S_{h,m}(z)\sqrt{2e} \tag{4.15}$$

Solution of the turbulent kinetic energy budget equation at each time step is given as

$$\frac{\partial e}{\partial t}\mid_{BL} = -K_h N^2 + K_m S_f^2 + \frac{\partial}{\partial z}\left[K_e \frac{\partial e}{\partial z}\right] - \frac{e^{\frac{3}{2}}}{l} \tag{4.16}$$

$$\frac{\partial e}{\partial t}\mid_{BL} = B + S + T - D \tag{4.17}$$

where the shear frequency, $S_f = \sqrt{(\frac{\partial u}{\partial z})^2 + (\frac{\partial v}{\partial z})^2}$. It is the balance of buoyancy (B), shear (S), transport (T), and dissipation (D) terms. According to the Grenier and Bretherton (2001) [157], the TKE diffusivity, K_e, equals to 5 times the eddy diffusivity,

K_m. The dynamical core of RegCM accounts for horizontal transport such as advection and diffusion of turbulent kinetic energy since the UW model is active.

4.3.4. Convective Precipitation Schemes

In RegCM convective precipitation is calculated by using one of three schemes such as modified-Kuo scheme [144], Grell scheme [145], and MIT-Emanuel scheme [146] [147]. The Grell parameterization is applied by using one of two closure assumptions such as the Arakawa and Schubert closure [140] and the Fritsch and Chappell closure [160].

4.3.4.1. Kuo Scheme. In the Kuo scheme, convective activity is started as M, the moisture convergence in a column of air, becomes larger than a given threshold value and the vertical sounding is convectively unstable. A portion of the moisture convergence β moisturises the column and the rest part is transformed into rainfall P^{CU} according to:

$$P^{CU} = M\left(1-\beta\right) \tag{4.18}$$

β is also given as a function of the average relative humidity $\overline{RH}$ of the sounding:

$$\beta = \left\{ \begin{matrix} 2\left(1-\overline{RH}\right) & \overline{RH} \geq 0.5 \\ 1.0 & otherwise \end{matrix} \right\} \tag{4.19}$$

The term related to moisture convergence is accounted for only the advective motions for water vapor. On the other hand, convergence term M indirectly includes evapotranspiration from the previous time step since it intends to moisturize the lower atmosphere. Therefore, increase in the evapotranspiration causes transformation more and more of it into rainfall by assuming the column is unstable. The latent heat as a result of condensation is distributed between the top and bottom layer of cloud by allocating the maximum heat to the upper part of the cloud layer. A horizontal diffusion term and a time release constant are accounted for in this scheme in order to eliminate numerical point storms. As a result of that, release of moisture and the latent heat are not redistributed instantaneously [161, 162].

4.3.4.2. Grell Scheme. In the Grell scheme [145], clouds are taken into account as two steady-state circulations such as an updraft and a downdraft same with Arakawa and Schubert parameterization. Except at the top and bottom of the circulations, no direct mixing takes place between the cloudy air and the environmental air. The mass flux does not change with height since there is no entrainment or detrainment taking place along the cloud edges. The levels of maximum and minimum moist static energy are the initiating levels of the updraft and downdraft, respectively. To activate the Grell scheme, a lifted air parcel should reach moist convection. Condensation occurring in the updraft is computed by lifting a saturated air parcel. The relation between the downdraft mass flux (m_0) and the updraft mass flux (m_b) is given as:

$$m_0 = \frac{\beta I_1}{I_2} m_b \tag{4.20}$$

where I_1 is the normalized condensation occurring in the updraft, I_2 is the normalized downdraft evaporation, and β is the fraction of updraft condensation that re-evaporates in the downdraft. The value of β changes between 0.3 and 0.5 and it depends on the wind shear. Then, rainfall is given by

$$P^{CU} = I_1 m_b (1 - \beta) \tag{4.21}$$

In the Grell scheme, heating and moistening are calculated both by the mass fluxes and the detrainment at the top and bottom of cloud. The cooling effect of moist downdrafts is also contained. Several closure assumptions can be coupled since the nature of the Grell Scheme is simple.

Arakawa and Schubert closure. Arakawa and Schubert closure assumes that convective clouds make the environment stable as fast as non-convective processes destabilize it as follows:

$$m_b = \frac{ABE'' - ABE}{NA\Delta t} \tag{4.22}$$

where ABE is the buoyant energy available for convection, ABE'' is the amount of buoyant energy available for convection in addition to the buoyant energy produced by some of the non-convective processes during the time interval Δt, and NA is the rate of change of ABE per unit m_b [140]. The difference $ABE'' - ABE$ can be considered as the rate of destabilization over time Δt. ABE'' is calculated by the current fields plus the future trends arising from the advection of heat and moisture and the dry adiabatic adjustment.

Fritsch and Chappell closure. The Fritsch and Chappell closure which is used in the latest RegCM4 version, by default, is a stability based closure assumption [160]. In this closure, convection is assumed to remove the ABE over a given time scale as follows:

$$m_b = \frac{ABE}{NA\tau} \tag{4.23}$$

where τ is the ABE removal time scale.

The two closure assumptions differ in that the Arakawa and Schubert closure assumption links the convective fluxes and rainfall with the trends in the state of the atmosphere, while the Fritsch and Chappell closure assumption links the convective fluxes with the instability degree in the atmosphere. A statistical equilibrium between convection and the large-scale processes is obtained in both schemes.

4.3.4.3. MIT-Emanuel scheme. In the MIT-Emanuel scheme, the mixing in clouds is assumed to be highly episodic and inhomogeneous opposite to a continuous entraining plume [146,147]. And it takes into account convective fluxes depending on an idealized model of sub-cloud-scale updrafts and downdrafts. When the neutral buoyancy level is greater than the cloud base level, convection is initiated. Air is raised and a portion of the condensed moisture transforms into precipitation while the remaining portion forms the cloud between these two levels. In this scheme, mixing of the cloud with the air from the environment is assumed. The entrainment and detrainment rates of mixing are functions of the vertical gradients of buoyancy in clouds. The portion of the mass flux of the total cloud base which mixes with its environment at each level is proportional to the undiluted buoyancy rate of change with altitude.

The MIT-Emanuel scheme also considers an expression of the transformation of cloud water into precipitation inside cumulus clouds. Ice processes are considered by letting the auto-conversion threshold water content depend on temperature. In this scheme, transportation of passive tracers is taken into account as well.

4.3.5. Large-Scale Precipitation Scheme

Nonconvective clouds and precipitation is resolved by Subgrid Explicit Moisture Scheme (SUBEX) in the model. In SUBEX, subgrid variability in clouds is considered by relating the average relative humidity of grid cell to the cloud fraction and cloud water using the work of Sundqvist *et al.* (1989) [16]. According to Sundqvist *et al.* (1989) [16], cloud fraction of the grid cell, FC, is calculated by,

$$FC = \sqrt{\frac{RH - RH_{min}}{RH_{max} - RH_{min}}} \tag{4.24}$$

where RH_{min} is the relative humidity threshold at which clouds begin to form, and RH_{max} is the relative humidity where FC becomes unity. When RH is less than RH_{min}, FC is assumed to be zero and when RH is greater than RH_{max}, FC is assumed to be unity. Precipitation P develops when the content of cloud water is greater than the autoconversion threshold Q_c^{th} according to the following relation:

$$P = C_{ppt}(\frac{Q_c}{FC} - Q_c^{th})FC \tag{4.25}$$

where $1/C_{ppt}$ can be regarded as the characteristic time for transformation of cloud droplets into raindrops. The autoconversion threshold is acquired by scaling the median cloud liquid water content equation according to the following:

$$Q_c^{th} = C_{acs} 10^{-0.49+0.013T} \tag{4.26}$$

where T is temperature in degrees Celsius, and C_{acs} is the autoconversion scale factor. In SUBEX, it is assumed that precipitation falls instantaneously.

SUBEX also involves simple equations for accretion and evaporation of raindrops. The equation for the accretion of cloud droplets by falling rain droplets is given by Beheng [1994] [163] and it is as follows:

$$P_{acc} = C_{acc} Q P_{sum} \tag{4.27}$$

where P_{acc} is the amount of accreted cloud water, C_{acc} is the coefficient of accretion rate, and P_{sum} is the accumulated precipitation falling through the cloud. Evaporation of precipitation is given as [16]:

$$P_{evap} = C_{evap}(1 - RH) P_{sum}^{1/2} \tag{4.28}$$

where P_{evap} is the amount of evaporated precipitation, and C_{evap} is the rate coefficient.

Table 4.1. Land Cover/Vegetation classes.

No	**Land Cover/Vegetation classes**
1	Crop/mixed farming
2	Short grass
3	Evergreen needle leaf tree
4	Deciduous needle leaf tree
5	Deciduous broadleaf tree
6	Evergreen broadleaf tree
7	Tall grass
8	Desert
9	Tundra
10	Irrigated Crop
11	Semi-desert
12	Ice cap/glacier
13	Bog or marsh
14	Inland water
15	Ocean
16	Evergreen shrub
17	Deciduous shrub
18	Mixed Woodland
19	Forest/Field mosaic
20	Water and Land mixture

5. SEMIEMPIRICAL CLOUDINESS PARAMETERIZATION

5.1. Performance of the RegCM4.0

In the framework of this dissertation, RegCM4.0 code, which was first developed by Giorgi [116, 139] is being used as a regional climate model for the Central Asia domain. Performance of the model in simulating the climate of central Asia domain was investigated. The results of an experiment with the RegCM 4.0 model that was run for seasonal mean air temperature and precipitation total series are presented. The experiment consists of one simulation from 1989 to 2010 using ERA-Interim reanalysis data as the boundary condition, another simulation for the period 1970−2000 using the reanalysis data ERA40 and the global climate model ECHAM5 for forcing.

The super-continent of Eurasia covers about 10.6% of the Earth's surface, with a 52 990 000 km^2 area located primarily in the Eastern and Northern hemispheres. Geographically, it is a single continent, comprising the traditional continents of Europe and Asia (Figure 5.1). Eurasia is inhabited by almost 5 billion people, more than 70% of the world's population [164]. Geologically, it formed about 325 to 375 million years ago, when the old continental plate fragments of Siberia, Kazakhstan and the Baltic joined, and the Chinese and Indian plates collided with Siberia's southeastern and southern borders, respectively. Thus, in terms of plate tectonics, the Eurasian Plate includes Europe and most of Asia but not the Indian subcontinent, the Arabian Peninsula, or the Russian far-east.

On the other hand, the arid and semi-arid Central Asian area is a core region of the Asian continent from the Caspian Sea in the west, China in the east, Afghanistan in the south and Russia in the north. It is also geographically known as Inner Asia. The varied geography of the Central Asian region includes high mountains (e.g. Tian Shan, Karakurum, Himalayas), large deserts (e.g. Kara Kum, Kyzyl Kum, Taklamakan, Gobi) and treeless, grassy, large semi-arid steppes.

Water is the most important resource in the arid and semi-arid Central Asian region, because the region is a kind of large continental rain shadow basin surrounded by the high mountains described above [3], with large quantities of water stored in mountain glaciers. The Amu Darya, the Syr Darya and the Hari River are the main rivers of the region, and the Aral Sea and Caspian Sea are the major water bodies. Complex precipitation occurrences and temperature and precipitation regimes over the region, which are due to the various pressure and wind systems during the year and the various physical geographic factors and conditions which prevail in the region, make it difficult to understand and model the climate in this arid/semi-arid region [3–5].

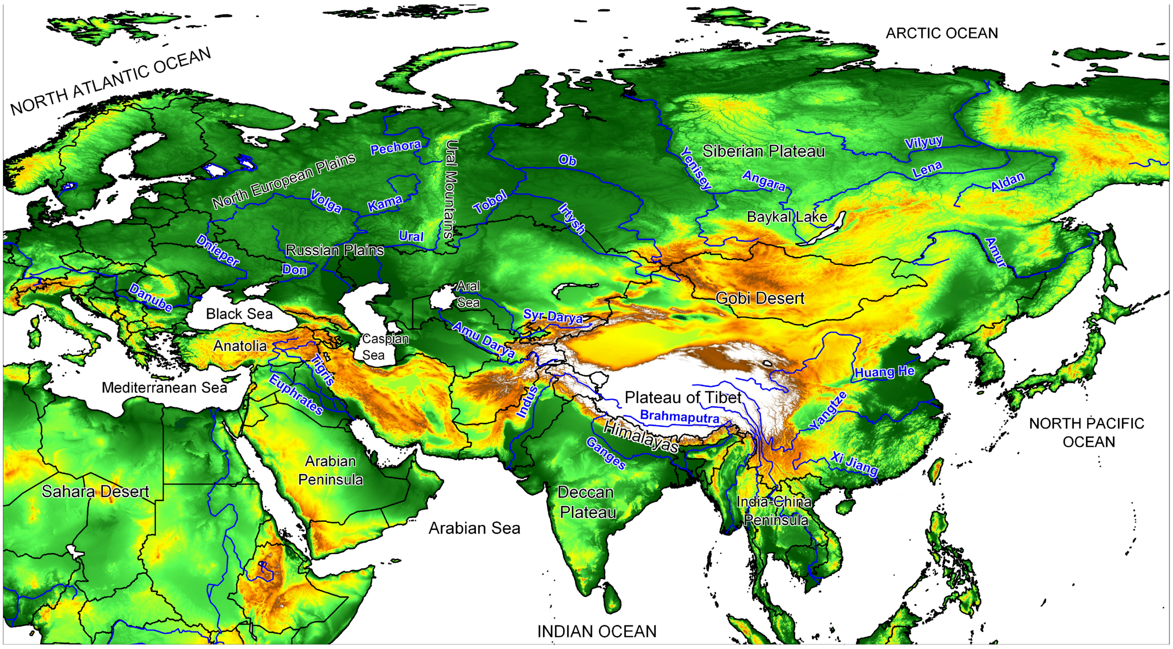

Figure 5.1. General physical/relief map of Eurasia and its surroundings.

5.1.1. Forcing Data

ERA-40, which is a 2.5° × 2.5° resolution 40 yr global reanalysis dataset, was used to provide lateral boundary conditions for the present-day simulation of the years 1970−2000. The ERA-40 global dataset was developed by the European Center for Medium- Range Weather Forecasts (ECMWF). For comparison, the ERA-Interim [18] reanalysis dataset, which is the latest ECMWF global atmospheric reanalysis of the period 1989 to 2010, with a grid resolution of 0.75° × 0.75° was also used in this experiment. There are specific differences between the ERA-40 and ERA-Interim datasets in the assimilation of data and use of observations as described in the previous chapters.

5.1.2. Parameterization

The model domain covers Central Asia with a spatial resolution of 50 km. The regional model simulation spans the time interval between December 1989 and February 2010 with the ERA-Interim dataset and the period 1970−2000 with the ERA-40 dataset for present-day simulation. For validation of the output of the present-day simulation, temperature and precipitation datasets from the CRU were used. In the present study, we could only validate the periods 1970−2000 and 1989−2002, since the CRU dataset is limited to the period 1900−2002.

During the parameterization part, we tested 3 different convection schemes (the modified-Kuo scheme, [144]; the Grell scheme, [145]; and the MIT-Emanuel scheme, [146, 147]) for shorter time periods (1989−1993). Using the Grell scheme, we worked with both the Arakawa-Schubert type closure and a Fritsch-Chappell type closure. Even though different convection schemes work better in other parts of the region, the best agreement with observational data was obtained by using the Grell scheme with the Fritsch-Chappell type closure. Therefore, we used this scheme in both hindcast and forecast simulations.

5.1.3. Results

5.1.3.1. ERA-interim dataset (1990−2002). A comparison of biases in surface mean air temperature data for the RegCM forced by ERA-interim with observations for four seasons is presented in Figure 5.2. During the winter (DJF), there is a strong warm bias (up to 12 °C degrees) on the northern part of the domain compared to other seasons. However, this bias is forced by the ERA-Interim reanalysis data shown in Figure 5.3. ERA-Interim itself has also warm bias in the northern part of the domain. But RegCM4.0 is also not able to decrease warm bias inherited from forcing data. There is also a cold bias which is again inherited by forcing data in the southern part of the domain. This cold bias is seen not only during the cold season but also in other seasons. As this cold bias is mainly observed around mountainous parts of the region, we conclude that this is a result of the station data bias, because the meteorological/climatological stations are mostly located in the valleys of this region. This situation may have resulted in higher representative temperature readings for the region. This may also be mainly due to the seasonal variability of the deep convective and orographically induced clouds between winter, with fewer clouds, and summer, with many cumulus type clouds [3]. In the spring (MAM) and autumn (SON) seasons, RegCM reduced the warm bias, inherited from the forcing data, in magnitude and also on a regional basis. In other parts of the region and in other seasons, the regional climate model has a relatively low bias and shows a reasonably good performance in simulating the present-day climate. In Figure 5.4, the precipitation climatology of the

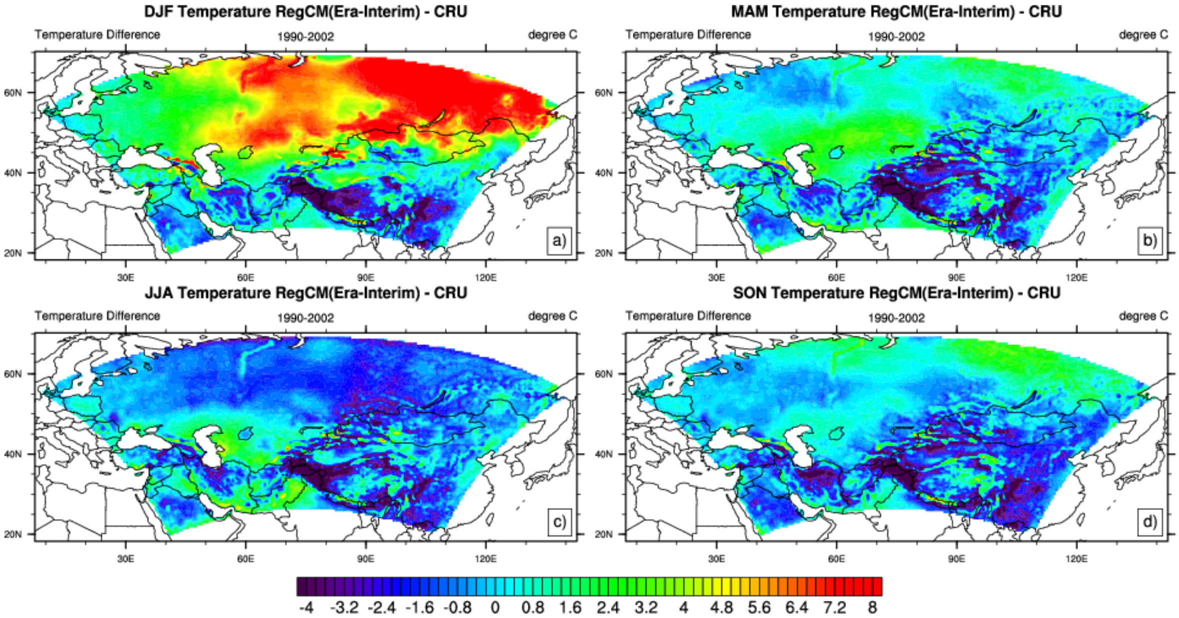

Figure 5.2. Comparison of the seasonal surface air temperatures of the RegCM, which is forced by the ERA-interim, with observations for the period 1990-2002. (a) winter season (DJF), (b) spring season (MAM), (c) summer season (JJA) and (d) autumn season (SON).

domain with the ERA-Interim data is presented. In all seasons, with the exception of

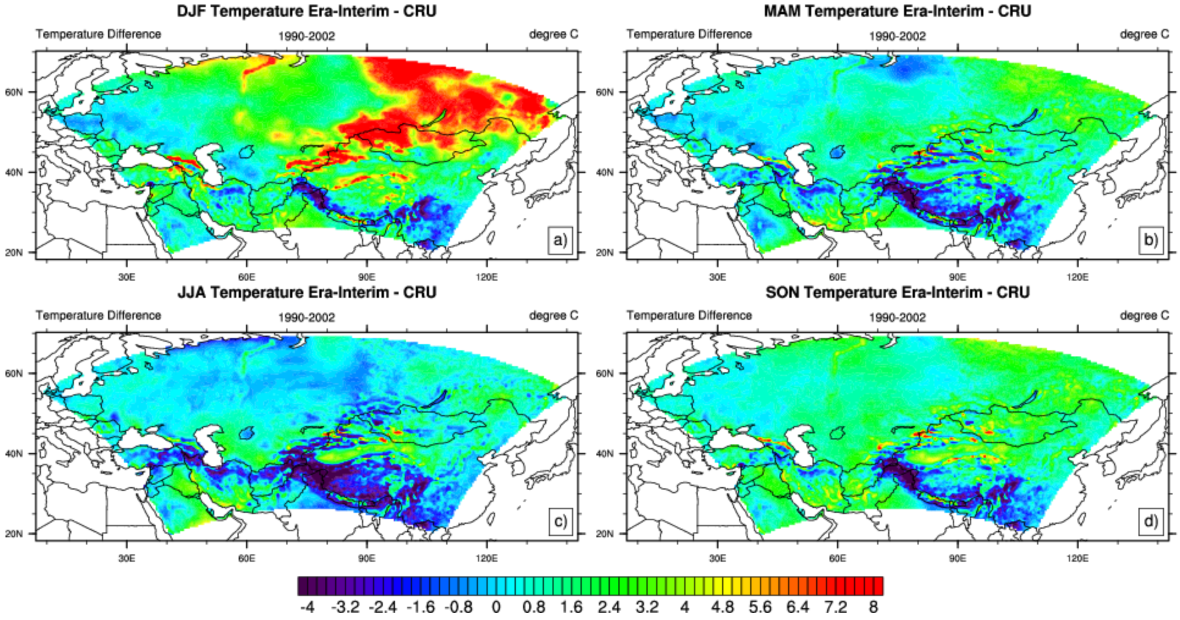

Figure 5.3. Seasonal surface air temperature differences between the ERA-Interim dataset and observations (CRU). (a) winter (DJF), (b) spring (MAM), (c) summer (JJA) and (d) autumn seasons (SON).

summer, some excess precipitation is generally estimated with respect to observational data for the northern and eastern parts of the area studied, while a deficient amount of precipitation is generally estimated for the south, with the exception of the western part and the Asian monsoon region (including the Himalayas and other mountainous areas) (Figure 5.4). During the spring, autumn and winter, a great deal of excess precipitation is estimated over the mountainous areas of the Asian monsoon region. The situation is apparently different in summer. In the summer, the mid-latitude frontal cyclones are weaker and are rare as a result of the northward migration of the polar jet and planetary polar front. This causes a weakening of the regional temperature and, thus, of pressure gradients over the Eurasia super-continent, resulting in the southern Asia monsoonal low. This low becomes stronger and begins its most active phase of the year associated with the northward migration of the intertropical convergence zone (ITCZ) and regional surface heating of southern Asia in the high sun season of summer [3]. Consequently, in summer, decreased precipitation is estimated for most of the modeling area, compared with the annual climatology, whereas notably increased precipitation is estimated, particularly, for the continental semiarid eastern and semi-humid/ humid southeastern parts of the study area (Figure 5.4). In these regions, the convective instability of precipitation events associated with surface warming and circulation-based monsoonal influences and some frontal precipitation occurrences are evident in summer. Precipitation regimes in these regions are defined as the continental mid-latitude and east-coast precipitation regimes of the continental inner and coastal eastern regions of the Northern Hemisphere. However, in the summer, when the monsoonal convectional precipitation is strengthened by orographically induced precipitation events on the southern slopes of the Himalayan Mountains and in the large tropical and sub-tropical India-China region, the observational data shows considerably less precipitation in the southern part of the study region. We have also shown the precipitation climatology of the region using the observational CRU dataset (Figure 5.4). With these results, we can conclude that the RegCM simulates the precipitation climatology of the region well, except in the South Asian monsoon region. As the South Asian region is a part of another CORDEX domain, we are not really concerned with the difference.

5.1.3.2. ERA-40 dataset (1970−2000). We also performed the same experiment with the ERA-40 forcing dataset for different time periods from 1970 to 2000. The surface temperature and precipitation climatology of the region according to the ERA-40 dataset are presented in Figure 5.5. We also observed a similar warm bias in the northern part of the domain in the cold season and a cold bias in the southern part of the region. For other parts of the domain, the regional climate model reproduces seasonal variability reasonably well. For the precipitation climatology of the region, our results were similar to those obtained with the ERA-Interim dataset.

Again, except for the southern part of the region, precipitation is well simulated by RegCM. As ERA-Interim is a new reanalysis product covering the period from 1989 to the present, as a precursor to a revised extended reanalysis product to replace ERA-40, the similarity between the results of the 2 datasets are to be expected. We have used ERA-40 in addition to ERA-Interim to be able to consider a standard time period

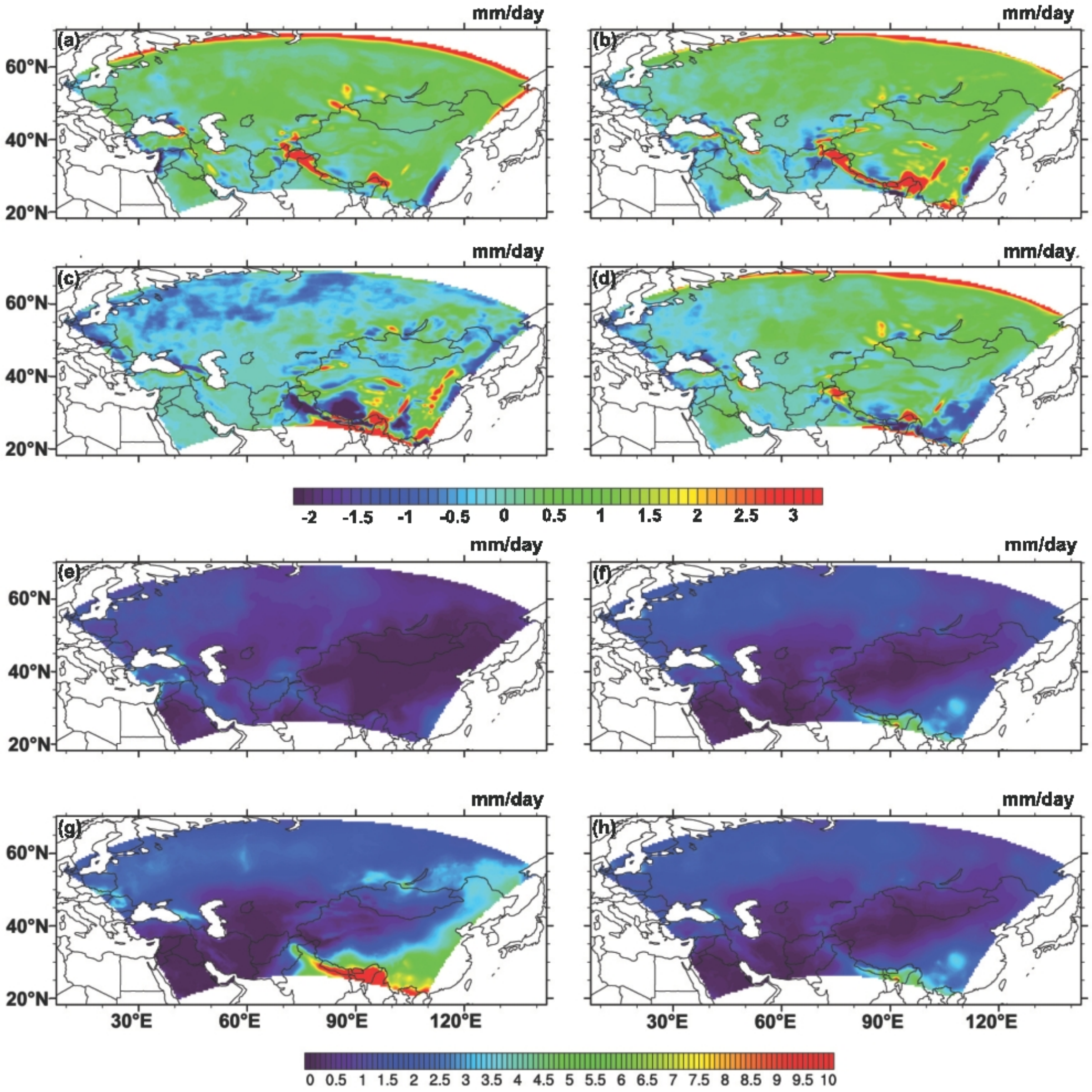

Figure 5.4. (a–d) Differences in precipitation climatology of the region using the regional climate model RegCM, which is forced by the ERA-Interim with observations for the periods 1990−2002: (a) winter (DJF), (b) spring (MAM), (c) summer (JJA) and (d) autumn (SON) seasons compared to the Climate Research Unit [CRU] dataset. (e–h) Precipitation climatology of the region using the original observational CRU dataset for the period 1970−2000: (e) winter (DJF), (f) spring (MAM), (g) summer (JJA) and (h) autumn (SON) seasons.

of 30 yr, between 1970 and 2000.

5.2. Cloud fraction scheme in RegCM4.0

Results of present-day simulations showed that there is a strong warm bias in the northeastern part of the domain in winter season. Since this bias exists only in cold season, because of having a snow cover during the winter season, possible warm bias in this region could be due to the calculations of snow processes and snow-albedo feedback [141], however our parameterization showed that changing the short and long wave snow albedo forcing had little effect on the warm bias. Therefore, we concluded that the warm bias in the northern part of the region is most probably because of model's insufficient ability to produce snow cover on the surface. Additionally, there are complex climate feedback factors including cloud-albedo or cloud forcing and ice/snow-albedo feedback during winter in the RegCM simulations over the Arctic region. There might be an error in getting snow in winter season. No snow might be more of an outcome of the bias, rather than a cause.

On the other hand, studies have shown that relative humidity (RH) based cloud fraction schemes are not well suited for high latitudes, particularly the extremely cold and dry conditions typical of polar winter [165]. Most of the relative humidity-based cloud schemes were generated by using data from sub polar latitudes [15]. In the Arctic region, the extreme cold causes persistent near saturated conditions (with respect to ice, which is the relevant saturation condition at cold, below-zero temperatures) in the shallow boundary layer particularly during winter. Clouds are not continually observed in these saturated conditions very likely because of extreme low density of condensation nuclei. In the absence of condensation nuclei, super-saturation is needed before homogeneous ice nucleation can effectively begin. Additionally, the frequent very stable boundary layers observed in the Arctic winter may not allow spatial variability in the humidity field due to the extreme stability. The assumption of spatial variability of relative humidity leading to subgrid scale saturation and fractional cloud formation may not be suitable for Arctic cold and stable boundary layers. In this assumption, the threshold values of relative humidity at which clouds form should be designed more

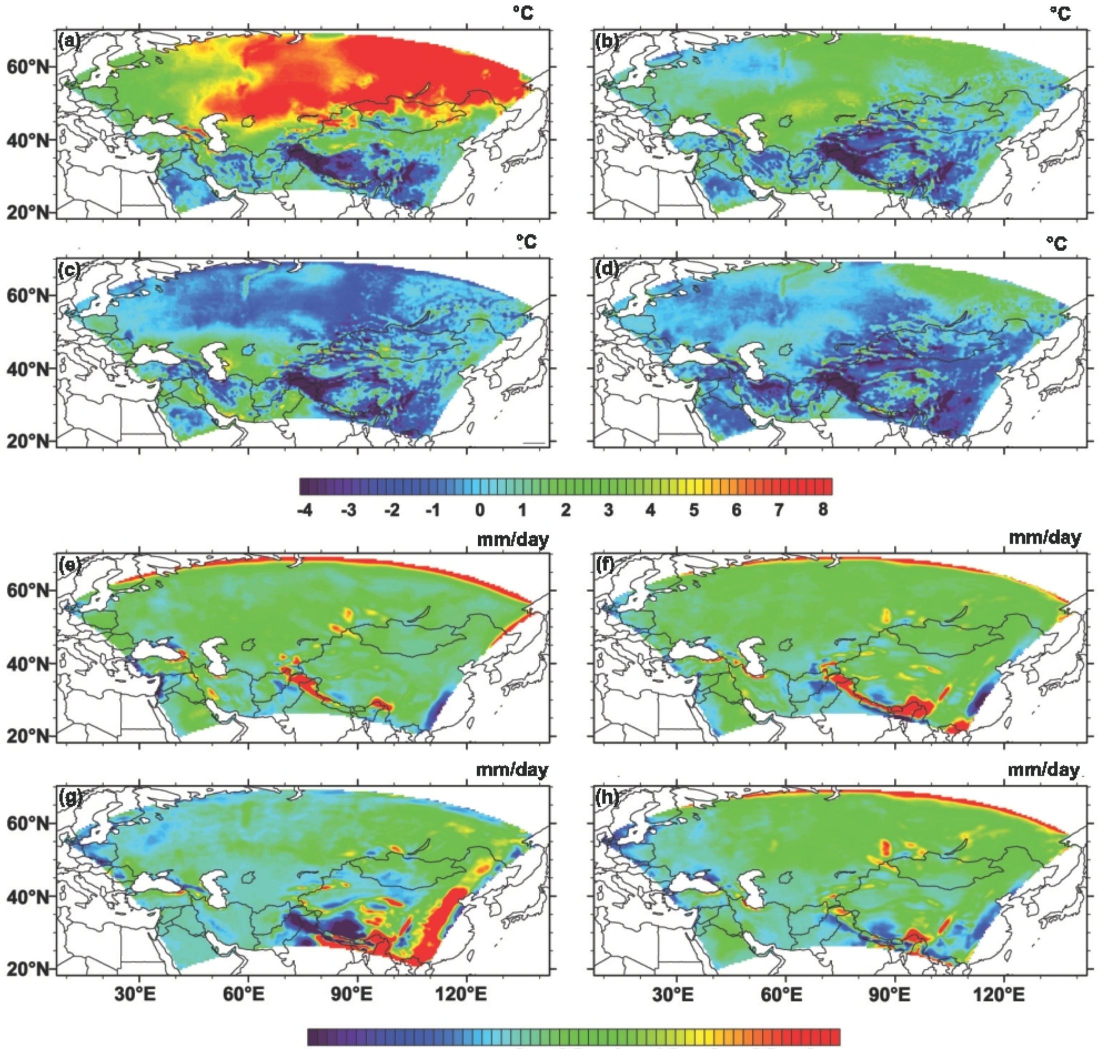

Figure 5.5. Comparison of the seasonal (a–d) surface temperatures and (e–h) precipitation of the region using the regional climate model RegCM, which is forced by the ERA-40 dataset, with observations (Climate Research Unit [CRU] dataset) for the period 1970−2000: (a,e) winter (DJF), (b,f) spring (MAM), (c,g) summer (JJA) and (d,h) autumn (SON) seasons.

complex and vary as a function of the decreasing model turbulence values under stable conditions.

Cloud fraction parameterization in RegCM 4.0 code also depends on relative humidity. Subgrid Explicit Moisture Scheme (SUBEX) is used to handle nonconvective clouds in RegCM. SUBEX accounts for the subgrid variability in clouds by relating the average grid cell relative humidity to the cloud fraction and cloud water following the work by Sundqvist *et al.* (1989) [16]. They assume that in a statically stable grid column condensation in a grid can occur only if the relative humidity in that grid is greater than threshold value. According to their assumption, the condensation processes cannot be resolved in 50 km grid, so that threshold value must be lower than unity. Thus, the grid scale relative humidity, U, can be written as a weighted average of the humidity in the cloudy part, $U_s = 1$, and the humidity in the cloud-free part,U_0,

$$U = bU_s + (1 - b)\,U_0 \tag{5.1}$$

U_0 depends on several quantities, such as cloudiness, stability, surface type, and height above the ground. First, a dependence on cloudiness is assumed to be controlled by the relation,

$$U_0 = U_{00} + b\,(U_s - U_{00}) \tag{5.2}$$

where, U_{00} is a basic threshold value, hence independent of cloudiness, but likely a function of other conditions. Then, when we combine Equation 5.1 and Equation 5.2, we get a diagnostic relation for cloud cover in terms of U and U_{00}:

$$b = 1 - \left(\frac{U_s - U}{U_s - U_{00}}\right)^{1/2} \tag{5.3}$$

Cloud fraction is assumed to be zero, when relative humidity is less than threshold value.

5.3. Ivan Guettler's Correction of Cloud Fraction Formula to RegCM4.0 code

Climate models commonly generate excessive wintertime Arctic clouds, particularly at low levels [15, 166–168], and the largest errors occur during winter. Since arctic clouds warm Earth-Atmosphere system in winter time, excessive wintertime clouds of models cause a warm bias in winter. To solve this warm bias problem of General Circulation Models, Vavrus *et al.* (2008) [165] proposed a simple alternative parameterization for predicting cloud fraction in the Community Climate System Model, Version 3 (CCSM3) global climate model that RegCM includes. Vavrus *et al.* (2008) [165] designed the formula to decrease the bias of excessive low clouds during polar winter by reducing the cloud amount under very dry conditions. In that study, the model's formula to compute the fraction of low-level stratiform clouds (where air pressure is 750 hPa or higher) is adjusted to decrease the excessive polar cloudiness simulated during much of the year. This cloud reduction leads to a decrease of 15 Wm^{-2} in surface cloud radiative forcing (CRF) during winter and about a 50% decrease in mean annual in CRF at Arctic region. Consequently, surface temperatures decrease by up to 4K on-land and 28K over the Arctic Ocean in winter, thus it reduces the model's pronounced warm bias. The formula is proposed to reduce the relative humidity-derived low cloud fraction (f), when the grid-box mean specific humidity (q) falls below a threshold value (0.003 kg/kg), which is realized only in extremely cold conditions.

$$f = f \times \left[max\left(0.15, min\right)\left(1.0, \frac{q}{0.003}\right)\right] \tag{5.4}$$

In this case, cloud fraction equation is only altered when very dry atmospheric conditions occur. It reduces the low cloud amount by as much as 85% of its relative humidity-based value. This adjustment affects mainly polar region although it is implemented globally in the low cloud subroutine of the model, due to threshold value of specific humidity. This adjustment to the cloud fraction is applied only to the low cloud amount, so that threshold pressure level (750 hPa) should be specified in the code. Ivan Guttler from Croatia Meteorological Office adopted this equation to the RegCM code.

5.3.1. Outputs of Corrected Code

5.3.1.1. ERA-Interim dataset (1990−2002). We have investigated the effects of this cloud cover correction code which will later be incorporated into the release version of RegCM 4.1 in addition to the standard code of RegCM 4.0. A comparison of biases with respect to CRU data in surface temperature data for the RegCM forced by ERA-Interim is presented in Figure 5.6. Figure 5.6 shows the temperature results of the original code of RegCM 4.0, as well as results taking the cloud cover correction into consideration. In the control run with the Era-Interim boundary conditions, we still obtained a warm bias in the northern part of our domain. However, this correction code helped us the decrease the warm bias observed during winter months in the colder part of the region. The warm bias during the cold season is 2−3°C lower in the northern part of the region as a result of this correction. There is still warm bias in the northern part of the domain.

5.4. New cloud fraction parameterization

Xu and Randall (1996) [17] proposed a semi-empirical cloud parameterization formula for using in climate models to improve relative humidity based cloud fraction scheme. They used observational data from the Global Atmospheric Research Program (GARP) Atlantic Tropical Experiment (ASTEX) in their studies. The large-scale average cloud water and cloud ice mixing ratio is used as the primary predictor and the large-scale relative humidity and cumulus mass flux are also used as secondary predictors for stratiform cloudiness in this parameterization. They assume that amount of cloud changes exponentially with the large-scale average saturated mixing ratio.

In that study, subgrid cloud amount can be determined as the statistical distribution of cloud water and cloud ice on the subgrid scale in general. The main arguments behind parameterizing the amount of cloud fraction are as follows. The small-scale distributions of liquid water and ice can strongly affect the radiative transfer. Since microphysical transformations among water droplets or particulates or ice crystals are local or cloud-scale processes, they must be defined in terms of the local concentration

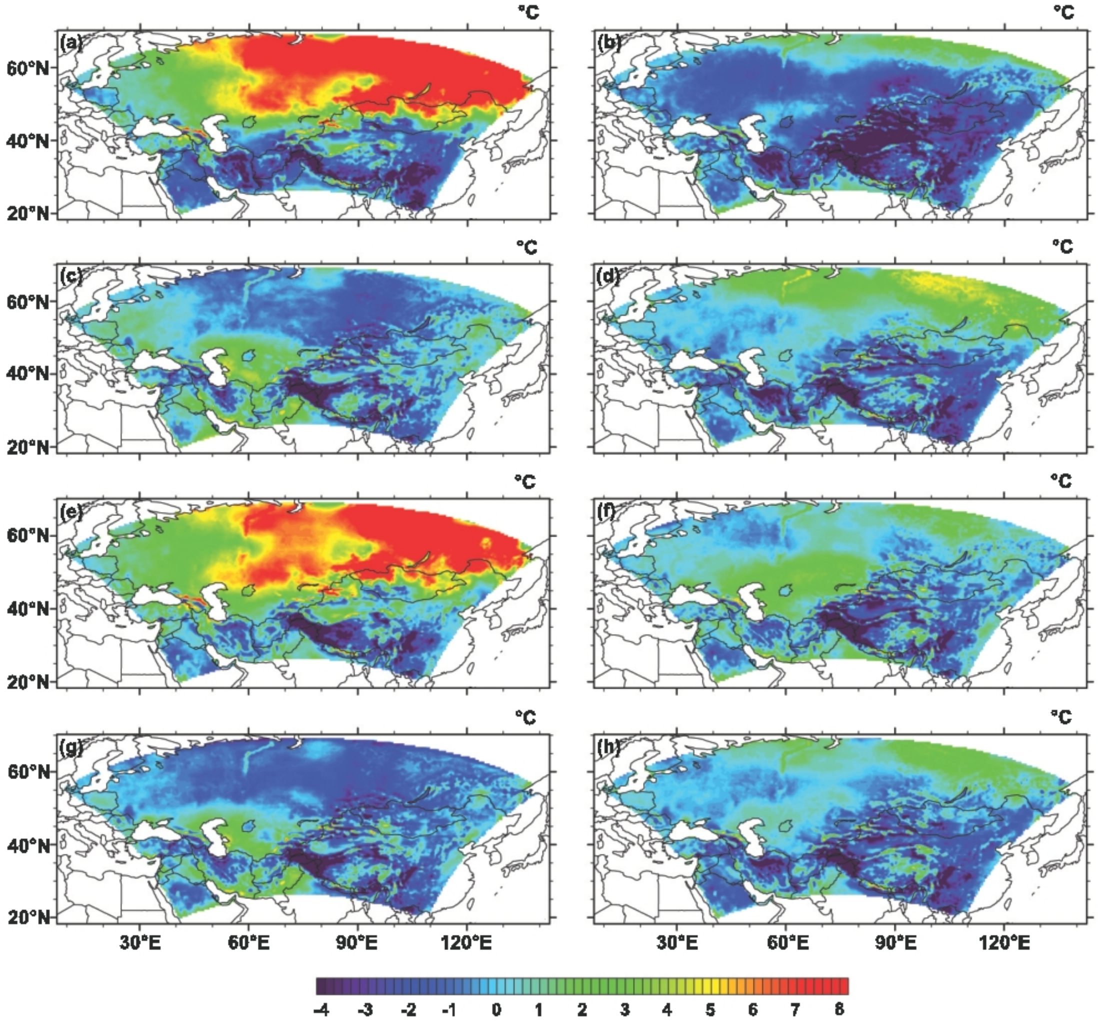

Figure 5.6. Comparison of the seasonal surface temperatures of the region using the regional climate model RegCM, which is forced by the ERA-Interim dataset, with observations (Climate Research Unit dataset) for the period 1990−2002: (a) winter, (b) spring, (c) summer, (d) autumn, and including the cloud cover correction (e) winter, (f) spring, (g) summer, (h) autumn seasons.

of cloud water and cloud ice instead of the predicted grid-cell averaged concentrations.

For use in a global climate model, fraction of cloudiness should be linked with large-scale variables such as large-scale RH, grid-averaged of saturated mixing ratio and convective intensity values. Since all these variables are almost interdependent, it is not convenient to use a single regression relationship including all correlated variables to parameterize fractional cloud amount. A formulated cloudiness parameterization should be independent of the grid size of a climate model and of the different cloud climatology.

Based on the understanding of the relationships between C_s and its predictors, they proposed an intuitive formulation as follows:

$$C_s = RH^p \left[1 - \exp\left(-\alpha \bar{q}_l\right)\right] \tag{5.5}$$

where C_s is the stratiform cloud amount, $\bar{q}_l$ is the cloud water and ice mixing ratio, RH is the relative humidity, p and α are nondimensional coefficients to be determined. From Equation 5.5, we can see that as $\bar{q}_l$ increases, C_s will gradually approach its upper limit which is 1 for $RH = 1$. Coefficients p and α must be positive for C_s not to exceed 1. It should be noticed that the dependency of C_s on M_c (convective mass flux) is not considered in Equation 5.5 since M_c is not available in most climate models. We also consider the derivative of C_s with respect to $\bar{q}_l$; that is,

$$\partial C_s / \partial \bar{q}_l = RH^p \alpha \exp\left(-\alpha \bar{q}_l\right) \tag{5.6}$$

This derivative depends only on $RH^p\alpha$, when condensation starts to occur ($\bar{q}_l \approx 0$). It means that a larger value of C_s can be obtained in a grid cell with a higher RH. The physical mechanism behind the Equation 5.5 is basically different from existing parameterizations based on RH alone due to the usage of RH here to define the slope of the change between C_s and $\bar{q}_l$, and Equation 5.6 implies that the derivative is getting smaller at a given RH as $\bar{q}_l$ increases.

If we assume that α is independent of RH, p has to approach the order of 10 to account for the dependency of C_s on RH at a given $\bar{q}_l$. Such a strong dependency of α on RH at any rate is not physically realistic. Therefore, it is assumed that α should be also a function of RH, that is, when RH is close to 1, C_s increases rapidly with $\bar{q}_l$.

On the other hand, it is more convenient that α should be related to saturation deficiency of the air parcel. Since saturation deficiency is proportional to the saturation mixing ratio q^*, α is given as,

$$\alpha = \alpha_0 \left[(1 - RH)\, q^* \right]^{-\gamma} \tag{5.7}$$

where, γ should be positive and α_0 is a constant. This indicates that C_s becomes 1 as RH approaches 1. 100% cloud amount is assumed when $RH \geq 1$ in a grid cell. In summary, the new parameterization can be written as

$$C_s = \left\{ \begin{array}{cc} RH^p[1 - \exp(-\alpha_0 \bar{q}_l/[(1-RH)q^*]^\gamma)] & , RH < 1 \\ 1 & , RH \geq 1 \end{array} \right\} \tag{5.8}$$

The values of p, α_0 and γ can be empirically defined from the simulated data using regression equation for the best-fit constants. It is assumed that all three coefficients in the proposed parameterization are independent of height. The determined p, γ and α_0 values from the GATE simulation are 0.25, 0.49, and 100, respectively. Finally, I adopted this semi-empirical parameterization to the RegCM code.

The regional climate model RegCM4.0 which was forced by ECHAM5 and ERA-Interim datasets for the period 1989-1994 was ran with and without corrections in order to see the effect of semi-empirical parameterization on the strong warm bias over Siberia region. First the regional model was run without any correction to see strong warm bias (Figure 5.7). We can see strong warm bias over north and Siberia region in winter season. This major error of the regional climate model in winter season is almost 9 °C. Then, RegCM which was forced by ECHAM5 dataset for period of 1989-1994 was ran by using semi-empirical cloud parameterization of Xu and Randall

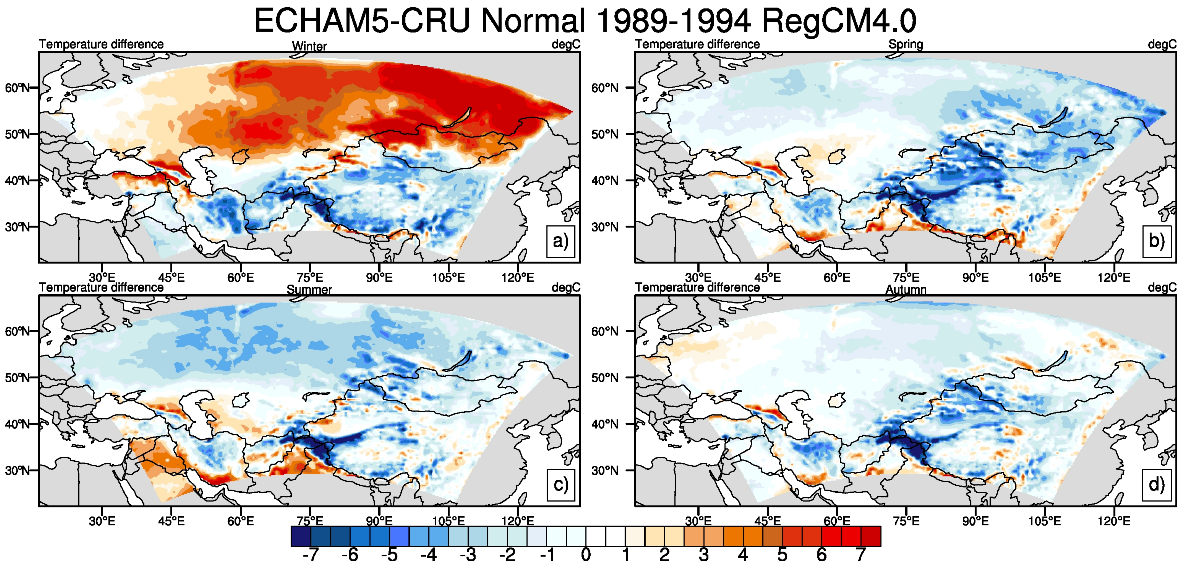

Figure 5.7. Comparison of the seasonal surface temperatures of the region using RegCM4.0, which is forced by the ECHAM5 dataset, with observations (Climate Research Unit dataset) for the period 1989-1994 without correction: (a) winter (DJF), (b) spring (MAM), (c) summer (JJA), and (d) autumn seasons (SON).

(1996) [17] for the cloud fraction (Figure 5.8). Results showed that corrected cloud fraction equation decreased almost all warm bias seen in the north part of the region in winter season. In winter season, cold bias was seen in the northern part of the region. However, if we compare the biases with or without corrected cloud fraction equation, cold bias is both less in magnitude and in spatial scale. For summer season, to use the new parameterization also improves the performance of the model over the north part of the region by decreasing the cold bias. There is not much difference between using corrected or uncorrected cloud fraction equation for spring season. On the other hand, cold bias is getting stronger in the northern part of the domain for autumn season. Consequently, overall performance of this new cloud fraction parameterization for the ECHAM5 dataset is remarkable.

We tested the new parameterization of cloud fraction equation by using the ERA-interim reanalysis dataset. ERA-interim is generally used to test the performances of models. First the regional model which was forced by ERA-interim dataset was run

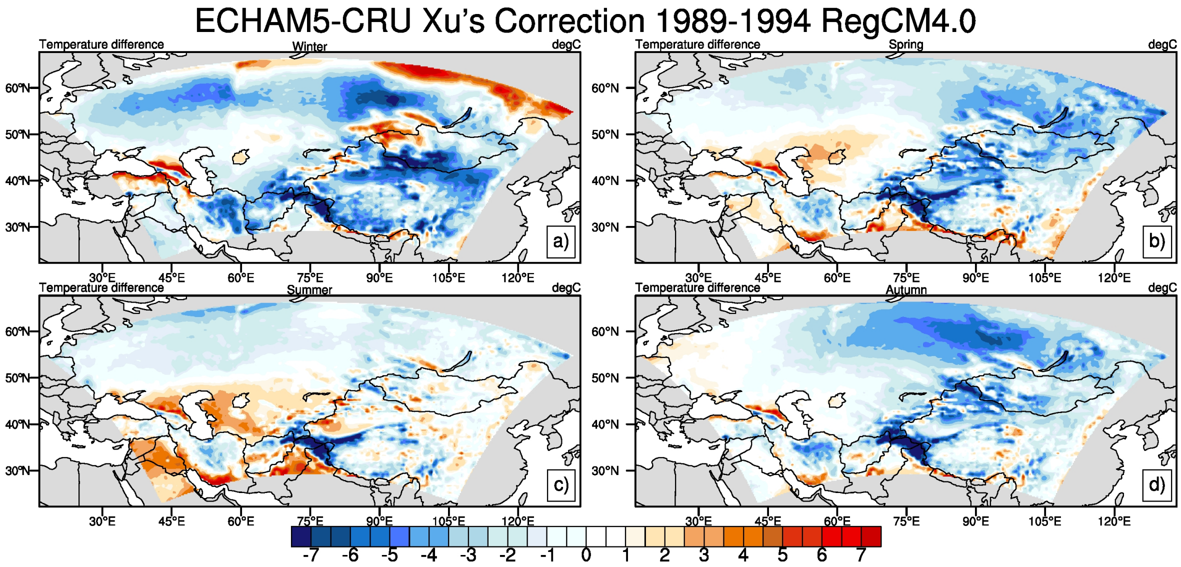

Figure 5.8. Comparison of the seasonal surface temperatures of the region using RegCM4.0 (with corrected cloud fraction equation - Xu), which is forced by the ECHAM5 dataset, with observations (CRU) for the period 1989-1994: (a) winter (DJF), (b) spring (MAM), (c) summer (JJA), and (d) autumn seasons (SON).

without any correction (Figure 5.9). Strong bias over north and Siberia region can easily be observed in winter season.

Then, RegCM which was forced by ERA-interim dataset was also run with corrected cloud fraction equation (Figure 5.10). The results showed that correction causes decrease in the magnitude of warm bias of code which is forced by ERA-Interim in the winter season. However, this effect is not large as in the corrected code which is forced by ECHAM5. We can observe that corrected cloud fraction equation decrease the warm bias over the region surrounding the Caspian Sea in both spring and summer seasons. However, the cold bias over Tibetan Plateau is getting much spread in the spring season. For autumn season, there is not much change. Overall performance of new cloud fraction parameterization for the ERA-interim dataset is reasonable.

During the testing process, regional climate model RegCM has upgraded to newer versions. In the latest stable version RegCM4.3.5, the Holtslag Planetary Boundary

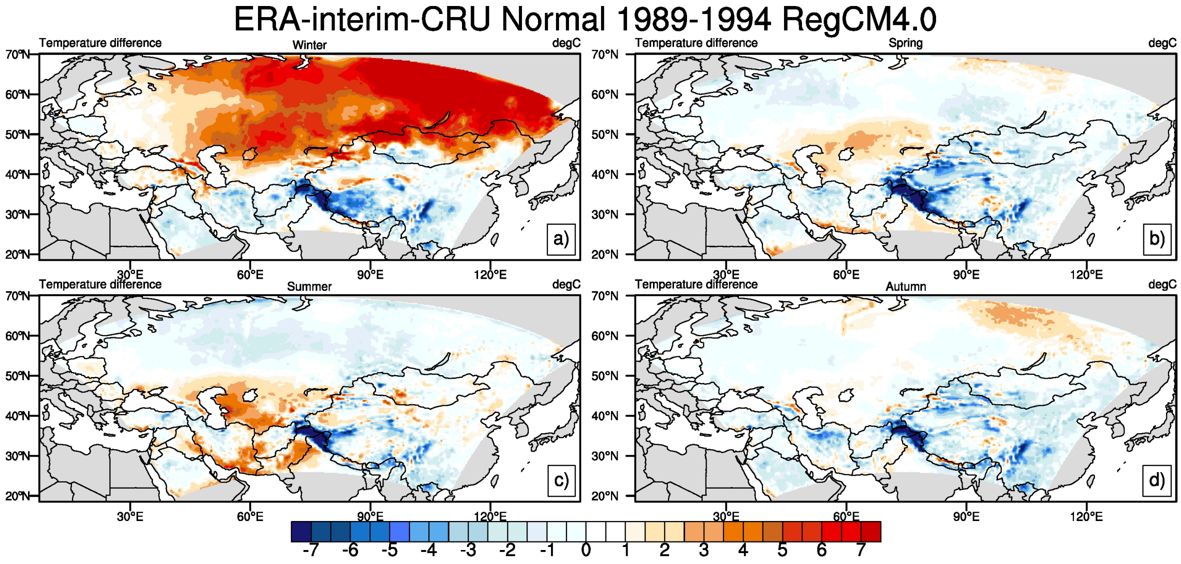

Figure 5.9. Comparison of the seasonal surface temperatures of the region using RegCM4.0, which is forced by the ERA-interim dataset, with observations (Climate Research Unit dataset) for the period 1989-1994 without correction: (a) winter (DJF), (b) spring (MAM), (c) summer (JJA), and (d) autumn seasons (SON).

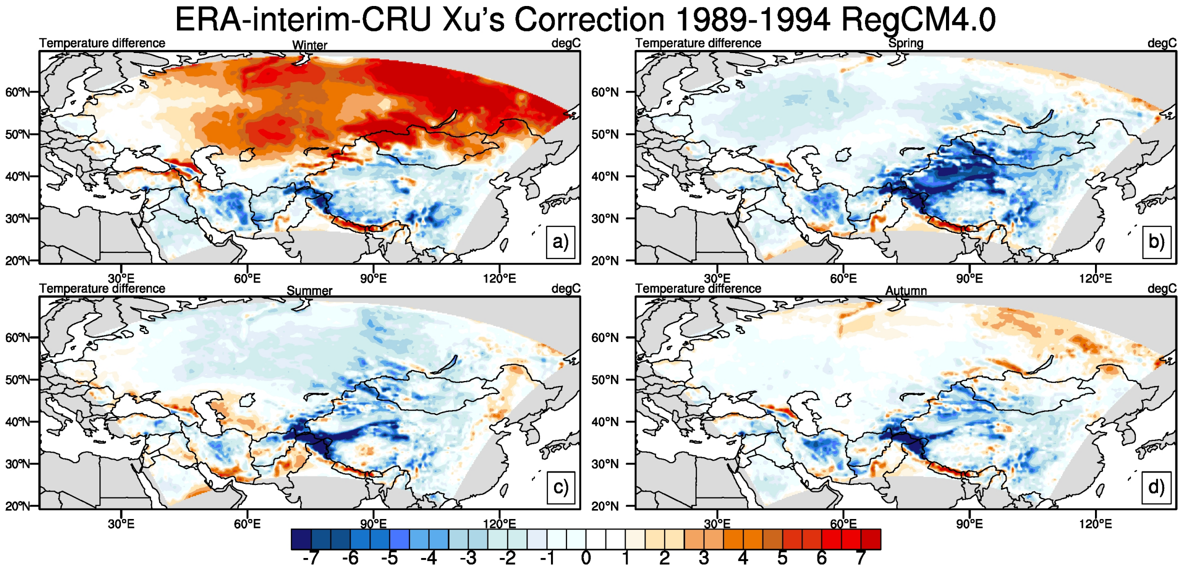

Figure 5.10. Comparison of the seasonal surface temperatures of the region using RegCM4.0 (with corrected cloud fraction equation - Xu), which is forced by the ERA-Interim dataset, with observations (CRU) for the period 1989-1994: (a) winter (DJF), (b) spring (MAM), (c) summer (JJA), and (d) autumn seasons (SON).

scheme was improved to solve the warm bias problem. We also tested the new cloud fraction parameterization with the latest version of RegCM for the Central Asia region. First the regional model RegCM4.3.5 which was forced by ERA-interim dataset was run without any correction (Figure 5.11). Surprisingly, we observed strong cold bias over north part of the region in the winter season. Cold bias can be observed in both spring and autumn seasons as well.

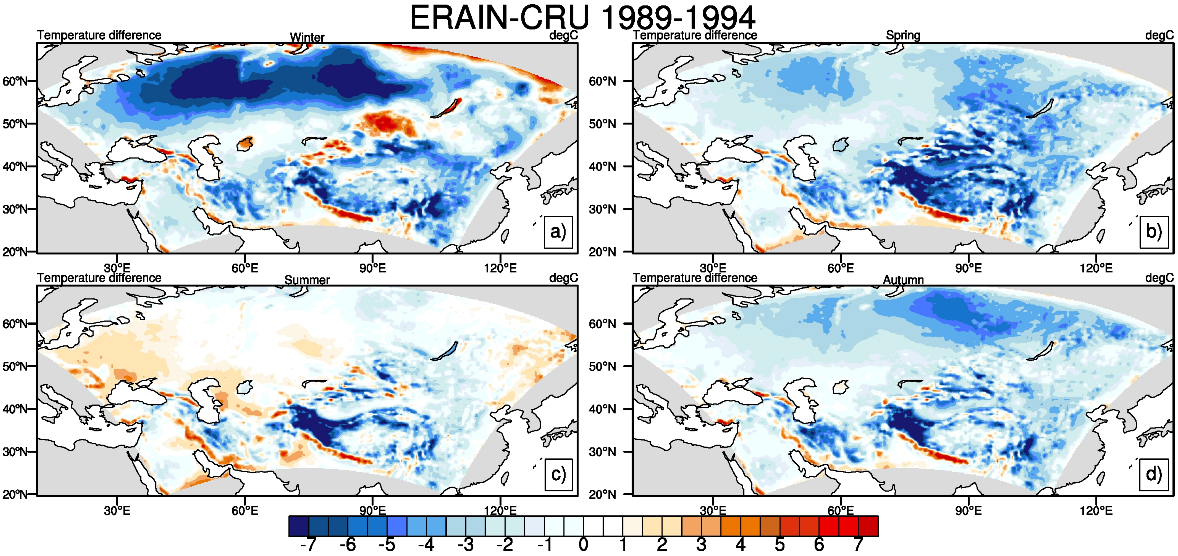

Figure 5.11. Comparison of the seasonal surface temperatures of the region using RegCM4.3.5, which is forced by the ERA-interim dataset, with observations (Climate Research Unit dataset) for the period 1989-1994 without correction: (a) winter (DJF), (b) spring (MAM), (c) summer (JJA), and (d) autumn seasons (SON).

Then, RegCM which was forced by ERA-interim dataset was also run with new parameterization for cloud fraction equation (Figure 5.12). The results showed that the corrected version of the code gives better results. Cold bias was decreased in magnitude and became less spread over the northern part of the domain in the winter season. We can also observe decrease in cold bias over Tibetan Plateau totally while the warm bias appears over there. In the summer season, cold bias over the Himalayas decreased but warm bias appeared over the southwest and mid part of the region. We generally observe decrease in cold bias all over the region in both spring and autumn seasons except Arabian Peninsula. Overall performance of new cloud fraction parameterization adopted into regional climate model version 4.3.5 for the ERA-interim dataset is also reasonable.

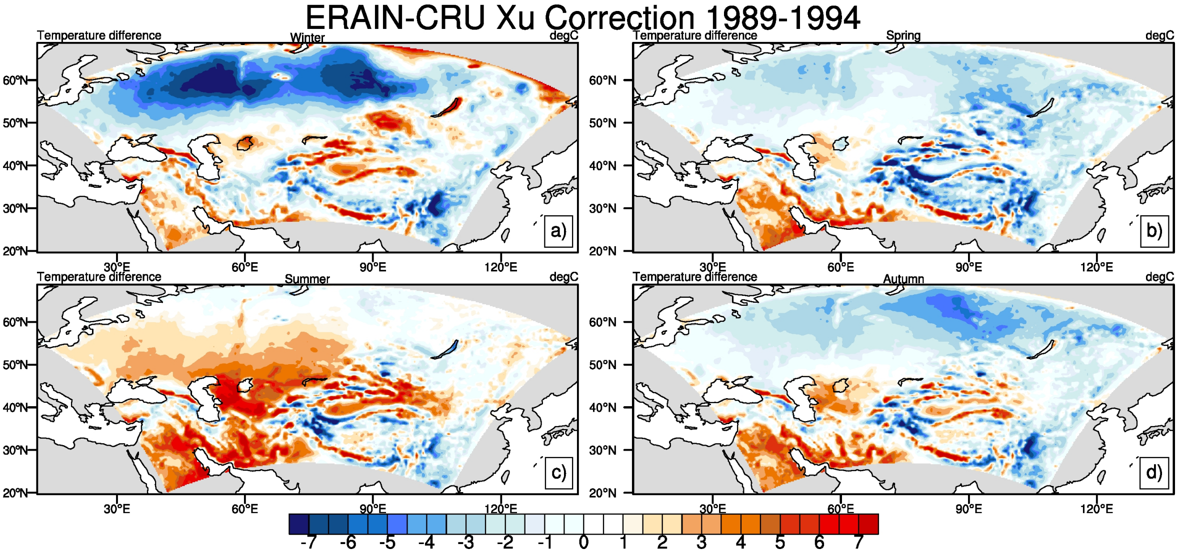

Figure 5.12. Comparison of the seasonal surface temperatures of the region using RegCM4.3.5 (with corrected cloud fraction equation - Xu), which is forced by the ERA-Interim dataset, with observations (CRU) for the period 1989-1994: (a) winter (DJF), (b) spring (MAM), (c) summer (JJA), and (d) autumn seasons (SON).

6. SIMULATIONS OF TEMPERATURE AND PRECIPITATION CLIMATOLOGY FOR THE CENTRAL ASIA CORDEX DOMAIN USING REGCM

6.1. Simulation of temperature and precipitation climatology of Central Asia domain by using RegCM4.0

In the present study, we investigated the seasonal time-scale performance of RegCM 4.0 in reproducing observed climatology over the large domain of Central Asia within the CORDEX framework. We evaluated the seasonal climate variability of the region by running the model for four climatological seasons (DJF, MAM, JJA and SON). The experiment includes simulation for the period 1970−2000 using the global climate model ECHAM5 data for forcing, and a simulation for the future period of 2070−2100 using the ECHAM5 A1B scenario projection data for forcing. By using these simulations, we determined the temperature and precipitation climatology obtained from RegCM 4.0 downscaling for Region 8 of the CORDEX framework. In spite of the diverse topography of the region, the temperature and precipitation climatology obtained by RegCM 4.0 from hindcast data captures the general characteristics of the climate of Central Asia.

6.1.1. Data and Methodology

In this work, RegCM Version 4.0 was used to simulate climate variables for the large Central Asian domain. Before applying the regional climate model to climate change studies of the region, we first tested the model's ability to reproduce the observed climatology. Two simulations were evaluated using the forcing data of the ERA-Interim (which the CORDEX framework prescribes) and ERA-40. We compared 2 different forcing datasets together with different parameterization and precipitation schemes to obtain the most reliable simulation for present-day runs (see Chapter 5). Investigation of seasonal climate variability in the Central Asian region was carried out for temperature and precipitation variables only. Validation of the present day climate for the region was performed by comparing the output of the model with observational data (i.e. the Climate Research Unit dataset). Then we applied RegCM 4.0 to investigate the climate variability of the Central Asia domain by downscaling the ECHAM5 global dataset for past and future periods.

CMIP3 global data ECHAM5 [169], which is the fifth generation of the ECHAM general circulation model developed by the Max Planck Institute for Meteorology, was used for past simulations for the period 1970−2000 as a forcing data for RegCM4.0. It originally developed from the spectral weather prediction model of ECMWF. Many advances in ECHAM5 have been made, in comparison to the previous version ECHAM4, in both the numerical handling and physics of the model. According to Roeckner *et al.* (2003) [169], these changes include a flux-form, semi- Lagrangian transport scheme for water components and chemical tracers, a new long-wave radiation code, separate treatment of cloud liquid water and cloud ice, new cloud microphysical and cloud cover parameterization formulations and sub-grid scale orographic effects.

6.1.2. Comparison between GCM and RegCM

To see the performance of the regional climate model, we first compared the outputs of ECHAM5 global climate model with outputs of regional climate model which is forced by ECHAM5 dataset. In general, while the difference between the ECHAM global dataset and CRU dataset for temperature climatology in the winter season is positive in Central, East and North Asia, the Caucasus, Northeast Anatolia and Azerbaijan, it is negative for the Central- East Arabian peninsula, the Himalayas, China and the mountainous and high plateau regions of Central Asia. In winter, the ECHAM global dataset produces approximately 7−8°C warmer climate conditions in Central Asia, especially in northwestern Mongolia, as compared to the CRU climatology (Figure 6.1). For the rest of the region, the ECHAM global climate model gives approximately 3−4°C warmer results. There are significant differences among the results for spring, summer and autumn seasons with respect to biases. The temperature climatology simulation of the ECHAM global climate model shows a cold bias of 3−5°C in the northern half of the domain, including the Himalayas, the high Tibetan Plateau and the mountainous regions of China, as compared to the CRU dataset in spring and summer. A warm bias of 2−3°C is seen in the rest of the domain.

The air temperature difference between the CRU and ECHAM-forced RegCM outputs shows a strong pattern in winter and summer (Figure 6.1). In winter, ECHAM-forced RegCM output generally produces a warmer climatology in the southern part of the domain, except the Himalaya Mountains and Tibetan Plateau. The large plains of southeastern Russia, northwest of Mongolia, and Northeast Asia (middle and north-eastern Siberia) are the regions in which ECHAM-forced RegCM output results in warmer temperatures, on the order of 7 to 8°C, with respect to the CRU dataset. In summer, the regional climate model produces cooler conditions in the whole region, except for the arid and semi-arid Karakum and Kyzyl-Kum plains, which are located east of the Caspian Sea Basin. The climatology of the spring and autumn seasons shows similarities in terms of the spatial distribution of differences. However, the magnitudes of the differences are not the same. In the western half of the domain, 2−3°C warmer conditions with respect to CRU results were obtained. The complex distribution of patterns including cold and warm conditions together generally dominates in spring over the eastern half of the domain.

As we observed from the temperature difference maps, the Himalayas, the Tibetan Plateau and the mountainous areas of China and Central Asia exhibit colder conditions in all seasons. While no significant differences are observed in climatology between ECHAM-forced RegCM output and the CRU dataset in Europe, 2−3°C warmer conditions are dominant in the Caspian Sea Basin and the arid and semi-arid plains of the east part of the Caspian Sea Basin. With respect to the CRU dataset, 4−5°C colder conditions are dominant for the Anatolian and Arabian Peninsulas, along with Iran and Mesopotamia, South, Southeast and most of East Asia.

When we examine the differences between the ECHAM RegCM and the GCM climatology, we find warmer conditions (although weak) in the RegCM outputs for the northern part of the domain in winter, spring, and autumn and warmer conditions in the GCM outputs for the mid-southern and southeastern parts of the domain for the same seasons. The latter region is affected by a shallow high pressure system (the cold-core Siberian anticyclone), which originates over the cold land surface of Siberia. In the summer, it is affected by a thermal monsoon low (the warm-core monsoon low), which originates over the warm land surface, and by the ITCZ. This situation is associated with the effects of particular conditions of the physical geography, the different regional circulation patterns between summer and winter and pressure and air mass conditions in the region. During the summer, positive differences are dominant in most of the domain, except South Asia and the Arabian Sea. In other words, the ECHAM GCM produces a warmer climatology than the ECHAM RegCM in summer.

6.1.3. Projection of Future Climatology

We have seasonal results for the period 2070−2100 from future simulations and for 1970−2000 from hind-cast simulations of the regional climate model. The past surface temperature and precipitation climatology is shown in Figure 6.1 and Figure 6.2. Warm biases for winter in the northern parts of the region and cold biases for the mountainous areas are again evident. In the precipitation climatology, the model overestimates the amounts of precipitation in almost all regions and seasons. The future surface temperature climatology difference for the region is presented in Figure 6.3. According to this model, in the winter season, the temperature climatology in almost all parts of the region shows an increase of at least 3°C in the 30 yr average with respect to the climate in the period 1970−2000. Temperatures in the southeast part of the region will increase by 11.4°C on average in the cold season, while the increase in the central part will be around 8°C on average. In spring an increase of up to 7.5°C can be expected in the central part. Temperature values in the southern and northern regions of the modelling area increase on average 4.5°C in this season. In summer, the southern part of the region shows an increase of 3°C in surface temperatures, while the northern part shows a slight cooling of surface temperatures. Finally, in autumn, a slight increase in temperatures in the center of domain is seen, while a 1.5°C increase is seen in the southern and northern areas with respect to the present climate.

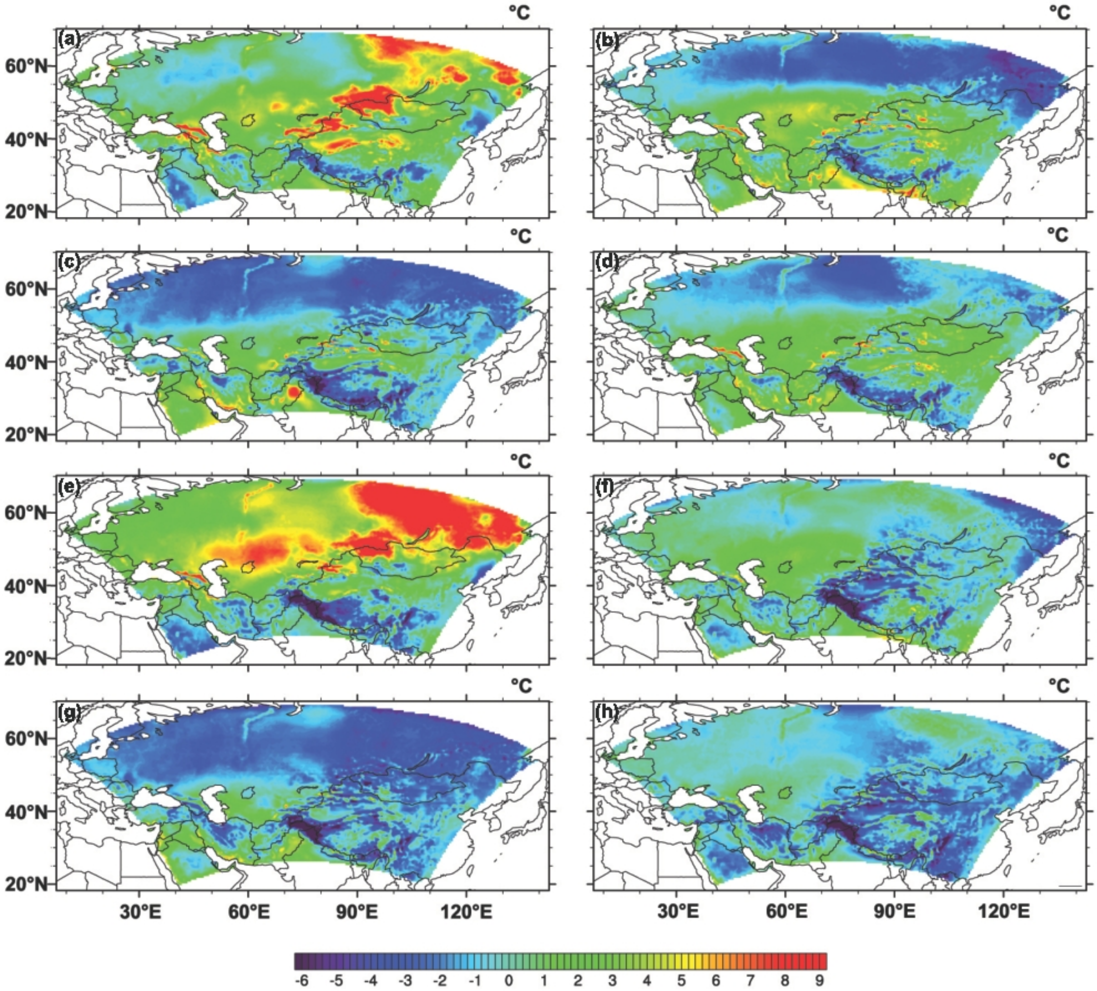

Figure 6.1. Comparison of the seasonal surface temperatures in the region using (a–d) the global climate model ECHAM5 and (e–h) the regional climate model RegCM, which is forced by the ECHAM5, with observations (Climate Research Unit dataset) for the period 1970−2000: (a,e) winter (DJF), (b,f) spring (MAM), (c,g) summer (JJA) and (d,h) autumn (SON) seasons.

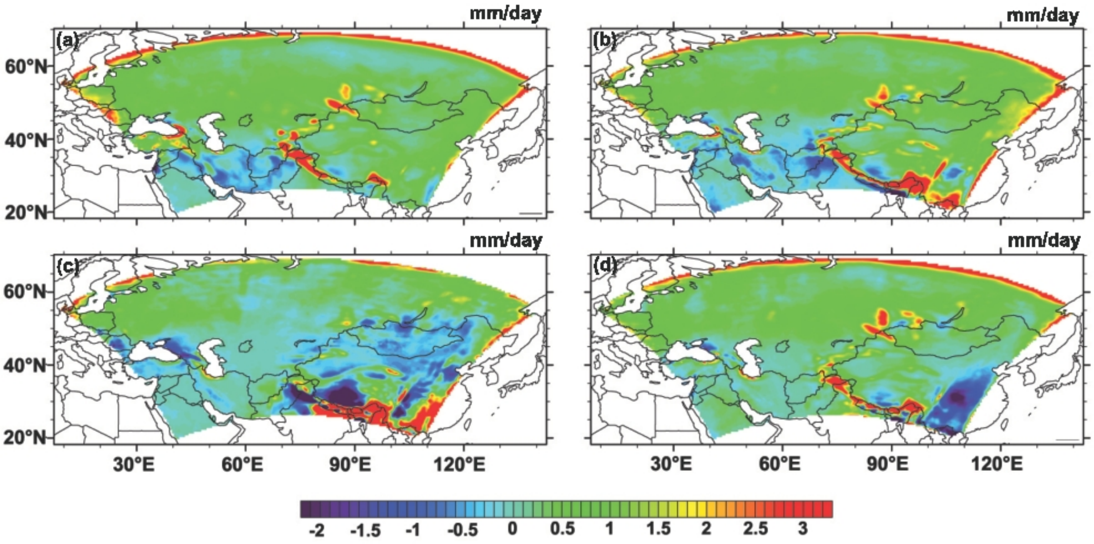

Figure 6.2. Comparison of the seasonal precipitation amounts of the regional climate model RegCM, which is forced by the global climate model ECHAM5, with respect to observations (Climate Research Unit dataset) for the period 1970−2000: (a) winter (DJF), (b) spring (MAM), (c) summer (JJA) and (d) autumn (SON) seasons.

The future precipitation climatology of the region with respect to the present climate is shown in Figure 6.3. In almost all seasons, amounts of precipitation in the northern part of the region do not change with respect to the present-day climate. In the warm season, results show a decrease in precipitation of up to 3 mm d^{-1}, especially in the southeastern part of the domain. There is also a decrease of 2 mm d^{-1} in autumn in the southeastern part of the domain. Since the nature of the Central Asian climate is already arid and semi-arid, relatively small changes in precipitation are expected. In the future, we expect the Central Asian region to become drier due to an increase in surface temperature.

6.2. Simulation of temperature and precipitation climatology of Central Asia domain by using RegCM4.3.5

In this part, projected future changes for three periods of 2010 – 2040, 2040 – 2070 and 2070 – 2100 in mean air temperature and precipitation climatology with respect to the control period of 1970 – 2000 were investigated for the domain of Central Asia via regional climate model simulations. In order to investigate the projected changes in near future climate conditions, Regional Climate Model, RegCM4.3.5 of ICTP was driven by two different CMIP5 global climate models. HadGEM2 global climate model of the Met Office Hadley Centre and MPI-ESM-MR global climate model of the Max Planck Institute for Meteorology were dynamically downscaled to 50 km for the domain. The projections were performed based on the RCP4.5 and the RCP8.5 emission scenarios of the Intergovernmental Panel on Climate Change (IPCC).

6.2.1. Seasonal temperature and precipitation climatology

First, we tested regional climate model's ability to simulate observed climatology by using ERA-interim reanalysis dataset for the period 1980-2000 and global climate models of HadGEM2 and MPI-ESM-MR for the period 1970-2000 as a forcing data to the model. We investigated model biases for four climatological seasons, which are December-January-February (DJF, winter), March-April-May (MAM, spring), June-July-August (JJA, summer) and September-October-November (SON, autumn). We

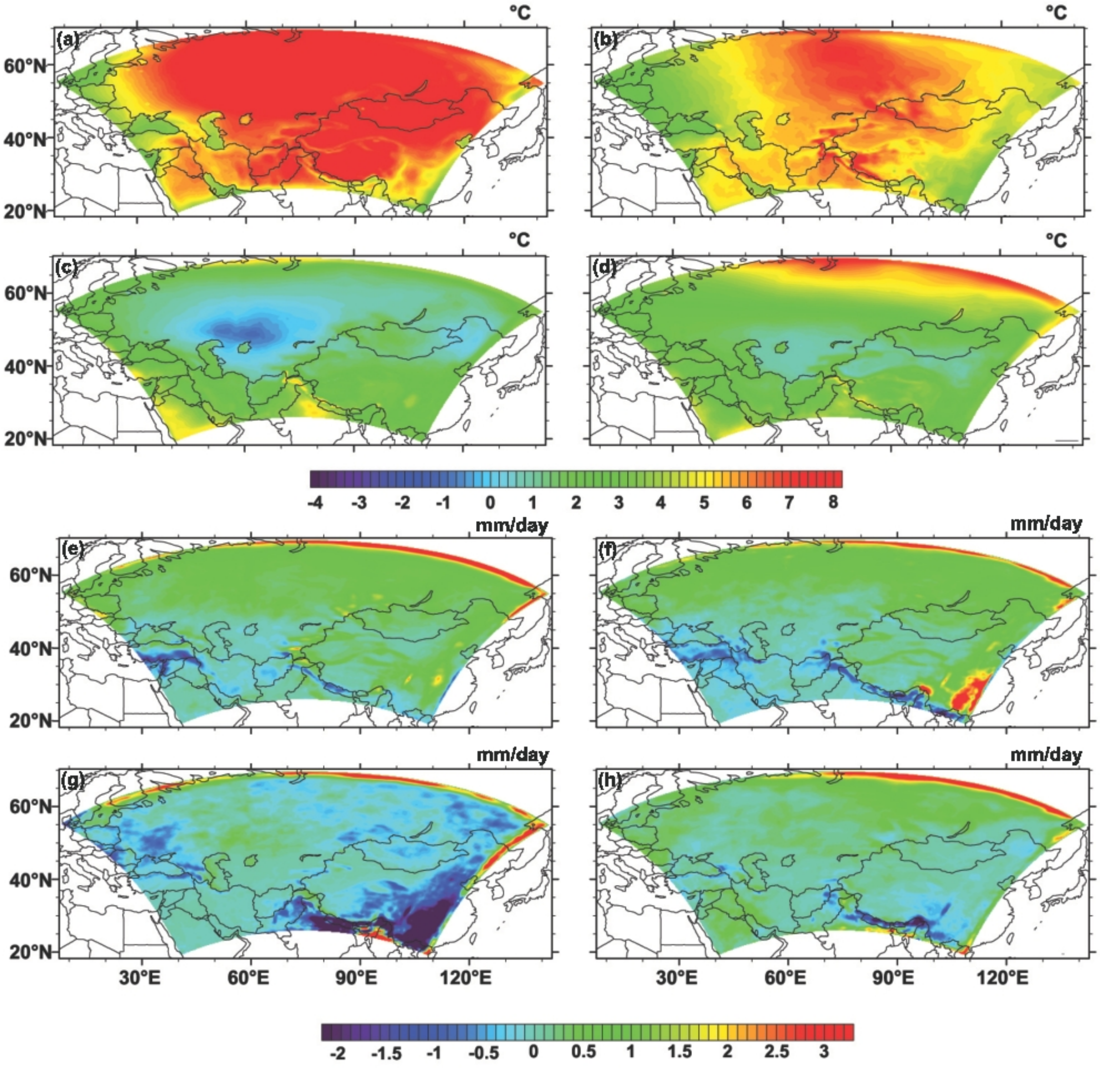

Figure 6.3. Seasonal (a–d) temperature and (e–h) precipitation projections from the regional climate model RegCM, which is forced by the global climate model ECHAM5 for the period 2070−2100, with respect to ECHAM5 for the period 1970−2000: (a,e) winter (DJF), (b,f) spring (MAM), (c,g) summer (JJA) and (d,h) autumn (SON) seasons.

compared outputs of regional climate model with the CRU observational dataset for seasonal temperature and precipitation. Comparisons of outputs of the regional climate model with observation are presented in Figure 6.4, Figure 6.5 and Figure 6.6. The results of the model which is run by the ERA-interim dataset show that there is a strong cold bias in the northern part of the domain for winter season (Figure 6.4). There is also similar but less intense cold bias in the outputs of model which is run by HadGEM2 global dataset (Figure 6.5). However, cold bias is not generated by the model which is run by MPI-ESM-MR global dataset (Figure 6.6). Inversely, it has a strong warm bias in northeast part of the region. Cold bias is seen during all four seasons and in all datasets around mountainous part of the domain like Himalayas and Plateau of Tibet. Since we observe this cold bias in all outputs of the model which is run by three different datasets, this could be due to station bias. The meteorological stations are probably constructed in the valleys of this region. In other parts of the domain, an overall bias of model is between -1.5 and 1.5 °C for temperature. Thus, performance of the regional climate model is reasonable in that parts of the Central Asia domain.

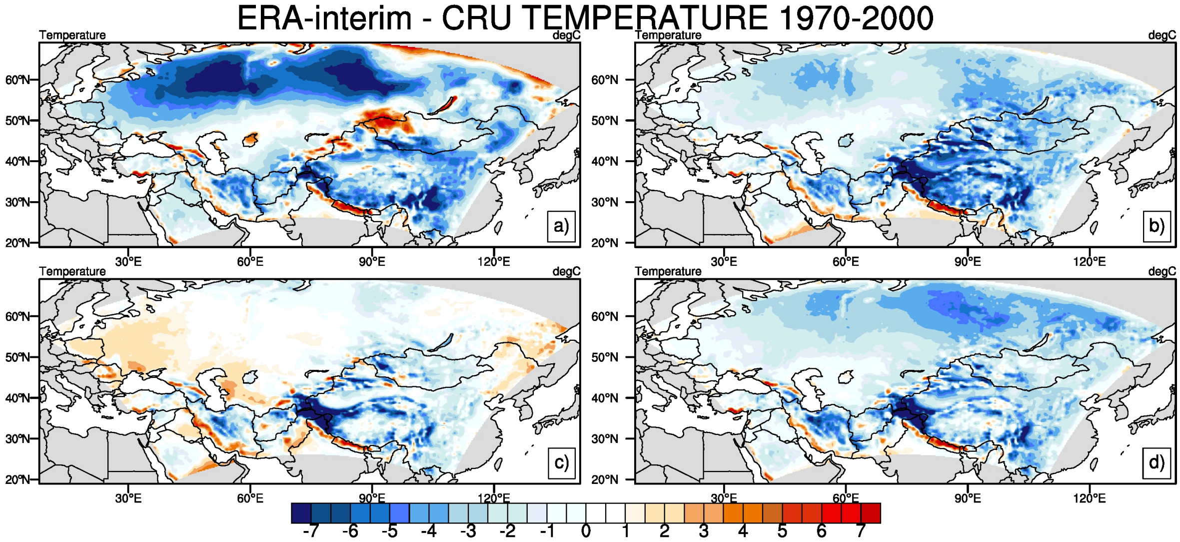

Figure 6.4. Comparison of simulated air temperatures of the RegCM4.3.5 regional climate model, which is run by the ERA-interim dataset, with the CRU observational temperature dataset over Central Asia for the period 1979 - 2000: (a) winter, (b) spring, (c) summer and (d) autumn seasons.

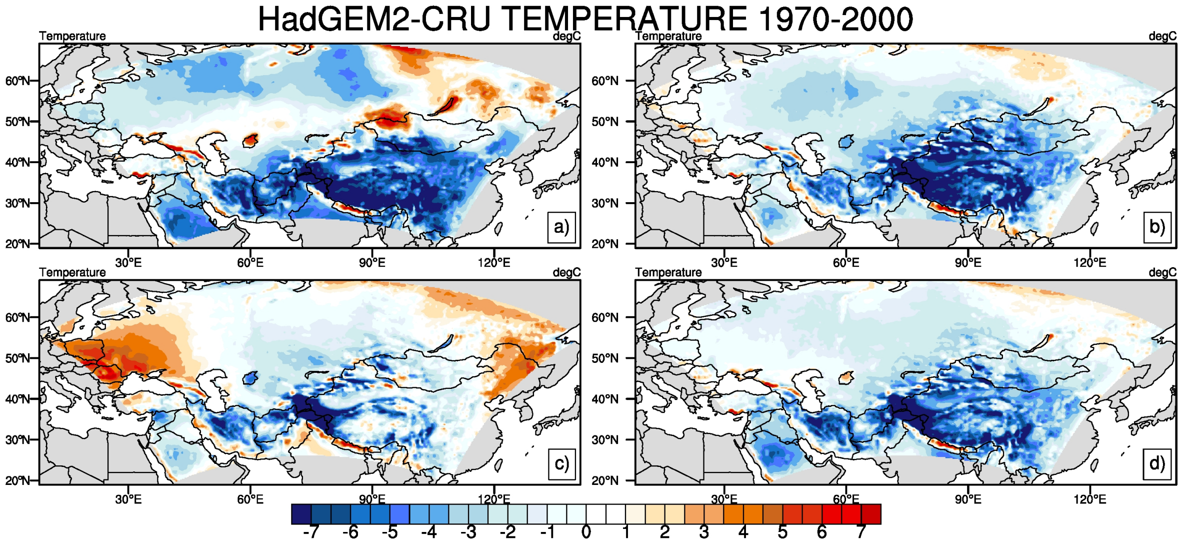

Figure 6.5. As in the Figure 6.4, but with the HadGEM2 dataset.

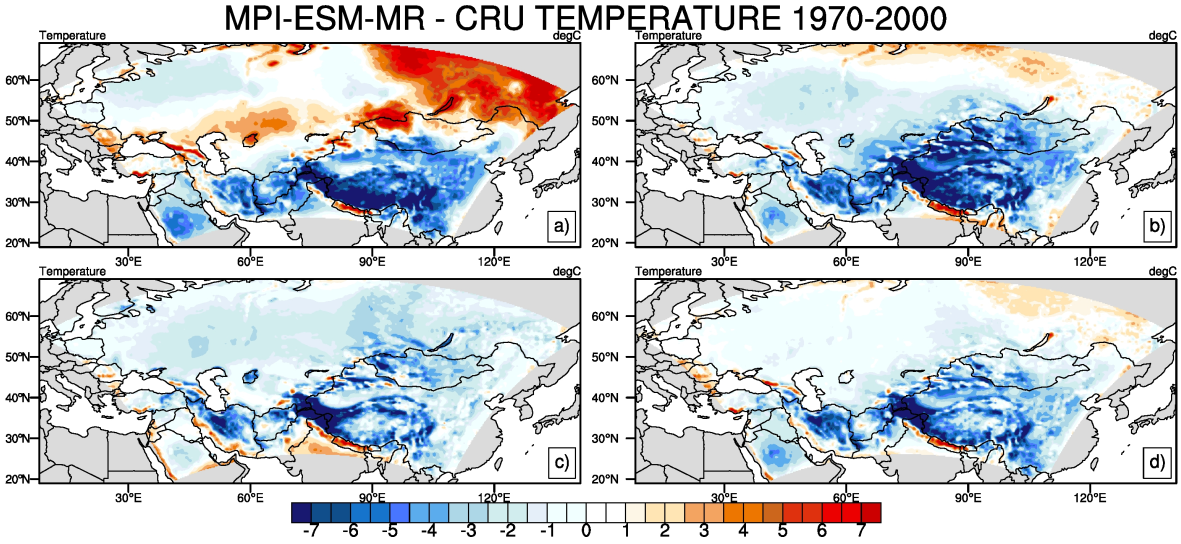

Figure 6.6. As in the Figure 6.4, but with the MPI-ESM-MR dataset.

In Figure 6.7, Figure 6.8 and Figure 6.9, the precipitation climatology of the domain with the ERA-Interim, HadGEM2 and MPI-ESM-MR data is presented respectively. For the northern and eastern parts of the domain, precipitation is generally overestimated especially for MPI-ESM-MR data with respect to observational data for all seasons except summer. Precipitation is slightly underestimated for the southern part of the domain except the Asian monsoon region including the Himalayas and other mountainous areas. During the spring, autumn and winter seasons, results of all datasets show excess precipitation over the mountainous areas of the Asian monsoon region. However, results are obviously different in summer season. In summer, precipitation is underestimated for most parts of the domain, compared with the observation, whereas highly increased precipitation is estimated for the continental semiarid eastern and semi-humid/ humid southeastern parts of the domain.

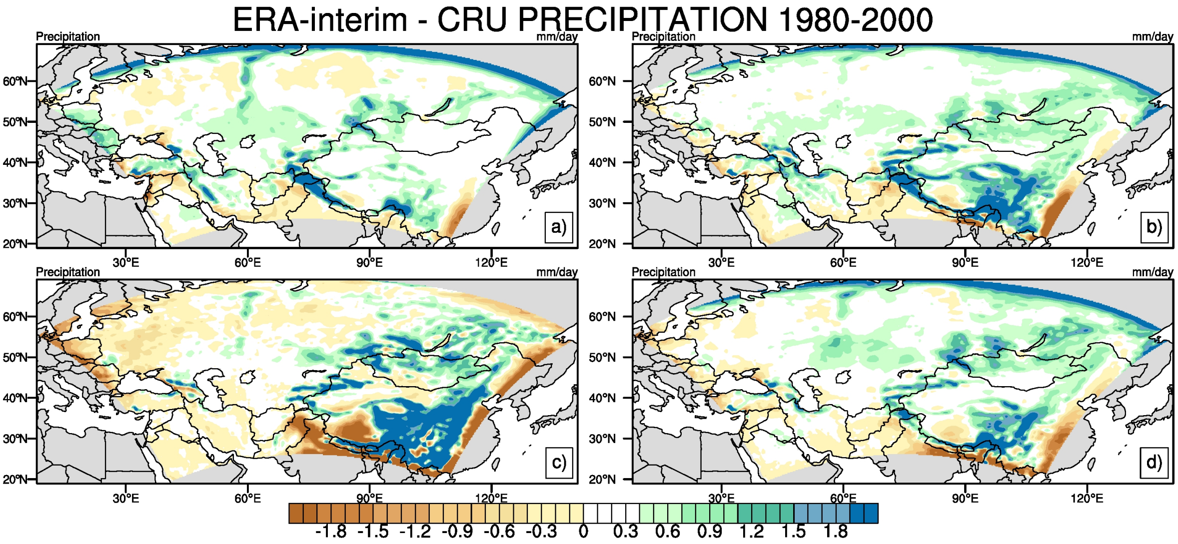

Figure 6.7. Comparison of simulated average precipitation amounts of the RegCM4.3.5 regional climate model, which is forced by the ERA-interim dataset, with the CRU observational precipitation dataset over Central Asia for the period 1980 - 2000: (a) winter, (b) spring, (c) summer and (d) autumn seasons.

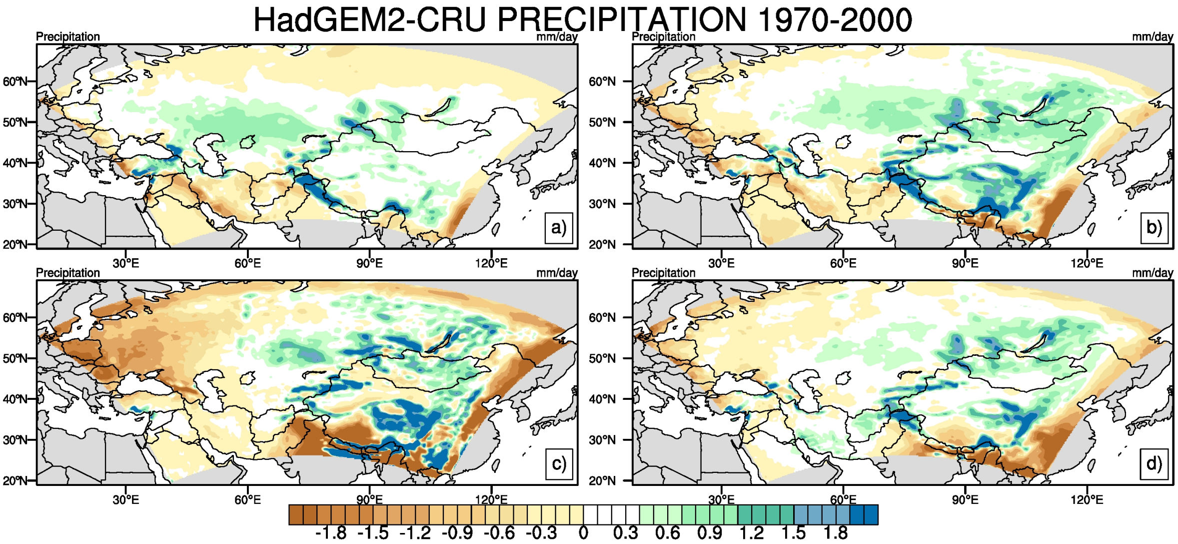

Figure 6.8. As in the Figure 6.7, but with the HadGEM2 dataset.

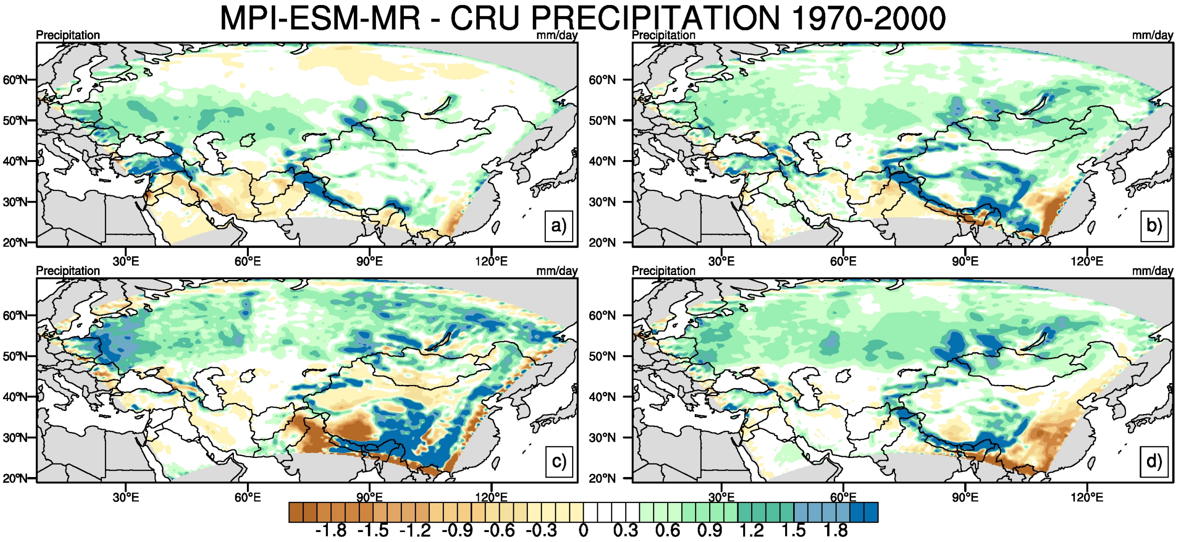

Figure 6.9. As in the Figure 6.7, but with the MPI-ESM-MR dataset.

6.2.2. Projected changes in future temperature and precipitation climatology

In this part, we presented temperature change projections for the future periods 2010-2040, 2040-2070 and 2070-2100 with respect to the present period 1970-2000 based on the IPCC's RCP4.5 and RCP8.5 emission scenarios. The results of RCP4.5 emission scenario outputs of HadGEM2 global model dataset for periods of 2010-2040, 2040-2070 and 2070-2100 are presented in Figures 6.10, 6.11 and 6.12 respectively, whereas RCP8.5 emission scenario based outputs are presented in Figures 6.13, 6.14 and 6.15. For all three future periods, general warming is estimated for all parts of the region. Warming trend is getting worse as time goes by according to the projection results. According to RCP 4.5 model scenario results, there will be 3-4 °C increase in temperature for summer season at all part of the region for period of 2070-2100. Warming will be the most at northern part of the domain at winter season. According to RCP 8.5 model scenario results, this increase will be more severe and it will be more than 7 °C for almost all part of the domain and for all seasons.

We presented here precipitation change projections for the future periods 2010-2040, 2040-2070 and 2070-2100 with respect to the present period 1970-2000 based on the IPCC's RCP4.5 and RCP8.5 emission scenarios. The results of RCP4.5 emission scenario outputs of HadGEM2 global model dataset for periods of 2010-2040, 2040-2070 and 2070-2100 are presented in Figures 6.16, 6.17 and 6.18 respectively, whereas RCP8.5 emission scenario based outputs are presented in Figures 6.19, 6.20 and 6.21. In almost all seasons and for all future periods, amounts of precipitation in the northern part of the domain do not change with respect to the present period of 1970-2000, except RCP8.5 scenario output for the period 2070-2100 in winter and autumn seasons. Both emission scenarios' output estimate similar results for future projections. Drier conditions will occur for the most part of the region which is already arid and semi-arid according to the projections.

The results of RCP4.5 emission scenario outputs of MPI-ESM-MR global model dataset for periods of 2010-2040, 2040-2070 and 2070-2100 are presented in Figures

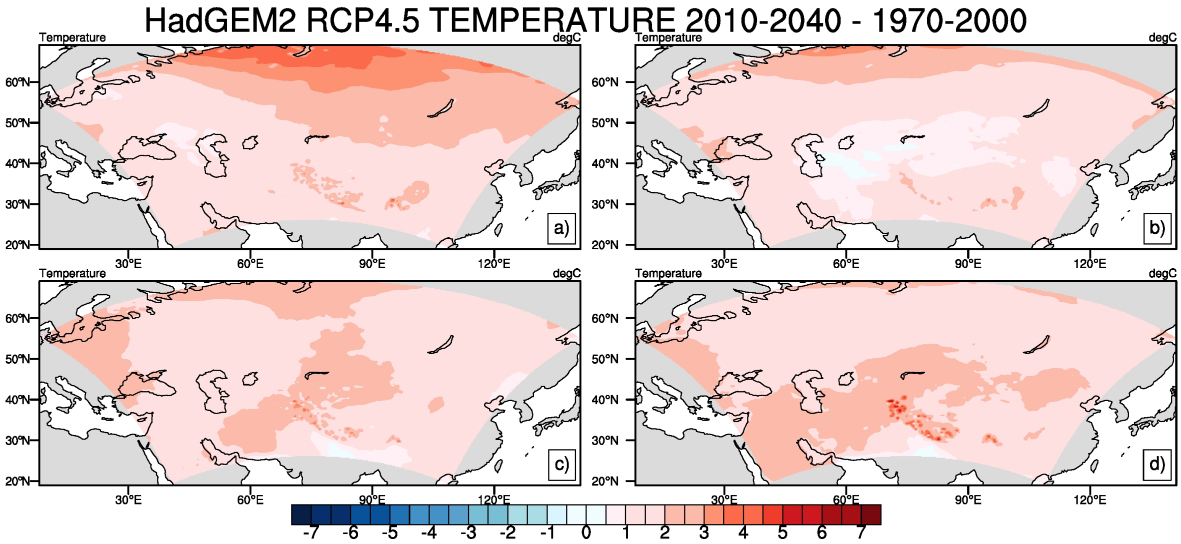

Figure 6.10. Geographical distribution patterns of changes in projected mean air temperatures over Central Asia from the regional climate model RegCM4.3.5, which is forced by the global climate model HadGEM2 with RCP4.5 emission scenario for the climatology of 2010 - 2040 future period with respect to the climatology of 1970 - 2000 reference period: (a) winter, (b) spring, (c) summer and (d) autumn seasons.

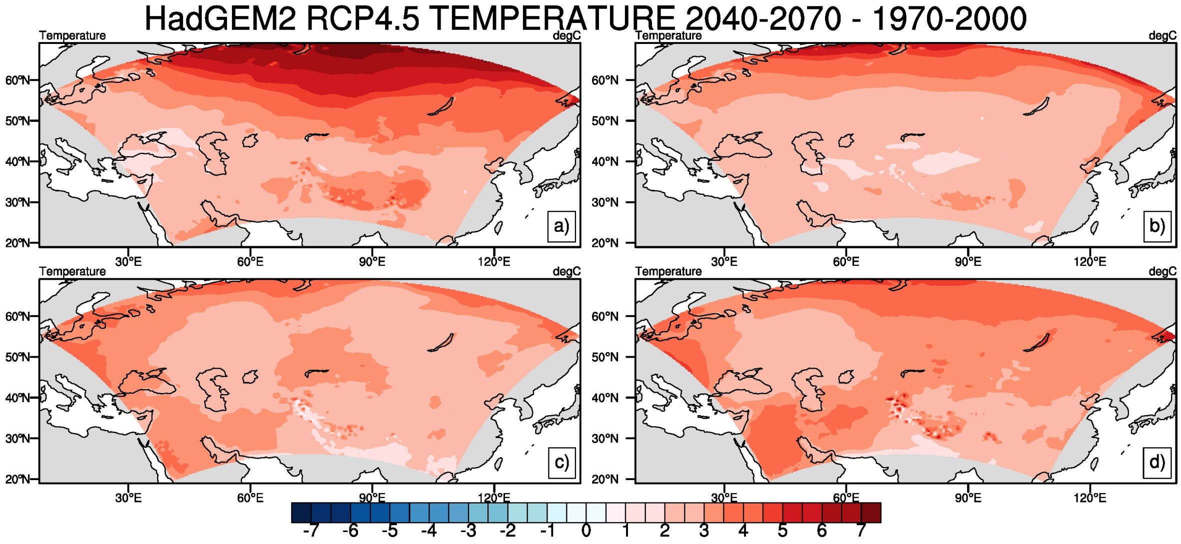

Figure 6.11. As in the Figure 6.10, but for the period of 2040 - 2070.

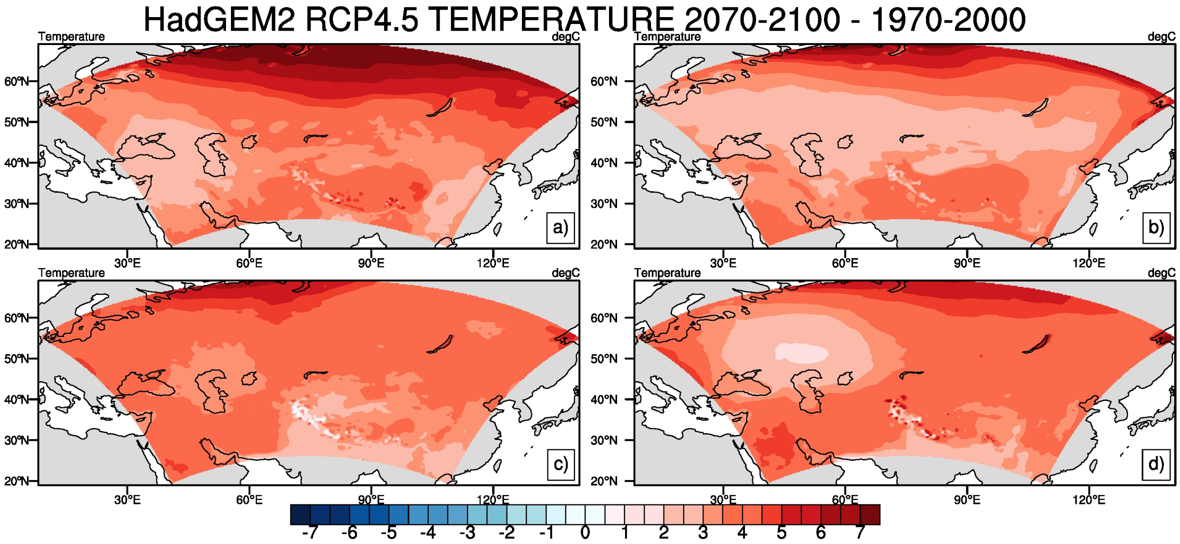

Figure 6.12. As in the Figure 6.10, but for the period 2070 - 2100.

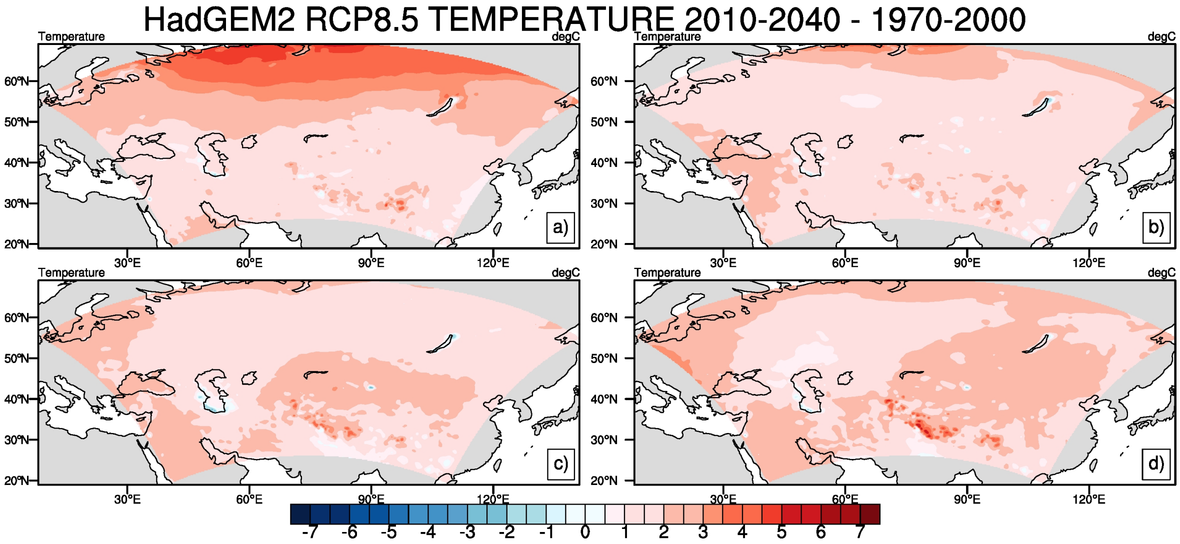

Figure 6.13. Geographical distribution patterns of changes in projected mean air temperatures over Central Asia from the regional climate model RegCM4.3.5, which is forced by the global climate model HadGEM2 with RCP8.5 emission scenario for the climatology of 2010 - 2040 future period with respect to the climatology of 1970 - 2000 reference period: (a) winter, (b) spring, (c) summer and (d) autumn seasons.

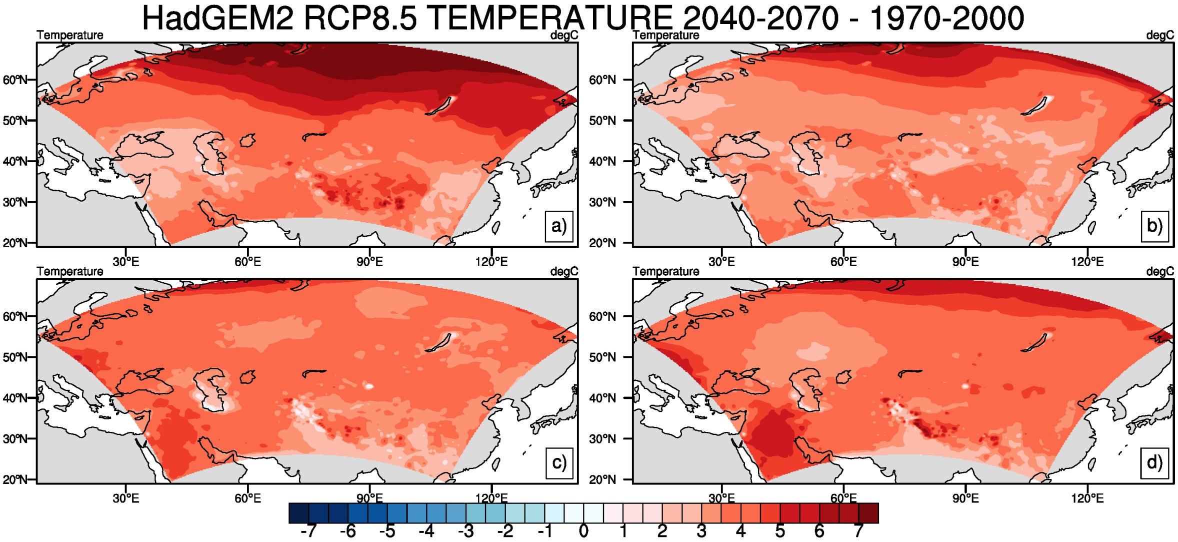

Figure 6.14. As in the Figure 6.13, but for the period 2040 - 2070.

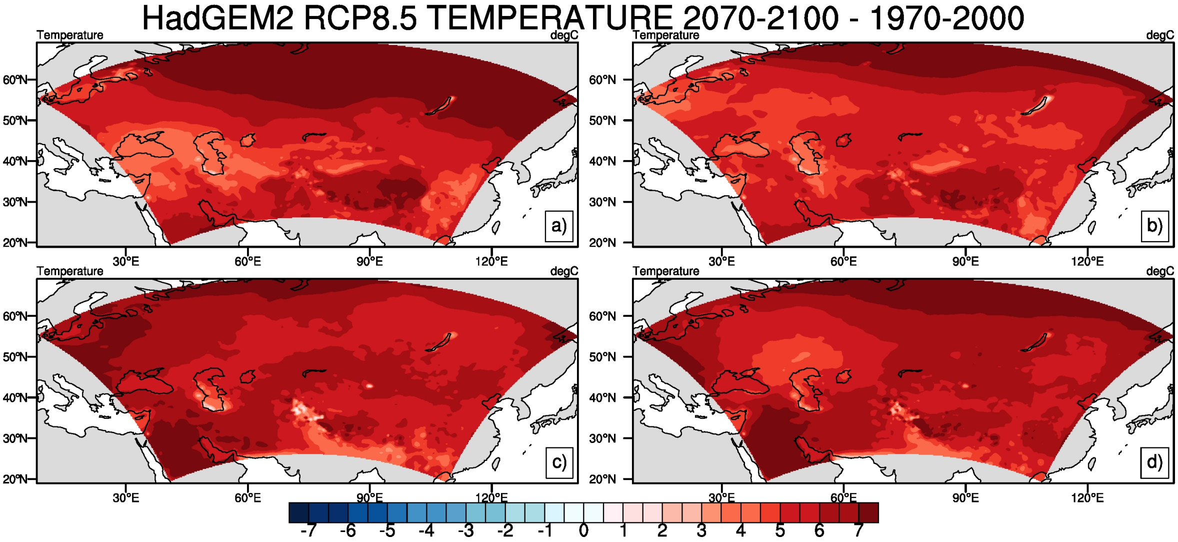

Figure 6.15. As in the Figure 6.13, but for the period 2070 - 2100.

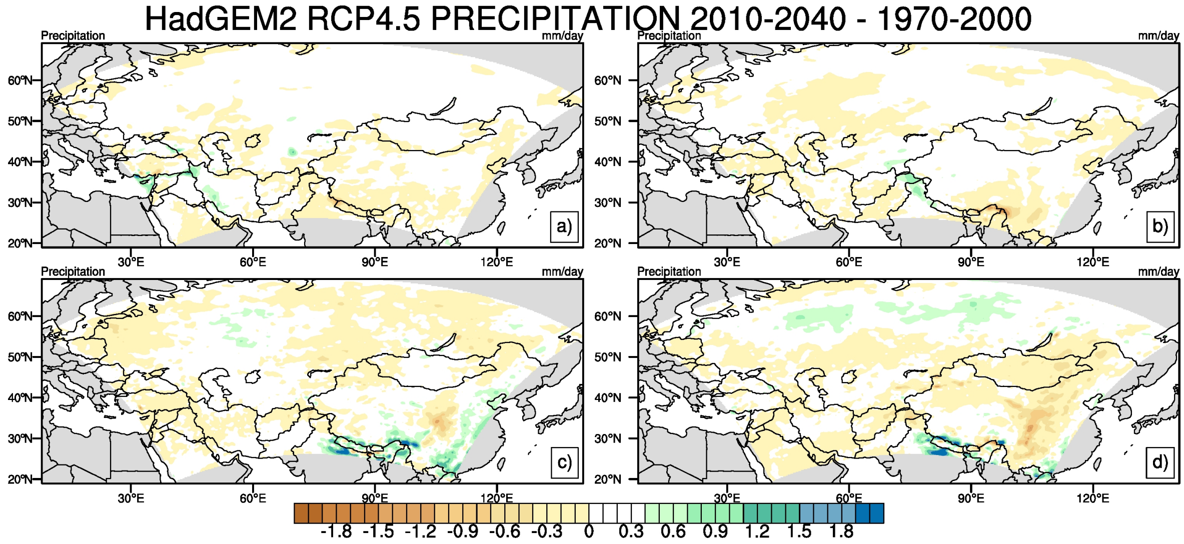

Figure 6.16. Geographical distribution patterns of changes in projected total precipitation amounts over Central Asia from the regional climate model RegCM4.3.5, which is forced by the global climate model HadGEM2 with RCP4.5 emission scenario for the climatology of 2010 - 2040 future period with respect to the climatology of 1970 - 2000 reference period: (a) winter, (b) spring, (c) summer and (d) autumn seasons.

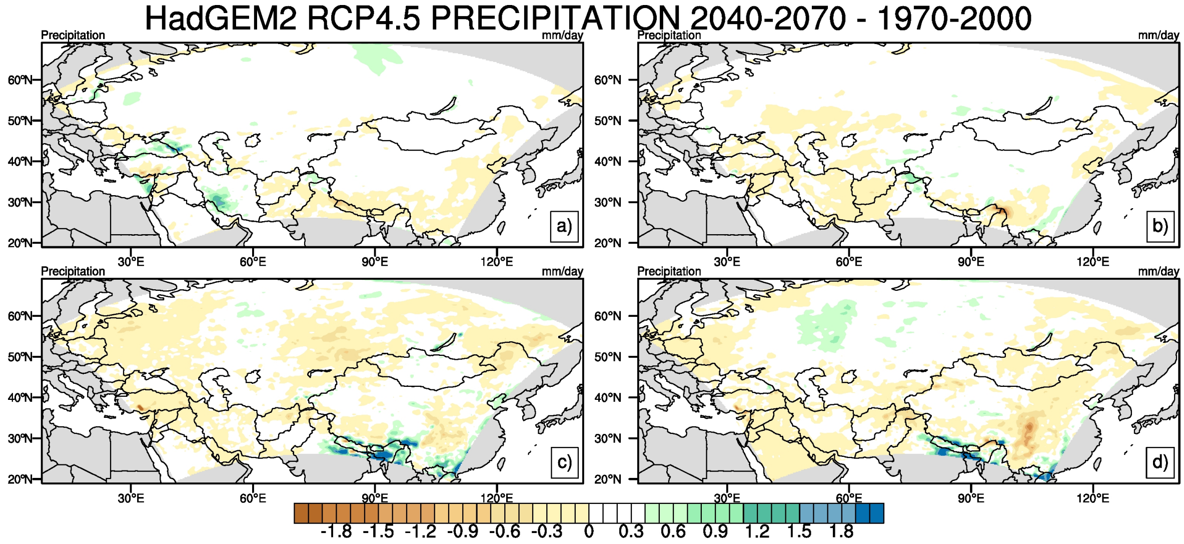

Figure 6.17. As in the Figure 6.16, but for the period 2040 - 2070.

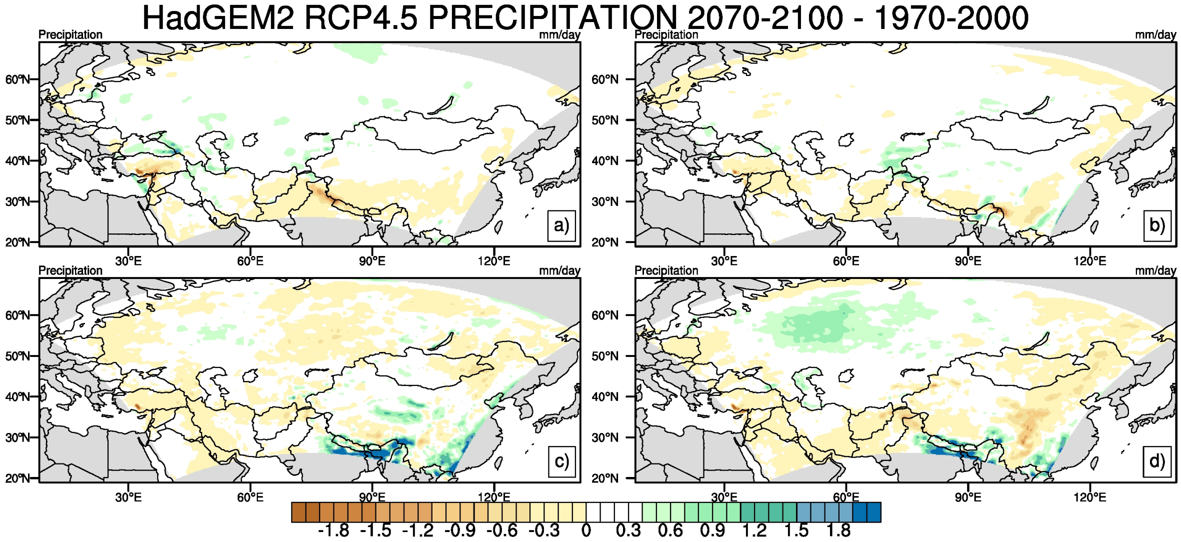

Figure 6.18. As in the Figure 6.16, but for the period 2070 - 2100.

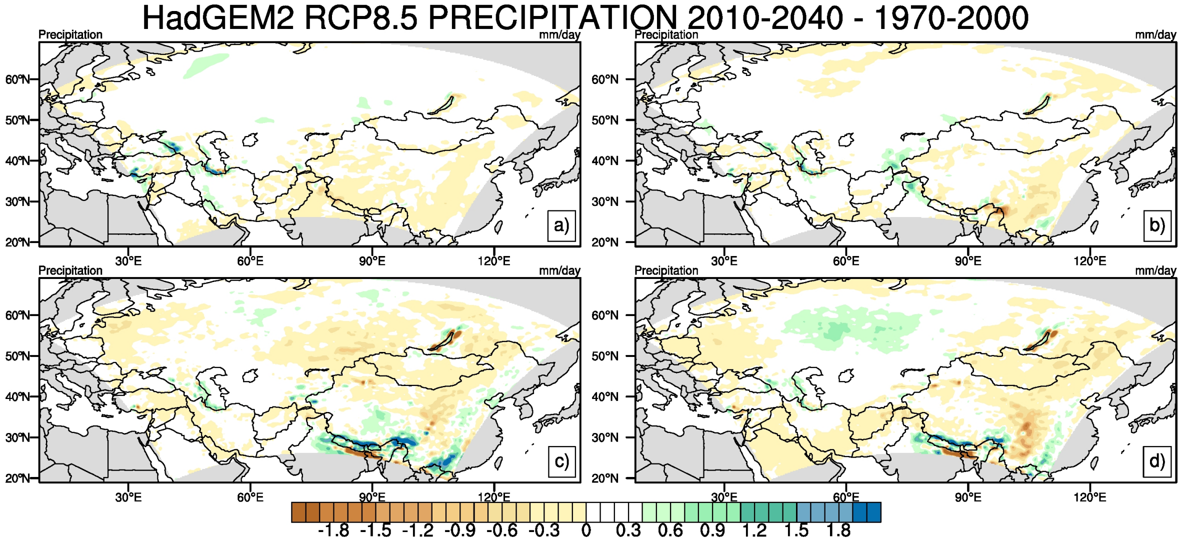

Figure 6.19. Geographical distribution patterns of changes in projected total precipitation amounts over Central Asia from the regional climate model RegCM4.3.5, which is forced by the global climate model HadGEM2 with RCP8.5 emission scenario for the climatology of 2010 - 2040 future period with respect to the climatology of 1970 - 2000 reference period: (a) winter, (b) spring, (c) summer and (d) autumn seasons.

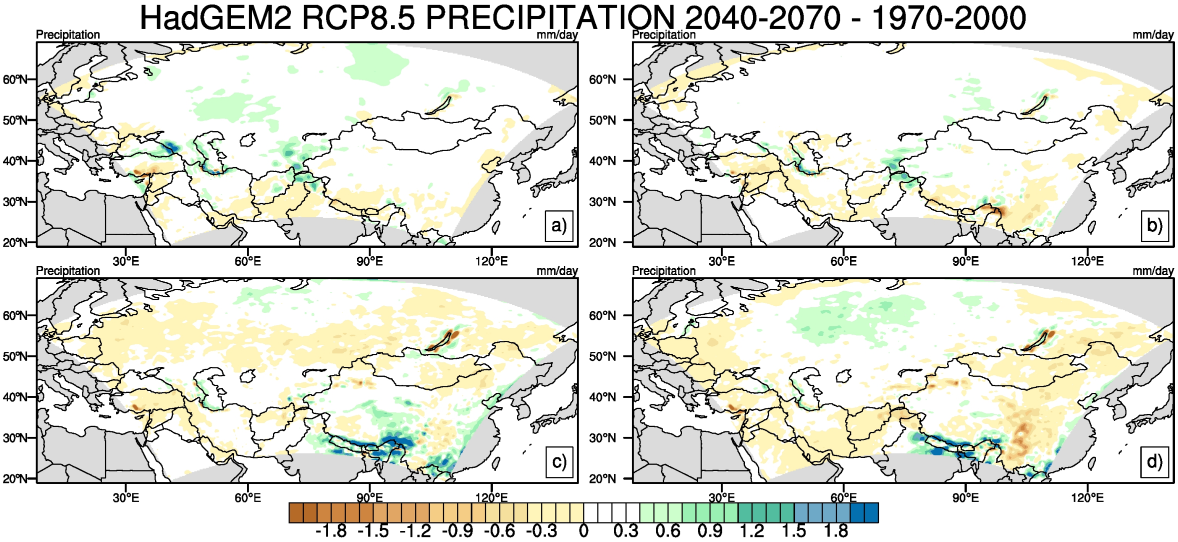

Figure 6.20. As in the Figure 6.19, but for the period 2040 - 2070.

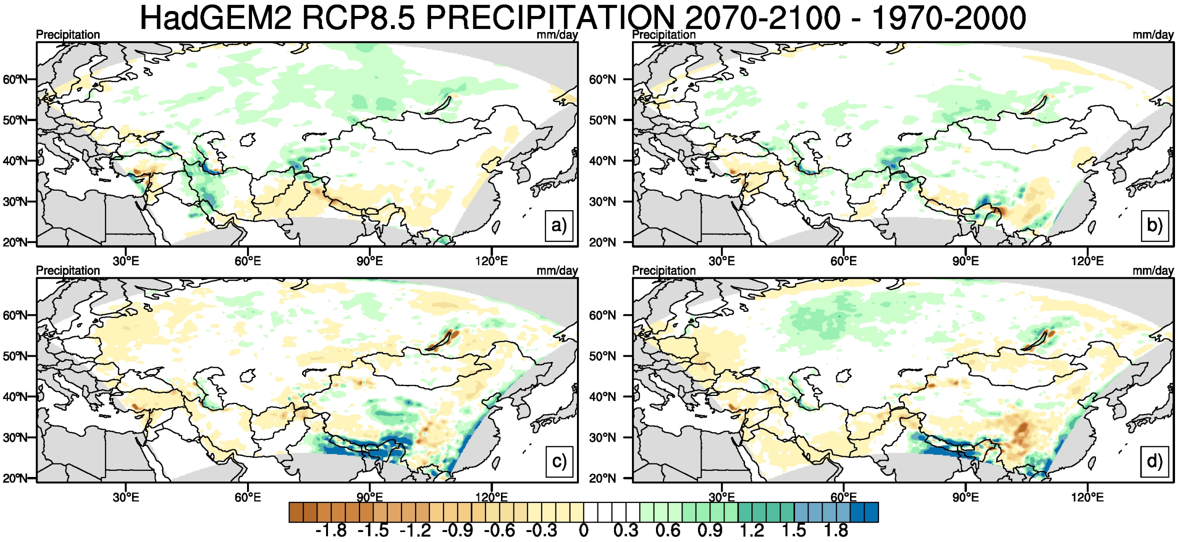

Figure 6.21. As in the Figure 6.19, but for the period 2070 - 2100.

6.22, 6.23 and 6.24 respectively, whereas RCP8.5 emission scenario based outputs are presented in Figures 6.25, 6.26 and 6.27. The outputs of MPI-ESM-MR global model dataset show similar trend with outputs of HadGEM2 global model dataset. However, the intensity of warming projected by using MPI-ESM-MR global model is less than HadGEM2 global model projections especially in RCP8.5 emission scenario based output for the period of 2070-2100.

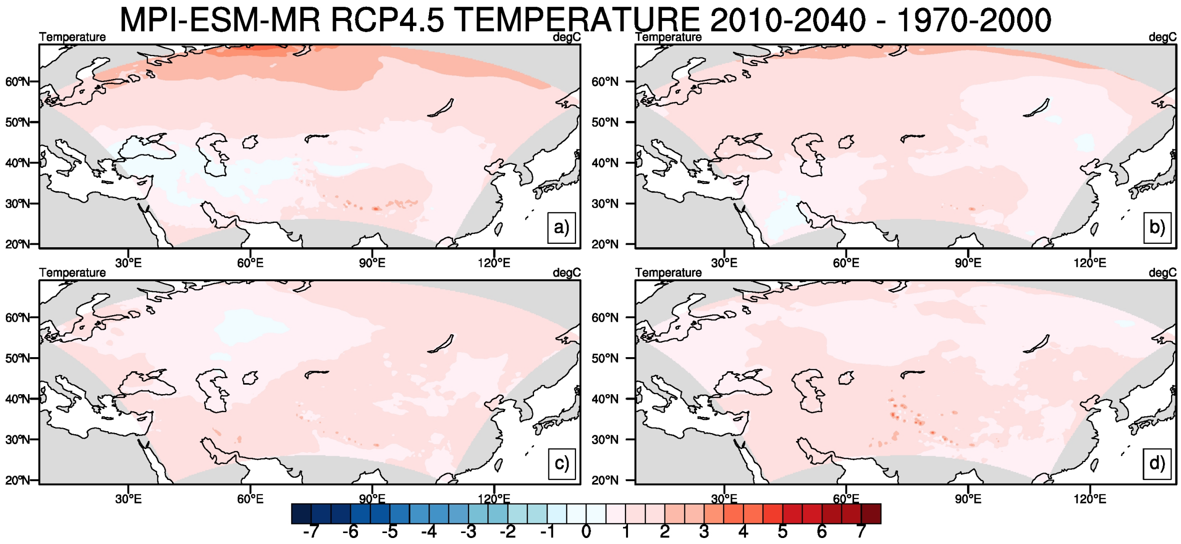

Figure 6.22. Geographical distribution patterns of changes in projected mean air temperatures over Central Asia from the regional climate model RegCM4.3.5, which is forced by the global climate model MPI-ESM-MR with RCP4.5 emission scenario for the climatology of 2010 - 2040 future period with respect to the climatology of 1970 - 2000 reference period: (a) winter, (b) spring, (c) summer and (d) autumn seasons.

The results of RCP4.5 emission scenario outputs of MPI-ESM-MR global model for periods of 2010-2040, 2040-2070 and 2070-2100 are presented in Figures 6.28, 6.29 and 6.30 respectively, whereas RCP8.5 emission scenario based outputs are presented in Figures 6.31, 6.32 and 6.33. All parts of the Central Asia domain, we observe almost no change and even decrease in precipitation except the RCP8.5 emission scenario outputs for the period 2070-2100. According to the RCP8.5 emission scenario output of regional climate model which is forced by MPI-ESM-MR global climate dataset, there will be an increase in precipitation in the northern part of the domain for all seasons. Decrease in precipitation is observed prominently, especially in the southeastern part of the

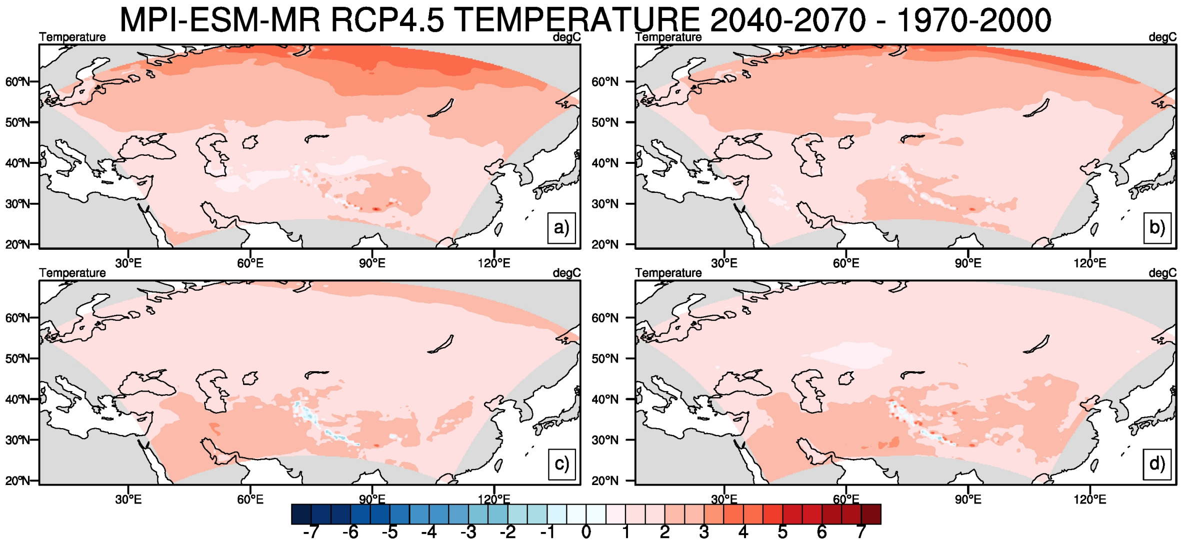

Figure 6.23. As in the Figure 6.22, but for the period 2040 - 2070.

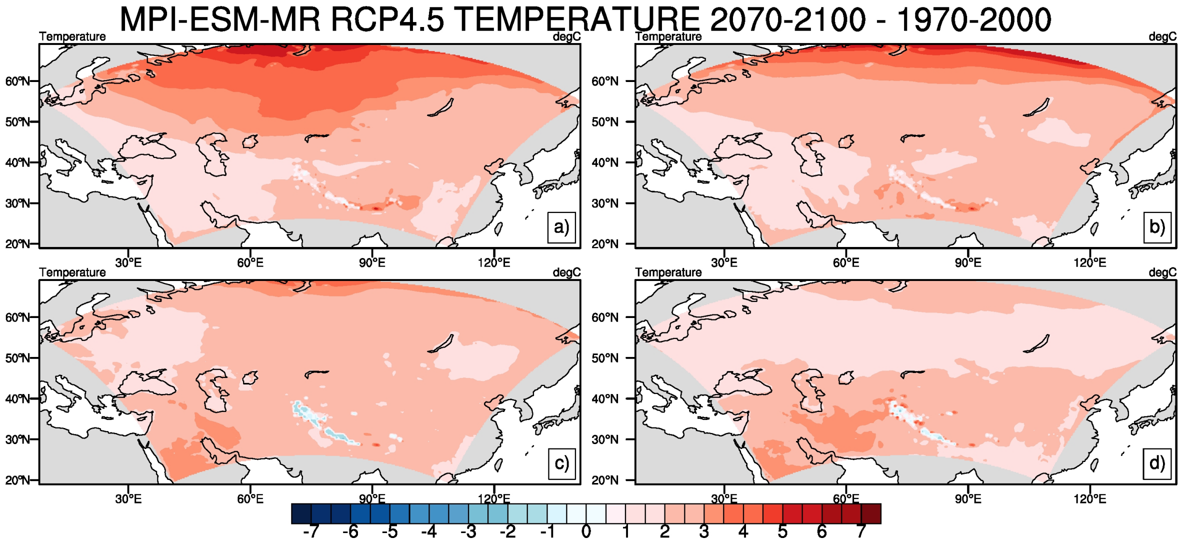

Figure 6.24. As in the Figure 6.22, but for the period 2070 - 2100.

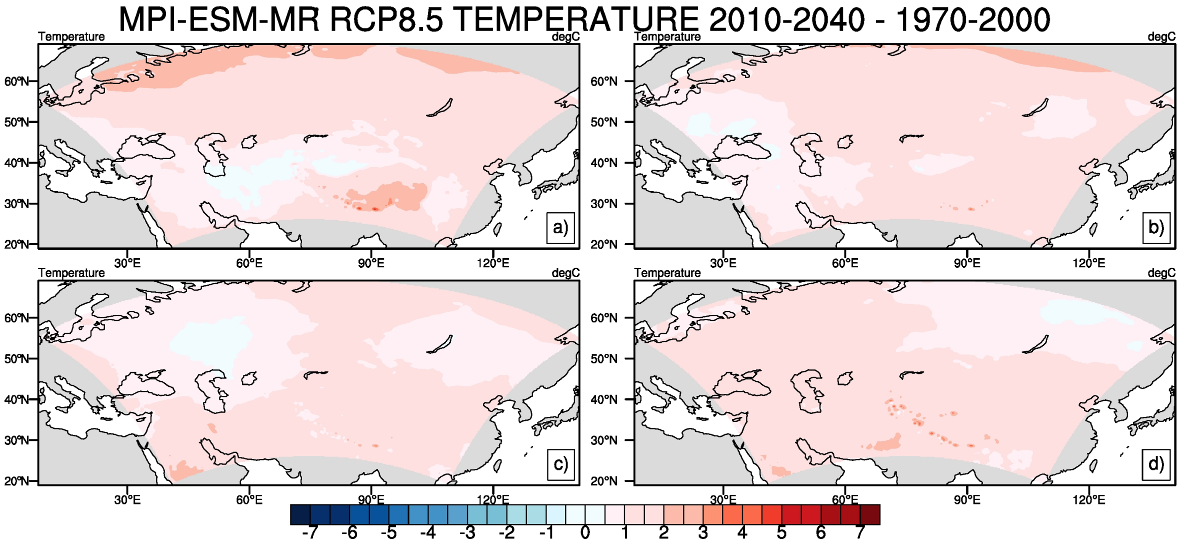

Figure 6.25. Geographical distribution patterns of changes in projected mean air temperatures over Central Asia from the regional climate model RegCM4.3.5, which is forced by the global climate model MPI-ESM-MR with RCP8.5 emission scenario for the climatology of 2010 - 2040 future period with respect to the climatology of 1970 - 2000 reference period: (a) winter, (b) spring, (c) summer and (d) autumn seasons.

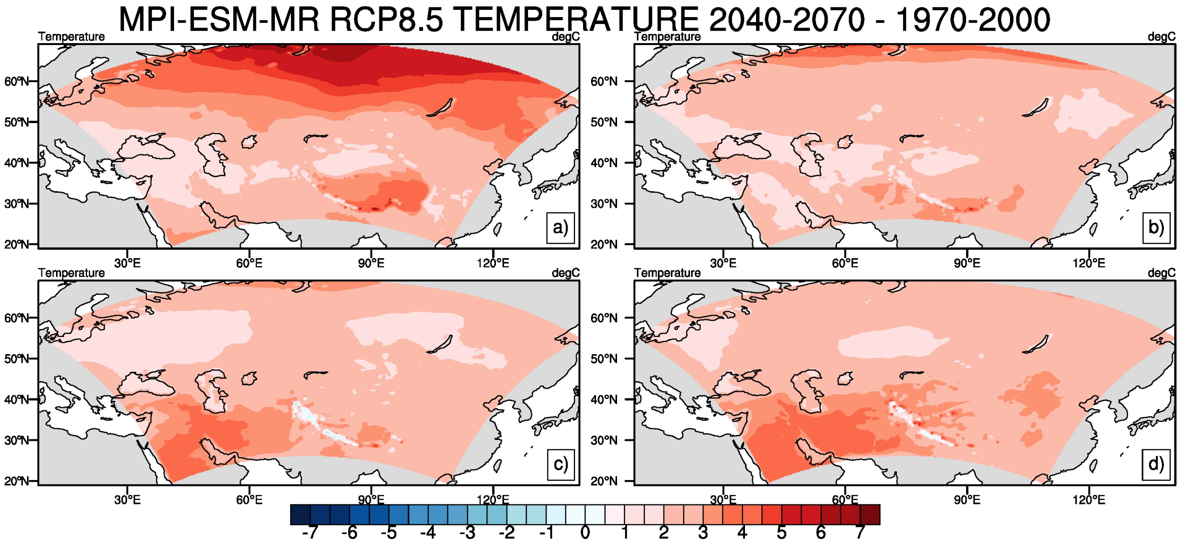

Figure 6.26. As in the Figure 6.25, but for the period 2040 - 2070.

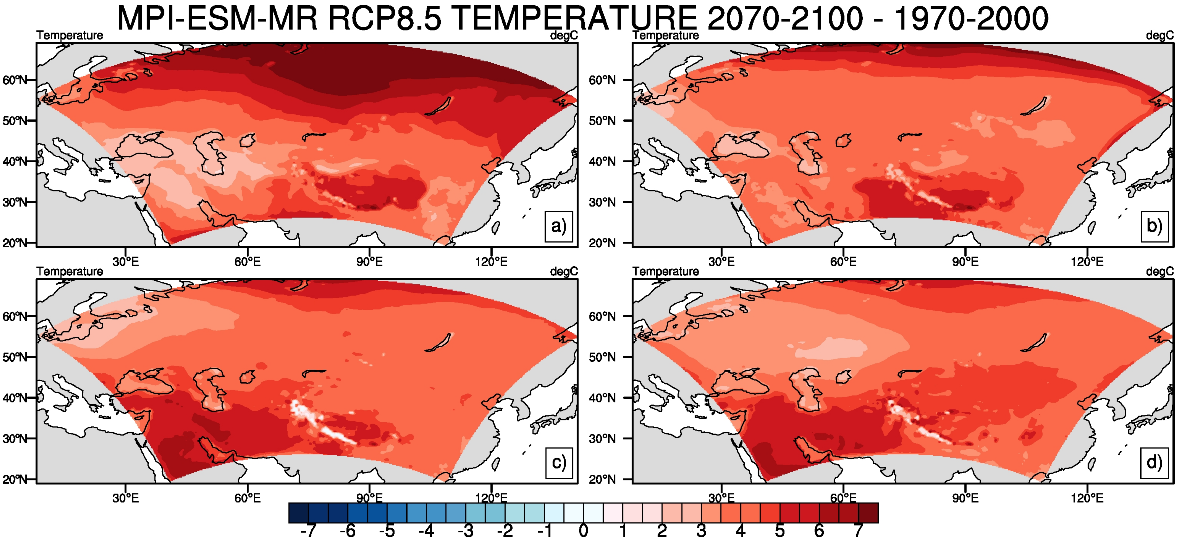

Figure 6.27. As in the Figure 6.25, but for the period 2070 - 2100.

domain.

We simulated future air temperature and precipitation climatology of the Central Asia domain by using regional climate model RegCM versions 4.0 and 4.3.5 with different forcing data. For the future climatology of the domain, the regional model which is forced by different global climate models predicts relatively high warming in the cold season and a decrease in precipitation almost all part of the domain. The large Central Asian region is an area which is extremely vulnerable to climate change. The results of our studies show that surface temperatures in the region will increase from 3°C up to 8°C on average for period of 2070-2100. In the future, a decrease in the amount of precipitation is also expected for the region. Even though we have used the results of different global climate models together with regional climate model run, warming and decrease in precipitation for the domain is projected by all models. Therefore, the projected warming and decrease in precipitation might strongly affect the ecological and socio-economic systems of this region, which is already a mostly arid and semi-arid environment.

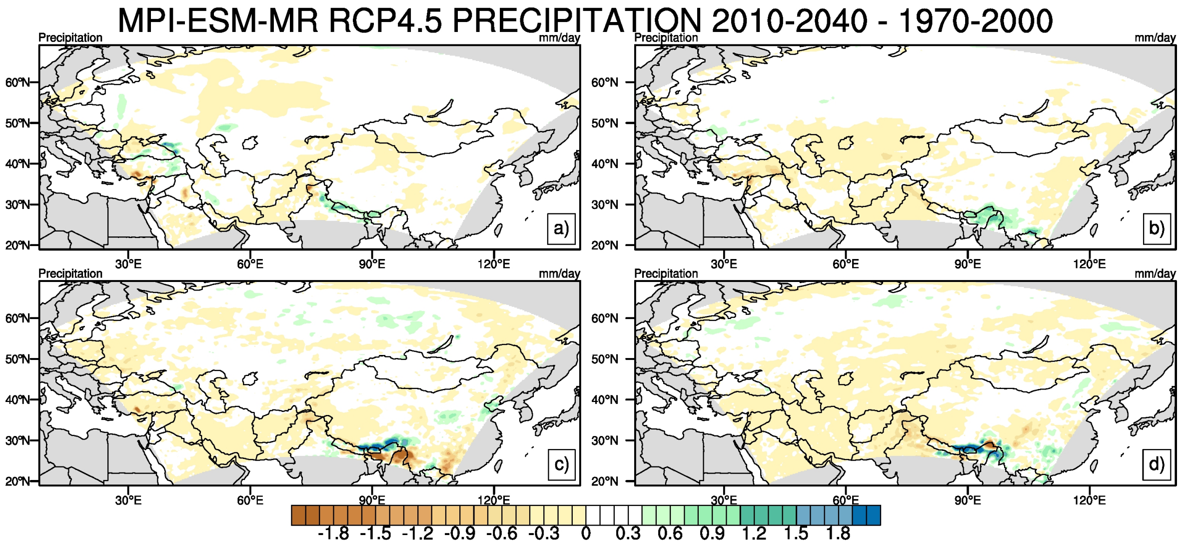

Figure 6.28. As Geographical distribution patterns of changes in projected total precipitation amounts over Central Asia from the regional climate model RegCM4.3.5, which is forced by the global climate model MPI-ESM-MR with RCP4.5 emission scenario for the climatology of 2010 - 2040 future period with respect to the climatology of 1970 - 2000 reference period: (a) winter, (b) spring, (c) summer and (d) autumn seasons.

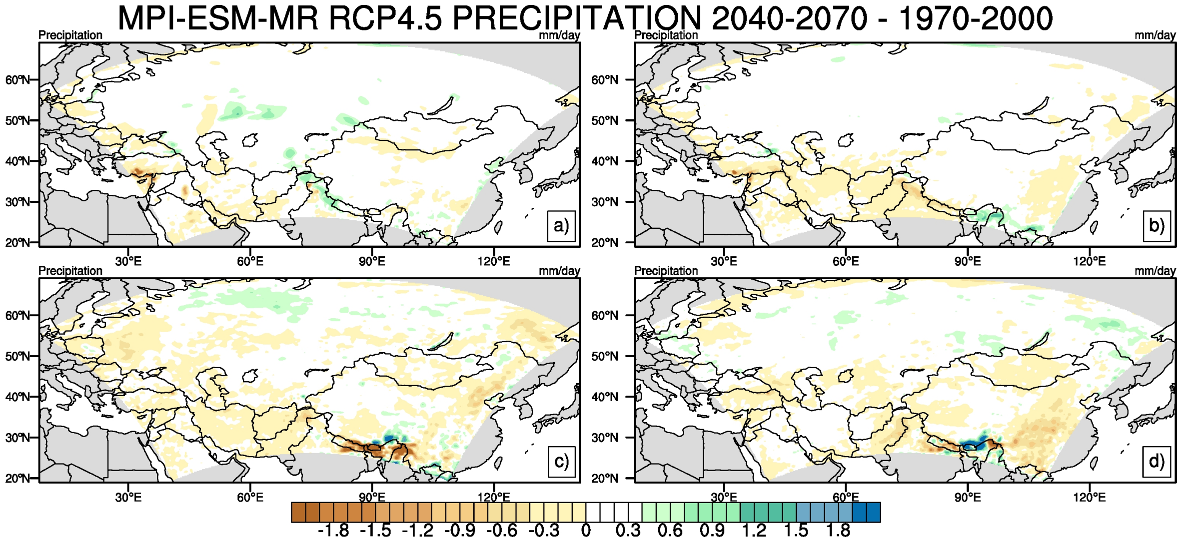

Figure 6.29. As in the Figure 6.28, but for the period 2040 - 2070.

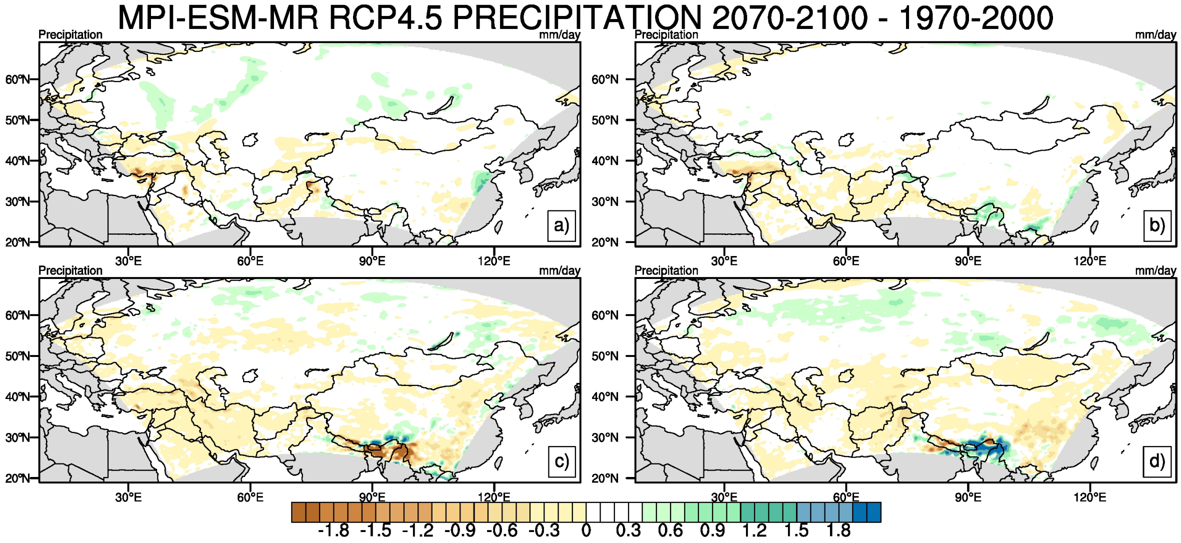

Figure 6.30. As in the Figure 6.28, but for the period 2070 - 2100.

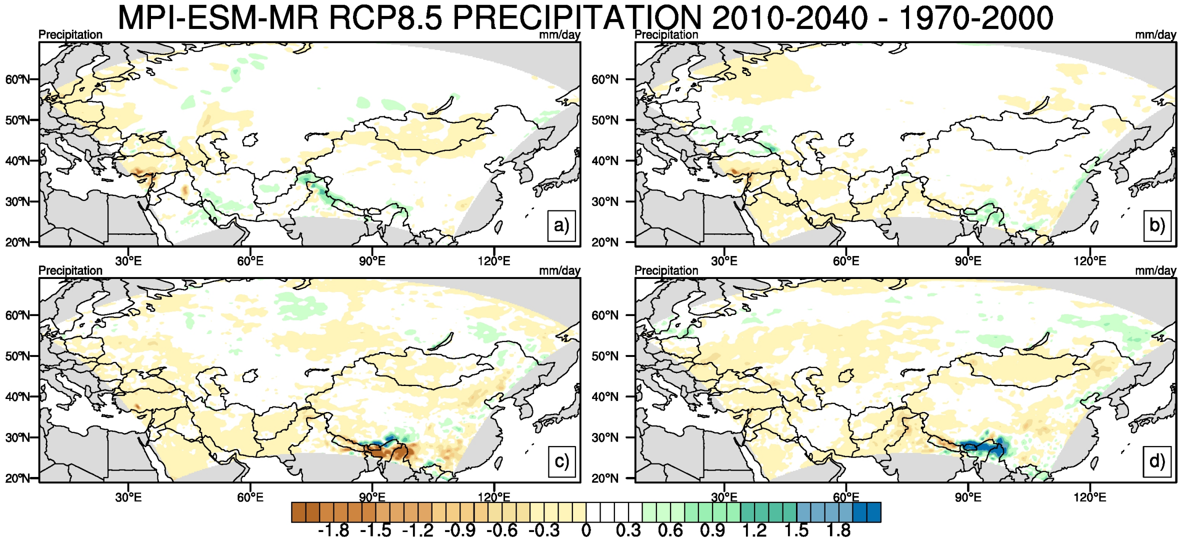

Figure 6.31. Geographical distribution patterns of changes in projected total precipitation amounts over Central Asia from the regional climate model RegCM4.3.5, which is forced by the global climate model MPI-ESM-MR with RCP8.5 emission scenario for the climatology of 2010 - 2040 future period with respect to the climatology of 1970 - 2000 reference period: (a) winter, (b) spring, (c) summer and (d) autumn seasons.

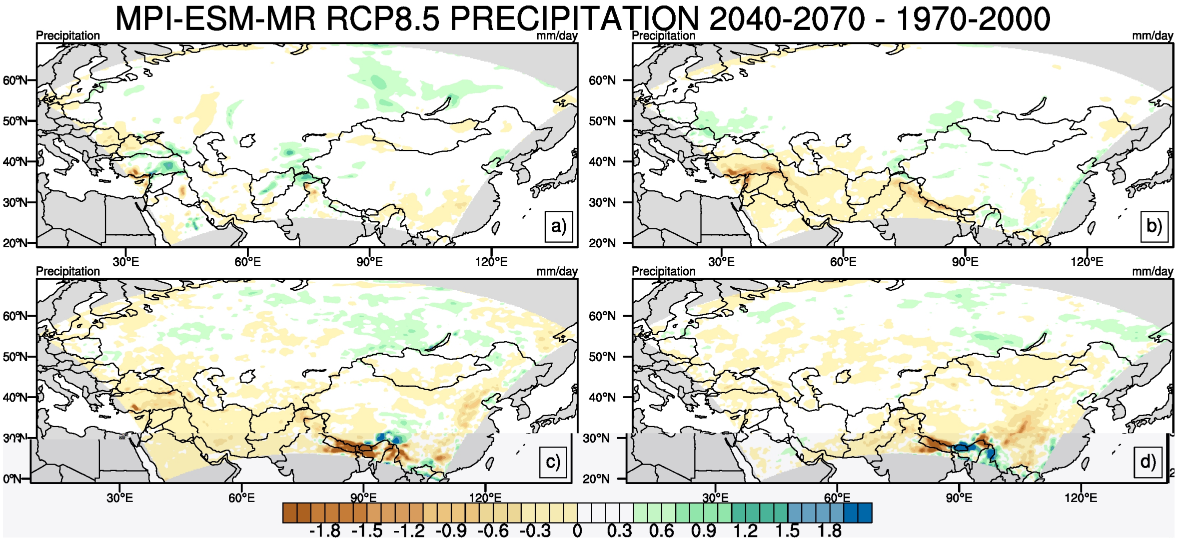

Figure 6.32. As in the Figure 6.31, but for the period 2040 - 2070.

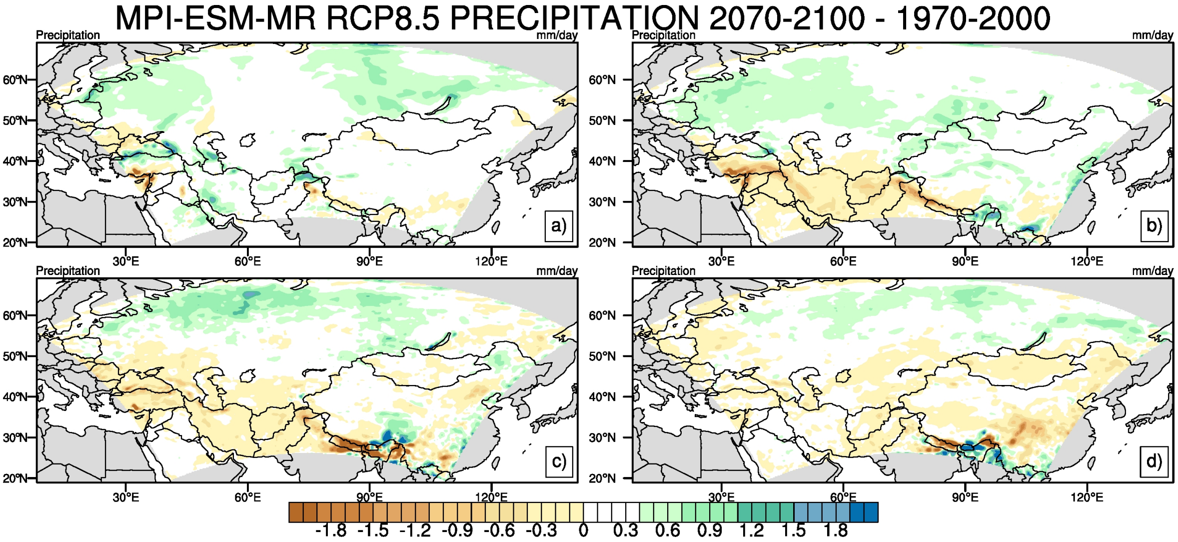

Figure 6.33. As in the Figure 6.31, but for the period 2070 - 2100.

7. PROJECTIONS OF FUTURE AIR TEMPERATURE AND PRECIPITATION CLIMATOLOGY AND VARIABILITY IN THE MEDITERRANEAN BASIN

7.1. Mediterranean Climate and Literature Review

Dry summer subtropical Mediterranean climates can be found along the west coasts of the continents between about 25° and 40° latitude [3]. The Mediterranean macro climate mainly results from the seasonal alternation between mid-latitude (frontal) cyclones, associated with polar air masses, during the winter and subtropical high pressure systems, from subsiding maritime and continental tropical air masses during the summer. The major characteristic of the Mediterranean climate is of high temporal variability varying from seasonal and inter-annual to centennial scales because it extends in a transition region between temperate and cold mid-latitudes and tropics (i.e. subtropical zone); it has been facing significant circulation (associated pressure and wind systems characterizing mid-latitude and tropical/monsoonal weather and climate, respectively) changes between winter and summer. It is closely associated with several atmospheric oscillation and/or teleconnection patterns during the year also varying depends on seasons, such as North Atlantic Oscillation (NAO), Arctic Oscillation (AO), Med. Oscillation (MO), El Niño-Southern Oscillation (ENSO), and North Sea – Caspian Pattern (NCP), etc. [170–177].

Mediterranean climate has major influences from sea and land distribution and the interactions between sea and lands, in addition to the ocean-atmosphere interaction, during the year particularly in the ‘true’ or ‘actual’ Mediterranean macro climate region. On the other hand, climate variables are also changing such as precipitation amounts and variability, snow and ice cover patterns and mean sea level. Precipitation is highly variable spatially and temporally, and precipitation data are limited in some regions. Significantly decreased precipitation amounts (drying) were observed particularly in the Sahel and the Mediterranean Basin including Turkey [20,36,173,178–194].

Substantial increases in heavy precipitation events have also been observed.

Therefore, the larger Mediterranean Basin is very important and among the most responsive regions to global climate change. There were many studies consisting of ensembles of global [195–204] and regional [205, 206] climate model simulations including the Mediterranean Basin. Regional climate change projections over the Europe, including totally or partially the Mediterranean Basin were presented by several studies [14, 83, 124, 127, 130, 206–221].

There have been many experiments consisting of global and regional climate projections for all parts of the world. Kripalani *et al.* (2007) [202] examined the South Asian summer monsoon precipitation and its variability. They used the outputs of the 22 global climate models and found significant changes in mean monsoon precipitation with an 8 % increase, and a possible extension of the monsoon period. Sheffield and Wood (2008) [203] analysed changes in drought occurrence for the SRES B1, A1B and A2 future climate scenarios relative to the reference period by using eight AOGCMs, where the models show decreases in soil moisture globally for all scenarios and long-term droughts becoming three times more common. A regional analysis is carried out of 18 AOGCM simulations of 21st century climate under the IPCC A2 emission scenario to assess regional changes in temperature and precipitation inter-annual variability by Giorgi and Bi (2005a) [199]. According to their studies, inter-annual variability of air temperatures has decreased in the Northern Hemisphere (NH) mid-latitudes in winter and increased in mid-latitude summer season and tropical cases, whereas inter-annual variability of precipitation amounts has increased in most cases. Giorgi (2006) [204] calculated the Regional Climate Change Index (RCCI) for 26 land regions from 20 global climate models for the A1B, A2 and B1 IPCC emission scenarios, and found that the Mediterranean and North Eastern European regions emerges as the primary hot-spots. Lelieveld *et al.* (2012) [201] suggested a relatively strong warming of about 3.5–7°C between the 1961–1990 reference period and the future period 2070–2099 by performing simulations using the PRECIS (Providing Regional Climates for Impact Studies) regional climate model, based on the United Kingdom (UK) Meteorological Office Hadley Centre HadRM3P model and the IPCC SRES scenario A1B. They found that daytime maximum temperatures appeared to increase most rapidly in the Balkan Peninsula and Turkey. Hot summer conditions that rarely occurred in the reference period may become normal by the middle and end of the 21st century. According to their study, annual precipitation totals were expected to decrease in the southern Europe and Turkey regions and the Levant, whereas in the Arabian Gulf area it may increase. There are also some studies performing simulation by using one regional climate model [213, 217, 219]. Multi-model ensemble simulations results showed that the Mediterranean Basin will be affected most by severe climate conditions. Gao and Giorgi (2008) [127] analysed the changes in all three aridity measures. They found that by the end of the 21st century the Mediterranean region might experience a substantial increase in the northward extension of dry and arid lands. Particularly the central and southern portions of the Iberian peninsula, and Italian, Hellenic and Anatolia peninsulas and areas of south-eastern Europe (e.g. Romania and Bulgaria), the Middle East, northern Africa and major Islands (Corsica, Sardinia and Sicily) will be affected due to a large warming and pronounced decrease in precipitation, especially during the spring and summer seasons. Beniston *et al.* (2007) [218] projected that by the end of the twenty first century, countries in Central Europe will experience the same number of hot days as they are currently experiencing in southern Europe. The intensity of extreme temperatures increases more rapidly than the intensity of more moderate temperatures over the continental interior. Heavy winter precipitation increases in Central and Northern Europe and decreases in the south and heavy summer precipitation increases in north-eastern Europe and decreases in the south. Christensen and Christensen (2003) [212] found an increase in the amount of precipitation that exceeds the 95th percentile in many areas of Europe, despite a possible reduction in average summer precipitation over a substantial part of the continent. Giorgi and Lionello (2008) [195] projected a pronounced decrease in precipitation amounts, especially in the summer season, except for some northern Mediterranean regions (e.g. the Alps) in winter, a pronounced warming, which is the biggest in the summer season, and increase in inter-annual variability especially in summer based on the ensembles of global and regional climate change simulations.

In this study, we investigated the projected future changes and variability in annual and seasonal averages of the surface mean air temperatures and total precipitation amounts for the Mediterranean macroclimate region, by using 16 global models with three emission scenarios. The study region covers the Mediterranean Basin as a whole from the North Atlantic to Syria and from the North Africa to the South Europe including Turkey and the Black Sea Basin. Projected future changes include the period of 2070-2100 in comparison with present climate (1970 to 2000), which have been estimated by 16 global climate model outputs from the WCRP‘s Coupled Model Intercomparison Project Phase 3 (CMIP3) multi-model dataset [222] with three different emission scenarios of the Intergovernmental Panel on Climate Change [32], including A2, A1B and B1. 16 global climate models were downscaled to 50 km resolution by using the bias-correction and spatial downscaling method [223]. Although there are many studies of global climate model ensembles [195,199,200,204,213], they are not in such a high resolution of 50 km since the resolution of global model simulations varies in the range of 100-500 km. Ensemble means of global model data provides us robustness of results and allows a much better assessment of climate change projections. It enables us to address the issues regarding uncertainty due to model configuration. In order to assess the trends across models, we presented the ensemble mean and intermodel standard deviation of the 21st century trends in mean and variability changes. We investigated the result of a wide range of global climate models to produce climate change projections over the Mediterranean region.

7.2. Experiments and datasets

We used 16 global climate model outputs for temperature and precipitation from the World Climate Research Program’s (WCRP’s) Coupled Model Intercomparison Project Phase 3 (CMIP3) multi-model dataset [222]. The global data with Intergovernmental Panel on Climate Change (IPCC) emission scenarios of A2, A1B and B1 [32] for temperature and precipitation, and downscaled as described by Maurer *et al.*, 2009 [224] using the bias-correction and spatial downscaling method [223]. They have a 0.5 degree grid resolution and are based on the 1950-1999 gridded observations of Adam and Lettenmaier (2003) [225]. Time period of monthly downscaled data is 1950-2099. There are IPCC emission scenario A2 (850 ppm CO_2 concentration by

2100), A1B (700 ppm CO_2 concentration by 2100) and B1 (550 ppm CO_2 concentration by 2100) output of each global model for future analysis [32]. By using global model outputs, we studied future changes (2070-2100) and variability of climate variables of annual seasonal mean surface air temperature and total precipitation for the Mediterranean macro region with respect to present period (1970-2000). Ensemble averages of global model outputs were calculated by first performing the calculations for the individual models and then compute the ensemble average [226]. We compared present day results with observed dataset from the Climatic Research Unit (CRU), which were established in the School of Environmental Sciences (ENV) at the University of East Anglia [19].

7.3. Results

7.3.1. Seasonal temperature and precipitation climatology

We evaluated model performances by comparing ensemble average model outputs with the CRU dataset for the period 1970-2000. Figures 7.1 and 7.2 show temperature and precipitation biases for model ensembles, respectively. We investigated model ensemble biases for four climatological seasons, which are December-January-February (DJF, winter), March-April-May (MAM, spring), June-July-August (JJA, summer) and September-October-November (SON, autumn). Regional averaged bias values are given in Table 7.1. Table 7.1 also shows standard errors in inter-annual variability with respect to CRU dataset.

For temperature, an overall bias of ensemble model average is between -0.8 and 0.8 °C which is less than 1 °C. There is 1.3 °C warm bias in the eastern part of Turkey in the winter season. This can result from the high topography and continental characteristics of that region (Figure 7.1). Ensemble model performance of surface air temperature is reasonable for the Mediterranean Basin. The regional (basin) average temperature biases for all seasons are even less than 0.05 °C 7.1.

For precipitation, ensemble average of model outputs give underestimated results

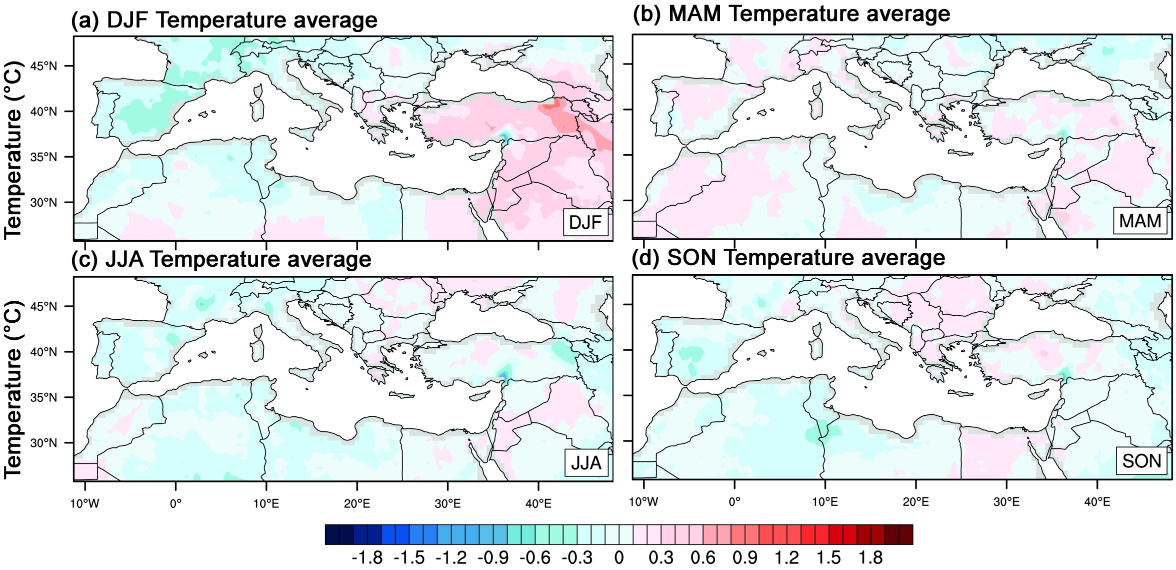

Figure 7.1. Ensemble average surface air temperature biases over the larger Mediterranean Basin for the CMIP3 Global Climate Models (GCMs) with respect to CRU dataset for (a) winter (DJF), (b) spring (MAM), (c) summer (JJA), and (d) autumn (SON).

of 2 mm/day over the Alpine region for all four seasons (Figure 7.2). It is due to the underestimation of the orographic uplift associated with the Alpine mountain chains by models. Coppola and Giorgi (2010) [226] also had similar results in their studies. On the other hand, there is an overestimation of precipitation amounts over northern Iraq in winter, because of high topography of the region. The regional averaged precipitation bias is not more than 0.2 mm/day (Table 7.1).

Table 7.1 also includes the standard errors in inter-annual variability of temperature and precipitation series with respect to the CRU dataset. Biases and future changes in the year-to-year variability (i.e. inter-annual variation) of seasonal total precipitation amounts over Turkey were examined by the coefficient of variation (CV), which was calculated by taking the long-term standard deviation as a percentage of the long-term average of the precipitation series [188]. On the other hand, the year-to-year variability of seasonal average mean air temperatures is expressed by the standard deviation of seasonal values [176].

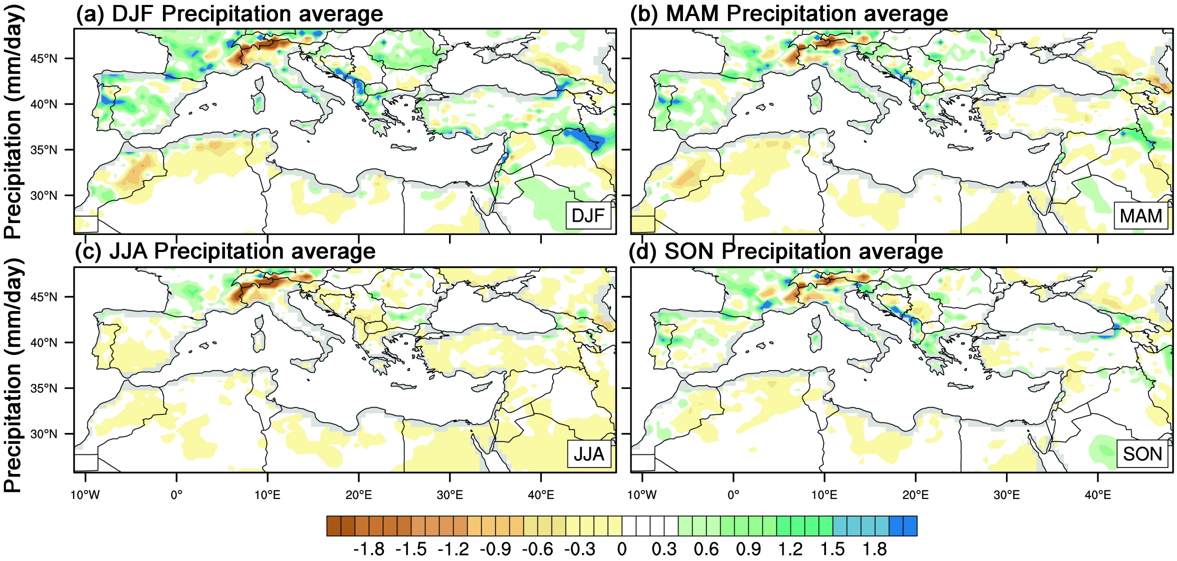

Figure 7.2. As in the Figure 7.1, but for ensemble average precipitation biases for the CMIP3 GCMs.

The ensemble average CMIP3 global climate model outputs show an underestimation of year-to-year temperature variability with a maximum of -0.20 °C in summer. Results are similar with year-to-year precipitation variability. Especially in summer, ensemble model outputs underestimate precipitation variability most. Overall performance of model ensemble in reproducing the observed temperature and precipitation variability is reasonable.

Table 7.1. Regional ensemble averages of the seasonal long-term mean (in °C for temperature and mm/day for precipitation) and inter-annual variability biases (in °C for temperature and % for precipitation) for temperature and precipitation series in the CMIP3 GCMs.

Seasons	**T-Mean-bias**	**T-Var-bias**	**P-Mean-bias**	**P-Var-bias**
DJF	0.042704	-0.11607	0.1664	-10.252
MAM	0.046848	-0.1291	0.13683	-7.1584
JJA	-0.043699	-0.20474	0.0052009	-157.7
SON	-0.036367	-0.049012	0.1664	-10.252

Individual model performances are shown in Figures 7.3 and 7.4 for winter, spring, summer and autumn seasons of period 1970-2000. Temperature biases range from -0.15 to 0.35 °C with maximum values in winter (Figure 7.3). For other seasons, model biases are somehow similar. Biases change from -0.05 to 0.35 mm/day for precipitation with small values especially in the summer season (Figure 7.4). Maximum values appeared during the winter season. Almost all CMIP3 models overpredict precipitation amounts with respect to CRU data. Model results of temperature are more consistent than precipitation results of individual models. It is expected that models give wide range of results due to their independency and different resolutions [227].

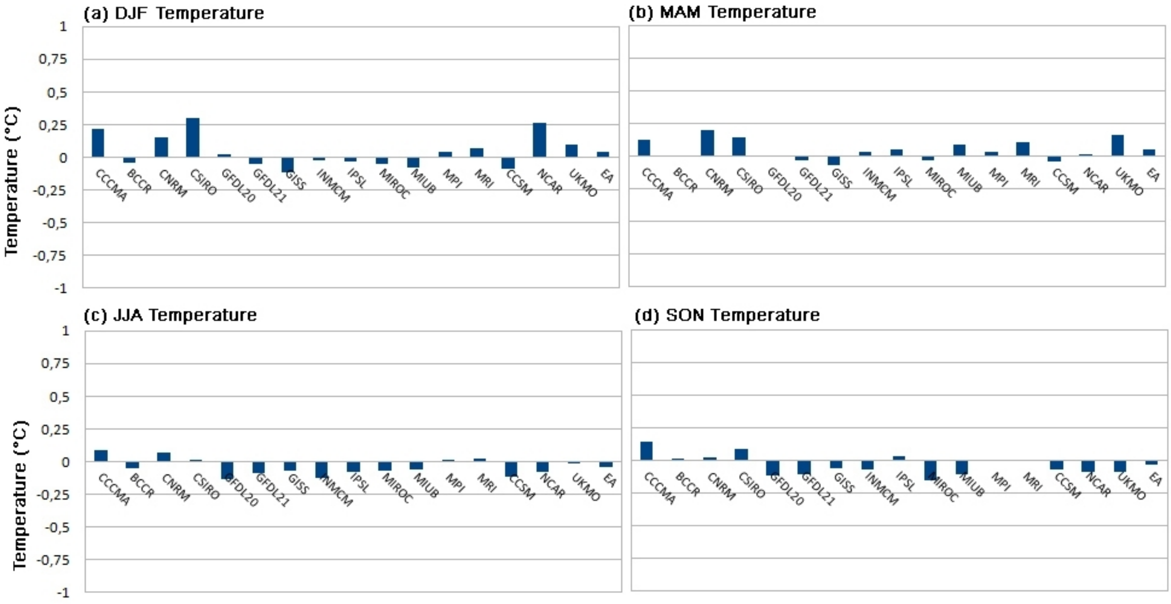

Figure 7.3. Regional averages of the individual Global Climate Model temperature biases for (a) winter, (b) spring, (c) summer, and (d) autumn.

7.4. Projected changes in mean and inter-annual variability

In this section, we presented ensemble averages of temperature change projections for the future period 2070-2100 with respect to the present period 1970-2000 based on the IPCC's A2, A1B and B1 emission scenarios in Figures 7.5, 7.6 and 7.7 respectively. According to all scenarios, surface air temperatures will very likely increase from a minimum of 1.5 to a maximum of 6.5 °C for all part of the Mediterranean region. According to the worst case scenario A2, maximum warming of 6.5 °C is found in Turkey, Morocco, Algeria, southeast Europe and Iberian Peninsula in the summer season. We

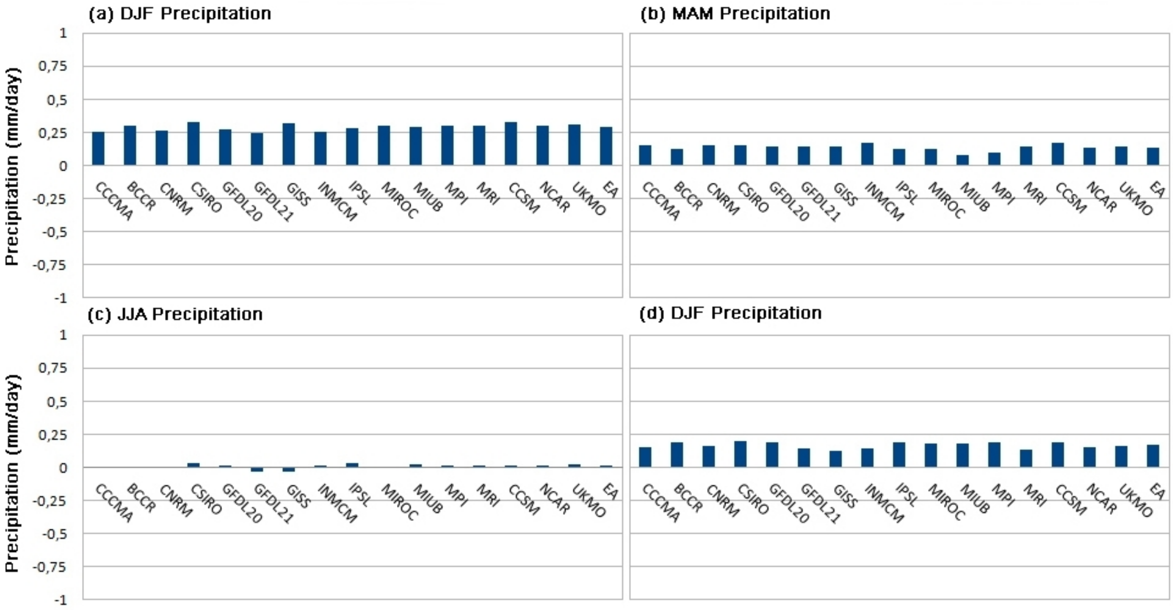

Figure 7.4. As in the Figure 7.3, but for precipitation biases.

observe more warming in North Africa and Central Europe in the winter season. For spring and autumn seasons, average surface air temperatures will very likely increase between 3.5 °C and 5.5 °C (Figure 7.5). Warming or increased temperature pattern is coherent for all scenarios with maximum warming in summer and less warming in winter. According to the best case scenario B1, warming range will be between a minimum 1.5 °C and a maximum 4 °C (Figure 7.7). Maximum temperature increase is again seen in summer same as in other scenario results mainly over the regions including south Balkans, continental central, eastern and south-eastern Turkey, Caucasia and most of Middle East (Figure 7.7).

Figures 7.8, 7.9 and 7.10 show ensemble average precipitation change projections for the 2070-2100 period with respect to 1970-2000 normal according to the worst, A2, middle, A1B and best, B1 case scenarios respectively. There will be a decrease in total precipitation series according to all three scenarios. Precipitation will decrease mostly in the northern part of the Mediterranean region including south Balkans, France, Italy and Caucasia in the summer season. An increase of 0.9 mm/day in precipitation is observed in Switzerland for the winter season. There will be a decrease from a

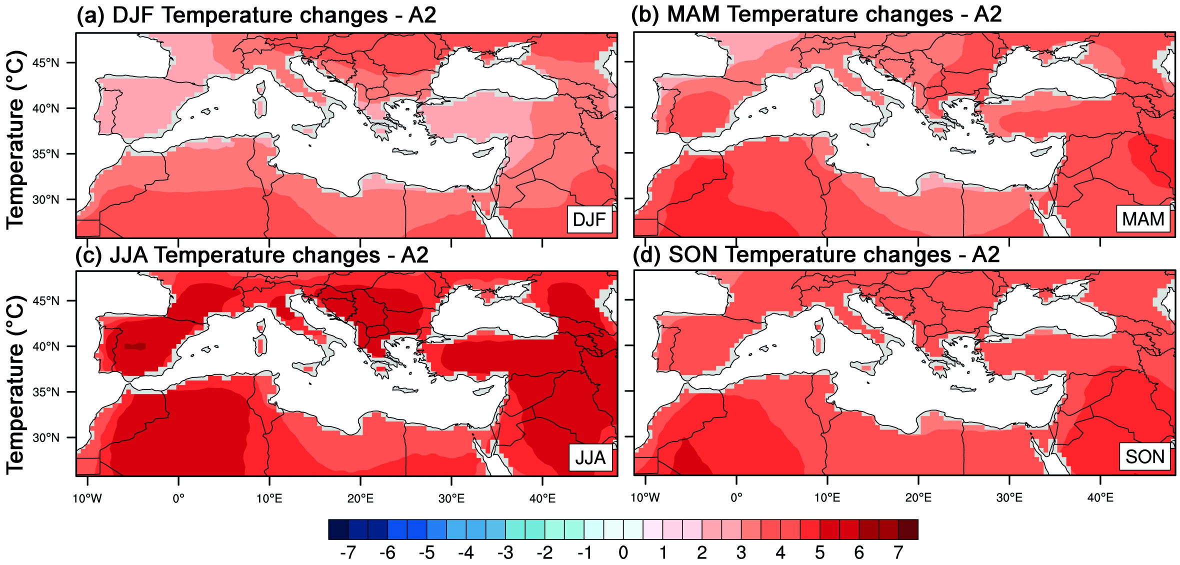

Figure 7.5. Ensemble average surface air temperature changes during the future period of 2070-2100 compared to present period of 1970-2000) based on the A2 scenario for CMIP3 GCMs in (a) winter, (b) spring, (c) summer, and (d) autumn.

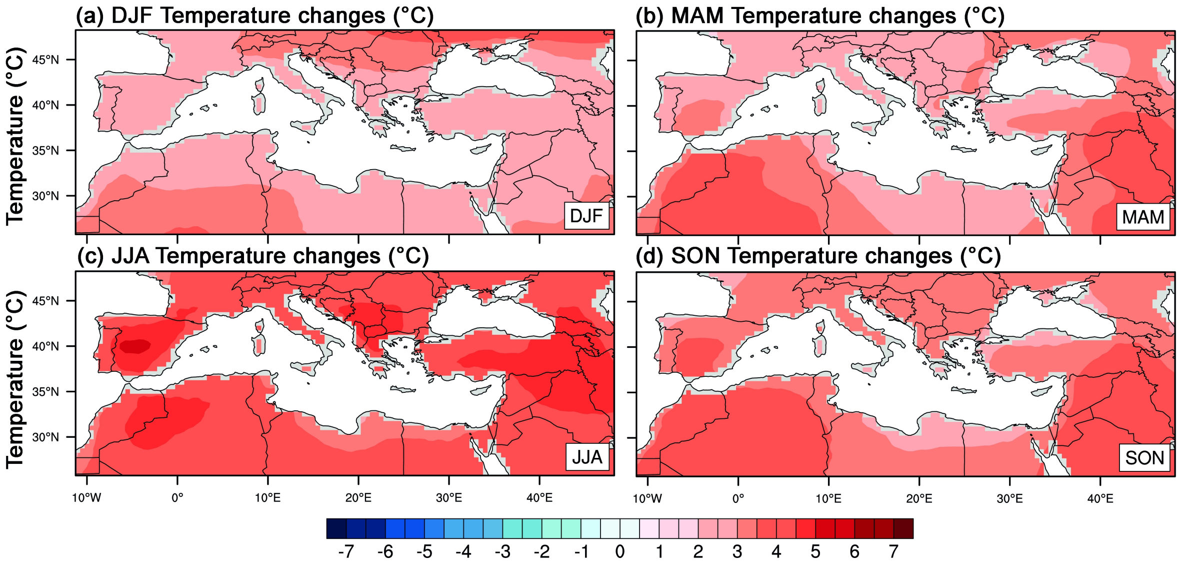

Figure 7.6. As in the Figure 7.5, but for the A1B scenario.

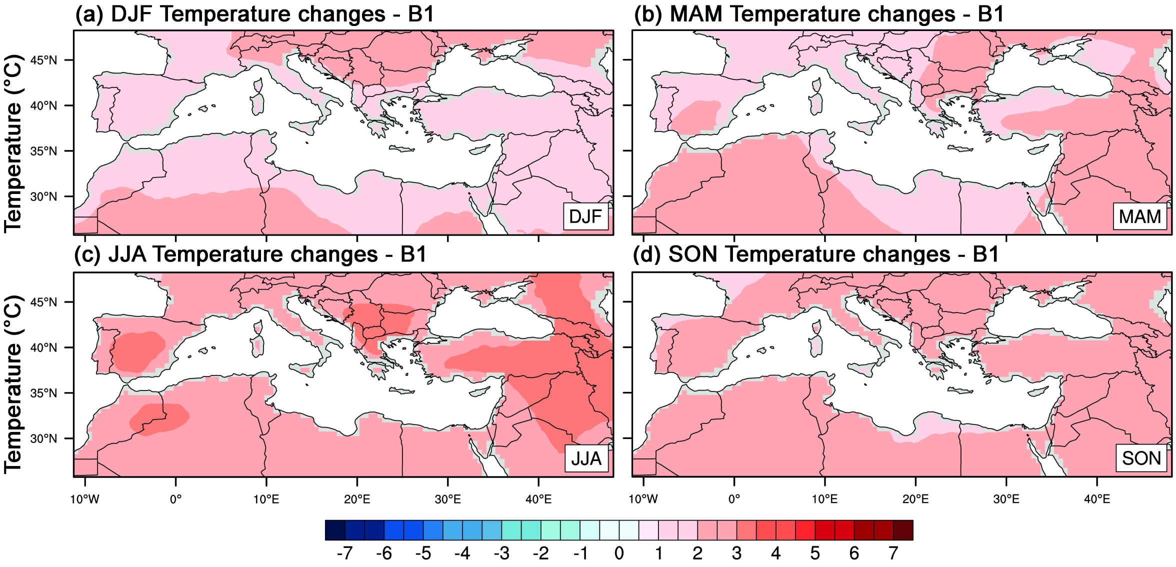

Figure 7.7. As in the Figure 7.5, but for the B1 scenario.

maximum of 1.2 mm/day to a minimum of 0 mm/day. We observe a decreasing trend in continental central region for spring and autumn seasons as well.

Figure 7.11 shows the ensemble average temperature and precipitation change over the Mediterranean Basin for the future period of 2070-2100 with respect to the present period of 1970-2000. Three different scenario (A2, A1B and B1) outputs of models are averaged over the domain for four seasons. Figure 7.6 also includes the corresponding inter-model standard deviations of the changes. It gives the uncertainty in results due to use of different models. Results are consistent among A2, A1B and B1 scenario outputs. Change signal is highest in A2 scenario outputs, and lowest in B1 scenario output for temperature and precipitation. Uncertainty for temperature is much lower than the change itself, indicating that all changes are robust. Percentage of uncertainty with respect to the value of precipitation is greater than temperature; however it is still lower than the change itself.

Figures 7.12, 7.13 and 7.14 show ensemble average changes in inter-annual temperature variability for period 2070-2100 with respect to 1970-2000 normal. Changes are calculated for A2, A1B and B1 scenarios. We observe a decrease in variability in

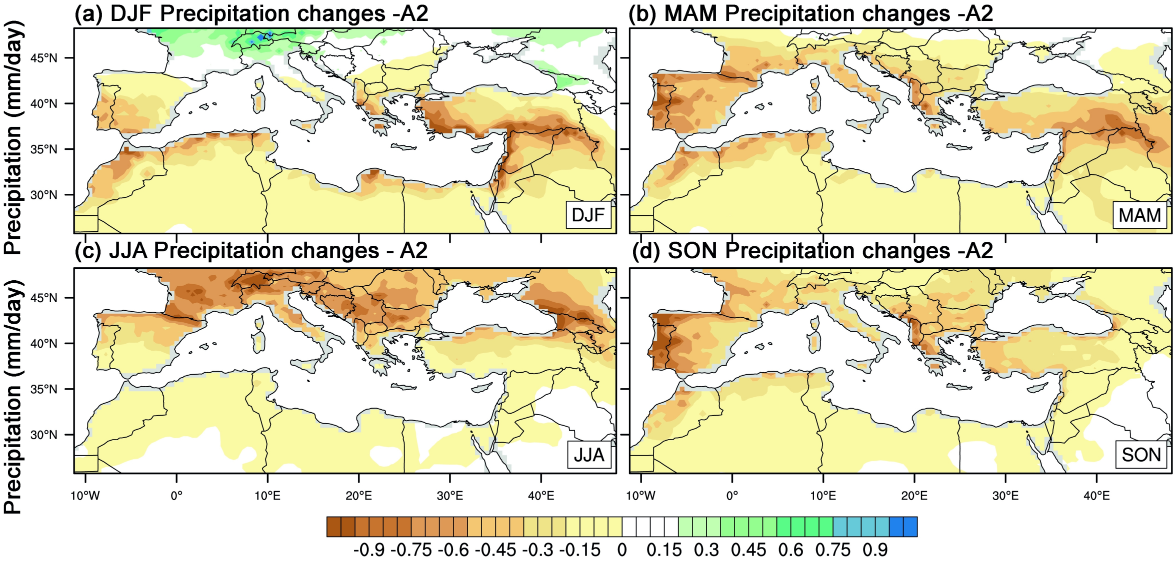

Figure 7.8. As in the Figure 7.5, but for precipitation changes based on the A2 scenario.

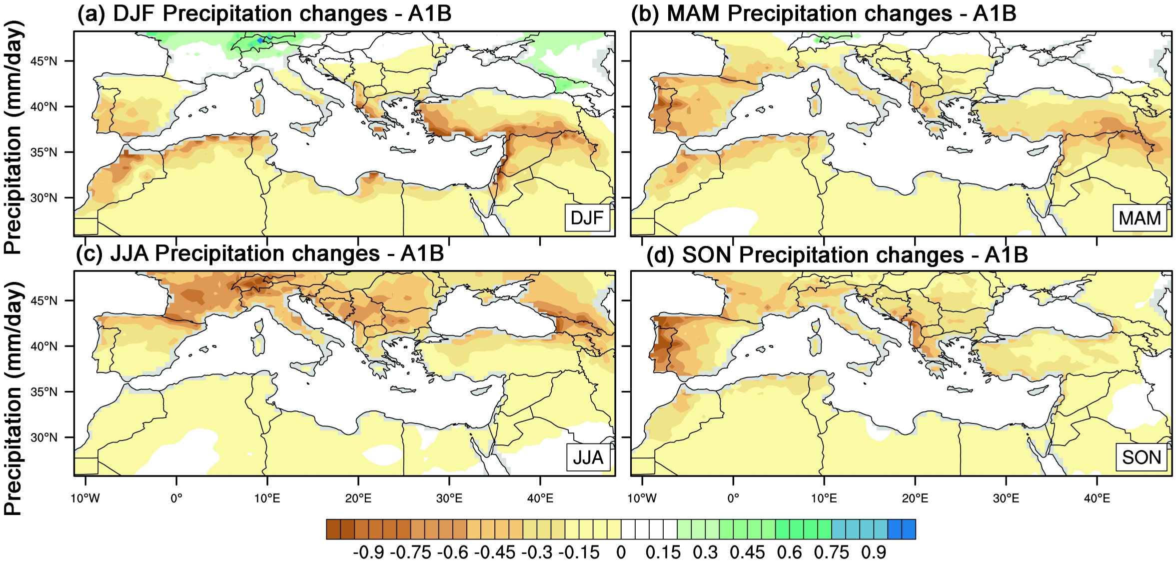

Figure 7.9. As in the Figure 7.5, but for precipitation changes based on the A1B scenario.

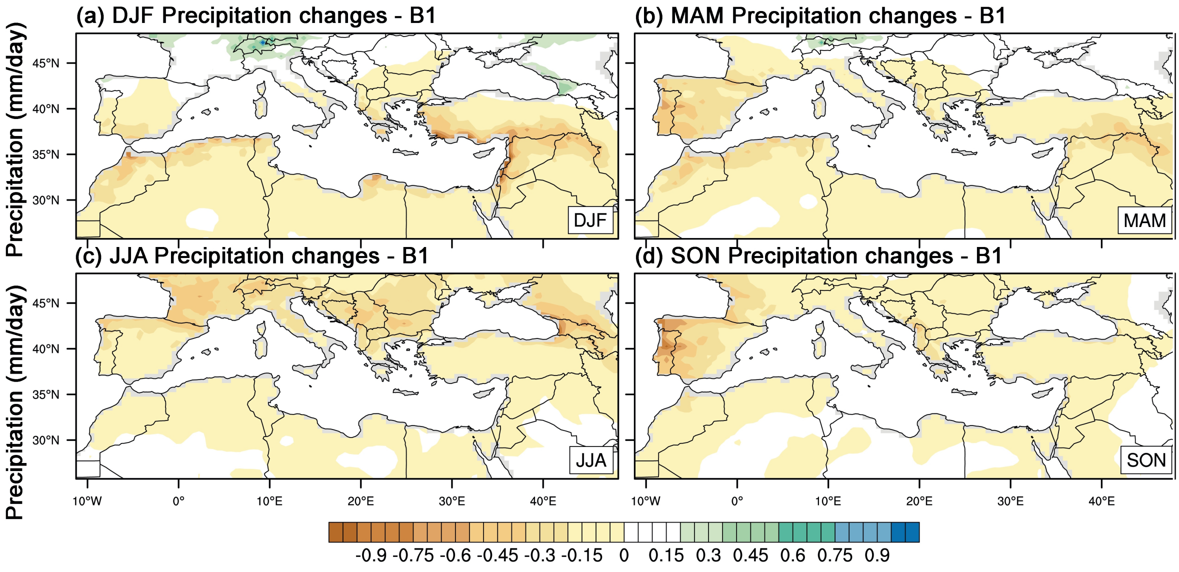

Figure 7.10. As in the Figure 7.5, but for precipitation changes based on the B1 scenario.

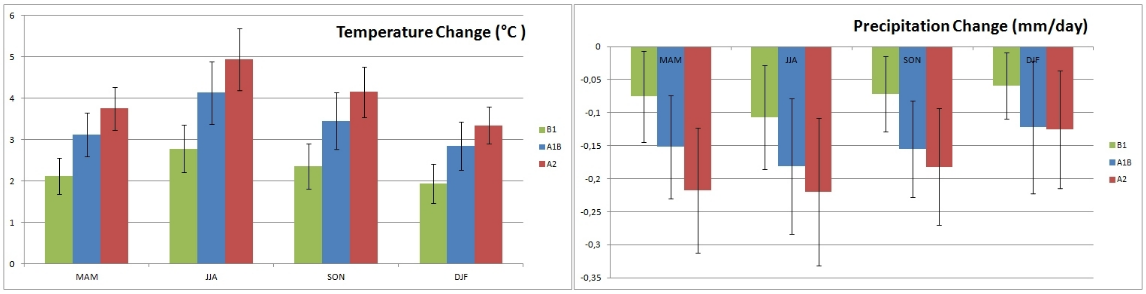

Figure 7.11. Ensemble average (a) surface air temperature (°C) and (b) total precipitation (mm/day) changes for the CMIP3 GCMs over the Mediterranean Basin based on the A2, A1B and B1 scenarios (2070-2100 to 1970-2000) with the corresponding inter-model standard deviations in (a) winter, (b) spring, (c) summer, and (d) autumn.

the northern part of the domain in winter for all three scenarios. On the other hand, temperature variability will increase in summer for all parts of the Mediterranean region according to A2 scenario outputs. For spring and autumn seasons, variability will increase in almost all parts of the domain as well, except for the Black Sea region.

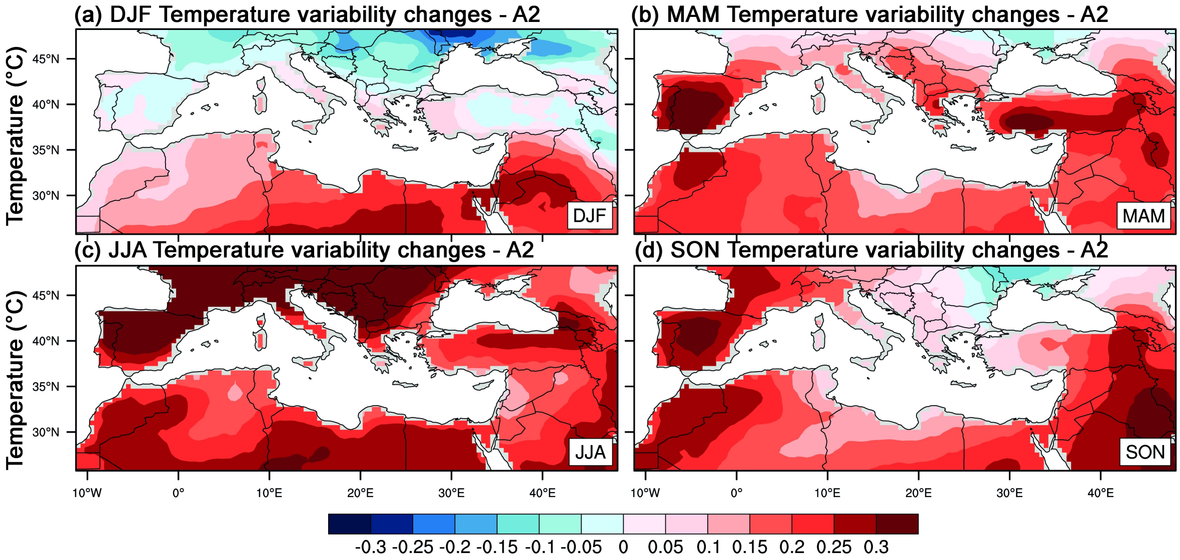
(a) DJF Temperature variability changes - A2

(b) MAM Temperature variability changes - A2

(c) JJA Temperature variability changes - A2

(d) SON Temperature variability changes - A2

Figure 7.12. Ensemble average changes in inter-annual variability of surface air temperature during the future period of 2070-2100 compared to present period of 1970-2000) based on the A2 scenario for CMIP3 GCMs in (a) winter, (b) spring, (c) summer, and (d) autumn.

Ensemble average changes in precipitation inter-annual variability for period 2070-2100 with respect to 1970-2000 normal for A2, A1B and B1 scenarios are shown in Figures 7.15, 7.16 and 7.17. We observe a decrease in the variability in the southeastern part of the domain during the summer season. On the other hand, a strong increase in precipitation variability is projected for A2 scenario output especially in the south part of the region (Figure 7.15). We see similar trends in other scenario (A1B and B1) outputs as well (Figure 7.16, Figure 7.17).

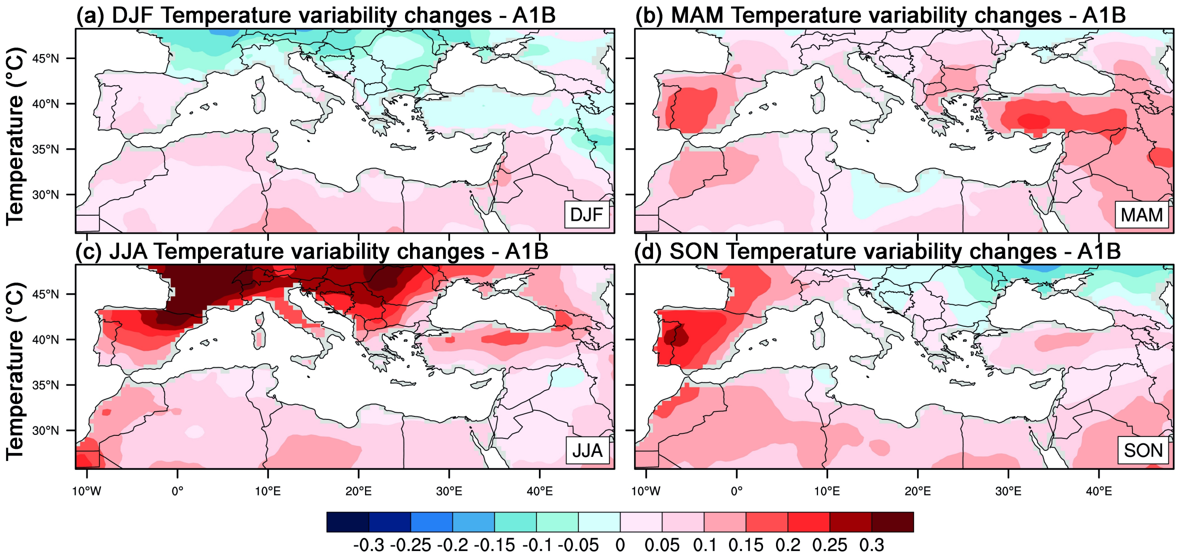

Figure 7.13. As in the Figure 7.12, but for the A1B scenario.

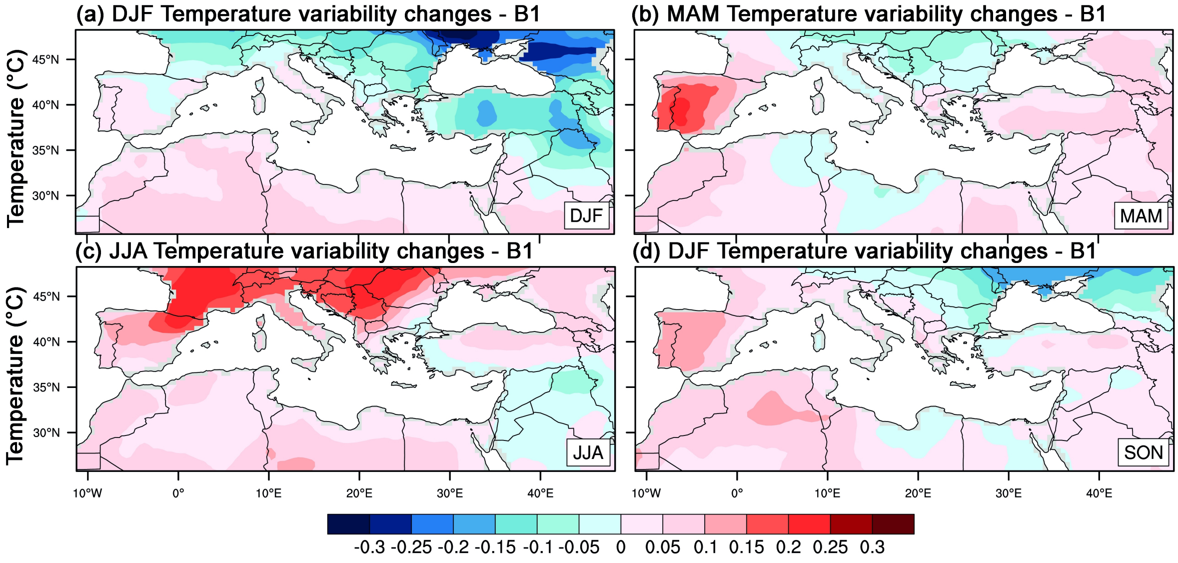

Figure 7.14. As in the Figure 7.12, but for the B1 scenario.

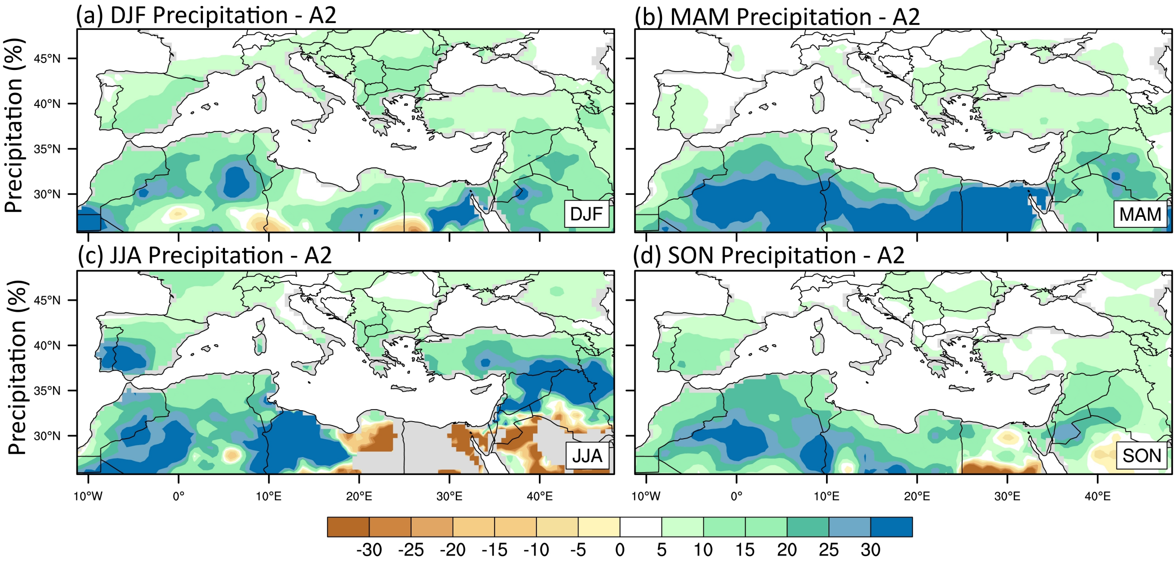

Figure 7.15. As in the Figure 7.12, but for precipitation variability based on the A2 scenario.

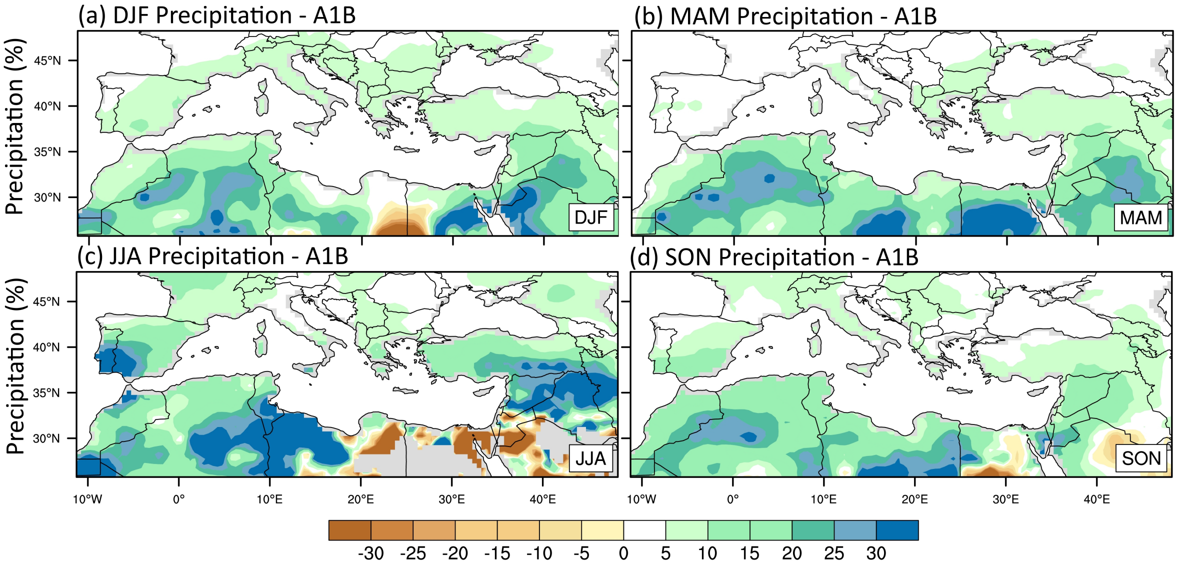

Figure 7.16. As in the Figure 7.12, but for precipitation variability based on the A1B scenario.

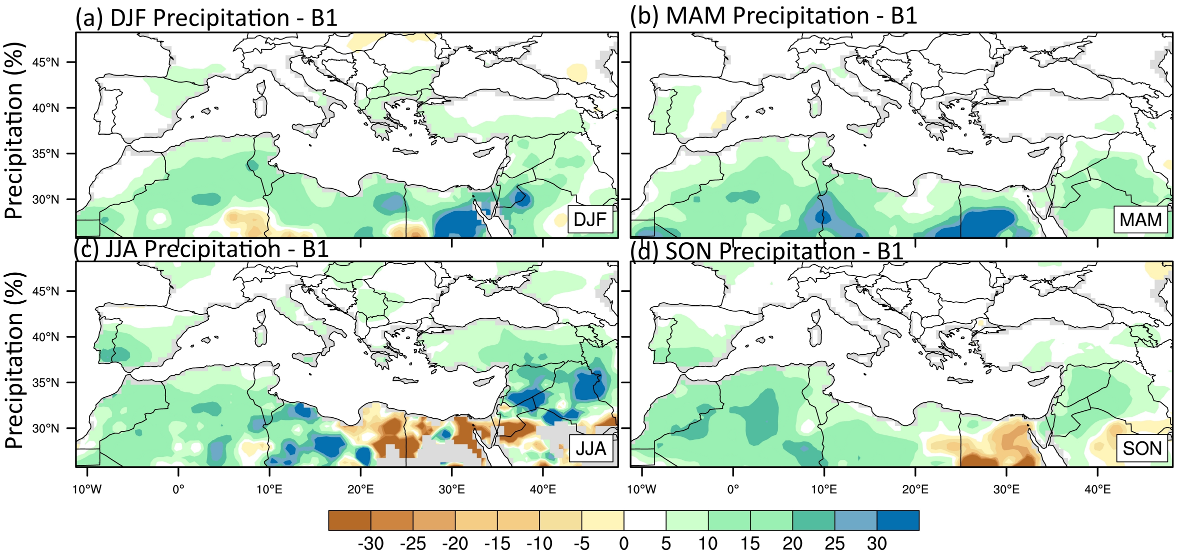

Figure 7.17. As in the Figure 7.12, but for precipitation variability based on the B1 scenario.

7.5. Changes in the distribution of seasonal climate anomalies

We present the probability distribution functions (PDFs) of seasonal temperature and precipitation anomalies for future and past periods in Figures 7.18 and 7.19. We show histograms of yearly individual seasonal anomalies with respect to the ensemble average mean for reference period 1970-2000 for four seasons. Histograms of seasonal anomalies for future period of 2070-2100 with respect to reference period are also shown in the same graphs for all three scenario outputs. We represent seasonal anomalies in the unit of standard deviation (σ). Red, blue and green dashed lines represent A2, A1B and B1 seasonal anomalies respectively. We tested normality distribution of the seasonal temperature and precipitation anomalies by using chi-square normality test. Results show that seasonal temperature anomalies for reference and future scenario outputs are normally distributed except in summer for A2 scenario output. Precipitation anomalies for reference and future periods for all scenario outputs are also normally distributed except in summer for A1B scenario output.

The descriptive statistics of the seasonal temperature and precipitation data are shown in Table 7.2 and Table 7.3 respectively. We observe that skewness and kurtosis values of all data are close to zero indicating that they are normally distributed. Seasonal temperature and precipitation data distributions are approximately symmetric. The change in skewness is mostly positive in scenario outputs and data are skewed right indicating increase in frequency of extreme warm events and high precipitation. The kurtosis values of seasonal distributions decrease in most cases in future periods with respect to reference period indicating that distribution becomes flatter with increase in occurrence of extreme temperature and precipitation. Seasonal temperature and precipitation data indicate persistence at all seasons. This is indicated by the positive Lag 1 autocorrelation coefficients. Persistence of seasonal temperature data is statistically significant at the 0.001 level of significance. Persistence of seasonal precipitation values is mostly statistically significant at the 0.001 level of significance except for the autumn season which is statistically significant at the 0.01 level of significance.

The PDF of the seasonal precipitation anomalies for future and past periods are shown in Figure 7.19. PDFs of reference period are relatively symmetric for all seasons. There will be a decrease in precipitation according to all scenario results mostly in the summer season. Scenario PDFs become flattened and shifted slightly to the left indicating that extreme drying conditions will occur more frequently with respect to the reference period. The statistical significance of equality of variances and means (long-term averages) of seasonal temperature and precipitation values for reference and future periods is checked by the Levene test and Student's t test. By using Levene test, the hypothesis that the two population variances are equal was rejected. The null hypothesis of "equal means assumed" was also rejected by using Student's t test. Results indicated that long-term averages and variances of seasonal temperature and precipitation series will change significantly in future periods with respect to the reference period.

7.6. Discussion

In the present study, we analyzed the future climate change projections of mean air temperature and precipitation climatology and variability over the Mediterranean region by using ensemble global climate model outputs. A2, A1B and B1 scenario out-

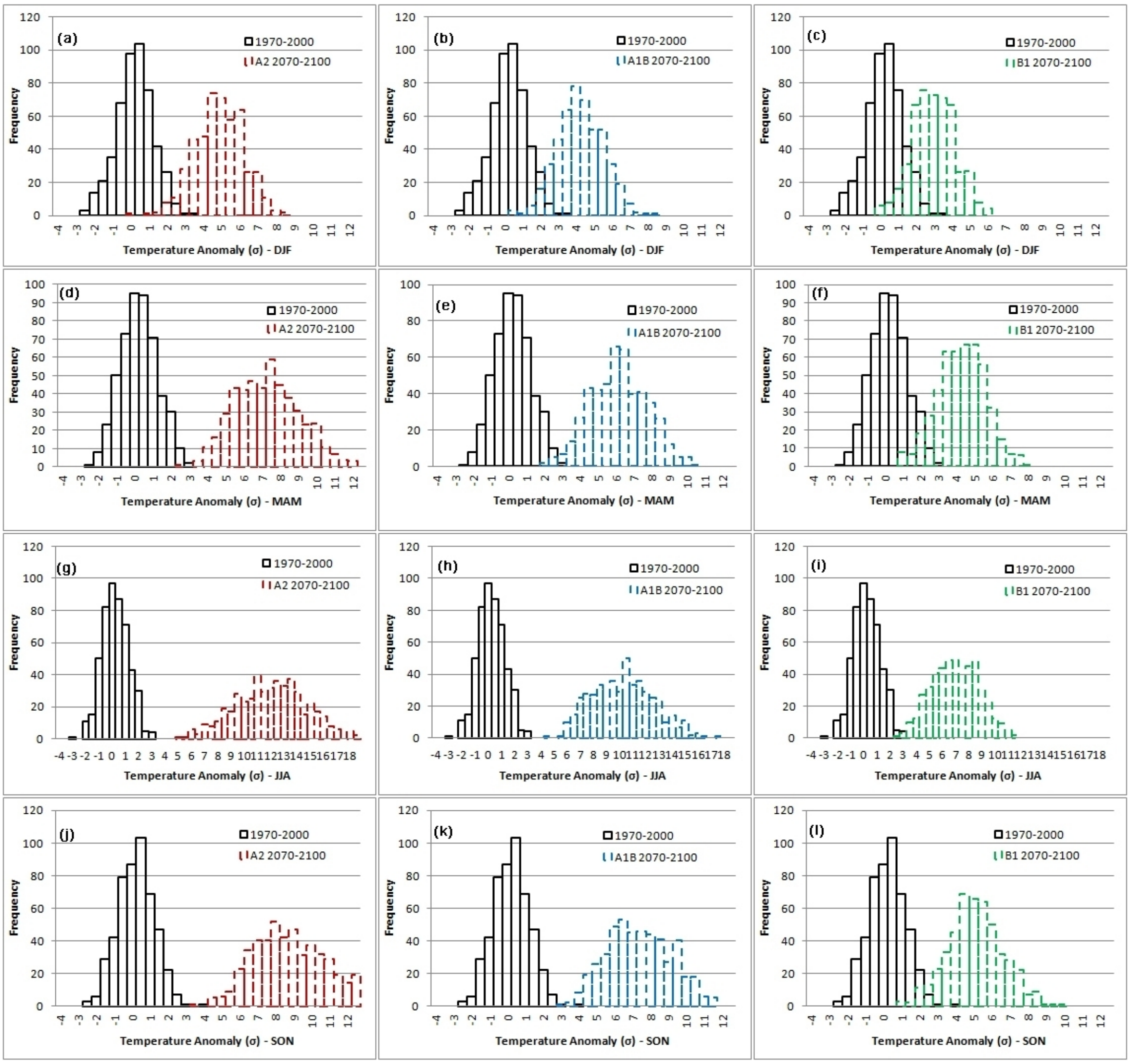

Figure 7.18. Statistical distribution patterns of seasonal surface air temperature anomalies in the CMIP3 GCMs for 1970-2000 (black line) and 2070-2100 (A2 scenario red dashed line, A1B scenario blue dashed line and B1 scenario green dashed line) period for winter (a, b, c), spring (d, e, f), summer (g, h, i) and autumn (j, k, l). The anomaly values are shown in σ units.

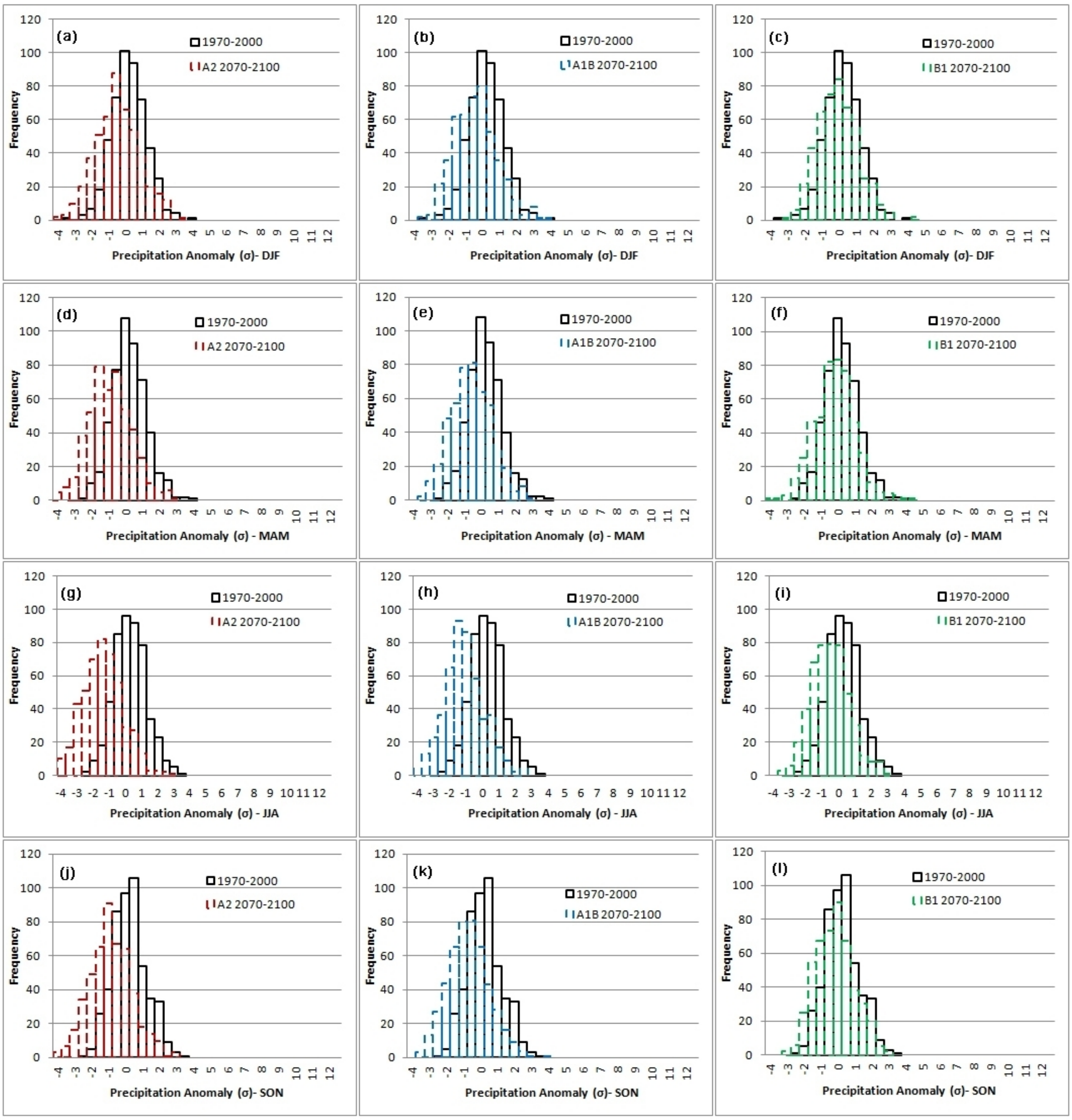

Figure 7.19. As in the Figure 7.18, but for seasonal precipitation anomalies.

puts of 16 global models are used to investigate climate signal for future period of 2070-2100 with respect to reference period of 1970-2000. Ensemble average of global model performance was reasonable in reproducing observed climatology over the domain of the Mediterranean region. Model outputs are in a good agreement with observational CRU dataset.

We analyzed ensemble average future climate change comparing to reference period. Warming trend in ensemble average model outputs for future period with respect to reference period was observed. The magnitude of future climate change signal depends on emission scenarios. Warming is maximum in summer up to 6.5 °C and minimum during the winter season.

Precipitation decreases in all seasons except increase in Switzerland during the winter season according to ensemble average of global climate model outputs, as also found by Pal *et al.* (2004) [124] and Gao *et al.* (2006) [219]. Ensemble average future change signals are generally greater than the inter-model standard deviation which is agreed with previous model experiments [83, 196, 198]. We can consider that future climate change signals are robust. For inter-annual variability change of temperature, there will be an increase in the summer season, whereas decrease for the northern part of our domain in the winter season. Increase in precipitation variability is also observed from the model results for all seasons in the whole domain except for the south-eastern part. These results correspond to an increase in frequency of extreme temperature and precipitation.

Additionally, we have investigated future change of probability distribution functions of seasonal anomalies for temperature and precipitation. Seasonal anomalies for temperature and precipitation are normally distributed according to the normality test. Results show that PDFs of seasonal temperature anomalies of future period is shifted to the right, flattened and asymmetric. It implies an increase in occurrence of extreme weather conditions. The precipitation seasonal anomalies are shifted to the left indicating a decrease in mean precipitation amounts. Therefore, the Mediterranean region will have warmer and dryer weather conditions in the future periods.

The AR5 of the IPCC [1] also stated that areas with abundant atmospheric moisture availability and high present-day temperatures such as Mediterranean coastal regions are expected to experience the greatest heat stress changes, because the heat stress response scales with humidity, which thus will become increasingly important to heat stress at higher temperatures. The large-scale drying in the Mediterranean Basin, southwest USA, and southern Africa appear across generations of projections and climate models and is deemed likely as global temperatures rise and will increase the risk of agricultural drought. Therefore, the Mediterranean Basin is a large region that is most vulnerable to climate change. The projected warming and decrease in precipitation for the domain might strongly affect the ecological and socio-economic systems of the region, which has already been characterized mostly with a semi-arid and dry sub-humid or semi-humid environment.

Table 7.2. Comparable representation of the descriptive statistics of minima (Min, in °C), maxima (Max in °C), long-term averages (Av in °C), standard errors of the long-term averages (SEAv in °C), standard deviations (StD in °C) and coefficients of variation (CV in per cent), and values of the skewness (Skew) and kurtosis (Kur) and the lag-one autocorrelation coefficients (RL) for the year-monthly temperature.

Parameter	**N**	**Min**	**Max**	**Av**	**SEAv**	**Skew**	**Kur**	**StD**	**CV**	**RL1**
MAMT	496	14.094	16.729	15.409	0.023	0.094	-0.359	0.519	3.369	0.000
MAMA2T	480	16.477	21.624	19.068	0.042	0.175	-0.390	0.922	4.834	0.569
MAMB1T	480	15.689	19.505	17.510	0.031	-0.063	-0.127	0.684	3.907	0.439
MAMA1BT	480	16.256	20.782	18.481	0.038	0.056	-0.387	0.827	4.475	0.519
JJAT	496	23.963	26.368	25.217	0.018	0.115	-0.215	0.407	1.615	0.201
JJAA2T	480	27.192	32.902	30.006	0.050	-0.012	-0.407	1.087	3.621	0.805
JJAB1T	480	26.131	29.897	27.961	0.033	0.041	-0.519	0.728	2.605	0.714
JJAA1BT	480	26.977	32.139	29.287	0.043	0.212	-0.476	0.949	3.240	0.789
SONT	496	15.660	18.802	17.084	0.021	-0.064	0.015	0.477	2.792	0.200
SONA2T	480	18.703	23.498	21.128	0.042	0.158	-0.539	0.919	4.351	0.698
SONB1T	480	17.465	21.662	19.395	0.033	0.094	0.021	0.721	3.719	0.603
SONA1BT	480	18.282	22.543	20.486	0.038	0.121	-0.634	0.836	4.079	0.671
DJFT	496	4.839	8.974	6.856	0.031	-0.175	0.092	0.697	10.173	0.190
DJFA2T	480	6.793	12.606	10.100	0.042	-0.163	0.020	0.919	9.100	0.427
DJFB1T	480	6.606	11.023	8.778	0.037	-0.036	-0.150	0.816	9.293	0.365
DJFA1BT	480	6.992	12.439	9.651	0.041	0.035	-0.070	0.897	9.294	0.387

Table 7.3. Comparable representation of the descriptive statistics of minima (Min, in °C), maxima (Max in °C), long-term averages (Av in °C), standard errors of the long-term averages (SEAv in °C), standard deviations (StD in °C) and coefficients of variation (CV in per cent), and values of the skewness (Skew) and kurtosis (Kur) and the lag-one autocorrelation coefficients (RL) for the year-monthly precipitation.

Parameter	**N**	**Min**	**Max**	**Av**	**SEAv**	**Skew**	**Kur**	**StD**	**CV**	**RL1**
MAMP	496	0.820	1.950	1.306	0.008	0.306	0.458	0.175	13.366	0.000
MAMA2P	480	0.460	1.760	1.107	0.010	0.200	0.059	0.219	19.770	0.208
MAMB1P	480	0.580	2.030	1.238	0.010	0.246	0.685	0.211	17.013	0.152
MAMA1BP	480	0.610	1.760	1.161	0.010	0.242	-0.037	0.210	18.084	0.134
JJAP	496	0.470	1.280	0.843	0.006	0.185	0.020	0.136	16.068	0.027
JJAA2P	480	0.180	1.240	0.619	0.008	0.291	0.330	0.167	27.047	0.461
JJAB1P	480	0.330	1.180	0.734	0.007	0.265	0.101	0.154	20.955	0.185
JJAA1BP	480	0.260	1.140	0.658	0.007	0.320	0.064	0.162	24.573	0.378
SONP	496	0.820	1.840	1.260	0.008	0.218	-0.079	0.173	13.740	0.026
SONA2P	480	0.410	1.740	1.072	0.010	0.179	0.219	0.214	19.915	0.096
SONB1P	480	0.670	1.710	1.186	0.009	0.132	-0.377	0.193	16.257	0.065
SONA1BP	480	0.600	1.880	1.102	0.010	0.306	0.174	0.209	18.937	0.023
DJFP	496	0.8309	2.210	1.514	0.009	0.070	0.332	0.192	12.652	0.057
DJFA2P	480	0.650	2.150	1.386	0.011	0.132	-0.095	0.246	17.711	0.153
DJFB1P	480	0.940	2.340	1.459	0.010	0.383	0.362	0.223	15.260	0.114
DJFA1BP	480	0.750	2.260	1.397	0.011	0.403	0.249	0.242	17.297	0.246

8. CONCLUSION

Dealing with clouds is one of the most complex tasks in generating global and regional climate models due to the fact that they cannot be determined by the usual grid size used in climate models, they cannot be in a linear interaction with radiative, dynamical and hydrological processes on a diverse range of timescales; and they play a role as one of the most important mechanisms for the vertical circulation of momentum, sensible and latent heat for the wide scale. There are several cloudiness parameterizations for use in climate models. Xu and Randall [17] proposed a semi-empirical cloudiness parameterization based on the relationships between stratiform cloud fraction and its large-scale predictors. The idea behind that it is better to use the grid-averaged mixing ratio of cloud water and cloud ice to predict stratiform cloudiness than to use grid-averaged relative humidity.

The semi-empirical cloudiness parameterization applied to the regional climate model of the Abdus Salam International Center for Theoretical Physics (ICTP), RegCM, to investigate the effects of new parameterization in ability of simulating the temperature climatology of Central Asia (Region 8 domain in the CORDEX framework) especially northern part of the domain. The results of the regional climate model which is forced by global dataset were compared with the observational (Climate Research Unit) dataset. In the first part of the experiment, we tested the regional climate model's capability to simulate the present climate of the domain. The regional climate model RegCM4.0 was run for the period of 1990 to 2002 by using ERA-interim reanalysis data as the boundary condition, and was run for the period 1970−2000 by using the reanalysis data ERA40 and the global climate model ECHAM5 as the boundary condition. Results showed that regional climate model is not capable of simulating the temperature climatology of the northern part of the domain in the winter season. We observed the strong warm bias over the north and Siberia region of the Central Asia domain in the winter. Therefore, the regional climate model RegCM cannot reduce warm bias inherited from forcing data. As previous findings show that climate models commonly produce excessive wintertime Arctic clouds, particularly at low levels, and it causes a warm bias in winter. We concluded that the relative humidity typed cloudiness parameterization of the regional climate model RegCM is not convenient to use in simulating cold climate.

We adapted the new cloudiness parameterization scheme to the RegCM4.0 code and observed the change. The corrected RegCM4.0 code was run for the period of 1989 to 1994 by using ERA-interim reanalysis dataset and ECHAM5 global dataset as a forcing data. We can observe from the results that the performance of corrected code with new cloud fraction parameterization is much better in the outputs of regional climate model which is forced by ECHAM5 global data than by ERA-interim reanalysis data. The reason behind that could be the stronger warm bias inherited from ERA-interim dataset. The warm bias in the outputs of ECHAM5 global dataset is weaker than that of ERA-interim dataset. Therefore, the regional climate model cannot improve the performance of the forcing data.

The new semi-empirical parameterization was also adapted to the latest stable version of RegCM. The performance of new cloudiness parameterization was tested for the period of 1989 to 1994 by using ERA-interim reanalysis dataset as a forcing data. After upgrading the regional climate model to version 4.3.5, strong cold bias over the northern part of the region were observed instead of warm bias in the winter season. Changing relative humidity typed cloudiness parameterization with the new semi-empirical parameterization made the RegCM4.3.5 better in simulating climate of northern part in the winter. On the other hand, in some parts of the region especially in summer, warm bias arose. We concluded from the results that the new cloudiness parameterization improves the performance of the regional climate model RegCM in simulating the cold climates.

In this thesis, the future temperature and precipitation climatology of the Central Asia were also projected for three future periods of 2010-2040, 2040-2070 and 2070-2100 with respect to reference period of 1970-2000 by using the regional climate model RegCM. According to the results of the projections based on latest emission scenarios of RCP4.5 and RCP8.5, relatively high warming in the cold season and a decrease in precipitation almost all part of the Central Asia domain will be observed for the future periods. Surface temperatures will rise from 3°C up to 8°C on average for the far future period of 2070-2100. With projected warming in surface temperatures and decrease in total precipitation, Central Asia region will be strongly affected by climate change due to its mostly arid and semi-arid characteristics of environment.

The projections of the future mean air temperature and precipitation climatology and variability over the Mediterranean region were done by using A2, A1B and B1 scenario outputs of 16 global models for future period of 2070-2100 with respect to reference period of 1970-2000 as well. According to the ensemble average of global model results, warming will be highest in summer up to 6.5 °C and lowest during the winter season. Precipitation will be lower in all seasons except an increase in Switzerland during the winter season. Future climate change results can be considered as robust since ensemble average future change signals are generally greater than the inter-model standard deviation. Due to the projected increase in the inter-annual variability change of temperature for the summer season and projected increase in precipitation variability for all seasons in the whole domain except for the south-eastern part, there will be an increase in frequency of extreme temperature and precipitation. According to the results projecting future probability distribution functions of seasonal anomalies for temperature and precipitation, there will be a rise in occurrence of extreme events. Consequently, the Mediterranean region will have warmer and dryer climatic conditions in the future periods.

The results given above are of great importance in terms of hydrological systems, water resources, drinking water, forestry and forest fires, and soil moisture, soil organic matter content and agricultural production in the Mediterranean countries including the Northern Africa and Middle East regions and Turkey, and impacts of the global- and regional-scale observed and estimated climate changes in these regions. As a consequence of the increased meteorological droughts, shortages in the water resources and losses in crop yields can also be expected. Even though the amount of decrease in precipitation total is somehow little, since the Mediterranean region is also a mostly semi-humid and semi-arid region with strong and long summer dryness, it will be affected with a little decrease in precipitation total value. While, on the other hand, much of the desertification processes are attributed to poor land uses practices, hotter and drier conditions will probably extend the desertification-prone areas northwards in the Mediterranean basin to encompass areas currently not at risk. In addition, the rate of desertification would increase due to increases in erosion, salinization and forest fire hazard and reductions in soil quality. As a result, the process of desertification is likely to become irreversible. It is likely that the first significant impacts of climate change will be felt in the Mediterranean hydrology and water resources systems including increased frequency of water shortages and droughts and decline in water quality.

As a conclusion, climate change is one of the most challenging problems in the 21st century. It affects the ecological, social and economic systems all around the world seriously. On the other hand, predicting and simulating the future climate becomes a significant task. For this purpose, the ability of climate models in predicting the present climatology is very important. In this context, the introduction of new cloudiness parameterization improves the performance of the regional climate model RegCM over cold climates.

REFERENCES

1. Stocker, T.F., D. Qin, G.-K. Plattner, M. Tignor, S.K. Allen, J. Boschung, A. Nauels, Y. Xia, V. Bex and P.M. Midgley (eds.), *IPCC, Climate Change 2013: The Physical Science Basis, Contribution of Working Group I to the Fifth Assessment Report of the Intergovernmental Panel on Climate Change*, Cambridge University Press, Cambridge, United Kingdom and New York, pp. 1535, 2013.

2. Perelet, R., "Central Asia: Background Paper on Climate Change", *UNDP Human Development Report Office Occasional Paper*, Moscow, 2007.

3. Türkeş, M., *Climatology and Meteorology*, 1st Edition, Kriter Publisher, Istanbul, pp. 650, 2010. (in Turkish)

4. Türkeş, M., "Analysis of The UN Convention to Combat Desertification with respect to The Climate, Climate Change and Drought, and Applications in Turkey", *In: Proc Symp Combating Desertification*, 17–18 June, 2010, Çorum, Turkey, pp. 601−616, 2010. (in Turkish)

5. Lioubimtseva, E., "Arid Environments", *In: Shahge - Danova M (ed) Physical Geography of Northern Eurasia*, pp. 267-283, Oxford University Press, Oxford, 2002.

6. Small E., F. Giorgi and L.C. Sloan, "Regional Climate Model Simulation of Precipitation in Central Asia: Mean and Interannual Variability", *Journal of Geophysical Research*, Vol. 104, No. D6, pp. 6563−6582, 1999.

7. Lee, D.K. and M.S. Suh, "Ten Year East Asian Summer Monsoon Simulation Using a Regional Climate Model (RegCM2)", *Journal of Geophysical Research*, Vol. 105, pp. 29565−29577, 2000.

8. Fu, C., S. Wang, Z. Xiong, W.J. Gutowski, D.K. Lee, J.L. McGregor, Y. Sato, H. Kato, J.W. Kim and M.S. Suh, "Regional Climate Model Intercomparison Project

for Asia (RMIP)", *Bulletin of the American Meteorological Society*, Vol. 86, No. 2, pp. 257−266, 2005.

9. Elguindi, N. and F. Giorgi, "Projected Changes in The Caspian Sea level for The 21st Century Based on The Latest AOGCM Simulations", *Geophysical Research Letters*, Vol. 33, L08706, 2006.

10. Elguindi, N. and F. Giorgi, "Simulating Future Caspian Sea Level Changes Using Regional Climate Model Outputs", *Climate Dynamics*, Vol. 28, pp. 365−379, 2007.

11. Lioubimtseva, E., R. Cole, J.M. Adams and G. Kapustin, "Impacts of Climate and Land-cover Changes in Arid Lands of Central Asia", *Journal of Arid Environments*, Vol. 62, pp. 285−308, 2005.

12. Giorgi, F., E. Coppola, F. Solmon, L. Mariotti, M.B. Sylla, X. Bi, N. Elguindi, G.T. Diro, V. Nair, G. Giuliani, U.U. Turuncoglu, S. Cozzini, I. Güttler, T.A. O'Brien, A.B. Tawfik, A. Shalaby, A.S. Zakey, A.L. Steiner, F. Stordal, L.C. Sloan and C. Brankovic, "RegCM4: Model Description and Preliminary Tests over Multiple CORDEX Domains", *Climate Research*, Vol. 52, pp. 7–29, 2012.

13. Giorgi, F. and C. Shields, "Tests of Precipitation Parameterizations Available in The Latest Version of The NCAR Regional Climate Model (RegCM) over The Continental United States", *Journal of Geophysical Research*, Vol. 104, pp. 6353–6375, 1999.

14. Ozturk, T., H. Altinsoy, M. Türkeş and M.L. Kurnaz, "Simulation of Temperature and Precipitation Climatology for The Central Asia CORDEX Domain by Using RegCM 4.0", *Climate Research*, Vol. 52, pp. 63–76, 2012.

15. Jones, C. and K. Wyser, "The Rossby Centre Regional Atmospheric Climate Model Part II: Application to The Arctic Climate", *Ambio*, Vol. 33, pp. 211–220, 2004.

16. Sundqvist, H., E. Berge and J. E. Kristjansson, "Condensation and Cloud Studies

with a Mesoscale Numerical Weather Prediction Model", *Monthly Weather Review*, Vol. 117, No. 8, pp. 1641–1657, 1989

17. Xu, K. M. and D. A. Randall, "A Semi Empirical Cloudiness Parameterization for Use in Climate Models", *Journal of Atmospheric Sciences*, Vol. 53, pp. 3084–3102, 1996.

18. Simmons A.S., D.D. Uppala and S. Kobayashi, "ERA-Interim: New ECMWF Reanalysis Products from 1989 Onwards", *ECMWF Newsletter*, Vol. 110, pp. 29−35, 2007.

19. Mitchell, T. D. and D. J. Philip, "An Improved Method of Constructing a Database of Monthly Climate Observations and Associated High-resolution Grids", *International Journal of Climatology*, Vol. 25, No. 6, pp. 693-712, 2005.

20. Houghton, J. T. Y., Y. Ding, D. J. Griggs, M. Noguer, P. J. van der Linden, X. Dai, K. Maskell and C.A. Johnson, (Eds.), *Climate Change 2001: The Scientific Basis. Contribution of Working Group I to the Third Assessment Report of the Intergovernmental Panel on Climate Change*, Cambridge University Press, pp. 881, 2001.

21. Le Treut, H., R. Somerville, U. Cubasch, Y. Ding, C. Mauritzen, A. Mokssit, T. Peterson and M. Prather, "Historical Overview of Climate Change", *In Solomon, S., D. Qin, M. Manning, Z. Chen, M. Marquis, K.B. Averyt, M. Tignor and H.L. Miller (eds.), Climate Change 2007: The Physical Science Basis. Contribution of Working Group I to the Fourth Assessment Report of the Intergovernmental Panel on Climate Change*, Cambridge University Press, Cambridge, United Kingdom and New York, 2007.

22. Türkeş, M., "Physical Science Basis of the Climate Change: Physical Climate System, Enhanced Greenhouse Effect, Observed and Projected Climate Variations", *In: 5th Atmospheric Science Symposium Proceedings Book*, pp. 135-151, İstanbul, 27-29 April 2011 (in Turkish).

23. Tans, P., *Recent Monthly Average Mauna Loa CO_2*, 2014, http://www.esrl.noaa.gov/gmd/ccgg/trends/, June 2014.

24. Taylor, F. W., *Elementary Climate Physics*, Oxford University Press, Oxford, 2005.

25. Rohde, R. A., *Solar Radiation Spectrum*, 2014, http://en.wikipedia.org/wiki/Sunlight, January 2014

26. Kiehl, J. T. and K. E. Trenberth, "Earth's Annual Global Mean Energy Budget", *Bulletin of the American Meteorological Society*, Vol. 78, No. 2, pp. 197–208, 1997.

27. Fleagle, R. G. and J. A. Businger, *An Introduction to Atmospheric Physics*, Academic Press, San Diego, California, 1980.

28. Andrews, D. G., *An Introduction to Atmospheric Physics*, Cambridge University Press, New York, 2010.

29. Rogers, R. R. and M. K. Yau, *A Short Course in Cloud Physics*, Elsevier Science and Technology, Oxford, 1996.

30. Tompkins, A., *Atmospheric Physics Handout*, 2013, http://users.ictp.it/ tompkins/diploma/lectures.handout.pdf, January 2014.

31. Schubert, E. F., *Light-Emitting Diodes*, Cambridge University Press, UK, 2006.

32. Nakicenovic, N., J. Alcamo, G. Davis, B. de Vries, J. Fenhann, S. Gaffin, K. Gregory, A. Grübler, T. Y. Jung, T. Kram, E. L. La Rovere, L. Michaelis, S. Mori, T. Morita, W. Pepper, H. Pitcher, L. Price, K. Raihi, A. Roehrl, H-H. Rogner, A. Sankovski, M. Schlesinger, P. Shukla, S. Smith, R. Swart, S. van Rooijen, N. Victor, and Z. Dadi, *IPCC Special Report on Emissions Scenarios*, Cambridge University Press, Cambridge, United Kingdom and New York, 2000.

33. Manabe, S. and R.T. Wetherald, "The Effects of Doubling the CO_2 Concentration on the Climate of a General Circulation Model", *Journal of the Atmospheric*

Sciences, Vol. 32, pp. 3–15, 1975.

34. Schlesinger, M.E. and J.F.B. Mitchell, "Climate Model Simulations of the Equilibrium Climatic Response to Increased Carbon Dioxide", *Reviews of Geophysics*, Vol. 25, No. 4, pp. 760–798, 1987.

35. Held, I. M., "The Gap between Simulation and Understanding in Climate Modelling", *Bulletin of the American Meteorological Society*, Vol. 86, pp. 1609–1614, 2005.

36. Solomon, S., D. Qin, M. Manning, Z. Chen, M. Marquis, K.B. Averyt, M. Tignor and H.L. Miller, Climate Change 2007: *The Physical Science Basis. Contribution of Working Group I to the Fourth Assessment Report of the Intergovernmental Panel on Climate Change*, Cambridge University Press, Cambridge, United Kingdom and New York, 2007.

37. Berger, A., M. F. Loutre and H. Gallée, "Sensitivity of the LLN Climate Model to The Astronomical and CO_2 Forcings over The Last 200 kyr", *Climate Dynamics*, Vol. 14, pp. 615–629, 1998.

38. Charney, J. G., A. Arakawa, J. Baker, B. Bolin, R. E. Dickinson, R. M. Goody, C. E. Leith, H.M. Stommel and C. I. Wunsch, "Carbon Dioxide and Climate: A Scientific Assessment", *Report of an Ad Hoc Study Group on Carbon Dioxide and Climate*, National Academy of Sciences, Washington D.C., 1979.

39. Houghton, J. T., G. J. Jenkins, and J.J. Ephraums (eds.), *Climate Change: The IPCC Scientific Assessment*, Cambridge University Press, Cambridge, United Kingdom and New York, 1990.

40. Manabe, S. and K. Bryan, "Climate Calculations with a Combined Ocean-Atmosphere model", *Journal of the Atmospheric Sciences*, Vol. 26, pp. 786–789, 1969.

41. Bryan, K., S. Manabe and R.C. Pacanowski, "A Global Ocean-Atmosphere Climate model. Part II. The Oceanic Circulation", *Journal of Physical Oceanography*, Vol. 5, pp. 30–46, 1975.

42. Manabe, S., K. Bryan, and M.J. Spelman, "A Global Ocean-Atmosphere Climate Model. Part I. The Atmospheric Circulation", *Journal of Physical Oceanography*, Vol. 5, pp. 3–29, 1975.

43. Trenberth, K. (ed.), *Climate System Modeling*, Cambridge University Press, Cambridge, UK, 1993.

44. Manabe, S. and R.J. Stouffer, "Two Stable Equilibria of a Coupled Ocean-Atmosphere Model", *Journal of Climate*, Vol. 1, No. 9, pp. 841–866, 1988.

45. Sausen, R., K. Barthel and K. Hasselman, "Coupled Ocean-Atmosphere Models with Flux Correction", *Climate Dynamics*, Vol. 2, pp. 145–163, 1988.

46. Lorenz, E.N., "Deterministic Non-periodic Flow", *Journal of the Atmospheric Sciences*, Vol. 20, pp. 130–141, 1963.

47. Lorenz, E.N., "The Physical Bases of Climate and Climate Modeling", In: *Climate Predictability. GARP Publication*, Series 16, pp. 132-136, World Meteorological Association, Geneva, 1975.

48. Cess, R.D., G. L. Potter, J. P. Blanchet, G. J. Boer, S. J. Ghan, J. T. Kiehl, H. Le Treut, Z. X. Li, X.Z. Liang, J. F. B. Mitchell, J.J. Morcrette, D. A. Randall, M. R. Riches, E. Roeckner, U. Schlese, A. Slingo, K. E. Taylor, W. M. Washington, R. T. Wetherald and I. Yagai, "Interpretation of Cloud-Climate Feedback as Produced by 14 Atmospheric General Circulation Models", *Science*, Vol. 245, pp. 513–516, 1989.

49. Taylor, K., *Program for Climate Model Diagnosis and Intercomparison*, 1989, http://www-pcmdi.llnl.gov/, February 2014.

50. Cubasch, U., B. D. Santer, A. Hellbach, G. Hegerl, H. Höck, E. Maier-Reimer, U.

Mikolajewicz, A. Stössel and R. Voss, “Monte Carlo Climate Change Forecasts with a Global Coupled Ocean-Atmosphere Model”, *Climate Dynamics*, Vol. 10, pp. 1–19, 1994.

51. Barnett, T.P., “Monte Carlo Climate Forecasting”, *Journal of Climate*, Vol. 8, No. 5, pp. 1005–1022, 1995.

52. Collins, W. D., C. M. Bitz, M. L. Blackmon, G. B. Bonan, C. S. Bretherton, J. A. Carton, P. Chang, S. C. Doney, J. J. Hack, T. B. Henderson, J. T. Kiehl, W. G. Large, D. S. McKenna, B. D. Santer and R. D. Smith, “The Community Climate System Model version 3 (CCSM3)”. *Journal of Climate*, Vol. 19, pp. 2122-2143, 2006.

53. Randall, D.A. and B.A. Wielicki, “Measurements, Models and Hypotheses in The Atmospheric Sciences”, *Bulletin of the American Meteorological Society*, Vol. 78, pp. 399-406, 1997.

54. Wigley, T.M.L., “The Kyoto Protocol: CO_2, CH_4, and Climate implications”, *Geophysical Research Letters*, Vol. 25, pp. 2285-2288, 1998.

55. Wigley, T.M.L. and S.C.B. Raper, “Thermal Expansion of Sea Water Associated with Global Warming”, *Nature*, Vol. 330, pp. 127-131, 1987.

56. Wigley, T.M.L. and S.C.B. Raper, “Implication for Climate and Sea Level of Revised IPCC Emissions Scenarios”, *Nature*, Vol. 357, pp. 293-300, 1992.

57. Kattenberg, A., F. Giorgi, H. Grassl, G.A. Meehl, J.F.B. Mitchell, R.J. Stouffer, T. Tokioka, A.J. Weaver and T.M.L. Wigley, “Climate Models — Projections of Future Climate”, In Houghton, J.T., L.G. Meira Filho, B.A. Callander, N. Harris, A. Kattenburg, and K. Maskell, (Eds.), *Climate Change 1995 – The Science of Climate Change: Contribution of Working Group I to the Second Assessment Report of the Intergovernmental Panel on Climate Change*, pp. 285-357, Cambridge University Press, Cambridge, England, 1996.

58. Raper, S.C.B., T.M.L Wigley and R.A. Warrick, “Global Sea-level Rise: Past and Future”, *In Sea-Level Rise and Coastal subsidence, Causes, Consequences and Strategies*, pp. 369, Kluwer Academic Publishers, Dordrecht, 1996.

59. Nordhaus,W.D., *Managing the Global Commons: The Economics of Climate Change*, The MIT Press, Cambridge, 1994.

60. Tol, R. S. J., “Spatial and Temporal Efficiency in Climate Change: Applications of FUND”, *Environmental and Resource Economics*, Vol. 14, No. 1, pp. 33-49, 1999.

61. Peck, S. C. and T. J. Teisberg, “International CO2 Emissions Targets and Timetables: An Analysis of the AOSIS Proposal”, *Environmental Modeling and Assessment*, Vol. 1, No. 4, pp. 219-227, 1996.

62. Manne, A. S. and R. G. Richels, “The Kyoto Protocol: A Cost-Effective Strategy for Meeting Environmental Objectives”, *Energy Journal*, Special Issue, pp. 1-23, 1999.

63. Flato, G., “Earth System Models: an Overview”, *WIREs Climate Change*, Vol. 2, No. 6, pp. 783-800, 2011.

64. Stocker, T.F., D.G. Wright and L.A. Mysak, “A Zonally-averaged, Coupled Ocean-Atmosphere Model for Paleoclimatic Studies”, *Journal of Climate*, Vol. 5, pp. 773-797, 1992.

65. Marchal, O., T.F. Stocker and F. Joos, “A Latitude-depth, Circulation Biogeochemical Ocean Model for Paleoclimate Studies: Model Development and Sensitivities”, *Tellus*, Vol. 50, No. 3, pp. 290-316, 1998.

66. Gallee, H., J.P. van Ypersele, T. Fichefet, C. Tricot, and A. Berger, “Simulation of The Last Glacial Cycle by a Coupled, Sectorially Averaged Climate-ice Sheet Model: I. The Climate Model”, *Journal of Geophysical Research*, Vol. 96, pp. 13139-13161, 1991.

67. Petoukhov, V., A. Ganapolski, V. Brovkin, M. Claussen, A. Eliseev, C. Kubatzki and S. Rahmstorf, “CLIMBER-2: A Climate System Model of Intermediate Complexity, Part I: Model Description and Performance for Present Climate”, *Climate Dynamics*, Vol. 16, pp. 1-17, 2000.

68. Petoukhov, V.K., I.I. Mokhov, A.V. Eliseev and V.A. Semenov, “The IAP RAS Global Climate Model”, *Dialogue-MSU*, Moscow, 110 pp., 1998.

69. Handorf, D., V.K. Petoukhov, K. Dethloff, A.V. Eliseev, A. Weisheimer, and I.I. Mokhov, “Decadal Climate Variability in a Coupled Atmosphere-Ocean Climate Model of Moderate Complexity”, *Journal of Geophysical Research*, Vol. 104, No. D22, pp. 27253-27275, 1999.

70. Opsteegh, J.D., R.J. Haarsma, F.M. Selten and A. Kattenberg, “ECBILT: A Dynamic Alternative to Mixed Boundary Conditions in Ocean Models”, *Tellus*, Vol. 50, No. 3, pp. 348-367, 1998.

71. Stocker, T.F. and A. Schmittner, “Influence of CO_2 Emission Rates on The Stability of The Thermohaline Circulation”, *Nature*, Vol. 388, pp. 862-865, 1997.

72. Rahmstorf, S. and A. Ganopolski, “Long-term Warming Scenarios Computed with an Efficient Coupled Climate Model”, *Climatic Change*, Vol. 43, pp. 353-367, 1999.

73. Dickinson, R.E., R.M. Errico, F. Giorgi, and G.T. Bates, “A Regional Climate Model for Western United States”, *Climatic Change*, Vol. 15, pp. 383–422, 1989.

74. Giorgi F., “Simulation of Regional Climate Using a Limited Area Model Nested in a General Circulation Model”, *Journal of Climate*, Vol. 3, pp. 941–963, 1990.

75. Hostetler, S.W., F. Giorgi, G.T. Bates and P.J. Bartlein, “Lake Atmosphere Feedbacks Associated with Paleolakes Bonneville and Lahontan”, *Science*, Vol. 263, pp. 665–668, 1994.

76. Hostetler, S.W., P.J. Bartlein, P.U. Clark, E.E. Small and A.M. Solomon, “Sim-

ulated Influence of Lake Agassiz on The Climate of Central North America 11,000 years ago", *Nature*, Vol. 405, pp. 334-337, 2000.

77. Giorgi, F. and L. O. Mearns, "Approaches to The Simulation of Regional Climate Change: A Review", *Reviews of Geophysics*, Vol. 29, No. 2, pp. 191–216, 1991.

78. Giorgi, F. and L. O. Mearns, "Introduction to Special Section: Regional Climate Modeling Revisited", *Journal of Geophysical Research*, Vol. 104, No. D6, pp. 6335–6352, 1999.

79. Ji, Y. and A. D. Vernekar, "Simulation of The Asian Summer Monsoons of 1987 and 1988 with a Regional Model Nested in a Global GCM", *Journal of Climate*, Vol. 10, No. 8, pp. 1965–1979, 1997.

80. Jones, R.G., J.M. Murphy and M. Noguer, "Simulations of Climate Change over Europe Using a Nested Regional Climate Model. I: Assessment of Control Climate, Including Sensitivity to Location of Lateral Boundaries", *Quarterly Journal of the Royal Meteorological Society*, Vol. 121, No. 526, pp. 1413–1449, 1995.

81. Jacob, D. and R. Podzun, "Sensitivity Study with The Regional Climate Model REMO", *Meteorology and Atmospheric Physics*, Vol. 63, pp. 119-129, 1997.

82. Noguer, M., R.G. Jones and J.M. Murphy, "Sources of Systematic Errors in The Climatology of a Nested Regional Climate Model (RCM) over Europe", *Climate Dynamics*, Vol. 14, pp. 691–712, 1998.

83. Jones, R.G., J.M. Murphy, M. Noguer, and A.B. Keen, "Simulation of Climate Change over Europe Using a Nested Regional Climate Model. II: Comparison of Driving and Regional Model Responses to a Doubling of Carbon Dioxide", *Quarterly Journal of the Royal Meteorological Society*, Vol. 123, No. 538, pp. 265–292, 1997.

84. Warner, T. T., R.A. Peterson and R.E. Treadon, "A Tutorial on Lateral Conditions as a Basic and Potentially Serious Limitation to Regional Numerical Weather

Prediction", *Bulletin of the American Meteorological Society*, Vol. 78, pp. 2599-2617, 1997.

85. Seth, A. and F. Giorgi, "The Effects of Domain Choice on Summer Precipitation Simulation and Sensitivity in a Regional Climate Model", *Journal of Climate*, Vol. 11, No. 10, pp. 2698–2712, 1998.

86. Bhaskaran, B., R.G. Jones, J.M. Murphy, and M. Noguer, "Simulations of The Indian Summer Monsoon Using a Nested Regional Climate Model: Domain Size Experiments", *Climate Dynamics*, Vol. 12, pp. 573–587, 1996.

87. Giorgi, F. and M.R. Marinucci, "An Investigation of The Sensitivity of Simulated Precipitation to Model Resolution and Its Implications for Climate Studies", *Monthly Weather Review*, Vol. 124, No. 1, pp. 148-166, 1996.

88. Laprise, R., D. Caya, M. Giguère, G. Bergeron, H. Côte, J.-P. Blanchet, G.J. Boer, and N.A. McFarlane, "Climate and Climate Change in Western Canada as Simulated by The Canadian Regional Climate Model", *Atmosphere-Ocean*, Vol. 36, No. 2, pp. 119–167, 1998.

89. Christensen O.B., J.H. Christensen, B. Machenhauer, and M. Botzet, "Very High-resolution Regional Climate Simulations over Scandinavia – Present Climate", *Journal of Climate*, Vol. 11, No. 12, pp. 3204-3229, 1998.

90. Leung, L.R. and S.J. Ghan, "Parameterizing Subgrid Orographic Precipitation and Surface Cover in Climate Models", *Monthly Weather Review*, Vol. 126, No. 12, pp. 3271-3291, 1998.

91. McGregor, J.L., J.J. Katzfey and K.C. Nguyen, "Recent Regional Climate Modeling Experiments at CSIRO", In H. Ritchie (ed), *Research Activities in Atmospheric and Oceanic Modelling*, CAS/JSC Working Group on Numerical Experimentation Report, 28, WMO/TD – no. 942, Geneva, WMO. P. 7.37–7.38, 1999.

92. Liston, G.E., R.A. Pielke, Sr. and E.M. Greene, "Improving First Order Snow-related Deficiencies in a Regional Climate Model", *Journal of Geophysical Research*, Vol. 104, No. D16, pp. 19559-19567, 1999.

93. Qian,Y. and F. Giorgi, "Interactive Coupling of Regional Climate and Sulfate Aerosol Models over East Asia", *Journal of Geophysical Research*, Vol. 104, No. D6, pp. 6477–6499, 1999.

94. Hostetler, S.W., F. Giorgi, G.T. Bates and P.J. Bartlein, "Lake-atmosphere Feedbacks Associated with Paleolakes Bonneville and Lahontan", *Science*, Vol. 263, No. 5147, pp. 665–668, 1994.

95. Lynch, A. H., W.L. Chapman, J.E. Walsh and G. Weller, "Development of a Regional Climate Model of the Western Arctic", *Journal of Climate*, Vol. 8, No. 6, pp. 1555–1570, 1995.

96. Lynch, A.H., M.F. Glück, W.L. Chapman, D.A. Bailey and J.E. Walsh, "Remote Sensing and Climate Modeling of the St. Lawrence Is. Polynya", *Tellus*, Vol. 49, pp. 277-297, 1997.

97. Lynch, A.H., D.L. McGinnis, W.L. Chapman and J.S. Tilley, "A Multivariate Comparison of Two Land Surface Models Integrated into an Arctic Regional Climate System Model", *Annals of Glaciology*, Vol. 25, pp. 127-131, 1997.

98. Lynch, A.H., D.L. McGinnis and D.A. Bailey, "Snow-albedo Feedback and the Spring Ttransition in a Regional Climate System Model: Influence of Land Surface Model", *Journal of Geophysical Research*, Vol. 103, No. D22, pp. 29037-29049, 1998.

99. Leung, L.R., M. S. Wigmosta, S.J. Ghan, D.J. Epstein and L.W. Vail, "Application of a Subgrid Orographic Precipitation/Surface Hydrology Scheme to a Mountain Watershed", *Journal of Geophysical Research*, Vol. 101, No. D8, pp. 12803–12817, 1996.

100. Bailey, D.A., A.H. Lynch and K.S. Hedström, "The Impact of Ocean Circulation on Regional Polar Simulations Using the Arctic Regional Climate System Model", *Annals of Glaciology*, Vol. 25, pp. 203-207, 1997.

101. Kim, J., N.L. Miller, A.K. Guetter and K.P. Georgakakos, "River Flow Response to Precipitation and Snow Budget in California During the 1994-95 Winter", *Journal of Climate*, Vol. 11, No. 9, pp. 2376–2386, 1998.

102. Small, E.E., F. Giorgi and L.C. Sloan, "Regional Climate Model Simulation of Precipitation in Central Asia: Mean and Interannual Variability", *Journal of Geophysical Research*, Vol. 104, No. D6, pp. 6563–6582, 1999.

103. Small, E.E., L.C. Sloan, S. Hostetler and F. Giorgi, "Simulating the Water Balance of the Aral Sea with a Coupled Regional Climate-lake Model", *Journal of Geophysical Research*, Vol. 104, No. D6, pp. 6583–6602, 1999.

104. Dee, D.P., S.M. Uppala, A.J. Simmons, P. Berrisford, P. Poli, S. Kobayashi, U. Andrae, M.A. Balmaseda, G. Balsamo, P. Bauer, P. Bechtold, A.C.M. Beljaars, L. van de Berg, J. Bidlot, N. Bormann, C. Delsol, R. Dragani, M. Fuentes, A.J. Geer, L. Haimberger, S.B. Healy, H. Holm, E.V. Hersbach, L. Isaksen, P. Kallberg, M. Köhler, M. Matricardi, A.P. McNally, B.M. Monge-Sanz, J-J Morcrette, B-K Park, C. Peubey, P. de Rosnay, C. Tavolato, J.-N. Thepaut, and F. Vitart, "The ERA-Interim Reanalysis: Configuration and Performance of the Data Assimilation System", *Quarterly Journal of the Royal Meteorological Society*, Vol. 137, No. 656, pp. 553–597, 2011.

105. Uppala, S.M., P.W. Kallberg, A.J. Simmons, U. Andrae, V. Da Costa Bechtold, M. Fiorino, J.K. Gibson, J. Haseler, A. Hernandez, G.A. Kelly, X. Li, K. Onogi, S. Saarinen, N. Sokka, R.P. Allan, E. Andersson, K. Arpe, M.A. Balmaseda, A.C.M. Beljaars, L. Van De Berg, J. Bidlot, N. Bormann, S. Caires, F. Chevallier, A. Dethof, M. Dragosavac, M. Fisher, M.Fuentes, S. Hagemann, E. H´olm, B.J. Hoskins, L. Isaksen, P.A.E.M. Janssen, R. Jenne, A.P. McNally, J.F. Mahfouf, J-J Morcrette, N.A. Rayner, R.W. Saunders, P. Simon, A. Sterl, K.E. Trenberth, A. Untch, D.

Vasiljevic, P. Viterbo and J. Woollen, “The ERA-40 Re-analysis”, *Quarterly Journal of the Royal Meteorological Society*, Vol. 131, No. 612, pp. 2961–3012, 2005.

106. Kalnay, E, M. Kanamitsu, R. Kirtler, W. Collins, D. Deaven, L. Gandin, M. Iredell, S. Saha, G. White, J. Woollen, Y. Zhu, M. Chelliah, W. Ebisuzaki, W. Higgins, J. Janowiak, K.C. Mo, C. Ropelewski, J. Wang, A. Leetma, R. Reynolds, R. Jenne and D. Joseph, “The NCEP/NCAR 40-year Reanalysis Project”, *Bulletin of the American Meteorological Society*, Vol. 77, No. 3, pp. 437–471, 1996.

107. Saha, S, S. Moorthi, H-L Pan, X. Wu, J. Wang, S. Nadiga, P. Tripp, R. Kistler, J. Woollen, D. Behringer, H. Liu, D. Stokes, R. Grumbine, G. Gayno, Y-T. Hou, H-Y. Chuang, H-M.H. Juang, J. Sela, M. Iredell, R. Treadon, D. Kleist, P. van-Delst, D. Keyser, J. Derber, M. Ek, J. Meng, H. Wei, R. Yang, S. Lord, H. van den Dool, A. Kumar, W. Wang, C. Long, M. Chelliah, Y. Xue, B. Huang, J-K. Schemm, W. Ebisuzaki, R. Lin, P. Xie, M. Chen, S. Zhou, W. Higgins, C-Z. Zou, Q. Liu, Y. Chen, Y. Han, L. Cucurull, R.W. Reynolds, G. Rutledge and M. Goldberg, “The NCEP Climate Forecast System Reanalysis”, *Bulletin of the American Meteorological Society*, Vol. 91, No. 8, pp. 1015–1057, 2010.

108. Onogi, K, J. Tsutsui, H. Koide, M. Sakamoto, S. Kobayashi, H. Hatsushika, T. Matsumoto, N. Yamazaki, H. Kamahori, K. Takahashi, S. Kadokura, K. Wada, K. Kato, R. Oyama, T. Ose, N. Mannoji and R. Taira, “The JRA-25 Reanalysis”, *Journal of the Meteorological Society of Japan*, Vol. 85, pp. 369–432, 2007.

109. Schubert, S. D., R. Rood and J. Pfaendtner, “An Assimilated Dataset for Earth Science Applications”, *Bulletin of the American Meteorological Society*, Vol. 74, No. 12, pp. 2331–2342, 1993.

110. Rienecker, MM, M.J. Suarez, R. Gelaro, R. Todling, J. Bacmeister, E. Liu, M.G. Bosilovich, S.D. Schubert, L. Takacs, G-K. Kim, S. Bloom, J. Chen, D. Collins, A. Conaty, A. da Silva, W. Gu, J. Joiner, R.D. Koster, R. Lucchesi, A. Molod, T. Owens, S. Pawson, P. Pegion, C.R. Redder, R. Reichle, F. R. Robertson, A.G. Ruddick, M. Sienkiewicz and J. Woollen, “MERRA – NASA’s Modern-Era Retro-

spective Analysis for Research and Applications", *Journal of Climate*, Vol. 24, No. 14, 2011.

111. Gibson, J.K., P. Kallberg and S.M. Uppala, A. Nomura, A. Hernandez, E. Serrano, "ERA Description", *ERA-15 Report Series*, No. 1, ECMWF, Reading, UK. 1997.

112. Simmons, A.S., D.D. Uppala and S. Kobayashi, "ERA-Interim: New ECMWF Reanalysis Products from 1989 Onwards", *ECMWF Newsletter*, Vol. 110, pp. 29−35, 2007.

113. *The European Centre for Medium-Range Weather Forecasts (ECMWF)*, 1975, http://www.ecmwf.int/en/forecasts/datasets, March 2014.

114. New, M., M. Hulme and P.D. Jones, "Representing Twentieth Century Space-time Climate Variability. Part 1: Development of a 1961-90 Mean Monthly Terrestrial Climatology", *Journal of Climate*, Vol. 12, pp. 829-856, 1999.

115. *The Coordinated Regional Climate Downscaling Experiment*, 2013, http://wcrp-cordex.ipsl.jussieu.fr/, March 2014.

116. Giorgi, F., M. R.Marinucci and G. T. Bates, "Development of a Second Generation Regional Climate Model (Regcm2) i: Boundary Layer and Radiative Transfer Processes", *Monthly Weather Review*, Vol. 121, No. 10, pp. 2794–2813, 1993.

117. Giorgi, F., M. R. Marinucci, G. T. Bates and G. De Canio, "Development of a Second Generation Regional Climate Model (Regcm2) ii: Convective Processes and Assimilation of Lateral Boundary Conditions", *Monthly Weather Review*, Vol. 121, No. 10, pp. 2814–2832, 1993.

118. Pal, J. S., E. E. Small and E. A. B. Eltahir, "Simulation of Regional-scale Water and Energy Budgets: Representation of Subgrid Cloud and Precipitation Processes within RegCM", *Journal of Geophysical Research*, Vol. 105, No. D24, pp. 29579–29594p, 2000.

119. Pal, J.S. and E. A. B. Eltahir, "A Feedback Mechanism Between Soil Moisture Distribution and Storm Tracks", *Quarterly Journal of the Royal Meteorological Society*, Vol. 129, pp. 2279–2297, 2003.

120. Abiodun, B.J., J.S. Pal, E.A. Afiesimama, W.J. Gutowski and A. Adedoyin, "Simulation of West African Monsoon Using RegCM3 Part II: Impacts of Deforestation and Desertification", *Theoretical and Applied Climatology*, Vol. 93, pp. 245–261, 2008.

121. Gao, X., D. Zhang, Z. Chen, J. Pal and F. Giorgi, "Land Use Effects on Climate in China as Simulated by a Regional Climate Model", *Science in China Series D: Earth Sciences*, Vol. 50, No. 4, pp. 620–628, 2007.

122. Zakey, A.S., F. Giorgi and X. Bi, "Modeling of Sea Salt in a Regional Climate Model: Fluxes and Radiative Forcing", *Journal of Geophysical Research*, Vol. 113, No. D14, 2008.

123. Syed F.S., F. Giorgi, J.S. Pal and K. Keayd, "Regional Climate Model Simulation of Winter Climate over Central–Southwest Asia, with Emphasis on NAO and ENSO Effects", *International Journal of Climatology*, Vol. 30, pp. 220–235, 2010.

124. Pal, J.S., F. Giorgi and X. Bi, "Consistency of Recent European Summer Precipitation Trends and Extremes with Future Regional Climate Projections", *Geophysical Research Letters*, Vol. 31, No. 13, 2004.

125. Boroneant, C., G. Plaut, F. Giorgi and X. Bi, "Extreme Precipitation over the Maritime Alps and Associated Weather Regimes Simulated by a Regional Climate Model: Present-day and Future Climate Scenarios", *Theoretical and Applied Climatology*, Vol. 86, pp. 81-99, 2006.

126. Giorgi, F., J.S. Pal, X. Bi, L. Sloan, N. Elguindi and F. Solmon, "Introduction to the Tac Special Issue: The Regcnet Network", *Theoretical and Applied Climatology*, Vol. 86, pp. 1–4, 2006.

127. Gao, X. and F. Giorgi, "Increased Aridity in the Mediterranean Region Under Greenhouse Gas Forcing Estimated from High Resolution Simulations with a Regional Climate Model", *Global and Planetary Change*, Vol. 62, pp. 195–209, 2008.

128. Im, E.S., J.B. Ahn, W.T. Kwon and F. Giorgi, "Multi-decadal Scenario Simulation over Korea Using a One-way Double-nested Regional Climate Model System. Part II: Future Climate Projection (2021–2050)", Climate Dynamics, Vol. 30(23), pp.9–254, 2008.

129. Giorgi, F., X. Bi, J. Pal, "Mean Interannual Variability and Trends in a Regional Climate Change Experiment over Europe. I: Present-day Climate (1961–1990)", *Climate Dynamics*, Vol. 22, pp. 733–756, 2004.

130. Giorgi F, X. Bi, J. Pal, "Mean Interannual Variability and Trends in a Regional Climate Experiment over Europe. II: Future Climate (2070–2100), *Climate Dynamics*, Vol. 23(7–8), pp. 839–858, 2004.

131. Lionello P., U. Boldrin and F. Giorgi, "Future Changes in Cyclone Climatology over Europe as Inferred from a Regional Climate Simulation", *Climate Dynamics*, Vol. 30, pp. 657–671, 2008.

132. Afiesimama, E.A., J.S. Pal, B.J. Abiodun, W.J. Gutowski and A. Adedoyin, " Simulation of West African Monsoon Using the RegCM3. Part I: Model Validation and Interannual Variability", *Theoretical and Applied Climatology*, Vol. 86, pp. 23–37, 2006.

133. Konare, A., A. Zakey, F. Solmon, F. Giorgi, S. Rauscher, S.S. Ibrah and X. Bi, "A Regional Climate Modeling Study of the Effect of Desert Dust on the West African Monsoon", *Journal of Geophysical Research*, Vol. 113, No. D12, 2008.

134. Solmon, F., M. Mallet, N. Elguindi, F. Giorgi, A. Zakey and A. Konare, "Dust Aerosol Impact on Regional Precipitation over Western Africa, Mechanisms and Sensitivity to Absorption Properties", *Geophysical Research Letters*, Vol. 35, No.

24, 2008.

135. Sylla, M.B., E. Coppola, L. Mariotti, F. Giorgi, P.M. Ruti, A. Dell'Aquila and X. Bi, "Multiyear Simulation of the African Climate Using a Regional Climate Model (Reg CM3) with the High Resolution ERA-Interim Reanalysis", *Climate Dynamics*, Vol. 35, pp. 231–247, 2010.

136. Chen, B., W.C. Chao and X. Liu, "Enhanced Climatic Warming in the Tibetan Plateau Due to Doubling CO2: A Model Study", *Climate Dynamics*, Vol. 20, pp. 401–413, 2003.

137. Dash, S.K., M.S. Shekhar and G.P. Singh, "Simulation of Indian Summer Monsoon Circulation and Rainfall Using RegCM3", *Theoretical and Applied Climatology*, Vol. 86, pp. 161–172, 2006.

138. Giorgi, F., "Two-dimensional Simulations of Possible Meso-scale Effects of Nuclear War Fires: 1. Model Description", *Journal of Geophysical Research*, Vol. 94, No. D1, pp. 1127–1144, 1989.

139. Giorgi, F., G.T. Bates and S.J. Nieman, The Multi-year Surface Climatology of a Regional Atmospheric Model over the Western United States, *Journal of Climate*, Vol. 6, pp. 75–95, 1993.

140. Grell, G.A., J. Dudhia and D.R. Stauffer, "Description of the Fifth Generation Penn State/NCAR Mesoscale Model (MM5)", *NCAR Technical Note*, NCAR/TN-398+STR, NCAR, Boulder, Colorado, 1994.

141. Dickinson, R.E., A. Henderson-Sellers and P.J. Kennedy, "Biosphere-atmosphere Transfer Scheme (BATS) Version 1e as Coupled to the NCAR Community Climate Model", *NCAR Technical Note*, NCAR/TN-387+STR, NCAR, Boulder, Colorado, 1993.

142. Kiehl, J.T., J.J. Hack, G.B. Bonan, B.A. Boville, B.P. Breigleb, D. Williamson

and P. Rasch, “Description of the NCAR Community Climate Model (CCM3)”, *NCAR Technical Note*, NCAR/TN-420+STR, NCAR, Boulder, Colorado, 1996.

143. Holtslag, A. A. M., E. I. F. de Bruijn and H.L. Pan, “A High Resolution Air Mass Transformation Model for Short-range Weather Forecasting”, *Monthly Weather Review*, Vol. 118, pp. 1561–1575, 1990.

144. Anthes, R. A., “A Cumulus Parameterization Scheme Utilizing a One-dimensional Cloud Model”, *Monthly Weather Review*, Vol. 105, pp. 270–286, 1977.

145. Grell, G., “Prognostic Evaluation of Assumptions Used by Cumulus Parameterizations”, *Monthly Weather Review*, Vol. 121, pp. 764–787, 1993.

146. Emanuel, K. A., “A Scheme for Representing Cumulus Convection in Large-scale Models”, *Journal of the Atmospheric Sciences*, Vol. 48, No. 21, pp. 2313–2335, 1991.

147. Emanuel, K. A. and M. Zivkovic-Rothman, “Development and Evaluation of a Convection Scheme for Use in Climate Models”, *Journal of the Atmospheric Sciences*, Vol. 56, No. 11, pp. 1766–1782, 1999.

148. Dudhia, J., D. Gill, Y.R. Guo, K. Manning, W. Wang and J. Chriszar, *PSU/NCAR Mesoscale Modeling System Tutorial Class Notes and User’s Guide: MM5 Modeling System Version3*, 2005. Available online at http://www.mmm.ucar.edu/mm5/documents/tutorial-v3-notes.html

149. Briegleb, B. P., “Delta-eddington Approximation for Solar Radiation in the NCAR Community Climate Model”, *Journal of Geophysical Research*, Vol. 97, No. D7, pp. 7603–7612, 1992.

150. Slingo, J. M., “A GCM Parameterization for The Shortwave Radiative Properties of Water Clouds”, *Journal of the Atmospheric Sciences*, Vol. 46, pp. 1419–1427, 1989.

151. Deardoff, J. W., “Efficient Prediction of Ground Surface Temperature and Mois-

ture with Inclusion of A Layer of Vegetation", *Journal of Geophysical Research*, Vol. 83, No. C4, pp. 1889–1903, 1978.

152. Dickinson, R. E., "Climate Processes and Climate Sensitivity, chap. Modeling Evapotranspiration Processes for Three-Dimensional Global Climate Models", *American Geophysical Union*, pp. 52–72, 1984.

153. Dickinson, R. E., P. J. Kennedy, A. Henderson-Sellers, and M. Wilson, "Biosphere-Atmosphere Transfer Scheme (BATS) for The NCAR Community Climate Model", *NCAR Technical Note*, NCAR/TN-275+STR, NCAR, Boulder, Colorado, 1986.

154. Giorgi, F., R. Francisco and J. S. Pal, "Effects of A Subgrid-Scale Topography and Land Use Scheme on The Simulation of Surface Climate and Hydrology, part 1: Effects of Temperature and Water Vapor Disaggregation", *Journal of Hydrometeorology*, Vol. 4, pp. 317–333, 2003.

155. Oleson, K. W., Y. Dai, G. Bonan, M. Bosilovich, R. Dickinson, P. Dirmeyer, F. Hoffman, P. Houser, S. Levis, G.Yue Niu, P. Thornton, M. Vertenstein, Z. L. Yang and X. Zenge, "Technical Description of The Community Land Model (CLM)", *NCAR Technical Note*, NCAR/TN-461+STR, NCAR, Boulder, Colorado, 2004.

156. Holtslag, A. A. M. and B. A. Boville, "Local Versus Nonlocal Boundary-Layer Diffusion in A Global Climate Model", *Journal of Climate*, Vol. 6, pp. 1825-1842, 1993.

157. Grenier, H. and C. S. Bretherton, "A Moist Pbl Parameterization for Large-Scale Models and Its Application to Subtropical Cloud-Topped Marine Boundary Layers", *Monthly Weather Review*, Vol. 129, No. 3, pp. 357–377, 2001.

158. Bretherton, C. S., J. McCaa and H. Grenier, "A New Parameterization for Shallow Cumulus Convection and Its Application to Marine Subtropical Cloud-Topped Boundary Layers. Part i: Description and 1d Results", *Monthly Weather Review*,

Vol. 132, No. 4, pp. 864–882, 2004.

159. Galperin, B., L. H. Kantha, S. Hassid, and A. Rosati, “A Quasi-Equilibrium Turbulent Energy Model for Geophysical Flows”, *Journal of the Atmospheric Sciences*, Vol. 45, No. 1, pp. 55–62, 1988.

160. Fritsch, J. M. and C. F. Chappell, “Numerical Prediction of Convectively Driven Mesoscale Pressure Systems. Part i: Convective parameterization”, *Journal of the Atmospheric Sciences*, Vol. 37, No. 8, pp. 1722–1733, 1980.

161. Giorgi, F. and G. T. Bates, “The Climatological Skill of A Regional Model over Complex Terrain”, *Monthly Weather Review*, Vol. 117, No. 11, pp. 2325–2347, 1989.

162. Giorgi, F., and M. R. Marinucci, “Validation of A Regional Atmospheric Model over Europe: Sensitivity of Wintertime And Summertime Simulations to Selected Physics Parameterizations and Lower Boundary Conditions”, *Quarterly Journal of the Royal Meteorological Society*, Vol. 117, No. 552, pp. 1171–1206, 1991.

163. Beheng, K. D., “A Parameterization of Warm Cloud Microphysical Conversion Processes”, *Atmospheric Research*, Vol. 33, pp. 193–206, 1994.

164. PRB *(Population Reference Bureau) World Population Data sheet*, Population Reference Bureau, Washington D.C., 2011.

165. Vavrus, S. and D. Waliser, “An Improved Parameterization for Simulating Arctic Cloud Amount in The CCSM3 Climate Model”, *American Meteorological Society*, Vol. 21, pp. 5673-5687, 2008.

166. Curry, J. A., W. B. Rossow, D. Randall, and J. L. Schramm, “Overview of Arctic Cloud and Radiation Characteristics”, *Journal of Climate*, Vol. 9, pp. 1731–1764, 1996.

167. Beesley, J. A. and R. E. Moritz, “Toward An Explanation of The Annual Cycle of Cloudiness over The Arctic Ocean”, *Journal of Climate*, Vol. 12, pp. 395–415, 1999.

168. Beesley, J. A., “Estimating The Effect of Clouds on The Arctic Surface Energy Budget”, *Journal of the Atmospheric Sciences*, Vol. 105, No. D8, pp. 10103–10117, 2000.

169. Roeckner, E., G. Bäuml, L. Bonaventur, R. Brokopf, M. Esch, M. Giorgetta, S. Hagemann, I. Kirchner, L. Kornblueh, E. Manzini, A. Rhodin, U. Schlese, U. Schulzweida, and A. Tompkins, “The Atmospheric General Circulation Model ECHAM5. Part I: Model Description”, *Max Planck Institute for Meteorology Report*, No. 349, 2003.

170. Hurrell, J.W., Y. Kushnir, G. Ottersen and M. Visbeck, “An Overview of The North Atlantic Oscillation”, *Geophysical Monograph Series*, Vol. 134, pp. 1–35, 2003.

171. Kutiel, H., P. Maheras, M. Türkeş and S. Paz, “North Sea – Caspian Pattern (NCP) – An Upper Level Atmospheric Tele-connection Affecting The Eastern Mediterranean – Implications on The Regional Climate”, *Theoretical and Applied Climatology*, Vol. 72, pp. 173-192, 2002.

172. Kutiel, H., M. Türkeş, “New Evidence for The Role of The North Sea – Caspian Pattern on The Temperature and Precipitation Regimes in Continental Central Turkey”, Geografiska Annaler: Series A, *Physical Geography*, Vol. 87, No. 4, pp. 501-513, 2005.

173. Trigo, R., E. Xoplaki, E. Zorita, J. Luterbacher, S. Krichak, P. Alpert, J. Jacobeit, J. Saenz, J. Fernandez, F. Gonzalez-Rouco, R. Garcia-Herrera, X. Rodo, M. Brunetti, T. Nanni, M. Maugeri, M. Türkeş, L. Gimeno, P. Ribera, M. Brunet, I. Trigo, M. Crepon, and A. Mariotti, “Relations Between Variability in The Mediterranean Region and Mid-Latitude Variability”, in Lionello P., P. Malanotte-Rizzoli and R. Boscolo (eds.), *Mediterranean Climate Variability*, pp. 179-226, Elsevier Developments in Earth and Environmental Sciences, Amsterdam, 2006.

174. Türkeş, M. and E. Erlat, “Precipitation Changes and Variability in Turkey Linked to The North Atlantic Oscillation During The Period 1930-2000”, *International*

Journal of Climatology, Vol. 23, pp. 1771-1796, 2003.

175. Türkeş, M. and E. Erlat, "Influences of The North Atlantic Oscillation on Precipitation Variability and Changes in Turkey", *Nuovo Cimento Della Societa Italiana Di Fisica C-Geophysics and Space Physics*, Vol. 29, pp. 117-135, 2006.

176. Türkeş, M. and E. Erlat, "Influence of The Arctic Oscillation on Variability of Winter Mean Temperatures in Turkey", *Theoretical and Applied Climatology*, Vol. 92, pp. 75-85, 2008.

177. Türkeş, M. and E. Erlat, "Winter Mean Temperature Variability in Turkey Associated with The North Atlantic Oscillation", *Meteorology and Atmospheric Physics*, Vol. 105, pp. 211–225, 2009.

178. Buffoni, L., M. Maugeri and T. Nanni, "Precipitation in Italy 1833 to 1996", *Theoretical and Applied Climatology*, Vol. 63, pp. 33–40, 1999.

179. Buffoni, L., M. Maugeri and T. Nanni, "Variation of Temperature And Precipitation in Italy from 1866 To 1995", *Theoretical and Applied Climatology*, Vol. 65, pp. 165–174, 2000.

180. Esteban-Parra, M.J., F.S. Rodrigo and Y. Castro-Diez, "Spatial and Temporal Patterns of Precipitation in Spain for The Period 1880–1992", *International Journal of Climatology*, Vol. 14, pp. 1557–1574, 1998.

181. Giorgi, F., "Variability and Trends of Sub-Continental Scale Surface Climate in The Twentieth Century. Part I: Observations", *Climate Dynamics*, Vol. 18, pp. 675–691, 2002.

182. Gonzalez-Rouco, J.F., H. Heyen, E. Zorita, and F. Valero, "Agreement Between Observed Rainfall Trends and Climate Change Simulations in Southern Europe" *Journal of Climate*, Vol. 13, pp. 3057–3065, 2000.

183. Gonzalez-Rouco, J.F., J.L. Jimenez, V. Quesada and F. Valero, "Quality Control

and Homogenization of Monthly Precipitation Data in The Southwest of Europe", *Journal of Climate*, Vol. 14, pp. 964–978, 2001.

184. Tatlı, H. and M. Türkeş, "Drought Events of 2006/2007 in Turkey And Determination of Its Association with Large-Scale Atmospheric Variables by Logistic Regression", *In: 4th Atmospheric Science Symposium Proceedings Book*, Istanbul, Turkey, pp. 516-527, 2008 (in Turkish with an English abstract).

185. Tatlı, H. and M. Türkeş, "Examinaton of The Dry and Wet Conditions in Turkey via Model Output Statistics (MOS)", *In: 5th Atmospheric Science Symposium Proceedings Book*, Istanbul, Turkey, pp. 219-230, 2011 (in Turkish with an English abstract).

186. Tatlı, H. and M. Türkeş, "Empirical Orthogonal Function Analysis of The Palmer Drought Indices", *Agricultural and Forest Meteorology*, Vol. 151, No. 7, pp. 981–991, 2011.

187. Tomozeiu, R., M. Lazzeri and C. Cacciamani, "Precipitation Fluctuations During The Winter Season from 1960 to 1995 over Emilia-Romagna, Italy", *Theoretical and Applied Climatology*, Vol. 72, pp. 221–229, 1995.

188. Türkeş, M., "Influence of Geopotential Heights, Cyclone Frequency and Southern Oscillation on Rainfall Variations in Turkey", *International Journal of Climatology*, Vol. 18, pp. 649–680, 1998.

189. Türkeş, M., "Vulnerability of Turkey to Desertification with Respect to Precipitation and Aridity Conditions", *Turkish Journal of Engineering and Environmental Sciences*, Vol. 23, pp. 363-380, 1999.

190. Türkeş, M. and E. Erlat, "Climatological Responses of Winter Precipitation in Turkey to Variability of The North Atlantic Oscillation During The Period 1930-2001", *Theoretical and Applied Climatology*,Vol. 81, pp. 45-69, 2005.

191. Türkeş, M. and H. Tatlı, "Use of The Standardized Precipitation Index (SPI) and Modified SPI for Shaping The Drought Probabilities over Turkey", *International Journal of Climatology*, Vol. 29: pp. 2270–2282, 2009.

192. Türkeş, M. and H. Tatlı, "Use of The Spectral Clustering to Determine Coherent Precipitation Regions in Turkey for The Period 1929-2007", *International Journal of Climatology*, Vol. 31, pp. 2055–2067, 2011.

193. Türkeş, M., T. Koç and F. Sarış, "Spatiotemporal Variability of Precipitation Total Series over Turkey", *International Journal of Climatology*, Vol. 29, pp. 1056-1074, 2009.

194. Xoplaki, E., J. Luterbacher, R. Burkard, I. Patrikas, and P Maheras, "Connection Between The Large-Scale 500 Hpa Geopotential Height Fields and Precipitation over Greece During Wintertime", *Climate Research*, Vol. 14, pp. 129–146, 2000.

195. Giorgi, F. and P. Lionello, "Climate Change Projections for The Mediterranean Region", *Global and Planetary Change*, Vol. 63, pp. 90–104, 2008.

196. Kittel, T.G.F., Giorgi F. and G.A. Meehl, "Intercomparison of Regional Biases and Doubled CO2 Sensitivities of Coupled Atmosphere–Ocean General Circulation Model Experiments", *Climate Dynamics*, Vol. 14, pp. 1–15, 1998.

197. Giorgi, F. and R. Francisco, "Evaluating Uncertainties in The Prediction of Regional Climate Change", *Geophysical Research Letters*, Vol. 27, pp. 1295–1298, 2000.

198. Giorgi, F., P.H. Whetton, R.G. Jones, J.H. Christensen, L.O. Mearns, B. Hewitson, H. von Storch, R. Francisco and C. Jack, "Emerging Patterns of Simulated Regional Climatic Changes for The 21st Century Due to Anthropogenic Forcings", *Geophysical Research Letters*, Vol. 28, pp. 3317–3320, 2001.

199. Giorgi, F. and X. Bi, "Regional Changes in Surface Climate Interannual Variability for The 21st Century From Ensembles of Global Model Simulations", *Geophysical*

Research Letters, Vol. 32, No. 13, L13701, 2005.

200. Giorgi, F. and X. Bi, “Updated Regional Precipitation and Temperature Changes for The 21st Century From Ensembles of Recent AOGCM Simulations”, *Geophysical Research Letters*, Vol. 32, No. 21, L21715, 2005.

201. Lelieveld, J., P. Hadjinicolaou, E. Kostopoulou, J. Chenoweth, C. Giannakopoulos, C. Hannides, M.A. Lange, M. El Maayar, M. Tanarthe, E. Tyrlis and E. Xoplaki, “Climate Change and Impacts in The Eastern Mediterranean and The Middle East”, *Climatic Change*, Vol. 114, pp. 667–687, 2012.

202. Kripalani, R.H., J.H. Oh, A. Kulkarni, S.S. Sabade and H.S. Chaudhari, “South Asian Summer Monsoon Precipitatioin Variability: Coupled Climate Model Simulations and Projections Under IPCC AR4”, *Theoretical and Applied Climatology*, Vol. 90, pp. 133–159, 2007.

203. Sheffield, J. and E.F. Wood, “Projected Changes in Drought Occurrence Under Future Global Warming from Multi-Model, Multi-Scenario, IPCC AR4 Simulations”, *Climate Dynamics*, Vol. 31, pp. 79–105, 2008.

204. Giorgi, F., “Climate Change Hot-Spots”, *Geophysical Research Letters*, Vol. 33, L08707, 2006.

205. Machenhauer, B., M. Windelband, M. Botzet, J.H. Christensen, M. Deque, R.G. Jones, P.M. Ruti, and G. Visconti, “Validation and Analysis of Regional Present-Day Climate and Climate Change Simulations over Europe”, *MPI Report*, No. 275, Max-Planck-Institut für Meteorologie, Hamburg, Germany, 1998.

206. Deque, M., R.G. Jones, M. Wild, F. Giorgi, H. Christensen, D.C. Hassell, P.L. Vidale, B. Rockel, D. Jacob, E. Kjellstrom, M. de. Castro, F. Kucharski and B. van den Hurk, “Global High Resolution vs. Regional Climate Model Climate Change Scenarios over Europe: Quantifying Confidence Level from PRUDENCE Results”, *Climate Dynamics*, Vol. 25, pp. 653–670, 2005.

207. Giorgi, F., M.R. Marinucci and G. Visconti, “A 2XCO2 Climate Change Scenario over Europe Generated Using A Limited Area Model Nested in A General Circulation Model. II: Climate Change Scenario”, *Journal of Geophysical Research*, Vol. 97, pp. 10011–10028, 1992.

208. Rotach, M.W., M.R. Marinucci, M. Wild, P. Tschuck, A. Ohmura and M. Beniston, “Nested Regional Simulation of Climate Change over The Alps for The Scenario of Doubled Greenhouse Gas Forcing”, *Theoretical and Applied Climatology*, Vol. 57, pp. 209–227, 1997.

209. Giorgi, F., J.W. Hurrell, M.R. Marinucci, and M.Beniston, “Elevation Signal in Surface Climate Change: A Model Study”, *Journal of Climate*, Vol. 10, pp. 288–296, 1997.

210. Deque, M., P. Marquet, and R.G. Jones, “Simulation of Climate Change over Europe Using A Global Variable Resolution General Circulation Model” *Climate Dynamics* , Vol. 14, pp. 173–189, 1998.

211. Raisanen, J., M. Rummukainen, A. Ullerstig, B. Bringfelt, U. Hansson and U. Willén, “The First Rossby Centre Regional Climate Scenario — Dynamical Downscaling of CO2-Induced Climate Change in The Hadcm2 GCM”, *SHMI Reports Meteorology and Climatology*, No. 85, Swedish Meteorological and Hydrological Institute, Norrkoping, Sweden, 1999.

212. Christensen, J.H. and O.B. Christensen, “Climate Modeling: Severe Summertime Flooding In Europe”, *Nature*, Vol. 421, pp. 805–806, 2003.

213. Semmler, T. and D. Jacob, “Modeling Extreme Precipitation Events — A Climate Change Simulation for Europe”, *Global and Planetary Change*, Vol. 44, pp. 119–127, 2004.

214. Schar, C., P.L. Vidale, D. Luthi, C. Frei, C. Haberli, M.A. Liniger and C. Appenzeller, “The Role of Increasing Temperature Variability in European Summer

Heatwaves", *Nature*, Vol. 427, pp. 332–336, 2004.

215. Raisanen, J., U. Hansson, A. Ullerstig, R. Doscher, L.P. Graham, C. Jones, H.E.M. Meier, P. Samuelsson and U. Willen, "European Climate in The Late Twenty-First Century: Regional Simulations with Two Driving Global Models and Two Forcing Scenarios", *Climate Dynamics*, Vol. 22, pp. 13–31, 2004.

216. Kjellstrom, E., L. Barring, D. Jacob, R. Jones, G. Lenderink, and C. Schär, "Modeling Daily Temperature Extremes: Recent Climate and Future Changes over Europe", *Climatic Change*, Vol. 81, pp. 249–265, 2007.

217. Alpert, P., S.O. Krichak, H. Shafir, D. Haim and I. Osetinsky. "Climatic Trends to Extremes Employing Regional Modeling and Statistical Interpretation over The E. Mediterranean", *Global and Planetary Change*, Vol. 63, pp. 163–170, 2008.

218. Beniston, M., D.B. Stephenson, O.B. Christensen, C.A.T. Ferro, C. Frei, S. Goyette, K. Halsnaes, T. Holt, K. Jylha, B. Koffi, J. Palutikof, R. Scholl, T. Semmler and K. Woth, "Future Extreme Events In European Climate: An Exploration Of Regional Climate Model Projections", *Climatic Change*, Vol. 81, pp. 71–95, 2007.

219. Gao, X., J.S. Pal and F. Giorgi, "Projected Changes in Mean and Extreme Precipitation over The Mediterranean Region from High Resolution Double Nested RCM Simulations", *Geophysical Research Letters*, Vol. 33, L03706, 2006.

220. Kjellstrom, E., "Recent and Future Signatures of Climate Change in Europe", *Ambio*, Vol. 33, pp. 193–198, 2004.

221. Ozturk, T., M. Türkeş and M. L. Kurnaz, "Projected Changes in Air Temperature and Precipitation Climatology in Turkey by Using Regcm 4.3", *In: Proceedings of European Geosciences Union General Assembly 2013*, Vienna, 2013.

222. Meehl, G. A., C. Covey, T. Delworth, M. Latif, B. McAvaney, J. F. B. Mitchell, R. J. Stouffer, and K. E. Taylor, "The WCRP CMIP3 Multi-Model Dataset: A New

Era in Climate Change Research", *Bulletin of the American Meteorological Society*, Vol. 88, pp. 1383-1394, 2007.

223. Wood, A. W., L.R. Leung, V. Sridhar and D. P. Lettenmaier, "Hydrologic Implications of Dynamical and Statistical Approaches to Downscaling Climate Model Outputs", *Climatic Change*, Vol. 62, pp. 189–216, 2004.

224. Maurer, E.P., J.C. Adam and A.W. Wood, "Climate Model Based Consensus on The Hydrologic Impacts of Climate Change to The Rio Lempa Basin of Central America", *Hydrology and Earth System Sciences*, Vol. 13, pp. 183-194, 2009.

225. Adam, J. C. and D. P. Lettenmaier, "Adjustment of Global Gridded Precipitation for Systematic Bias", *Journal of Geophysical Research*, Vol. 108, No. D9, 2003.

226. Coppola, E. and F. Giorgi., "An Assessment of Temperature and Precipitation Change Projections over Italy from Recent Global and Regional Climate Model Simulations", *International Journal of Climatology*, Vol. 30, pp. 11–32, 2010.

227. Giorgi, F., "Climate Change Prediction", *Climatic Change*, Vol. 73, pp. 239-265, 2005.